JUSTUS-LIEBIG-
UNIVERSITÄT
GIESSEN

Development of mass spectrometric tools for the structural characterization of glycosphingolipids in parasitic samples

Cumulative dissertation

by

David Luh, geb. Lüke

Submitted to the

Faculty of Biology and Chemistry (FB08)

and prepared at the

Institute of Inorganic and Analytical Chemistry

for the degree of

Doctor rerum naturalium (Dr. rer. nat.)

Justus Liebig University Giessen, Germany

Giessen 2025

This thesis was accepted as a doctoral dissertation in fulfillment of the requirements for the degree of *Doctor rerum naturalium* by the Faculty of Biology and Chemistry, Justus Liebig University Giessen, Germany

1. Referee: Prof. Dr. Bernhard Spengler

2. Referee: Prof. Dr. Sven Heiles

Table of Content

List of Publications

This thesis is based on the following two publications:

Publication I:

D. Luh, S. Heiles, M. Roderfeld, C. G. Grevelding, E. Roeb, B. Spengler, Hepatic Topology of Glycosphingolipids in Schistosoma mansoni-Infected Hamsters, *Analytical Chemistry* **2024,** *96* (16), 6311-6320, doi: 10.1021/acs.analchem.3c05846

Publication II:

D. Luh, S. Gramberg, P. Ghezellou, S. Heiles, S. Haeberlein, B. Spengler, Glycolipidomics of Liver Flukes and Host Tissues during Fascioliasis: Insights from Mass Spectrometry Imaging, *ACS Infectious Diseases* **2024**, 10 (12), 4233-4245, doi: 10.1021/acsinfecdis.4c00551

Further Publications:

P. Ghezellou, V. von Bülow, **D. Luh**, E. Badina, W. Albuquerque, M. Roderfeld, E. Roeb, C. G. Grevelding, B. Spengler, Schistosoma mansoni infection induces hepatic metallothionein and S100 protein expression alongside metabolic dysfunction in hamsters; *PNAS Nexus* **2024**, 3 (4), 104, doi: 10.1093/pnasnexus/pgae104

J.-P. Kanter, P. J. Honold, **D. Luh**, S. Heiles, B. Spengler, M. A. Fraatz, H. Zorn, A. K Hammer, Biocatalytic Production of Odor-Active Fatty Aldehydes from Fungal Lipids, *J. Agric. Food Chem.* **2023**, 71 (21), 8112–8120, doi: 10.1021/acs.jafc.3c01972

J.-P. Kanter, P. J. Honold, **D. Lüke**, S. Heiles, B. Spengler, M. A. Fraatz, C. Harms, J. P. Ley, H. Zorn, A. K. Hammer, An enzymatic tandem reaction to produce odor-active fatty aldehydes, *Appl. Microbiol. Biotechnol.* **2022**, 106, 6095–6107, doi: 10.1007/s00253-022-12134-3

List of Abbreviations

2,5-dihydroxyacetophenone	DHAP
atmospheric pressure	AP
collision-induced dissociation	CID
Dalton	Da
electrospray ionization	ESI
exudative-productive	EP
Fasciola	*F*.
Fourier transform ion cyclotron resonance	FT-ICR
GalNAcβ1-4(Fucα1-3)GlcNAc	LDN-F
GalNAcβ1-4GlcNAc	LDN
Galβ1-4(Fucα1-3)GlcNAc	Lewis X
glycosphingolipids	GSLs
haematoxylin and eosin	H&E
hepatic stellate cells	HSC
higher collision induced fragmentation	HCD
(ultra)-high performance liquid chromatography	(U)HPLC
hydrophilic interaction liquid chromatography	HILIC
liquid chromatography	LC
Galβ1–4GlcNAc	LN
macrophage Gal/GalNAc lectin 2	MGL2+
mass drug administration	MDA
mass spectrometry	MS
mass spectrometry imaging	MSI
mass-to-charge-number ratio	*m*/*z*
matrix-assisted laser desorption/ionization	MALDI
neglected tropical diseases	NTDs
newly excysted juveniles	NEJ
parts per million	ppm
phosphatidylcholine	PC
phosphatidylinositol	PI
pre-granulomatous exudative	PGE
principal component analysis	PCA
red-green-blue	RGB
region of interest	ROI
reversed-phase chromatography	RPC
Schistosoma	*S*.
species pluralis	*spp*.
tandem MS	MS/MS
time-of-flight	TOF
triglycerides	TGs
T helper type-1	Th1
T helper type-2	Th2
ultra-long chain fatty acids	ULCFA
ultraviolet photodissociation	UVPD
world health organization	WHO

Abstract

In this dissertation, the analyses of glycosphingolipids (GSLs) in parasitic samples was addressed. For this, the combination of mass spectrometry imaging (MSI) and nano liquid chromatography mass spectrometry (nano-LC MS) data yielded an overview about GSLs on a molecular level in parasitic samples. Especially the MSI data for each model system, which was investigated, were necessary to pinpoint possible functions of GSLs.

In a first project, *Schistosoma* (*S*.) *mansoni*-infected hamsters were selected as a model system for schistosomiasis. Here, the incorporation of *S*. *mansoni* eggs in the liver of the hamster provokes an immune response, leading to granuloma formation, which is the main cause of chronic pathogenesis. For the bulk-analysis, experimental parameters such as the extraction and purification of GSLs and the nano-LC MS analysis, were optimized. The statistical data analysis revealed a significant upregulation of GSL species compared to control groups. To associate different GSL species more specifically to the host-parasite interaction, MSI experiments were performed. But first, the matrix application of 2,5-dihydroxyacetophenone was optimized for high-resolution MSI down to 3 µm step size. With the MSI workflow, GSL species were unambiguously localized within granulomas. Even substructures within the granulomas and the *S*. *mansoni* eggs were revealed. There are strong indications that observed distributions of specific GSL species matched immune cells, which are subsequently recruited during the immune response. In addition, a semi-quantitative evaluation of MALDI MSI data is proposed. The evaluation is in-line with the semi-quantitative data analysis of the nano-LC MS experiments, demonstrating that the MSI methodology is suitable for qualitative and semi-quantitative analyses.

In the second project, the GSLs during a *Fasciola hepatica* infection were in focus. First, the nano-LC MS method was validated for isolated adult *F*. *hepatica* through comparison with the literature. Besides already reported GSL species, we were able to identify previously unknown GSL species for *F*. *hepatica*. Further, we analysed the acute and chronic infection stage of rats, infected with *F*. *hepatica*. For this, a semi-automatic data analysis was established, reducing the analysis time of the nano-LC MS data drastically. To study the host-parasite interaction in more depth, MSI experiments were performed with liver of rats during the acute infection stage. Here, the immature *F*. *hepatica* is migrating through the liver parenchyma, causing severe damage to the host. Again, distributions of specific GSL species were correlated to potential immune cell distributions. This is also true for other lipid classes, which were simultaneously detected during the MSI experiments. Furthermore, MSI experiments of isolated *F*. *hepatica* may help to better understand the metabolism of GSL species. The comparison to immature *F*. *hepatica* also revealed variations in GSL distributions and contributes to a better understanding of the development of *F*. *hepatica*.

Overall, the developed method allows researchers to structurally and locally study the GSL profile in parasitic samples. The method is also applicable for other sample systems. Additionally, to further improve the sensitivity for GSL detection in MSI experiments, which is a perquisite for on-tissue tandem MS experiments, salt doping MSI experiments were performed with isolated adult *F*. *hepatica*. Compared to normal MSI experiments, an increased number of GSL distributions were revealed, providing a promising outlook to further extended studies on GSLs.

Zusammenfassung

In der vorliegenden Dissertation wurde eine Methode für die Analyse von Glykosphingolipiden (GSLs) in parasitären Proben entwickelt und angewandt. Die Kombination der orthogonalen Datensätze der bildgebenden Massenspektrometrie (MSI) und der nano-Flüssigkeitschromatographie (nano-LC) ermöglichen einen Überblick über verschiedene Spezies von GSLs in parasitären Proben. Insbesondere die räumlich aufgelöste Verteilung einzelner Spezies im jeweiligen Modelsystem liefert Hinweise auf deren mögliche Funktionen.

In einem ersten Projekt wurden die Methoden der MSI sowie die der nano-LC für die Analytik von GSLs verbessert. Als Modelsystem wurden *S. mansoni*-infizierte Hamster gewählt. Die Einlagerung von *S. mansoni*-Eiern im Lebergewebe führt hierbei zu einer Granulombildung um die Eier. Dies ist die Hauptursache für die chronische Pathogenese der Infektion. Es wurden für die Bulk-Analyse experimentelle Parameter der GSL-Extraktion, der Probenvorbereitung und der nano-LC-Analyse optimiert. Anhand der Daten wurde durch eine statistische Auswertung eine ausgeprägte Hochregulierung der GSL-Spezies im Lebergewebe während der Infektion im Vergleich zu Kontrollgruppen festgestellt. Um neben den Bulk-Daten auch die räumliche Verteilung der GSL-Spezies aufzulösen, wurde für die MSI die Matrixapplikation von 2,5-Dihydroxyacetophenon für räumlich hochaufgelöste Experimente (bis zu 3 µm Schrittgröße) optimiert. So konnten eindeutig GSL-Spezies in den Granulomen identifiziert und auch die Substruktur der Granulome durch verschiedene spezifische GSL-Signale aufgelöst werden, ebenso wie eine Substruktur in *S. mansoni*-Eiern. Als Ergebnisse lassen sich so Zuordnungen von spezifischen GSL zu bestimmten Immunzellen während der subsequent ablaufenden Immunreaktion treffen. Zudem wurde eine semi-quantitative Auswertung der MSI-Daten vorgeschlagen, welche im Einklang mit den nano-LC-Daten ist. Dies demonstriert, dass unsere MSI-Methode zuverlässige Ergebnisse, sowohl qualitativ als auch semi-quantitativ, liefert.

In einem weiteren Projekt wurde die entwickelte Methode im Zusammenhang mit einer *F. hepatica*-Infektion angewandt. Zunächst wurde die optimierte nano-LC-Methode für isolierte adulte *F. hepatica* angewandt und ein Vergleich mit der Literatur angestellt. Neben den bereits bekannten GSL-Spezies, konnten weitere, bisher unbekannte GSL-Spezies identifiziert werden. Zudem wurden die Stadien der akuten und chronischen Infektion anhand des Modelsystems Ratte verglichen. Um die nano-LC-Datensätze von insgesamt sechs verschiedenen biologischen Gruppen, gemessen in biologischen und technischen Replikaten, zu analysieren, wurde eine semi-automatische Datenauswertung etabliert. Die akute *F. hepatica*-Infektion wurde mittels MSI untersucht, um die Wirts-Parasiten-Wechselwirkung *in situ* zu studieren. Während dieses Infektionsstadiums migrieren immature *F. hepatica* durch das Lebergewebe. Hierdurch konnten erneut GSL-Spezies identifiziert werden, welche potentiell die Verteilung von Immunzellen widerspiegeln. An dieser Stelle wurden die MSI-Experimente, wenn auch für GSLs optimiert, für weitere Lipidklassen analysiert und auch hier ein möglicher Zusammenhang mit Immunzellen aufgedeckt. Es wurden weiterhin, durch zusätzliche MSI-Experimente von isolierten *F. hepatica,* mögliche Rückschlüsse auf den Metabolismus von GSL erhalten. Der Vergleich zu immaturen *F. hepatica* konnte zudem Unterschiede von GSL-Verteilungen aufdecken und trägt bei, die Entwicklung von *F. hepatica* besser zu verstehen.

Zusammengefasst wurde eine Methodik entwickelt, um zuverlässig und umfassend ein GSL-Profil in parasitären Proben mit räumlicher Auflösung zu erhalten. Um die Sensitivität von GSL-Spezies in MSI-Experimenten weiter zu steigern, werden erste vielversprechende Ergebnisse für das Salzdoping für MSI-Experimente mit *F. hepatica* vorgestellt. Hierdurch konnten über das zweite Projekt hinaus weitere Verteilungen von GSL-Spezies aufgedeckt werden.

Chapter I – Synopsis

Mass Spectrometry

Mass spectrometry (MS) is a powerful analytical technique used to determine the mass-to-charge-number ratio (*m*/*z*) of ionized compounds. In a mass spectrum, the *m*/*z*-value is plotted on the x-axis, while the signal intensity is plotted on the y-axis. The signal intensity is related to the abundance or concentration of the analyte. A higher signal intensity generally indicates a higher concentration and a larger number of ions for the same molecular species with a specific *m/z* value being detected. This allows MS to provide both, qualitative analysis, by identifying compounds based on their *m/z* values, and quantitative analysis, by measuring concentration-related signal intensities of analytes.[1]
The mass resolution *R* and the mass accuracy *Δm*/*m* are two important instrument parameters for interpreting a mass spectrum. The mass resolution, defined in Eq. 1, describes the capability to separate neighbouring *m*/*z*-values. To calculate the mass resolution, the mass of a selected ion signal is divided by the full width at half maximum. Besides this 50%-definition, other definitions such as 5% or 0.5% are used.[2]

$$R = \frac{m}{\Delta m} \qquad \text{Equation 1}$$

R = mass resolution
m = mass of a selected peak
Δ*m* = width at 50% of the selected peak

The relative mass accuracy, defined in Eq. 2, describes how a measured accurate mass differs from the theoretical exact mass. Usually, the mass accuracy is given in parts per million (ppm).[1]

$$\frac{\Delta m}{m} = \frac{m_{accu.} - m_{exact}}{m_{exact}} \cdot 10^6 \text{ ppm} \qquad \text{Equation 2}$$

Δm/*m* = mass accuracy
$m_{accut.}$ = measured mass of an ion
m_{exact} = theoretical (calculated) exact mass of an ion

Important key features of modern MS are high mass resolution and high mass accuracy, but also low limit of detection, and high speed of analysis. Together, these characteristics facilitate the analysis of complex biological samples, setting MS as an indispensable analytical method in life sciences.[3,4] However, the fundamental development for modern MS dates back to the year 1898, when W. Wien (Nobel prize in 1911) used magnetic deflection to analyse rays carrying a positive charge.[5] By modifying Wien's apparature, J.J. Thomson (Nobel prize in 1906) built what is recognized as the first mass spectrometer and in 1912 reported the first mass spectrums for N_2, O_2, CO_2, CO and $COCl_2$.[6] Soon, in 1918, A.J. Dempster developed a more modern mass spectrometer, using magnetic fields for focusing and in 1919, F. W. Aston (Nobel prize in 1922) utilized velocity focusing in MS for the first time.[7,8] Since then, many outstanding contributions were made in the field of MS, so that nowadays, many different types of mass spectrometers are available. They share the same building blocks, which are the ion source, the mass analyzer and the detector. It is essential that the mass analyzer and detector are operated in high vacuum, whereas the ion source can be operated under atmospheric pressure (AP) as well.[9]
The existing mass spectrometers can be classified according to the mass analyzer used. One of the most prevalent are time-of-flight (TOF) mass analyzers. The concept was already described in 1946 from W. Stephens, and the first instrument was introduced by A. E. Cameron and D. F. Eggers in 1948.[10,11] Another frequently employed mass analyzer is the quadrupole ion trap, first described in 1953 by W. Paul, who received the Nobel prize in 1989 for his invention.[12] Further innovations led to the Fourier transform ion cyclotron resonance (FT-ICR) mass spectrometer, which is a high-resolution

mass analyzer, developed by M. B. Comisarov and A. G. Marshall in 1974.[13] The most recent type of mass analyzer, which was used throughout this doctoral thesis, is the Orbitrap mass analyzer.
The fundamentals of orbital trapping were already applied in the Kingdon trap in 1923 and further developed in 1983 by R. D. Knight.[14,15] However, it was until 2000 when A. Makaraov introduced the Orbitrap as a novel mass analyzer.[16] The Orbitrap mass analyzer consists of a spindle-shaped inner electrode and an outer barrel-shaped electrode, which is divided into two separate electrodes. Ions, which are trapped inside the analyzer, move in orbits around the central electrode, but also oscillate along the z-axis. Importantly, this movement along the z-axis is independent of the other motions. It can be described as a harmonic oscillator with the frequency ω, which is only dependent on the charge number *z* and mass *m*.

$$\omega = \sqrt{\frac{z}{m} \cdot k} \qquad \text{Equation 3}$$

ω = frequency of the oscillation along the z-axis
z = charge of the ion
m = mass of the ion
k = instrumental constant

During the movement, the ions induce an image current on the outer electrodes, which is subsequently transformed via Fourier transformation into a mass spectrum. This can be done with high accuracy. Thus, in addition to FT-ICR and multipass TOF MS, another high-resolution mass analyzer has been developed.[17] Compared to FT-ICR mass analyzers, an Orbitrap is working with an electrostatic field instead of a magnetic field, which has the advantage that no complex cooling using liquid helium is required.
In addition to the choice of mass analyzer, ion formation plays an equally important role during mass spectrometric analysis.[18] Formation of ions in the gas phase can be achieved by different techniques, which can be grouped into hard- and soft ionization techniques. Hard ionization techniques, such as electron impact ionization, lead to excessive fragmentation of the analytes.[19] This can be helpful for elucidating structures of small isolated compounds, for example of reaction products from organic synthesis.[20] However, for complex biological samples consisting of large and sensitive molecules such as proteins, lipids, or carbohydrates, fragmentation during ionization is inappropriate for the interpretation of the resulting mass spectra. Here, the development of soft-ionization techniques like matrix-assisted laser desorption/ionization (MALDI) and electrospray ionization (ESI) marked a historical breakthrough.[21–24]
ESI, with the principles introduced in 1964 and 1968 by Sir G. Taylor and M. Dole, who failed to successfully introduce ESI because of limited experimental setup, was demonstrated to work in 1988 by J. Fenn (Nobel prize in 2002).[23,25,26] In this work, protein ions with a mass larger than 5000 Dalton (Da) were transferred into the gas phase and subsequently analyse. Since then, ESI was further developed making it the most widespread ionization technique in MS of large biomolecules.[23]
The ionization process in ESI begins by transferring a liquid through a stainless-steel capillary to which a voltage of several kilovolts versus the counter electrode (MS inlet) is applied. The voltage causes a charge separation within the liquid. As a result, the so-called Taylor cone is formed, an equilibrium between the surface tension, pulling the liquid back into the capillary and the electrostatic coulomb attraction, where the liquid is pulled by the counter electrode. From the tip of the cone a fine mist is emitted, rapidly forming a fine spray. Subsequently, the neutral solvent evaporates, and the surface charges increase until the Rayleigh limit is reached and the droplets split into smaller, secondary droplets. This cascade repeats several times until small droplets with diameters in the nanometer range are formed.[27] The final formation of the ions is still not fully understood. Different mechanisms were developed with the ion evaporation model, mainly for small molecules, and the charge residue model, for lager ions such as proteins, being widely accepted.[28]
In addition to the soft ionization of large biomolecules, ESI has other advantages that are particularly useful for applications in the life sciences. Among others, it is an ionization technique operated under AP conditions, thus simplifying sample handling.[23] Further, ESI can generate both, singly and multiple

charged ions. Usually, $[M+zH]^{z+}$ ions are generated, with *z* depending on the type and size of the molecule.[28] A major advantage of multiple charged ions is that large molecules such as proteins, can readily be analysed by mass spectrometers with a limited *m*/*z* range. Together with the tolerance of different flow rates (µL/min to mL/min) and various solvent compositions of the liquid, ESI is also ideally suited for the combination with liquid chromatography (LC).[29,30]

Nano-ESI is a miniaturized version of conventional ESI. The main difference in the design of the ion source is the much smaller diameter of the capillary tip, which is in the range of a few micrometers for nano-ESI.[31,32] Compared to conventional ESI, nano-ESI has the advantages that it requires considerably less solvent and that the spray process starts with smaller droplets.[33] This brings some benefits. In general, the sensitivity of the analysis is increased as less analyte is lost.[34] The tolerance to salts is also improved.[33,35] Furthermore, the analysis of non-surface-active analytes is improved. Literature indicates that the analysis of oligosaccharides or glycoproteins is facilitated using nano-ESI compared to analysis using ESI.[36,37] However, the disadvantages of nano-ESI are the fragile emitters and decreased reproducibility compared to ESI.[37] This is partly due to the positioning of the emitter, which often requires adjustment for each analysis.

MALDI, the second pioneering ionization method for use in the life sciences, was developed in the 1980s by M. Karas and F. Hillenkamp. Already in 1985, M. Karas and F. Hillenkamp showed that laser-light-absorbing amino acids support the ionization of non-absorbing amino acids.[21,24] Then, in 1987, they used different organic matrices to improve the detection of non-volatile compounds.[21] At the same time, Tanaka used ultrafine cobalt powder in glycerol to desorb and ionize proteins with molecular masses of up to 100,000 Da, for which he received the Nobel Prize in 2002.[22] Today, the use of organic matrices instead of ultra-fine cobalt powder in glycerol is established.

For a successful MALDI MS experiment, the choice of matrix is of utmost importance and different requirements should be met by the matrix.[38] For matrix application, it is important that the solubility of the matrix is compatible with the solubility of the analytes. There are different methods of matrix application. Traditionally, the dried droplet method was used.[39] Here, the analyte and matrix solutions are mixed, deposited onto a surface and dried under ambient conditions. Although fast and easy to perform, there are inhomogeneities in analyte/matrix crystals.[40] More advanced methods include pneumatic spraying or sublimation of the matrix to get homogenous matrix layers.[41] Nowadays, the application is automated, and different commercial devices are available.

The matrix itself must also have good miscibility with the analytes, as this results in co-crystallization in the solid state of matrix and analyte molecules.[42] Furthermore, a large excess of matrix is required in comparison to the analytes in order to isolate the analyte molecules from each other.[43] This also ensures that the energy of the laser is absorbed mostly by the matrix. Therefore, when selecting the matrix, it must be considered that the matrix has strong absorption of the laser wavelength, which is often in the ultraviolet range for MALDI experiments.[44] Furthermore, the matrix should have good co-desorption and support the ionization of the analyte molecules.[38] However, the ionization mechanism of MALDI is still not fully understood.[45] When dividing the ionization mechanism into primary ionization and secondary reactions, the formation of the primary matrix ions in particular remains controversial. Secondary processes, on the other hand, can be explained using classical reaction kinetics and thermodynamic principles.[45] Traditionally, MALDI MS was performed under vacuum, but at the beginning of the 2000s, various approaches for atmospheric-pressure (AP)-MALDI were introduced.[46,47] To support the transport of the ions generated under AP, a high voltage is applied to the conductive MALDI probe. The ionization mechanism is comparable to vacuum MALDI, yielding mainly singly-charged, protonated, sodiated or potassiated quasimolecular ions in the positive-ion mode and deprotonated species in the negative-ion mode. However, non-vacuum-stable matrices as well as volatile samples are more easily analysed with AP-MALDI MS. In addition, soft collisions of the desorbed matrix molecules and analytes with gas molecules provide an additional cooling effect, as vibrational energy can dissipate. As a result, fragmentation processes are reduced, making AP-MALDI even softer than conventional MALDI.

Mass Spectrometry Imaging

In the life sciences, revealing the spatial distribution of biomolecules in tissues or cells is inevitable to understand local biochemical processes. For this purpose, mass spectrometry imaging (MSI) is ideally suited.[48,49] Outstanding features of MSI are little to no sample preparation, non-targeted and label-free analysis. Additionally, data of hundreds to thousands of biomolecules can be acquired within one single experiment. Compared to traditionally performed methods such as optical or fluorescence microscopy, more structural, molecular information is obtained. If staining or labelling is applied in microscopy one must know the targets before the experiment and is limited to the available antibodies. The underlying work for MSI of biomolecules was introduced in 1994 by B. Spengler, using MALDI MSI for the spatially resolved, intact ionization of Substance P.[50] Later, MALDI MSI was applied to the analysis of animal tissue sections.[51] To date, MALDI MSI is still the most common MSI technique for the analysis of biomolecules because of its versatility regarding substance classes, softness and high lateral resolution of routinely 5-20 µm.[52] With the aim of using MALDI MSI for single cell analysis, spatial resolutions of 1.4 µm have already been achieved in recent work.[53]

However, a higher spatial resolution with a smaller laser focus results in less ablated material, and therefore fewer ions are generated. A promising, instrumental approach to enhance the ion yield is post-ionization, termed MALDI-2 in the literature.[54] Here, a second laser is directed to the MALDI plume, and it has been shown, that the intensity for non-polar lipids and metabolites is increased by several orders of magnitude in several cases. However, the implementation of a second laser makes MALDI-2 an instrumentally complex and expensive methodology.

Another challenge for high spatial resolution experiments is the focal depth of the laser, which gets smaller for a more focused laser beam. For a laser focus of 1.4 µm the focal depth is <6 µm, and even "flat" tissue sections have height differences, which can be larger than the focal depth. An elegant workaround was the implementation of a triangulating autofocusing system, enabling high spatial resolution measurements with stable laser fluence and laser spot size and 3-dimensional measurements of, for example, biological surfaces such as those of *Schistosoma* (*S*.) *mansoni* worms.[55,56]

For the analysis of large biomolecules, such as intact proteins, MALDI is preferentially coupled to TOF analyzers, because there is no theoretical limitation in the mass range.[57] However, for the analysis of small molecules, like metabolites or lipids, high mass resolution and accuracy is a prerequisite to get reliable annotations from the complex mass spectra.[58] Here, state-of-the art is the coupling of the imaging ion source to high mass resolution and high accuracy orbitrap devices, utilizing the C-trap to collect ions deriving from the desorption process initiated by the high-energetic, short-pulsed laser probe.[58]

Beside choosing the best instrumentational setup for the MALDI MSI analysis, sample preparation is another crucial building block for a successful experiment. In a first step, thin, flat cryo-sections are prepared using either fresh frozen or formalin-fixed paraffin-embedded samples.[59] Different factors, such as orientation of fixation, temperature, cutting angle, and fragility of the sample must be considered when optimizing the cutting protocol. A common approach is embedding of the sample, especially important for small sensitive samples, such as parasites.[60] For this it is necessary that the embedding media do not interfere with the MALDI MSI analysis. Afterwards, optional sample preparation steps can be included, which can be derivatization strategies to enhance the ionization efficacy, washing procedures, or on-tissue digestions.[61–66]

Next, matrix selection and application are crucial. There is no matrix available covering all molecule classes equally well. The development of novel matrices is still an ongoing field to improve MALDI MSI analysis, even reactive matrices for on-tissue structure elucidation are available.[38,67] Therefore, careful selection of the matrix for the own purpose is important. The matrix application for MALDI MSI experiments is usually performed by pneumatic spraying or sublimation to cover the dried sample with

a homogenous matrix layer.[41] The extraction and incorporation into the matrix of analyte molecules is stronger for pneumatic spraying and, as a result, higher signal intensities are obtained.[53] However, the solubility of matrices in adequate spraying solvents can be limited and therefore, developing a spraying protocol may be demanding. In addition, the crystal size of the matrix must be smaller than the step size of the MALDI MSI experiment. Especially, for high spatial resolution experiments this can be challenging for pneumatic spraying. In this regard, sublimation can prove beneficial.[68]

For the actual MALDI MSI measurement, the sample is attached to a sample holder and placed into the ion source. Then, typically a rectangular region of interest (ROI) with a defined step size is determined. Other parameters which can be chosen are the mass range, mass resolution, ion source settings as well as the energy of the laser. Here, careful selection of the laser energy, to avoid ablation spots larger than the step size (oversampling), is crucial.[49] During the measurement, the laser rasterizes across the sample in the defined ROI, generating a mass spectrum for each spot. For data analysis, different software solutions, like Mirion, MSI Reader or SCILS, are available.[69–72] All have in common that ion-images can be generated which show the distribution and signal intensities in a heat map for a selected *m*/*z* value within the sample. It is also common to show red-green-blue (RGB) ion-images, with each colour channel representing the distribution of a chosen *m*/*z* value. To get biological information out of the experiment, databases, such as METASPACE, can be used to annotate the observed signals (e.g. lipids, metabolites, and glycans).[73] However, high mass resolution and accuracy are essential to obtain reliable annotations, and even then there is no absolute certainty that it is an unambiguous annotation.[58] This may be due to isomeric or isobaric compounds with very similar *m*/*z* values. On-tissue tandem MS (MS/MS) experiments can validate annotated species, but the amount of molecular species and the intensities to get information-rich MS/MS spectra is still a challenge in MSI experiments.[74] Another common approach is to compare the data of MSI experiments to LC MS/MS data of the same sample, as both methods show a good orthogonality.[49]

Liquid Chromatography

(Ultra-) high performance liquid chromatography ((U)HPLC) is a highly regarded analytical technique widely employed for the analysis of complex chemical mixtures. It is particularly effective for both qualitative and quantitative assessments of liquid extracts, including those obtained from homogenized biological samples.[75] Its ability to achieve high resolution and sensitivity in separation makes (U)HPLC an invaluable tool in various fields, including pharmaceutical research, environmental analysis, and biochemistry. While chromatography was introduced in 1903 by M. Tswett[76], and the principles and fundamental techniques were awarded with the Nobel prize in 1952 for A. J. P. Martin and R. L. M. Synge[77], HPLC had its breakthrough in the 1960s.[78–82] As the development progressed stepwise, it is difficult to name pioneers without missing important contributors, but often J.F. Huber, J.J. Kirkland, C. Horvath and J. C. Giddings are considered as the early pioneers of HPLC.[83] Generally, in HPLC analysis a defined mixture of analytes, such as extracts from biological samples, is transported through a column by a pressurized liquid known as the mobile phase. Within the column, which contains the stationary phase, the analytes are separated based on their differing strength of interaction with the stationary phase. The mobile phase composition can either remain constant (isocratic elution) or can alter (gradient elution) during the analysis.[84] For analytical needs, stainless-steel columns (1 mm to 4.6 mm inner diameter) are usually packed with small silica particles (<10 µm).[85] As the mixture passes through the column, different analytes form sharp bands due to specific interactions with both the mobile and stationary phase. However, predicting chromatographic separation patterns is complex due to various factors, such as hydrodynamics, pore- and solid diffusion, absorption and desorption processes, and mass transfer reactions.[84]

Types of HPLC can be classified based on the stationary phase used in conjunction with the mobile phase.[84] Commonly employed in the life sciences are reversed-phase chromatography (RPC) and

hydrophobic interaction chromatography, both of which rely on hydrophobic interactions to separate analytes based on their hydrophobicity. Another technique is ion-exchange chromatography, which separates charged molecules. Size exclusion chromatography, which separates molecules based on their size; normal-phase chromatography, which is effective for neutral compounds; and hydrophilic interaction liquid chromatography (HILIC) for polar compounds are further examples.[84,86,87] For detection, ultraviolet/visible detectors are frequently used, along with mass spectrometers, particularly since the advent of electrospray ionization (ESI), which has gained popularity for its sensitivity and ability to analyse complex biological samples.[84]

HILIC, introduced by Alpert in 1990, usually employs organic-rich solvents, mostly acetonitrile, along with a small amount of water as mobile phases.[88,89] Various polar stationary phases are available, including unmodified silica, diol-, amino-, amide-, cyano-, zwitterionic-bonded phases, each offering unique interaction characteristics that can be tailored for specific analyte types. The retention mechanism is still not completely elucidated as different interactions are involved.[87,90,91] Probably the greatest influence on retention and the most widely accepted explanation is the partitioning of analytes between the eluent and the water-rich layer adsorbed on the polar surface of the stationary phase. Nevertheless, not all observations for analyte retention can be solely explained by this, and it is rather a "mixed-mode" retention mechanism. There is evidence that also hydrogen bonding, dipole-dipole interactions as well as electrostatic forces contribute to the retention of analytes.

Additionally, the choice of mobile and stationary phases can significantly influence the resolution and selectivity of the separation, making method optimization crucial for specific applications. HILIC has proven particularly effective in the analysis of small polar molecules, metabolites, and glycoproteins, making it an invaluable tool in various fields, including pharmaceutical development, environmental analysis, and clinical diagnostics.

Nanoscale Liquid Chromatography

Equation 4 describes the dilution of an analyte during a chromatographic separation.[92] From this equation it is obvious that a small column inner diameter reduces sample dilution and therefore increases sensitivity.

$$D = \frac{c_0}{c_{max}} = \frac{\varepsilon_i \pi r^2 (1+k)\sqrt{2\pi LH}}{V_{inj}} \qquad \text{Equation 4}$$

D = dilution
c_0 = initial concentration
c_{max} = final compound concentration at the peak maximum
ε_i = column permeability
r = column radius
k = retention factor
L = column length
H = column plate height
V_{inj} = injection volume

As a consequence, researchers developed capillary- and nano-LC platforms with columns of a small inner diameter, and pioneering work dates back to 1978 and 1979.[93,94] Further advantages of nano-LC compared to HPLC are less solvent consumption and low sample demands.[95] As the bed in the column can be more uniformly packed for columns of smaller inner diameter, the column efficiency and resolution are also improved for nano-LC applications. However, one of the major early challenges was extra-column band broadening.[95] With only low flow rates in the range of nL/min to a few µL/min during the analysis, all parts of the LC system need downscaling, such as the injection system and all possible connections to minimize the void volume. As only low sample volumes can be injected, the

injection system was redesigned. Today, the preconcentration setup is one of the most common designs, allowing to inject larger quantities of the sample.[96] For the hyphenation with MS the introduction of nano-ESI in 1996 allowed to combine the advantages of nano-LC and nano-ESI, which is why this combination is favored.[32,97] Today, the focus is on the development of more stable nano-LC devices (lab-on-a-chip), as the technology is still less robust compared to conventional HPLC due to the low flow rates and sample volumes.[98–100]

Glycosphingolipids

In a living organism, mono-, oligo-, and polysaccharides can be found in a vast diversity. Polysaccharides, which consist by definition of at least eleven monosaccharides linked via an O-glycosidic bond, are named glycans according to the International Union of Pure and Applied Chemistry.[101] However, we will use the term "glycans" also for shorter saccharides, as it is common in the literature. Glycans can exist as free biomolecules, or are covalently linked to a non-saccharide biomolecule and then called glycoconjugates.[102] In vertebrates, glycoproteins (N-glycans and O-glycans), proteoglycans, glycosylphosphatidylinositol anchors, and glycosphingolipids (GSLs) are the most widespread glycoconjugates.[103–105] In general, glycans can mediate intra- or intercellular signalling events, are required for stability and rigidity of cell membranes, and are important for interactions between organisms, like host-pathogen interactions.[106] However, elucidating the glycome is still a challenging field of research for various reasons. For example, glycosylation of the same protein can show microheterogeneity. Additionally, the same glycan motif can have different functions, depending on the type of glycoconjugate, and glycosylation can change when cells are not in their native surrounding.[107–110] It is therefore advantageous to analyse the glycoconjugates in their intact form. Ideally, the spatial distribution of glycans is also preserved during the analysis, as glycans are more important for multicellular interactions than for the development of single cells.[102,110] Additionally, detailed structural analysis of glycans/glycoconjugates is challenging, because of their structural diversity.[111]

For example, GSLs, which are the main class of analytes described throughout this thesis, are amphiphilic molecules.[112] They have a hydrophilic glycan head group linked via a β-glycosidic bond to the C-1 hydroxyl group of a hydrophobic ceramide lipid, representing the backbone. The glycan head group can vary in the number and composition of monosaccharides. Most common monosaccharides as part of GSLs from vertebrates or parasites are shown in Figure 1. They might furthermore be modified by one or more sulfate or acetyl groups.

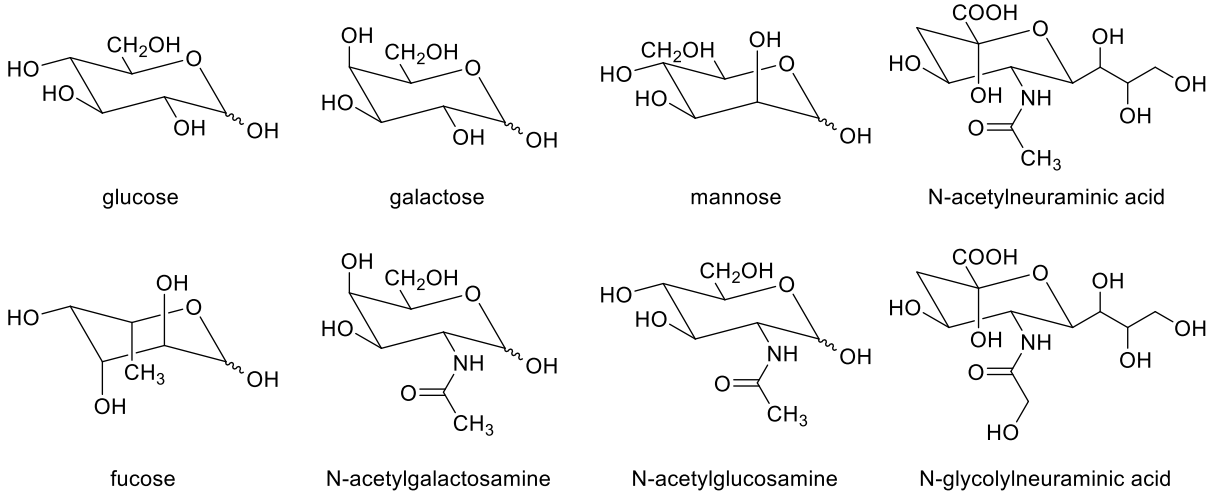

Figure 1: Monosaccharide building blocks commonly found in GSLs of vertebrates and parasites.

If the GSL consists of at least two monosaccharides, the sequence, linkage position, and the configuration of the anomeric C-atoms involved in glycosidic bonding can vary. More structural diversity arises from the heterogeneity of the ceramide backbone. A ceramide is a subclass of sphingolipids, with a sphingoid base linked by an amide bond to a fatty acid. Thereby, the fatty acids vary usually in length between C14 and C36 for humans. The most common sphingoid bases are shown in Figure 2.[105,113] Most frequently, sphingosine is part of the ceramide but other regularly encountered sphingoid bases in vertebrates are sphinganines and phytosphingosines. The latter is the major sphingoid base in plants and is also prevalent in parasites.

Structural variations of the ceramide backbone can be attributed to differing chain lengths, degree of unsaturation, orientation and position of double bonds, and number as well as position of hydroxylation.[114] All these aspects together make the theoretical number of GSLs unimaginably high. However, the actual quantity of existing molecular species is much smaller, because the number of enzymes, responsible for building GSLs, is limited. Yet, with around 600 estimated GSL glycans in combination with hundreds of different ceramides the number of individual GSLs for vertebrates is still expected to be very high.[105] In Figure 3, an intact GSL is shown, with indications that summarize the possible structural variations.

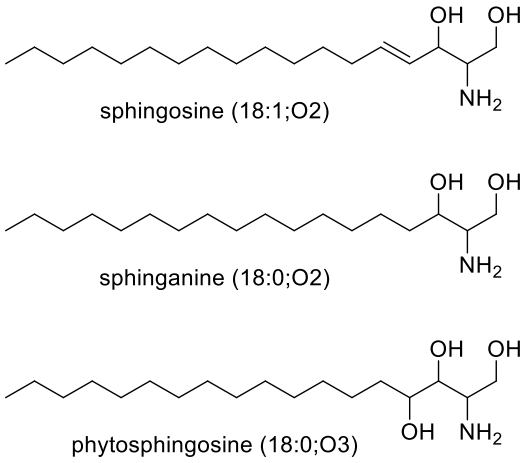

Figure 2: Typical sphingoid bases as part of GSLs in vertebrates and parasites.

To describe GSLs and other lipids, the shorthand nomenclature of LIPIDMAPS and the nomenclature for glycans are used.[115–117] Simple hexoses, like glucose, galactose or mannose, are abbreviated as Hex. Hexosamines are abbreviated as HexNac and fucose as Fuc. The acidic saccharides N-acetylneuraminic acid and N-glycolylneuraminic acid are abbreviated as NeuAc and NeuGc, respectively.

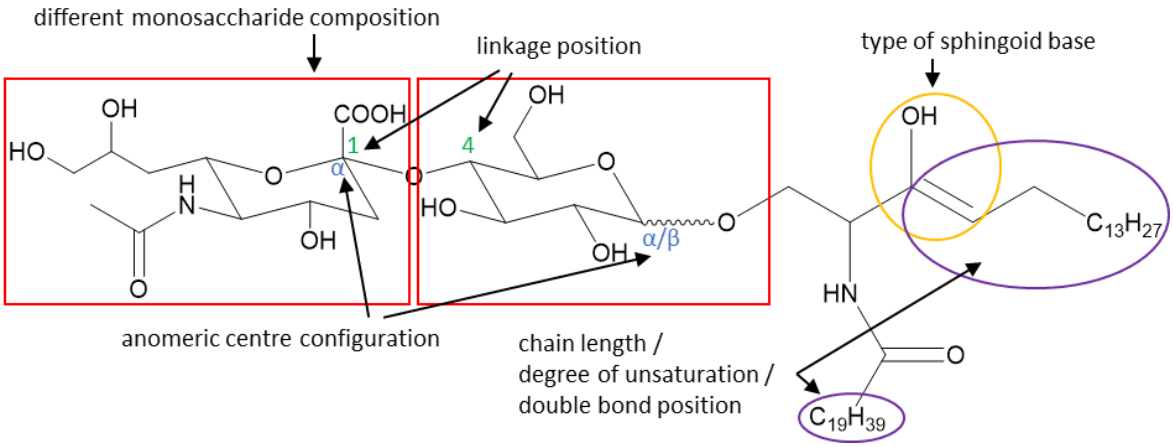

Figure 3: Schematic GSL with indications for the various possible structural variations. For the saccharide head group, different monosaccharide building blocks, different linkage positions or anomeric configurations of the O-glycosidic bond are possible. For the ceramide backbone, the type of sphingoid base can vary as well as the length of both, the sphingoid base and fatty acid. Further, the degree of unsaturation, hydroxylation and double bond position are possible structural variations.

The analysis of GSLs is, as described, very complex for various reasons. To date, it is not possible to characterize all structural features of a GSL with only one analytical method. Typical methods used are thin-layer chromatography, nuclear magnetic resonance, lectin assays, staining, ion mobility spectrometry and liquid chromatography, often in combination with MS.[118–123] Here, MALDI and ESI are the ionization methods of choice, although loss of labile constituents, like sialic acid, and low ionization efficiency of large GSLs have to be considered.[112,124] The low ionization efficiency is mainly attributed to the decreasing hydrophobicity and volatility. High mass resolution devices, such as Orbitrap analysers, are beneficial to distinguish isobars. In routine MS experiments, MS/MS spectra are obtained by low-energy collision-induced dissociation (CID) or higher-energy collision-induced fragmentation (HCD), thereby allowing to determine the composition and sequence of the glycan head group and the composition of the ceramide backbone. However, a known phenomenon is the migration of saccharide residues upon CID experiments, especially for fucose.[125–127] As this phenomenon is attributed to $[M+H]^+$ ions, sequence determination can be performed with $[M+Na]^+$ or $[M-H]^-$ ions. The nomenclature for the diagnostic fragments of GSLs after Domon and Costello and Merrill et al. is indicated in Figure 4.[128,129] For CID/HCD, B/C and Y/Z fragment ions are typical for the glycan head group, and the N^{II} fragment ion for the ceramide backbone, and the fragmentation pattern behaviour is strongly dependent on the ion polarity.[130] Over the years, several other fragmentation methods were applied for GSL analysis, such as electron capture dissociation, radical-directed dissociation, ozone-induced dissociation or ultraviolet photodissociation (UVPD).[131–134] UVPD in particular enables improved structural elucidation of GSLs compared to CID/HCD, because cross-ring fragments (A/X fragment ions) are obtained in addition, which allows isomeric differentiation.

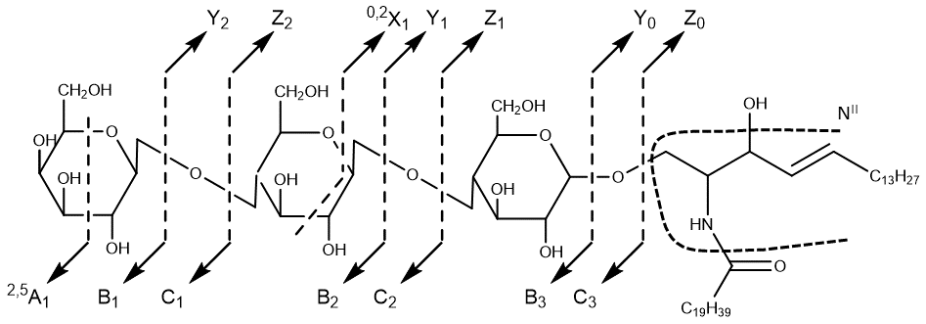

Figure 4: A GSL consisting of three monosaccharide units and a ceramide backbone. Cleavage sites upon fragmentation are indicated by dotted lines resulting in Y-, Z-, B, and C-fragment ions for the glyosidic cleavage of the saccharide units and the N^{II}-fragment ion for the sphingoid base. Cross-ring fragments of the saccharide head group (A- and X- ions) are exemplarily indicated. Nomenclature according to Domon and Costello and Merrill et al.[128,129]

Additional possibilities to elucidate the structure of GSLs by MS include the enzymatic cleavage of GSLs or the derivatization of GSLs prior to analysis.[135–138] A classical derivatization method is the permethylation of glycans which makes it possible to obtain more reliable MS/MS spectra for structure elucidation.[139,140] Furthermore, the ionization efficiency is increased.

Neglected tropical diseases

Neglected tropical diseases (NTDs) are defined by the World Health Organization (WHO) and currently comprise 20 different diseases and disease groups.[141,142] NTDs mainly affect poverty-related countries and communities where people have limited access to fresh water, sanitation or appropriate housing.[143] Research into these NTDs was neglected for a long time, but the London Declaration from 2012 represents a turnaround.[144] The London Declaration was one of the largest health efforts to eradicate NTDs, bringing together governments, non-governmental organizations, pharma companies and donors. Even if the initial goals have not been fully achieved, the campaign against NTDs remains a focus of the WHO, with goals that are bundled in the current guideline "Ending the neglect to attain the Sustainable Development Goals: A roadmap for neglected tropical diseases 2021-2030".[145] A focus in the research against NTDs is, for example, the development of novel drugs and vaccines. To date, drugs are mostly used in mass drug administration (MDA) programs for the treatment of helminth infections. A re-administration is usually necessary, either because of incomplete eradication or re-infection, increasing the risk for drug resistance.[146] Therefore, novel vaccines against helminths are potential game changers. As a potential molecular class for new treatments, glycans are already investigated as they are known to modulate the host immune system.[147]

Schistosomiasis

The parasitic infectious disease schistosomiasis is defined as an NTD by the WHO with around 250 million people requiring treatment.[148] The causative parasites belong to the class of trematodes with *Schistosoma* (*S*.) *mansoni*, *S*. *japonicum* and *S*. *haematobium* being the most prevalent species affecting humans.[149] *S*. *mansoni* and *S*. *haematobium* co-exist in Africa and the Middle East. Further, *S*. *mansoni* is distributed across several countries in South America. *S*. *japonicum*, on the other hand, is widespread in China, Indonesia and the Philippines. Other, but more locally distributed *S*. *species pluralis* (*spp*.) affecting humans, are *S*. *menkongi*, *S*. *guineesis* and *S*. *intercalatum*.[149] The infectious disease is treated with the chemotherapeutic praziquantel, which is effective against all *S*. *spp.*.[150] The mechanism of action is not fully understood, but it is most effective against the adult parasites. However, praziquantel does not prevent re-infection. Therefore, in endemic areas, regular MDA programs are common. Although no resistance to the drug has been observed in the field, resistance has already been induced in mice in laboratory experiments.[151]

A common characteristic of the various *S*. *spp*. is that they are dioecious.[149] The blood flukes mate and live most of their lives *in copula* (the female resides in the gynaecophoric canal of the male) at the final location in the definitive host. For *S*. *mansoni* and *S*. *japonicum,* the final locations are the mesenteric veins and for *S*. *haematobium* the perivascular veins, respectively. There, the female sheds hundreds to thousands of eggs per day, which are fertilized by the male worm. The eggs are excreted via the faeces or urine, but some of them are trapped inside the host. For. *S*. *mansoni,* around half of the shedded eggs get trapped inside the liver or intestine.[152] From the excreted eggs, which are vital for 1-2 weeks after release by the female, free-living ciliated miracidia will hatch upon contact with freshwater. These ciliated miracidia then infect their intermediate host. The intermediate hosts are aquatic freshwater snails, and schistosomiasis can only become endemic in areas where these snails are prevalent. In the snails, asexual replication of the snails leads to the release of tens of thousands of cercariae into the freshwater. The cercariae are infective for 1-3 days and penetrate the skin of their mammalian host upon contact. In the human host, the cercariae transform into schistosomula by losing their tail and enter the vasculature of the host. There, they mature while migrating to their final destination, where they eventually pair and the life cycle repeats.

The morbidity of schistosomiasis-affected humans is mainly attributed to the eggs, which are trapped inside the organs. These eggs and their soluble-egg antigens shift the immune response from an initial

T helper type-1 (Th1) immune response to a T helper type-2 (Th2) immune response, and granuloma formation around the trapped eggs is observed.[153,154] Various different immune cells are involved in immune response and subsequent granuloma formation. For *S. mansoni* infection, the most prominent cells are T and B cells, M2 macrophages and eosinophils.[155] The granulomas are important to protect the surrounding hepatic tissue physically and by sequestering toxins released by the eggs. On the other hand, the constant immune response is the cause for liver fibrosis development.[154]

Schistosoma glycans

The relevance of glycans for host-parasite interaction was already recognized by studies in the 1960s and 1970s.[156–160] Initial characterizations of glycoproteins at the beginning of the 1980s confirmed the assumption that these are primarily responsible for eliciting an immune response.[161] This was most clearly demonstrated at that time using the example of glycoproteins from *S. mansoni* eggs.[162] Many more studies on glycans associated with schistosomiasis followed, often using MS as the analytical method, and were reviewed in several articles.[163–166] In summary, there are now plenty of studies suggesting that glycans play an important role in host-parasite interaction. Thereby, schistosomes have several different glycan motifs, mostly localized on the surface of the parasite, like the tegument or oral sucker, but also as free agents or in the adult gut and parenchyma.[167–172] Additionally, the glycan expression changes during development.[173] Several studies described glycan motifs of schistosomes and immunogenic glycans during the disease, and some biological roles are known.
For instance, various host proteins belonging to the C-type lectin receptor family can recognize Galβ1-4(Fucα1-3)GlcNAc (Lewis X) and GalNAcβ1-4(Fucα1-3)GlcNAc (LDN-F), which are typical for schistosomes, as well as GalNAcβ1-4GlcNAc (LDN) and mannose- and fucose-containing glycans.[169,174,175] These antigens are secreted by *S. mansoni* eggs, and the binding of molecule-3-grabbing nonintegrin to Lewis X potentially triggers a modified Th2 immune response.[169] Furthermore, an antibody response is also induced by glycans. In particular, (multi)fucosylated LDN glycan motifs are highly immunogenic and trigger an immunoglobulin M and immunoglobulin G antibody response.[176,177] Glycans also play a role in the diagnosis of schistosomiasis. For example, schistosomes excrete many circulating cathodic antigens, which can be detected with commercially available urine tests for the diagnosis of schistosomes.[178] Furthermore, a study has shown that of the various glycan motifs of schistosomes, LDN and Galβ1–4GlcNAc (LN) are primarily involved in the formation of granulomas.[179] In conclusion, it is clear today, that glycans play an important role in host-parasite interaction. However, there are still large gaps in the understanding of the effects and functions of glycans in particular.

Fascioliasis

The parasitic, zoonotic infectious disease fascioliasis is a major economic challenge with an annual loss of several billion USD.[180] The disease-causing foodborne trematodes *Fasciola* (*F.*) *hepatica* and *F. gigantica*, also referred to as liver flukes, infect not only human livestock (cattle, sheep, water buffalo) but also wild animals such as hares, rats and deer.[181] Also, fascioliasis has been classified as an NTD by the WHO since 2020, as an estimated 2.4 million people are infected and many millions more are at risk.[182] Fascioliasis is found on all inhabited continents and is therefore geographically the most widespread disease caused by helminths.[183] Fascioliasis is mainly treated with triclabendazole, which is effective against adult and juvenile worms. However, the emerging resistance to the drug necessitates the search for new treatment methods.[184,185]
The life cycle of *F. spp*. is complex, as in the case of most other trematodes. Undeveloped eggs produced by adult *F. spp*., which reside in the bile duct of the definitive host, are excreted via the

faeces. Outside the host, the eggs can continue to develop once they are separated from the faeces. When the eggs are fully developed, mobile miracidia can hatch. Within a short period of time, the miracidia need to find an intermediate host, which is usually a *Galba truncatula* snail. However, other snail species also serve as intermediate hosts. The miracidia develop further. Firstly, sporocysts develop, which then turn into rediae and finally cercariae, which leave the intermediate host. These cercariae develop further into metacercariae, which either attach themselves to plants or float on water. The final hosts can become infected by feeding on the infested plant or by ingesting free metacercariae floating on the water. In the intestine, the freshly excysted juveniles hatch from the cysts and penetrate the intestinal wall to reach the liver. This typically happens within 4-6 days. There, the immature worms migrate through the liver tissue for several weeks and feed on it until they have developed into adult (mature) flukes. The adult worms live in the bile duct and the life cycle repeats.[181] The clinical picture of a fascioliasis infection can vary and depends, among other things, on the parasite load. In humans, the disease can be asymptomatic. However, infections with a clear clinical appearance are also possible.[181] A distinction can be made between the acute and the chronic phase of the infection.[186] The migratory phase of the parasites during the acute infection can lead to various symptoms such as fever, anaemia, weight loss or abdominal pain. In addition to the parasite load, the host's immune response also plays an important role.[181] During the chronic phase, bile duct obstruction can occur due to inflammation and hyperplasia and the size of the adult parasites, whereby *F. hepatica* can grow up to 4 cm long and up to 1.5 cm wide.[187]

Fasciola glycans

The number of studies on the structural elucidation of glycans in *F. spp*. is limited compared to other helminths, such as schistosomes. In the early 2000s, the glycolipids of *F. spp*. were analysed.[188–190] Mammalian-like structures were described, as well as highly antigenic glycolipids, including specific acidic glycolipids. For adult *F. hepatica* it is now known that they carry in particular high-mannose, complex and phosphorylated glycans on their surface.[191] In contrast, newly excysted juveniles (NEJ) mainly have a truncated and also high-mannose structure.[192] In addition, the glycan profiles of *F. hepatica* extracellular vesicles were analysed using lectin assays, and it was shown that N-glycans are resistant to exo- and endo-glycosidases.[193] In a recent study, the N- and O-glycan profiles of somatic and excreted-secreted extracts from NEJ were analysed in detail and new, unusual structures were identified.[194]

For the function of glycans, it has been shown that lectin receptors, such as the mannose receptor (MR), stimulate dendric cells and activate a signalling cascade.[195] This influences the interaction with T cells and enhances the Th2 immune response. It has also been shown that macrophage Gal/GalNAc lectin 2 (MGL2+) cells, which recognise GalNAc-glycosylated parasite components, are particularly important for the expansion of modified Th2 immune responses and the suppression of Th1 polarisation.[196] Thus, MGL2+ antigen-presenting cells in the peritoneum have been shown to be critical for parasite survival during infection and to promote the induction of T cells in the spleen. This was demonstrated by using MGL2- diphtheria toxin receptor transgenic mice in which MGL2+ cells were depleted by diphtheria toxin. Depletion of these cells resulted in partial resistance to the infection and prevented the parasite-induced increase of CD4+/CD25+ FoxP3+ T cells in the spleen. In addition, it is known that the migration of NEJ can be inhibited by specific lectins that bind to mannose-containing glycans of *F. hepatica* larvae.[197] Thus, it seems possible that glycans of NEJ are important for binding with the host tissue, more specifically the intestinal epithelial cells, to penetrate the intestinal wall.

Motivation and aim of this work

GSLs are a class of molecules that are difficult to analyse by MALDI MSI due to low ionisation efficiencies and suppression effects by other lipid classes.[198,199] To date, only a few MALDI MSI studies focused on GSLs, the majority of which have analysed brain tissue, which is known to have a high concentration of GSLs.[199–208] Analysis of other tissue types has rarely been reported. One application describes the examination of cancer tissue using MALDI-2 post-ionisation.[199] Here, with a lateral resolution of 15 µm, the highest lateral resolution for MALDI MSI focusing on GSLs was demonstrated, even though the instrumental effort is significantly higher compared to a conventional MALDI MSI setup. The distribution of GSLs in parasites or in relation to host interactions has not yet been investigated using MALDI MSI. However, imaging lectin assays showed that the localisation of glycans in parasites can provide information about possible interactions.[194,209–211] Furthermore, different immune cells are often involved in parasitic infections.[212,213] It is generally known that immune cells can fulfil important functions.[213] However, there is limited knowledge about GSLs of immune cells and their specific roles during parasitic infections, which can also be attributed to the lack of adequate analytical methods.

Therefore, **publication I** focussed on the development of an analytical method to provide local information on the distribution of intact GSLs in parasitic samples. In *S. mansoni* infected hamsters, the GSLs of liver tissue surrounding *S. mansoni* eggs were analysed. In a first step, a nano-HILIC MS/MS method was established in order to obtain the most accurate overview possible of the GSLs present. This is necessary because existing databases for analysing GSLs have so far been inadequate. This is particularly true for parasitic GSLs, as the ceramide motifs of GSLs differ from those of mammals. For the MALDI MSI analysis, the matrix application of 2,5-dihydroxyacetophenone (DHAP) was optimised to enable high spatial resolution MALDI MSI measurements with a focus on GSLs. The application of state-of-the-art AP-MALDI MSI instrumentation yielded convincing results. Based on the results, specific GSLs were identified as markers for certain immune cells during *S. mansoni* infection. The high spatial resolution of the MALDI MSI experiments, routinely established with 10 µm lateral resolution and demonstrated with an experimental setup of 3 µm, was essential to resolve histological features.

In **publication II**, shortcomings of the previously developed method were solved. A bottleneck of the previously developed method was the manual data analysis of the nano-HILIC MS/MS experiments due to a lack of software solutions. In this work, a semi-automatic approach for data analysis was established, which significantly reduced the time required to curate a GSL database. In addition, valuable MALDI MSI data about other lipid classes, which did not require additional imaging experiments, was considered and compared to RPC MS/MS analysis. A further motivation was the question whether GSLs show a different, organ-specific distribution in the parasite, which can provide indications for possible functions or metabolism. Therefore, our method for GSL analysis was first validated for isolated parasites. Using adult *F. hepatica*, the existing knowledge about GSLs was confirmed and extended. With the help of semi-automatic data analysis, novel GSLs specific to *F. hepatica* were discovered. In addition, the distribution of many different GSL species in the parasite were determined simultaneously with a lateral resolution down to 5 µm. Furthermore, liver tissue from *F. hepatica* infected rats was examined during the migratory, acute phase of the infection. For the first time, the GSLs, which may be involved in the *in vivo* host-parasite interaction, were examined *in situ*. A comparison of nano-HILIC MS/MS data of the acute infection stage to the chronic infection stage confirms that GSLs may be important for the direct host-parasite interaction. Distribution images of GSL in the tissue also allowed the possible assignment to immune cells for this model system. Furthermore, the distribution of GSLs of immature *F. hepatica* in liver tissue was compared with that of isolated adult *F. hepatica*, thus providing information on metabolic processes during the development of the parasite.

Publication I - Hepatic Topology of Glycosphingolipids in *Schistosoma mansoni* Infected Hamsters

In case of infection with *S*. *mansoni*, the formation of granulomas around the encapsulated eggs is the main cause of pathogenesis.[154] However, so far mainly glycoconjugates from the different parasite stages have been analysed and especially the host's GSLs, which are involved in immune response, were ignored.[173,214,215] Nevertheless, due to the association of glycoconjugates during immune response in general, such as cell-cell communication and pathogen recognition, it is necessary to elucidate the molecular level of the response for a fundamental understanding of infection.[106] This can provide support for the development of new drugs or vaccines. Therefore, the aim of this work was to establish a global and local profile of GSLs during *S*. *mansoni* infection in hamster liver. However, the analytical characterization of GSLs is a major challenge. We saw a promising approach in the combination of nano-HILIC MS/MS with AP-SMALDI MSI to characterize GSLs both structurally and locally.

To investigate the possibilities of combining these two state-of-the-art methods, we focused on liver tissue from *S*. *mansoni*-infected hamsters. We analysed liver tissue from bi-sex-infected hamsters (n=3) and healthy control samples (n=3). In addition, we analysed liver samples from single-sex-infected hamsters (n=3). In contrast to bi-sex-infected hamsters, no eggs are produced.

In a first step, we established a nano-HILIC MS/MS method for the analysis. In order to map the GSL profile as comprehensively as possible, it was essential to use both, the aqueous and the organic phase of the extraction of GSL from liver homogenate in combination, for the subsequent desalting using SPE cartridges. In addition, it was decided not to separate anionic from neutral GSLs, although this is a classic step in the preparation of GSL extracts.[112] However, this step would not allow a complete analysis of the GSL profile. The gradient for the nano-HILIC MS/MS method was adapted from the method published by Bindila et al. with modifications.[216] A crucial step in the nano-LC method for the sensitive detection of GSLs is the sample injection. Because GSLs can be important for the functions despite low concentrations in the tissue, the pre-concentration setup was used for sample injection in order to be able to detect GSLs with high sensitivity. For nano-LC applications, pre-concentration was used to increase the amount of sample injected compared to direct injection. However, it is necessary to optimize various parameters such as the solvent of the sample or switching times of the valve in conjunction with the flow rate of the loading pump. Figure 5a shows an example of the final separation of the nano-HILIC MS method, which is based on the glycan composition of the GSLs. A good separation of the different glycans was achieved. For example, the species NeuAcHexCer 18:1;O2/16:0 and NeuGcHexCer 18:1/16:0 (Figure 5b), which have only a minimal structural deviation from each other, were also separated.

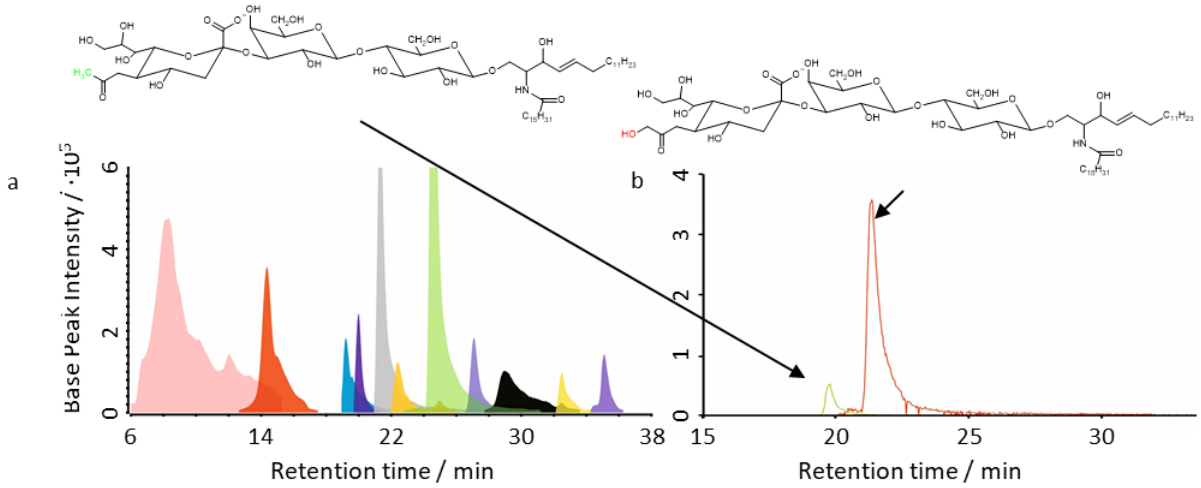

Figure 5: (a) Extracted ion chromatogram (EIC) for GSLs from liver of bs-infected hamsters. (b) EIC of NeuAcHexCer 18:1;O2/16:0 and NeuGcHexCer 18:1/16:0 with structures. Although these two species only differ in one hydroxyl group, they are still separated by our nano-HILIC method.

Based on the data-dependent MS/MS spectra, it was possible to elucidate the structure of GSLs in terms of glycan sequence and ceramide composition. A total of 59 GSL compounds were identified and curated in a database. The high mass resolution and mass accuracy in conjunction with the retention time supported the correct identification in the case of an incomplete fragment scheme of the MS/MS data. Additionally, a semi-quantitative analysis was performed. Firstly, a principal component analysis (PCA) (Figure 6) was used to separate the different groups. Significant differences ($p < 0.001$) between the bi-sex-infected and the other groups were determined at species level. If any significant differences in GSLs had been identified, these were upregulations in the bi-sex-infected sample. This was expected, as various immune cells, such as T and B cells, macrophages and also eosinophils, are important for granuloma formation.[155] Based on the PCA analysis, a small difference between the single-sex-infected group and the healthy control can be assumed. In fact, significant differences between single-sex and non-infected samples can be detected for certain GSL species. One possible explanation is the excretion of bacteria and hemosides during a single-sex infection, which accumulate in the liver.[217] There is also the possibility that unpaired parasites are present in the liver and that they induce an immune response, leading to an accumulation of inflammatory cells in the blood and liver.[218] Accidental excretion of unfertilised egg-like structures has also been reported.[219]

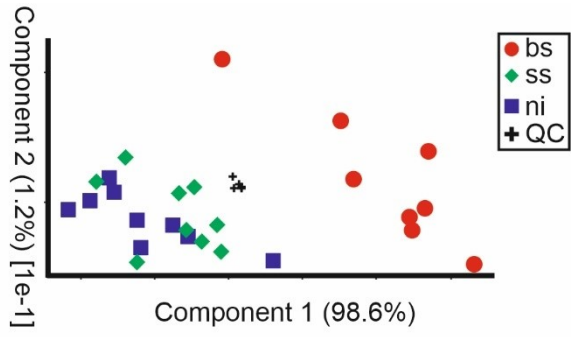

Figure 6: Principle component analysis of nano-HILIC MS/MS data in positive-ion mode with "●" for bi-sex-infected, "◊" for single-sex-infected, "□" for non-infected hamster, and "+" for quality control samples.

After establishing the global GSL profile, the localisation of the GSLs in the liver tissue was the main requirement to be able to assign changes in the GSL profile to histological characteristics. To this end, we first optimized the matrix application of DHAP by sublimation in our laboratory. Compared to other frequently used matrices, DHAP showed the highest intensity for GSL species during MALDI MSI analysis in the mouse brain both, for neutral GSLs, measured in positive-ion mode, and for acidic GSLs, measured in negative-ion mode.

The optimized DHAP sublimation protocol was subsequently used to analyse tissue sections from the different hamster liver conditions using MALDI MSI. The annotations were guided by the GSL database generated by nano-HILIC MS/MS experiments. The distributions of different neutral GSLs in positive-ion mode were visualized, especially for the liver sections of bi-sex-infected hamsters. With a total of 21 distribution images for neutral GSLs compared to 31 molecular species in the in-house GSL database, a reasonable overlap was achieved. However, due to the high sensitivity of the nano-HILIC MS/MS method, a larger number of GSL species was identified by this approach. Similar results were obtained in the experiments in negative-ion mode. Here, distribution images could be generated for 17 of 30 GSL species in the database.

The importance of the new information about the distribution patterns of the GSLs becomes apparent when the MALDI MSI data is evaluated. For this purpose, it is relevant to consider the theoretical compositions of the granulomas with the most frequently occurring immune cells displayed in Figure 7. The early phase of granuloma development, the so-called pre-granulomatous exudative (PGE) stage, is mainly characterized by B and T cells, which accumulate around the *S. mansoni* eggs. In the further course, a disorganized accumulation of various immune cells subsequently leads to an ordered structure of the granulomas, which can be divided into three layers. The inner layer around the *S. mansoni* egg, which is formed by eosinophils and macrophages, accounts for the largest proportion of the granuloma in terms of cell mass. The cells are surrounded by collagen fibers and hepatic stellate cells (HSC), representing the middle layer. B and T cells surround the granulomas as their outer layer. This highly organized structure is also known as the exudative-productive (EP) stage.[155,220,221]

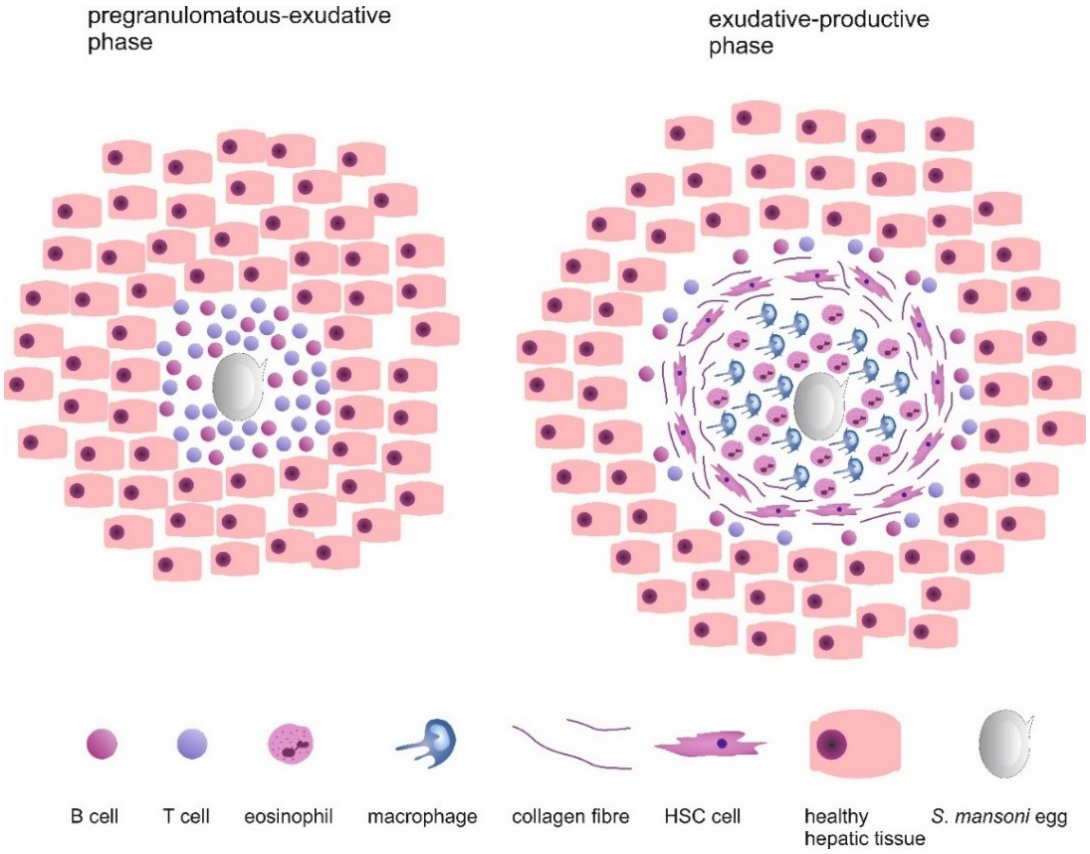

Figure 7: (left) Granuloma model of the pre-granulomatous-exudative (PGE) stage. B and T cells are surrounding the *S. mansoni* eggs. (right) Granuloma model of the exudative-productive (EP) stage, representing a highly ordered structure. Eosinophils and macrophages build the inner layer around the egg, surrounded by collagen fibers and hepatic stellate cells as a middle layer and B and T cells as the outer layer. In both granuloma stages, cell types with low abundance are not included in the scheme.

Using the granuloma model in conjunction with the MALDI MSI results, we propose that the distributions of different GSL species are not only organism-specific but also immune-cell-specific. Figure 8a shows an optical microscopic image of a liver section of a bi-sex-infected hamster before measurement and Figure 8b shows a corresponding RGB-overlay ion-image of exemplary selected signals in positive-ion mode. The organism-specific complex GSL $Fuc_3HexNac_6HexCer$ 36:0;O3 for *S. mansoni* eggs is shown in red. In comparison with the optical image, a clear assignment is possible. The magnification in Figure 8d suggests that the GSL is only present on the surface of the *S. mansoni* eggs. The lateral resolution of 10 µm allows a clear differentiation of the signal from the surrounding granuloma and enables the detection of signals in small histological features such as the *S. mansoni* eggs, which have a size of approximately 117-150 x 40-70 µm. We also detected signals specific to the granuloma stages. In Figure 8b, the GSL $HexNac_2Hex_3$ 34:1;O2 is specific for most granulomas. Based on the time of infection and the size of the granulomas, we expected most granulomas to be in the EP stage. During this stage, eosinophils and macrophages are the immune cells immediately surrounding the eggs. Further experiments are needed to determine for which immune cells this GSL species may be specific. We also observed the presence of other GSLs for small granulomas in a few examples. Figure 8b shows an example of $HexNacHex_3$ 34:1;O2 in blue. Accordingly, this signal could be specific for T or B cells surrounding the *S. mansoni* egg during the PGE stage.

The comparison with the two other sample groups (single-sex infected, non-infected) clearly supports that GSLs in our example reflect immune cell-specific signals. Figures 8f and 8h show the RGB-overlay ion-images of the three signals described above as examples for single-sex and non-infected liver sections. In both examples, only noise can be recognised and no enhancement of the GSLs is observed.

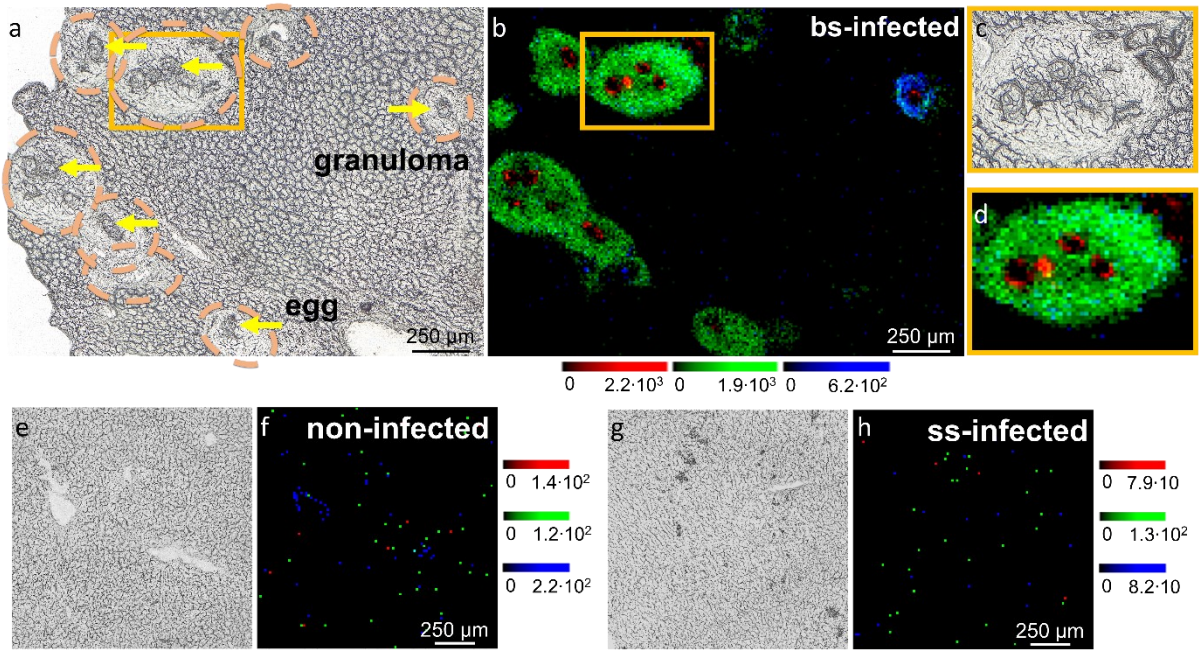

Figure 8: AP-SMALDI analysis of neutral GSLs. (a) Optical microscopic image of a *S. mansoni* liver tissue section of bi-sex-infected hamster. *S. mansoni* eggs are indicated by yellow arrows, and orange dotted circles highlight granulomas. (b) RGB-overlay ion-image corresponding to the optical microscopic image in (a), showing $Fuc_3HexNac_6HexCer$ 20:0;O3/16:0 ($[M+K]^+$, at *m/z* 2442.2211) in red, $HexNac_2Hex_3Cer$ 18:1;O2/16:0 ($[M+K]^+$, at *m/z* 1468.7919) in green and $HexNacHex_3Cer$ 18:1;O2/16:0 ($[M+K]^+$, at *m/z* 1265.7134) in blue. Magnifications of (a) and (b) are shown in (c) and (d). Optical microscopic image of liver tissue sections of a non-infected and a single-sex-infected hamster in (e) and (g). RGB-overlay ion-images in (f) and (h) corresponding to the optical microscopic images (e) and (g), respectively. The same *m/z*-values as for the bi-sex-infected sample are displayed.

Compared to the positive-ion mode, selected distribution ion-images for acidic GSL species in the negative-ion mode may represent the outer and middle layer of granulomas in the EP stage. Figure 9a shows the optical microscopic image before the measurement and in comparison in Figure 9b the

distribution for NeuAcHex$_2$Cer 18:1;O2/16:0 in red, which represents the middle layer. All acidic glycolipids containing N-acetylneuraminic acid show this distribution, which suggests a specificity for collagen fibers or HSC during granuloma formation. This signal is surrounded by NeuGcHex$_2$Cer 18:1;O2/16:0 in green. This signal could be specific for T and B cells. This assumption is supported by the fact that this signal is also observed in non-granulomatous tissue as these immune cells also occur in small populations in normal hepatic tissue.

However, an overlap is apparent between the two species, which leads to a different explanation. The enzyme phosphate-N-acetylneuraminic acid hydroxylase, which catalyses the transformation of the very similar acidic saccharide NeuAc into NeuGc, is present in hamsters.[222] It is therefore possible that the simultaneous detection of the many different acidic GSLs provides us with indications of metabolic processes in the organism. The detection of the different molecular acidic GSLs is advantageous here. It can be observed that the distributions of different NeuGcHex$_2$ species in the liver tissue show different distribution patterns. In the case that NeuGcHex$_2$ and NeuAcHex$_2$ have the same ceramide motifs, the distribution can be observed as in the example described above.

In addition, sulfatides can be detected in the negative-ion mode, showing a partially accumulated distribution around the granuloma, Figure 9c. This is a good example to demonstrate the increased sensitivity of MALDI MSI analyses compared to chromatographic methods. Due to the potentially high local concentration, detection by MALDI MSI is possible, but the dilution during the bulk-analysis is too high, so that the analyte can no longer be detected.

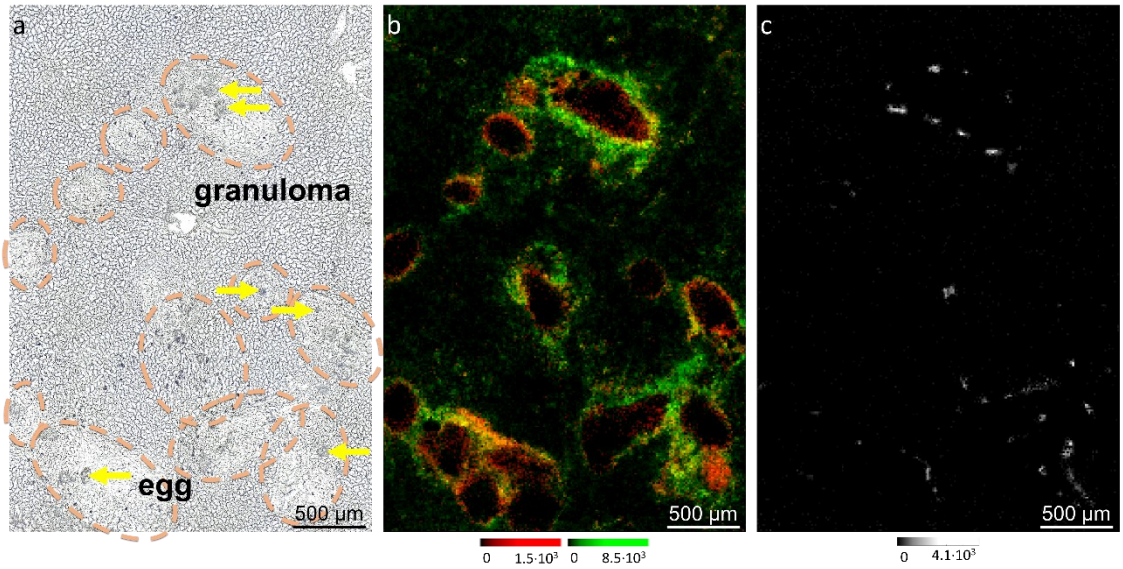

Figure 9: AP-SMALDI analysis of acidic GSLs. (a) Optical microscopic image of a liver tissue section of bi-sex-infected hamster. *S. mansoni* eggs are indicated by yellow arrows, and orange dotted circles highlight granulomas. (b) RG-overlay ion-image corresponding to the optical microscopic image in (a), showing NeuAcHex$_2$Cer 18:1;O2/16:0 ([M-H]$^-$ at *m/z* 1151.7058) in red, NeuGcHex$_2$Cer 18:1;O2/16:0 ([M-H]$^-$ at *m/z* 1167.7008) in green. (c) Ion-image corresponding to the optical microscopic image in (a), showing SHexCer 18:1;O2/16:0 ([M-H]$^-$ at *m/z* 778.5148).

In addition to the solely visual impressions of the GSL distributions, we also propose an approach to make semi-quantitative statements based on MALDI MSI data. For this purpose, we determined the total-ion-count-normalized signal intensities per pixel for selected signals in defined ROIs. The results shown in Figure 10 for both, the positive-ion mode and the negative-ion mode are comparable with the nano-HILIC MS/MS results. It should be noted that the liver sections from bi-sex-infected hamsters show comparable levels of GSLs in the healthy liver tissue compared to the single-sex and non-infected sample. Only the granuloma region shows increased levels of GSLs, which emphasises the association of GSLs with immune cells of the granulomas.

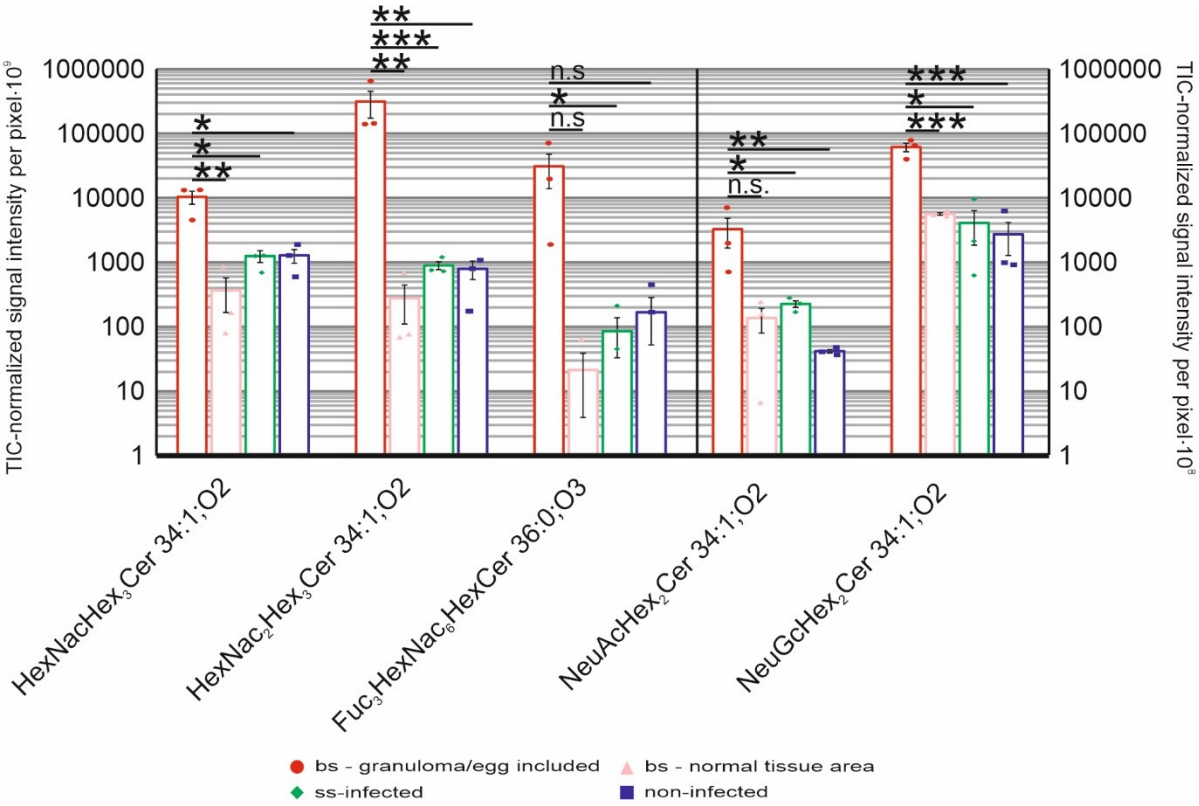

Figure 10: Semi-quantitative evaluation of ion-images of $Fuc_3HexNac_6HexCer$ 20:0;O3/16:0, $HexNac_2Hex_3Cer$ 18:1;O2/16:0 and $HexNacHex_3Cer$ 18:1;O2/16:0, shown in Figure 8b and $NeuAcHex_2Cer$ 18:1;O2/16:0 and $NeuGcHex_2Cer$ 18:1;O2/16:0 shown in Figure 9b with a 50x50 pixel ROI showing the intensity per pixel for n=3 with standard error as error bars. Red – bi-sex-infected sample ROI with granuloma included, pink – bi-sex-infected samples without granuloma included, green – single-sex-infected sample and blue – non-infected sample. Black lines centered above two bars indicate the difference between the two corresponding ROIs, with "***" representing a significant difference with $p < 0.001$, "**" with $p < 0.01$, "*" with $p < 0.05$. "n.s." indicates a non-significant difference.

In this work, we were also able to demonstrate the detection of GSLs with 3 µm lateral resolution for the first time. In Figure 11b, the signal of HexCer 20:0;O3/16:0 can be clearly assigned to the surface of the *S. mansoni* egg. These experiments demonstrate for the first time the possibility of our developed method to track GSL at the cellular level.

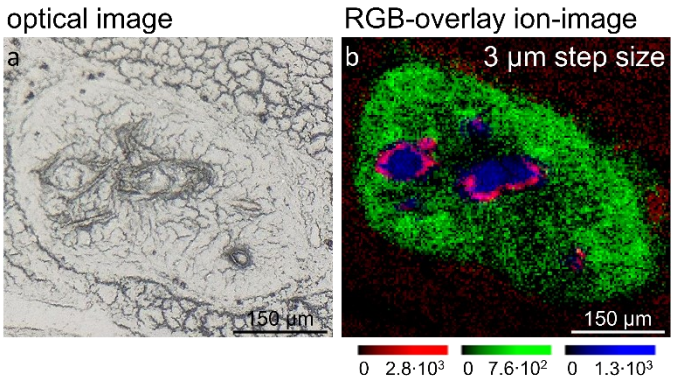

Figure 11: High spatial resolution MALDI MSI measurement. (a) Optical microscopic image of a liver tissue section of bi-sex-infected hamster showing a granuloma with *S. mansoni* eggs. (b) RGB-overlay ion-image with 3 µm step size using an experimental AP-SMALDI imaging setup, showing HexCer 20:0;O3/16:0 ($[M+K]^+$ at *m/z* 784.5715) in red, $HexNac_2Hex_3Cer$ 18:1;O2/16:0 ($[M+K]^+$, at *m/z* 1468.7913) in green and PC 38:1 ($[M+K]^+$ at *m/z* 854.6042) in blue.

Publication II – Glycolipidomics of liver flukes and host tissues during fascioliasis – insights from mass spectrometry imaging

During Fascioliasis, GSLs or other glycoconjugates may play an important role in the immune response. Studies on GSLs show that they have a high antigenicity or possess host-like GSL structures.[188–190] However, spatially resolved information on the different GSL species is lacking. Therefore, we first analysed the GSLs of isolated adult *F. hepatica* using our previously developed method, the combination of nano-HILIC MS/MS and AP-SMALDI MSI. Furthermore, we were interested in the immune response of the host. To this end, we analysed the GSL profiles of rat liver in the acute infection stage, rat liver in the chronic infection stage and the bile duct in the chronic infection stage using nano-HILIC MS/MS experiments. For the rat livers, the livers of healthy rats were also analysed. AP-SMALDI experiments were also carried out in order to assign changes in the GSL profile to different processes (migration of the parasite and the resulting mechanical and enzymatic damage to the liver parenchyma, immune response of the host, liver regeneration) in the rat liver of the acute infection stage.

In total, this study design resulted in six different groups for the nano-HILIC MS/MS experiments, which were measured as both biological and technical triplicates. This makes a manual evaluation of the data as in the previous project unrealistic, so that the focus was initially on optimising the data evaluation. For this purpose, the open-source analysis software MS-DIAL was used in a semi-automatic approach. The decisive factor for the identification is that the GSLs have recurring fragments, starting from the sugar residue, and also recurring mass differences as neutral losses due to the masses of the saccharide building blocks. In addition, there are typical fragments for the sphingoid base of the ceramide motif. Taken together, various rules for the MS/MS search option of MS-DIAL can be created and the GSLs identified. However, the determination of the sequence of the saccharide head group and the exact composition of the ceramide must still be determined manually in the following. Nevertheless, the time saving compared to a manual evaluation is enormous and the GSL database created in-house comprises all groups together 212 different molecular species.

A total of 108 different GSLs were identified for isolated *F. hepatica* alone. The identifications correspond to previously published studies by Wuhrer et al. and could be extended further.[188,189] It should be emphasised that it was also possible to identify many GSLs with ultra-long chain fatty acids (ULCFA), example MS/MS shown in Figure 12a. This would not have been possible with existing software solutions, which usually have a limited database. In addition, unknown species such as Hex-HPO_3-Hex-Cer 18:0;O3/18:0, Figure 12b, were identified. Similar species specific for *F. hepatica* with the general composition GlcNacα1-HPO_3-6Gal(1-1)-Cer have already been identified by Wuhrer et al.[189] However, the biological function of these phosphate-containing species for *F. hepatica* is unknown.

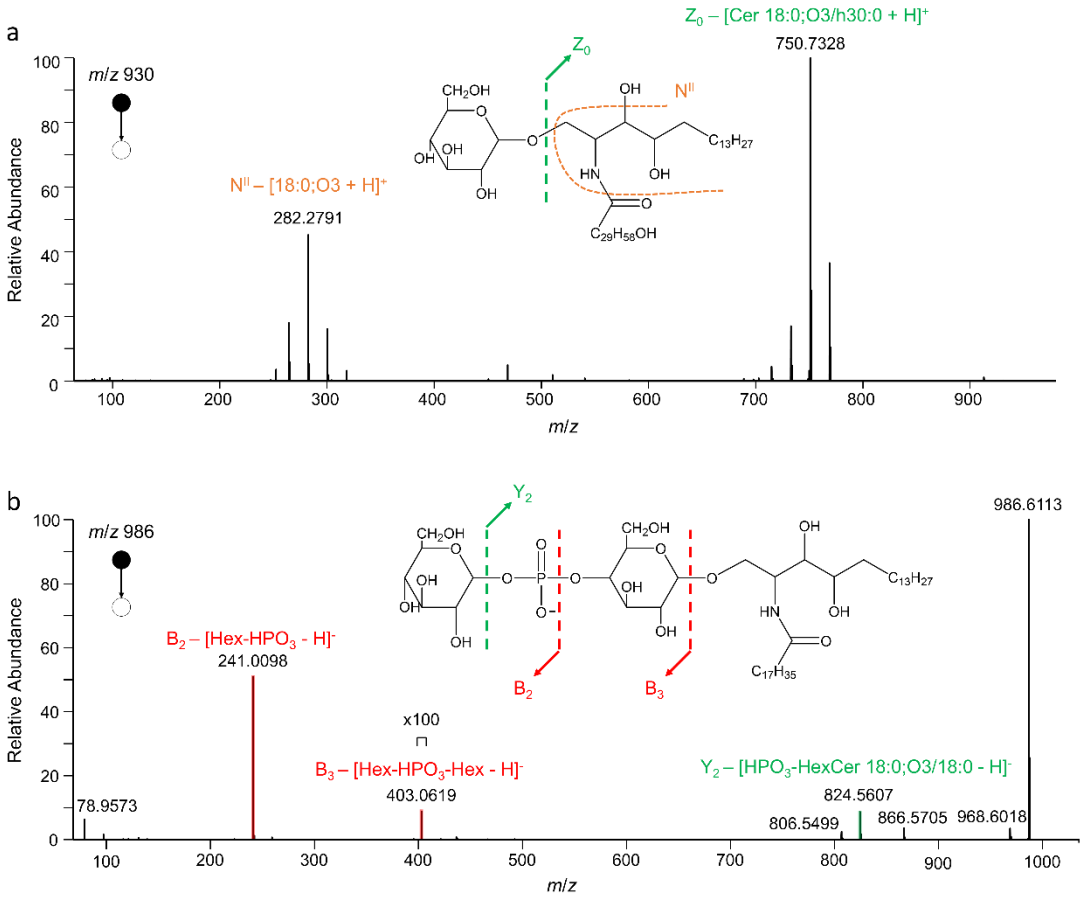

Figure 12: (a) Tandem mass spectrum for HexCer 18:0;O3/h30:0 ($[M+H]^+$ at *m/z* 930.7978). The fragment ion at *m/z* 282.2791 corresponds to the N^{II}-fragment. The fragment ion at *m/z* 750.7328 represents the Z_0-fragment ion with a neutral loss of 180.0650 Da (Hex) from the parent ion. (b) Tandem mass spectrum for Hex-HPO_3-HexCer 18:0;O3/18:0 ($[M-H]^-$ at *m/z* 986.6113). The fragment ion at *m/z* 241.0098 represents the B_2-fragment ion. The fragment ion at *m/z* 403.0619 corresponds to the B_3-fragment ion. The fragment ion at *m/z* 824.5607 corresponds to the Y_2-fragment ion.

In addition to the identification of GSLs in bulk-analysis, we focused on spatially resolving the GSL distributions in *F. hepatica*. For this purpose, we applied our previously optimised MALDI MSI workflow. Based on various examples, we can determine from the distribution of the phosphate-containing GSL species that they are mainly distributed in the intestine or the tegument, Figure 13. It has been shown that the distribution of GSLs is presumably related to the fatty acid of the ceramide motif. If this is hydroxylated, it is distributed in the tegument and intestine. However, phosphate-containing GSLs with non-hydroxylated FAs are primarily accumulated in the intestine. This observation may indicate metabolic processes in the parasite. Although they are not capable of *de novo* fatty acid synthesis, they can modify the host's own FAs.[223] The comparison of AP-SMALDI MSI results with the immature parasites migrating through the liver tissue allows conclusions to be drawn about the biological relevance. As shown in Figure 13, the distribution of phosphate-containing GSLs with non-hydroxylated FAs of immature *F. hepatica* is comparable to that of adult *F. hepatica*. However, phosphate-containing GSLs with hydroxylated FAs are hardly detectable. Thus, this group of molecular species could be an example to visualise tegument remodelling, a well-known phenomenon for *F. hepatica*.[224] Thus, it can be hypothesised that the phosphate-containing GSLs with hydroxylated FAs have a higher relevance for adult *F. hepatica* compared to immature *F. hepatica*.

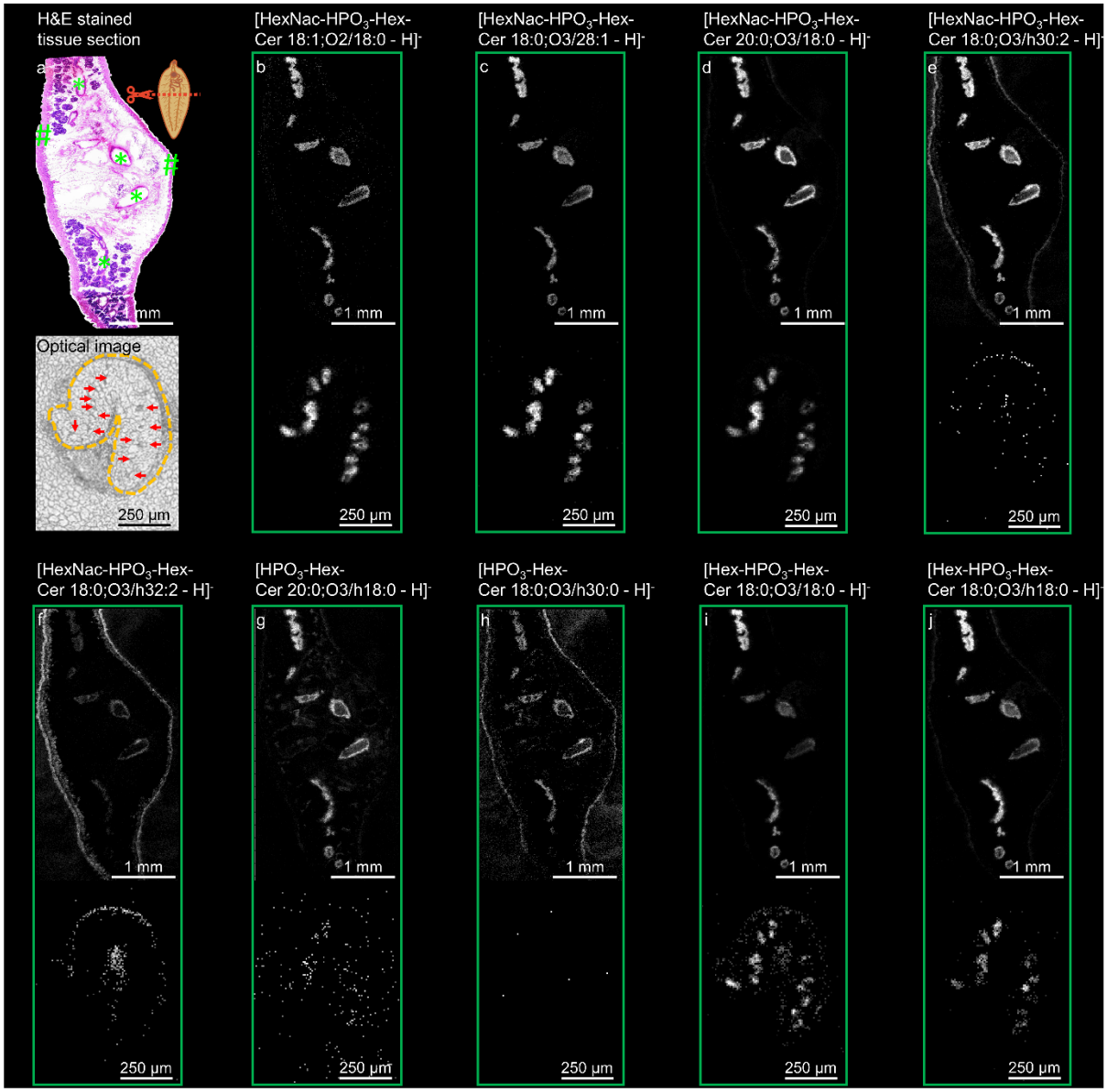

Figure 13: (a) Haematoxylin and eosin (H&E) staining of a *F. hepatica* transversal section after AP-SMALDI MSI measurement (first row). The *F. hepatica* pictogram illustrates the transverse sectional plane. Intestine signed with asterisks and the tegument with hashes. Optical microscopic image of an immature parasite (second row), emphasized by an orange dotted line, surrounded by hepatic tissue. The intestine of the parasite is highlighted by red arrows. (b) single-ion image of HexNac-HPO_3-Hex-Cer 18:1;O2/18:0 ($[M-H]^-$ at *m/z* 1009.6349). (c) single-ion image of HexNac-HPO_3-Hex-Cer 18:0;O3/28:1 ($[M-H]^-$ at *m/z* 1165.7861). (d) single-ion image of HexNac-HPO_3-Hex-Cer 20:0;O3/18:0 ($[M-H]^-$ at *m/z* 1055.6769) (e) single-ion image of HexNac-HPO_3-Hex-Cer 18:0;O3/h30:2 ($[M-H]^-$ at *m/z* 1207.8279). (f) single-ion image of HexNac-HPO_3-Hex-Cer 18:0;O3/h32:2 ($[M-H]^-$ at *m/z* 1235.8279). (g) single-ion image of HPO_3-Hex-Cer-20:0;O3/h18:0 ($[M-H]^-$ at *m/z* 868.5921). (h) single-ion image of HPO_3-Hex-Cer-18:0;O3/h30:0 ($[M-H]^-$ at *m/z* 1008.7822. (i) single-ion image of Hex-HPO_3-Hex-Cer 18:0;O3/18:0 ($[M-H]^-$ at *m/z* 986.6187). (j) single-ion image of Hex-HPO_3-Hex-Cer 18:0;O3/h18:0 ($[M-H]^-$ at *m/z* 1002.6136). The AP-SMALDI MSI measurement was performed with 10 µm step size for the adult parasite and 7 µm for the immature parasite, respectively.

In addition to the role of phosphate-containing GSLs, the abundance of ULCFA is also striking. In addition to the phosphate-containing GSLs (example Figure 13 c,e,f and h), neutral GSLs with ULCFA as part of the ceramide were also detected. While the function for *F. hepatica* is unknown, we may be able to learn from mammals. For example, it is known that ceramides with very-long-chain fatty acids are important for epidermal permeability.[225,226] Therefore, the incorporation of GSLs with various ceramides bearing an ULCFA into the glycocalyx could represent a protective mechanism for the parasite.

While already gaining a lot of information from the GSL profile and distributions of different GSL species in the parasite, the host immune response is equally important to gain a fundamental understanding of the infection. Since it is already known that GSLs play a role during the immune response, we therefore additionally analysed the GSLs of the host.
Based on the nano-HILIC MS/MS experiments and data analysis, we can already determine that many GSL species are accumulated in the liver tissue during the acute infection compared to the control sample, shown in the volcano plot Figure 14b. Especially GSL species with fucose as a saccharide building block clearly appear as a major feature. In comparison, the GSL level in the liver tissue during chronic infection is normalised compared to the control sample, Figure 14a. Here it can be assumed that liver regeneration has already progressed and therefore the liver during the chronic phase reflects healthy liver tissue again.[227] Compared to the acute stage, where the parasite is actively migrating through the liver parenchyma, the liver tissue is not in direct contact with the host during chronic infection. During this stage, the parasite is already in the bile duct. Therefore, we analysed the GSLs in the bile duct during the chronic phase. As for the liver sample of the acute infection, several GSLs with fucose as a component could be identified as an abnormality. Although there was no comparison of the bile duct with a control sample, high numbers of GSLs were also observed for this tissue type.

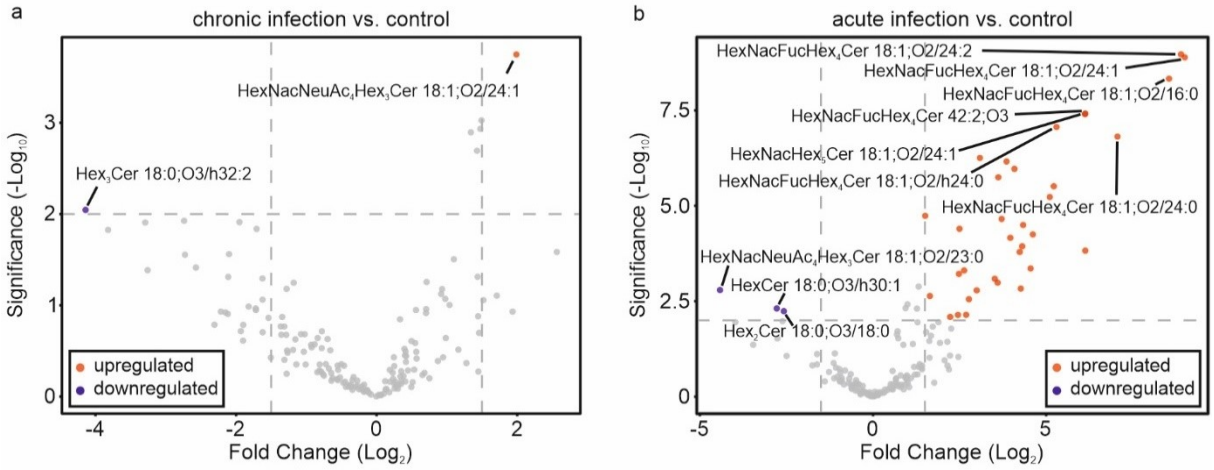

Figure 14: Volcano plot comparing the results from MS-DIAL data analysis for GSLs after normalization. (a) Livers from rats at the chronic infection stage were compared to same-aged healthy control livers. (b) Livers from rats at the acute infection stage were compared to same-aged healthy control livers. The fold-change threshold was set to -1.5 to 1.5 and the significance threshold was set to $p < 0.01$ for both plots. Red circle corresponds to an increased species and a blue circle to decreased species.

In a next step, we resolved the local GSL profile in the liver tissue of the acute infection stage using AP-SMALDI. Here, the migration of the immature *F. hepatica* results in both enzymatic and mechanical damage, which provokes an immune response from the host. In addition, liver regeneration processes can already begin in parallel.[181,227]
Therefore, a spatially resolved GSL profile is essential to identify the possible involvement in the different processes. In positive-ion mode, for example, we were able to detect *F. hepatica*-specific GSLs in the tegument and intestine of the immature parasite, Figure 15c. However, it was also possible, for example, to detect HexCer 38:1;O2 locally in the parasite, but also in the host tissue (Figure 15c). This observation allows two interpretations. Either this species is excreted by the parasite in order to inhibit liver regeneration. Another study has already shown that this is possible with glucosylceramides.[228] Another interpretation results from the increased accumulation at the host-parasite interface and the centre of tissue damage and the simultaneous apparently low occurrence in healthy tissue. Although the presence of eosinophils in healthy tissue is low, eosinophils are known to reduce tissue damage during *F. hepatica*.[229] Eosinophils also promote liver regeneration.[230] These three aspects combined may explain the distribution pattern of HexCer 38:1;O2, and may allow this species to be used as an immune cell marker for eosinophils during *F. hepatica* infection.

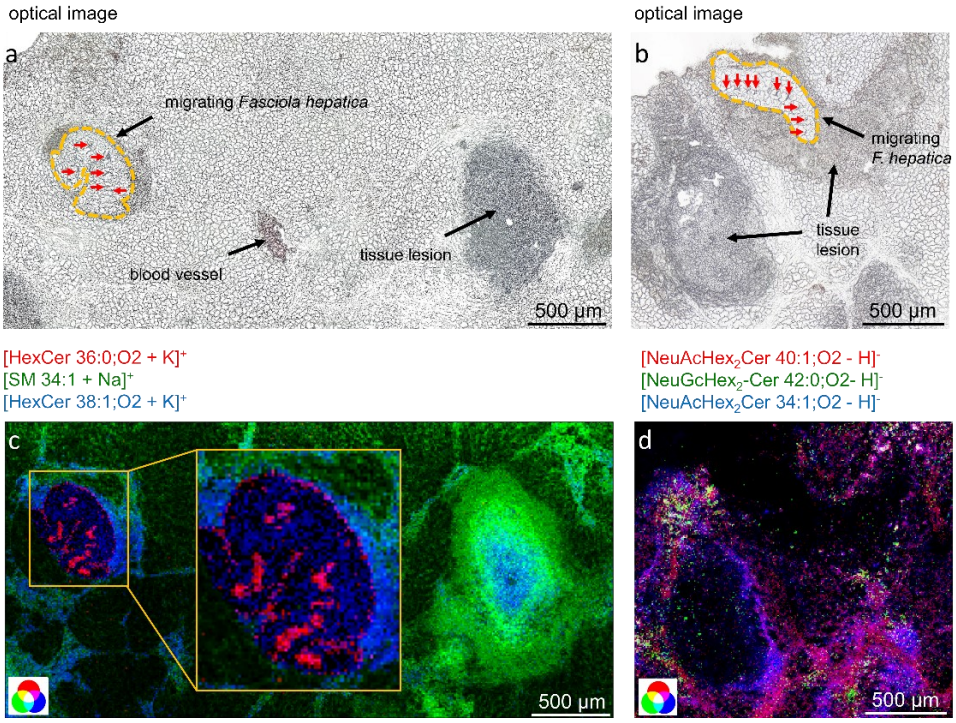

Figure 15: (a, b) Optical microscopic images of liver tissue sections of rat during the acute infection stage. The outlines of the migrating parasites are emphasized with an orange dotted line, and the intestine is indicated by red arrows. (c) Positive RGB-overlay ion-image corresponding to (a) with HexCer 36:0;O2 ($[M+K]^+$ at *m/z* 768.5750) in red, SM 34:1 ($[M+Na]^+$ *m/z* 725.5568) in green and HexCer 38:1;O2 ($[M+K]^+$ at *m/z* 794.5907) in blue. The measurement was performed with 10 µm step size. (d) Negative-ion RGB-overlay ion-image corresponding to (b), showing $NeuAcHex_2Cer$ 40:1;O2 ($[M-H]^-$ at *m/z* 1235.8002) in red, $NeuGcHex_2Cer$ ($[M-H]^-$ at *m/z* 1279.8246) in green and $NeuAcHex_2Cer$ 34:1;O2 ($[M-H]^-$ at *m/z* 1151.7063) in blue. The measurement was performed with 7 µm step size.

The local profile for acidic GSLs obtained by AP-SMALDI experiments in negative-ion mode mainly allowed us to detect $NeuAc_2HexCer$/$NeuGc_2HexCer$ species. These show an accumulation in the connective tissue around the tissue damage, Figure 15d. Thus, we can hypothesise that these species may not play a role in direct host-parasite interaction, but are rather important for liver regeneration during the infection. This is consistent with the fact that the production of gangliosides, a class of acidic glycolipids, is increased several days after partial hepatectomy.[231]

In addition to GSLs, the AP-SMALDI MSI data of rat liver during the acute infection stage was additionally analysed with regard to other lipid classes to learn as much as possible about the host-pathogen interaction. During parasite migration, a general decrease in phospholipids is expected, as *F. hepatica* has phospholipases in the tegument, or in vomit, which result in phospholipid degradation.[232,233] Here, our RPC MS/MS results and MALDI MSI support the decrease in phospholipids. Figure 16a shows the optical microscopic image of a liver section during acute infection, which includes two tissue lesions. One is directly around the migrating parasite and the other one seems not to be in direct contact with the parasite. Using the example of phosphatidylcholine PC 36:4 in Figure 16b in green, a reduction of this signal can be seen in the tissue lesions. In the control sample of healthy liver tissue, however, a homogeneous distribution is recognisable. Another example of how our data generate meaningful distribution images can be described using triglycerides (TGs). An increase of neutral glycerolipids in tissue lesions is expected, because it is already known, that TGs are important for energy supply during liver tissue repair in partial hepatectomy.[234] The distribution of TG 58:8 in Figure 16b confirms this, as the analyte is most abundant in tissue damage, whereas it is only detectable as noise in the control tissue. Interestingly, the accumulation seems to be highest directly around the parasite. This could be a direct effect of the parasite, as it is known to induce oxidative stress.[235] This in turn can result in an accumulation of TGs.[236]

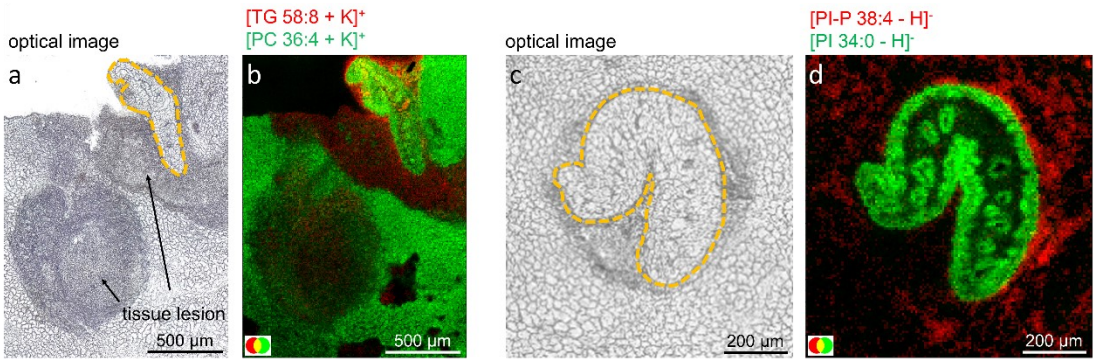

Figure 16: (a) Optical microscopic image before analysis of a rat liver tissue section during the acute infection stage. The outline of the migrating *F. hepatica* is emphasized with an orange dotted line, and arrows pointing at tissue lesions. (b) Positive-ion RG-overlay image corresponding to the optical microscopic image (a), showing TG 58:8 ($[M+K]^+$ at *m/z* 969.7308) in red and PC 36:4 ($[M+K]^+$ at *m/z* 820.5253) in green. (c) Optical microscopic image before analysis of a rat liver tissue section during the acute infection stage. The outline of the migrating *F. hepatica* is emphasized with an orange dotted line. (d) Negative-ion RG-overlay image corresponding to (c), showing PI-P 38:4 ($[M-H]^-$ at *m/z* 869.5549) in red and PI 34:0 ($[M-H]^-$ at *m/z* 837.5499) in green. MSI measurements in this figure were performed with 7 µm step size.

Due to the high spatial resolution it is also possible to identify lipids that have accumulated at the host-parasite interface. An example is shown with plasmalogen phosphatidylinositol (PI) 34:0 in Figure 16d in red. Other plasmalogen phospholipids also show a similar distribution pattern, which can possibly be assigned to immune cells. For example, macrophages are known to be involved in the immune response during *Fasciola* infection and are generally rich in plasmalogen species. In addition, parasite-specific lipids, such as PI 34:0 in Figure 16d in green were detected. Although not capable of *de-novo* lipid synthesise, *F. hepatica* can enzymatically modify FAs from the host.[223] Future in-depth studies seem rational to build a detailed lipid atlas of *F. hepatica*, which, in conjugation with other localized data, will prove beneficial to better understand the fundamental biology of the parasite.

Conclusion

The objective of this work was to develop a method for analysing GSLs in parasitic samples, focusing on both, their identification and spatial localization. Two advanced analytical techniques, nano-HILIC MS/MS and AP-SMALDI MSI, were employed to achieve this goal.

In the first publication, we successfully established a nano-HILIC MS/MS method to analyse the GSL profile of hamster livers infected with *Schistosoma mansoni* for the first time. The liver homogenate extraction process was optimized to extract a range of GSLs from simple to complex forms. Sample preparation involved minimal processing, limited to the saponification of phospholipids and purification via solid-phase extraction (SPE) cartridges. Acidic and neutral GSLs were not separated, as the high separation efficiency and sensitivity of the nano-HILIC MS/MS method enabled simultaneous, comprehensive analysis of various GSL species. Using the generated database, distribution maps of identified GSL species were produced through AP-SMALDI MSI experiments. For these experiments, the DHAP matrix application was optimized to achieve high spatial resolution detection, with lateral resolutions up to 3 µm. The resulting distribution images of different GSL species within granulomas and their structures were correlated with specific immune cell populations and their differentiation. The congruence between the relative quantitative results from AP-SMALDI and nano-HILIC MS/MS data further validated the method's applicability for semi-quantitative MSI analysis.

In the second publication, we demonstrated the effectiveness of the nano-HILIC MS/MS method in analysing isolated *Fasciola hepatica* parasites. To manage the extensive data from six distinct groups (including *F. hepatica*, rat liver during acute and chronic infection, and corresponding controls), a semi-

automatic data analysis workflow was developed. This approach allowed for the identification of previously unknown GSLs, culminating in the creation of a database comprising 212 distinct molecular GSL species. This database facilitated the analysis of AP-SMALDI MSI experiments, showcasing, for the first time, the distribution of GSLs at the molecular level in both parasite and host tissues. The detection of intact molecular species proved crucial, revealing significant differences in the distribution of GSLs with similar headgroup compositions in adult *F. hepatica*, which may hold biological relevance. The high spatial resolution also enabled isolated AP-SMALDI analysis of immature migrating *F. hepatica* in liver tissue, with comparisons to adult forms offering insights into tissue remodelling and the roles of specific GSLs during developmental stages. As in the first study, GSL distributions in host tissues were associated with immune cells, and similar analyses were extended to plasmalogen species. The AP-SMALDI MSI technique, while optimized for GSL detection using DHAP, also facilitated the detection of other lipid species in the same experiment. These findings linked the distribution profiles of various lipid species to processes such as tissue damage and liver repair during *F. hepatica* infection.

Future Work

With this work, we provide a comprehensive toolbox for the initial analysis of GSLs in a given sample system. These experiments and results lay the foundation for further, more detailed investigations. Through our studies, we reduced the number of GLS species, which are potentially involved in host-parasite-interaction by locally resolving the GSL profile. For instance, we identified GSL species in the tegument of *F. hepatica*, with several of these GSL bearing an ULCFA. In a multimodal approach with local transcriptomic data, we may have already revealed pathways of GSLs modification by *F. hepatica*. Here, future knockdown experiments of the four identified elongase genes (D915_006030, D915_002071, D915_002072, D915_004203) can help to verify our hypothesis and, more importantly, to elucidate the importance of these GSLs for host-parasite interaction.[237]

A similar approach can be applied for another finding. As previously described, several GLS species with a hydroxylated fatty acid are located within the tegument. Identifying the genes responsible for hydroxylation of FA's in *F. hepatica* and subsequent knockdown experiments, can help to reveal the significance of this small structural feature in a biological context.

Additionally, we found that *F. hepatica* potentially converts mono- to trihexosylceramides, with the latter being accumulated within the tegument. Therefore, *in vitro* cultivation of *F. hepatica* may allow the incorporation of chemical probes by utilizing modified monohexosylceramides, for which a large variety of derivates is available.[238] Subsequent activity-based protein profiling may help to understand the mode of action between parasite's GSLs and the host proteins.

Besides parasite-specific GLSs, we can associate GSLs to immune cells from the host. As some correlations are ambiguous, combination of MALDI MSI results with cell-type specific immunohistostaining can strengthen our results. This is important, as the GSL profiles and functions of immune cells is dependent on different factors, such as pathogenesis or stage of differentiation.[213,239] For example, GSLs on immune cells during cancer can reduce the apoptosis capacity of the immune system.[240] It has to be evaluated in more detail, if similar or other functions, like orchestrating granuloma formation, are fulfilled of host GSLs during schistosomiasis. For this, inhibitor or CRISPR/Cas9 studies targeting metabolic pathways of GSL species can be performed. However, to target the right metabolic pathways, the precise structural elucidation of the GSL species, which we identified, is required.

For this, more detailed analysis including distinguishing between monomers (Gal vs. Glc) and determining linkage positions are essential. Amidation experiments are already known for N-glycan MALDI MSI experiments in order to investigate the isomerism of the linkage of sialic acid.[124] In addition to the on-tissue derivatisation approach, on-tissue MS/MS experiments may also resolve the

distribution of isomers. For example, in nano-ESI MS/MS experiments, a distinction can be made between α- and β-hexosylceramides on the basis of the relative intensity of the fragments.[241] To achieve this level of resolution, however, further improvements in the detection sensitivity of GSLs are necessary. One promising strategy is salt doping, which has already been shown to increase signal intensity in MALDI MSI experiments for neutral lipids.[242]

Therefore, in initial experiments we performed AP-SMALDI MSI experiments with additional salt doping for isolated *F. hepatica*, as we only visualised a limited number of neutral GSL of our in-house database during the experiments in publication II. For the salt-doping experiments we also performed matrix sublimation of DHAP. Accordingly, a salt solution is sprayed beforehand. In initial screening experiments, a 10 mmol/L potassium carbonate solution in methanol/water (3/1, v/v) with 80 µL spray volume has proven to be the best approach for our application so far.

The comparative analysis between AP-SMALDI MSI with salt doping and normal sample preparation is presented in Figure 17, focusing on two GSL species. Specifically, Hex_3Cer 20:0;O3/h18:0 (depicted in Figure 17 b and c) exhibits a consistent distribution across the tegument and abdominal sucker in both measurements. On the other hand, Hex_2Cer 18:1;O2/24:1 (Figure 17 d and e) only reveals a distinct distribution in the salt-doped tissue section. Upon comparison with the H&E staining of a *F. hepatica* longitudinal section (Figure 5a) post-measurement, it is evident that this GSL accumulates in the uterus. Overall, our investigation allowed for the local identification of 42 neutral GSLs out of 69 of *F. hepatica* deriving from our nano-HILIC MS/MS database from publication II. These findings are visualized in the index images provided in Figure 18. Out of these 42 compounds, only 13 showed the same distribution for salt doped experiments compared to normal experiments, highlighted by a red box in Figure 18. For the remaining 29 GSLs, we observed either similar distributions with additional signal in other histological features of *F. hepatica* in the salt-doped MSI experiments or exclusive detection for the salt-doped experiment. These distinct ion-images are highlighted by a green box in Figure 18.

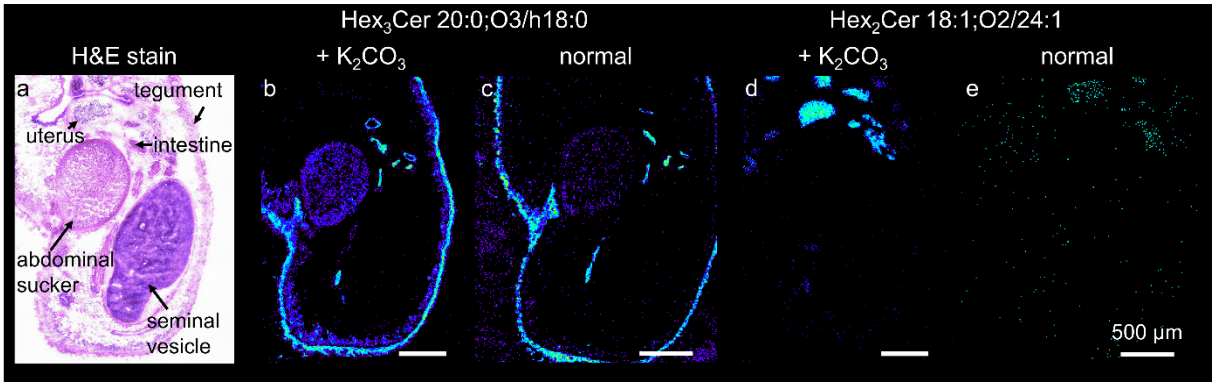

Figure 17: (a) H&E staining of a *F. hepatica* longitudinal section of the salt-doped experiment after MSI measurement. (b) Index image of the Hex_3Cer 20:0;O3/h18:0 ($[M+H]^+$ at *m/z* 1114.7459, $[M+Na]^+$ at *m/z* 1136.7279, and $[M+K]^+$ at *m/z* 1152.7018) of a salt-doped tissue section. (c) Index image of the Hex_3Cer 20:0;O3/h18:0 without salt doping of a consecutive tissue section. (d) Index image of the Hex_3Cer 20:0;O3/h18:0 ($[M+H]^+$ at m/z 972.7347, $[M+Na]^+$ at *m/z* 994.7165, and $[M+K]^+$ at *m/z* 1010.6904) of a salt-doped tissue section. (e) Index image of the Hex_3Cer 20:0;O3/h18:0 without salt doping of a consecutive tissue section. The AP-SMALDI MSI measurements were performed with 10 µm step size.

To test the robustness of the salt doping we already performed biological replicate measurements. The trend of improved detection of GSLs for salt-doped tissue sections persisted across two additional biological replicates, and the corresponding numerical data is detailed in Table 1. For the third replicate, we find a non-negligible number of images, where we observe different distributions for salt-doped and normal *F. hepatica* sections. However, the results for the biological replicate 1 and 3 represent a similar number of species showing the same distribution and similar results for improved

detectability for salt-doped experiments. In both replicates, parts of the reproductive system were analysed. In contrast, the results for the second biological replicate, not bearing histological features linked to the reproductive system, show less overlap in total numbers. These results then guided us to evaluate the GSLs in the reproductive system.

Table 1: Comparison of *F. hepatica* AP-SMALDI measurements with and without additional salt doping for 69 neutral GSL species identified by nano-HILIC MS/MS experiments.

biological replicate	matching distribution	only/additional distribution for salt doped experiments	different distribution	not detected
1	13	29	1	27
2	23	20	-	26
3	12	31	9	17

We found, that the more intricate GSL structures are frequently localized in histological features like uterus or vitellarium. This underscores the potential significance of complex GSLs in the reproductive processes of *F. hepatica*. Therefore, we performed AP-SMALDI MSI measurements with a salt-doped *F. hepatica* longitudinal tissue section bearing several intact eggs. Indeed, the five-monosaccharide-containing species Hex_5Cer 18:1;O2/24:1 shows an accumulation in the eggs as shown in Figure 19. For *S. mansoni* it is known that high-mannose N-glycans can drive the immune response, and that glycosylated antigens from the schistosome eggs polarize the Th2 immune response.[243] It is tempting to speculate that similar mechanisms appear for *F. hepatica* eggs when deposited in the bile duct, of which some enter the bile duct tissue.

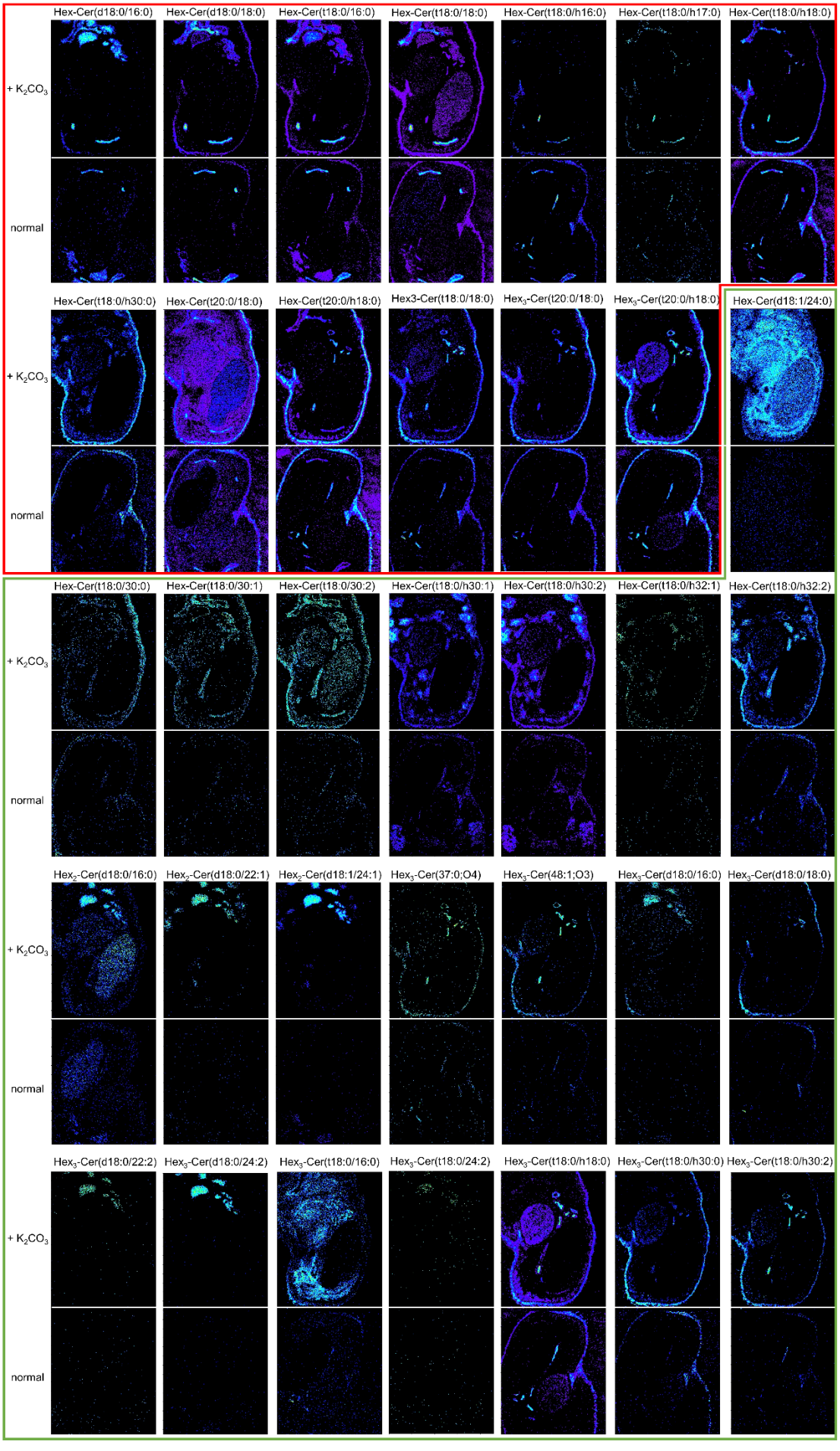
Hex-Cer(d18:0/16:0)
Hex-Cer(d18:0/18:0)
Hex-Cer(t18:0/16:0)
Hex-Cer(t18:0/18:0)
Hex-Cer(t18:0/h16:0)
Hex-Cer(t18:0/h17:0)
Hex-Cer(t18:0/h18:0)
+ K2CO3
normal
Hex-Cer(t18:0/h30:0)
Hex-Cer(t20:0/18:0)
Hex-Cer(t20:0/h18:0)
Hex3-Cer(t18:0/18:0)
Hex3-Cer(t20:0/18:0)
Hex3-Cer(t20:0/h18:0)
Hex-Cer(d18:1/24:0)
Hex-Cer(t18:0/30:0)
Hex-Cer(t18:0/30:1)
Hex-Cer(t18:0/30:2)
Hex-Cer(t18:0/h30:1)
Hex-Cer(t18:0/h30:2)
Hex-Cer(t18:0/h32:1)
Hex-Cer(t18:0/h32:2)
Hex2-Cer(d18:0/16:0)
Hex2-Cer(d18:0/22:1)
Hex2-Cer(d18:1/24:1)
Hex3-Cer(37:0;O4)
Hex3-Cer(48:1;O3)
Hex3-Cer(d18:0/16:0)
Hex3-Cer(d18:0/18:0)
Hex3-Cer(d18:0/22:2)
Hex3-Cer(d18:0/24:2)
Hex3-Cer(t18:0/16:0)
Hex3-Cer(t18:0/24:2)
Hex3-Cer(t18:0/h18:0)
Hex3-Cer(t18:0/h30:0)
Hex3-Cer(t18:0/h30:2)

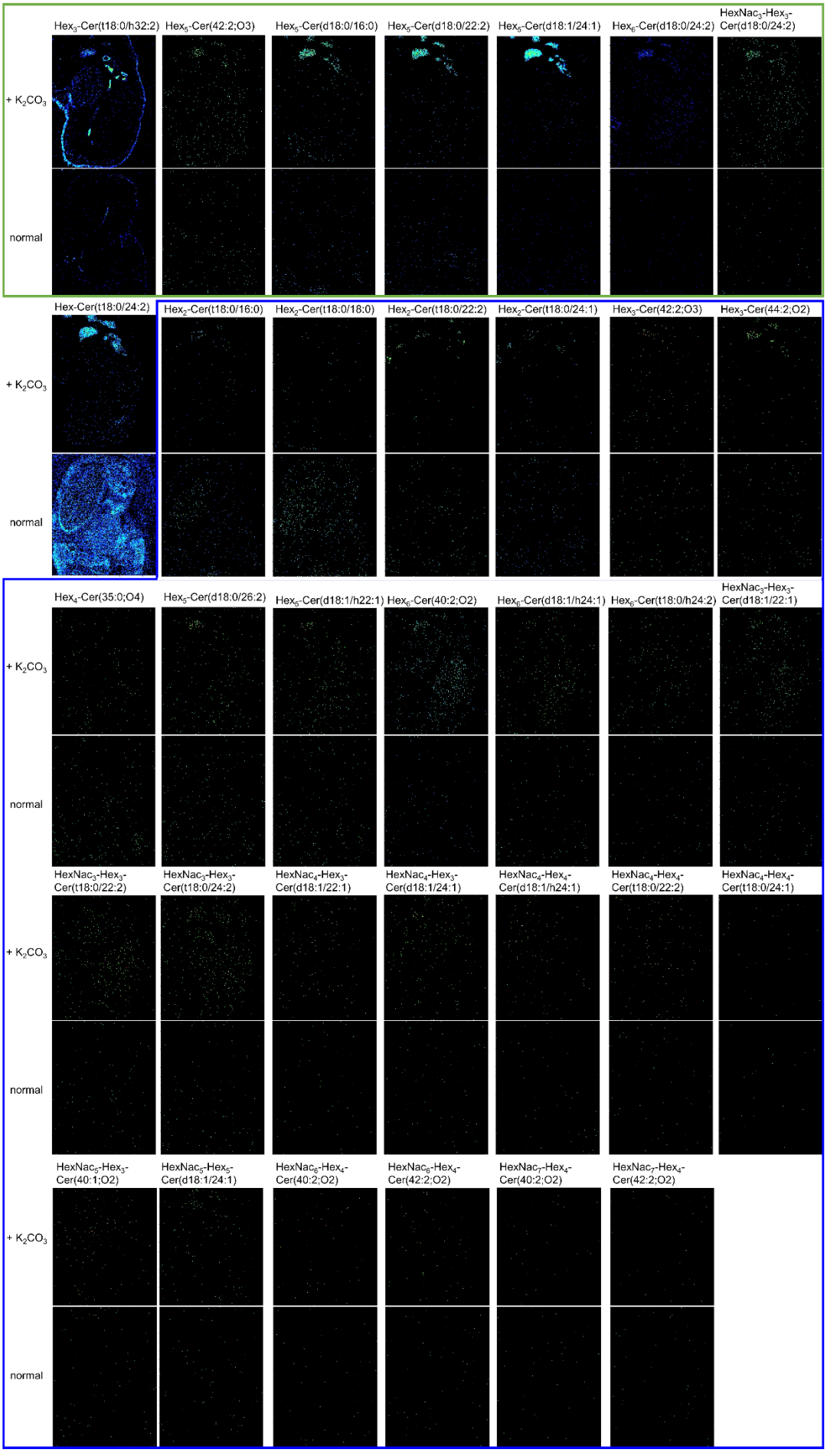
Hex3-Cer(t18:0/h32:2)
Hex5-Cer(42:2;O3)
Hex5-Cer(d18:0/16:0)
Hex5-Cer(d18:0/22:2)
Hex5-Cer(d18:1/24:1)
Hex6-Cer(d18:0/24:2)
HexNac3-Hex3-Cer(d18:0/24:2)
+ K2CO3
normal
Hex-Cer(t18:0/24:2)
Hex2-Cer(t18:0/16:0)
Hex2-Cer(t18:0/18:0)
Hex2-Cer(t18:0/22:2)
Hex2-Cer(t18:0/24:1)
Hex3-Cer(42:2;O3)
Hex3-Cer(44:2;O2)
+ K2CO3
normal
Hex4-Cer(35:0;O4)
Hex5-Cer(d18:0/26:2)
Hex5-Cer(d18:1/h22:1)
Hex6-Cer(40:2;O2)
Hex6-Cer(d18:1/h24:1)
Hex6-Cer(t18:0/h24:2)
HexNac3-Hex3-Cer(d18:1/22:1)
+ K2CO3
normal
HexNac3-Hex3-Cer(t18:0/22:2)
HexNac3-Hex3-Cer(t18:0/24:2)
HexNac4-Hex3-Cer(d18:1/22:1)
HexNac4-Hex3-Cer(d18:1/24:1)
HexNac4-Hex4-Cer(d18:1/h24:1)
HexNac4-Hex4-Cer(t18:0/22:2)
HexNac4-Hex4-Cer(t18:0/24:1)
+ K2CO3
normal
HexNac5-Hex3-Cer(40:1;O2)
HexNac5-Hex5-Cer(d18:1/24:1)
HexNac6-Hex4-Cer(40:2;O2)
HexNac6-Hex4-Cer(42:2;O2)
HexNac7-Hex4-Cer(40:2;O2)
HexNac7-Hex4-Cer(42:2;O2)
+ K2CO3
normal

Figure 18: Salt doping experiments with a longitudinal *F. hepatica* tissue sections for the first biological replicate. Index images of the protonated, sodiated and potassiated adduct for 69 neutral GSLs are shown. For each ion-image, two measurements were stitched to one hypercube, with the salt-doped experiments above the normal AP-SMALDI experiments from a consecutive tissue section. A mass deviation of ± 5 ppm was used for the generation of the images. The AP-SMALDI MSI measurements were performed with 10 µm step size.

Overall, our salt doping methodology has improved the MALDI MSI outcome, revealing the additional distribution of many more GSLs compared to MSI experiments without salt doping. While consistent with results of a previous study, our use of potassium carbonate in conjunction with DHB matrix, though not as potent as the combination with DHAP matrix, represents a novel approach for AP-MALDI MSI. Notably, the resulting index images without salt doping exhibited satisfactory quality, but the application of salt doping provides a decisive advantage. To enhance the detection of species near the limit of detection, the addition of an excess of a specific adduct ion, in our case the potassium ion, proved beneficial. Notably, our experimental parameters are compatible with high spatial resolution AP-SMALDI MSI experiments, as wash-out effects were not observed. While we only conducted a brief screening to identify the optimal salt doping conditions, future in-depth studies would be valuable to optimize salt doping conditions under AP-MALDI MSI analysis.

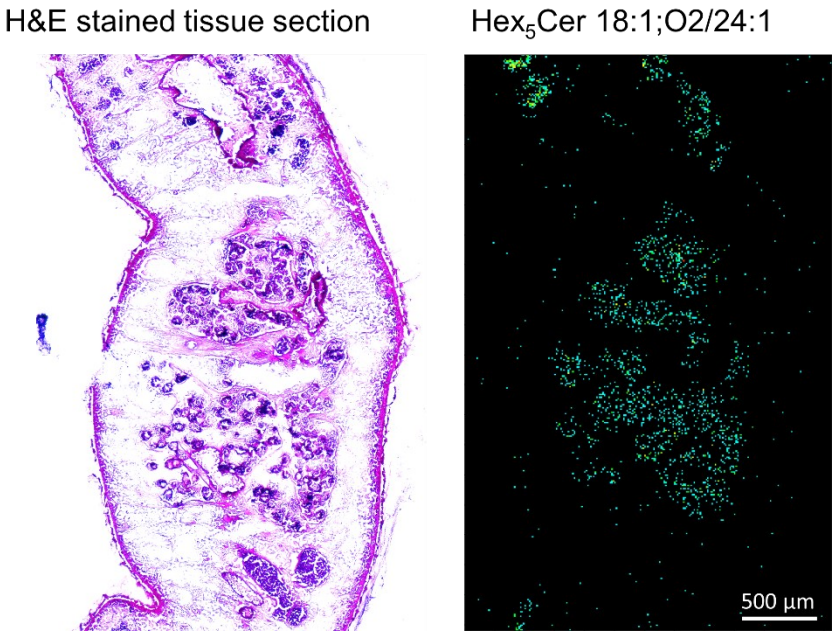

Figure 19: (left) H&E stained transversal *F. hepatica* section after AP-SMALDI MSI (left). (right) Ion-image showing the accumulation of Hex_5Cer 18:1;O2/24:1 ($[M+K]^+$ at *m/z* 1496.8489) in *F. hepatica* eggs.

References

(1) Gross, J. H. *Massenspektrometrie*: *Ein Lehrbuch*; Springer Spektrum Berlin, Heidelberg, 2013. DOI: 10.1007/978-3-8274-2981-0.

(2) Todd, J. F. Recommendations for nomenclature and symbolism for mass spectroscopy. *International Journal of Mass Spectrometry and Ion Processes* **1995**, *142* (3), 209–240. DOI: 10.1016/0168-1176(95)93811-F.

(3) Lössl, P.; van de Waterbeemd, M.; Heck, A., JR. The diverse and expanding role of mass spectrometry in structural and molecular biology. *EMBO J.* **2016**, *35* (24), 2634–2657. DOI: 10.15252/embj.201694818.

(4) Ren, J.-L.; Zhang, A.-H.; Kong, L.; Wang, X.-J. Advances in mass spectrometry-based metabolomics for investigation of metabolites. *RSC Adv.* **2018**, *8* (40), 22335–22350. DOI: 10.1039/C8RA01574K.

(5) Wien, W. Untersuchungen über die electrische Entladung in verdünnten Gasen. *Ann. Phys. (Berlin)* **1898**, *301* (6), 440–452. DOI: 10.1002/andp.18983010618.

(6) Thomson, J. J. *Rays of positive electricity and their application to chemical analysis.*, 1st ed.; Longmans, Green & Co., 1913.

(7) Dempster, A. J. A new Method of Positive Ray Analysis. *Phys. Rev.* **1918**, *11* (4), 316–325. DOI: 10.1103/PhysRev.11.316.

(8) Aston, F. W. LXXIV. A positive ray spectrograph. *The London, Edinburgh, and Dublin Philosophical Magazine and Journal of Science* **1919**, *38* (228), 707–714. DOI: 10.1080/14786441208636004.

(9) Hoffmann, E. de; Stroobant, V. *Mass Spectrometry*: *Principles and Applications*, 3rd ed.; Newark, John Wiley & Sons, 2007.

(10) Stephens, W. E.; Serin, B.; Myerhof, W. E. Erratum: A Method for Measuring Effective Contact e.m.f. between a Metal and a Semi-Conductor. *Phys. Rev.* **1946**, *69* (5-6), 244. DOI: 10.1103/PhysRev.69.244.2.

(11) Cameron, A. E.; Eggers, D. F. An Ion ``Velocitron''. *Rev*. *Sci*. *Instrum*. **1948**, *19* (9), 605–607. DOI: 10.1063/1.1741336.

(12) Paul, W.; Steinwedel, H. Notizen: Ein neues Massenspektrometer ohne Magnetfeld. *Z. Naturforsch. A* **1953**, *8* (7), 448–450. DOI: 10.1515/zna-1953-0710.

(13) Comisarow, M. B.; Marshall, A. G. Fourier transform ion cyclotron resonance spectroscopy. *Chem. Phys. Lett.* **1974**, *25* (2), 282–283. DOI: 10.1016/0009-2614(74)89137-2.

(14) Kingdon, K. H. A Method for the Neutralization of Electron Space Charge by Positive Ionization at Very Low Gas Pressures. *Phys. Rev.* **1923**, *21* (4), 408–418. DOI: 10.1103/PhysRev.21.408.

(15) Knight, R. D. The general form of the quadrupole ion trap potential. *Int. J. Mass Spectrom. Ion Physics* **1983**, *51* (1), 127–131. DOI: 10.1016/0020-7381(83)85033-5.

(16) Makarov, A. Electrostatic axially harmonic orbital trapping: a high-performance technique of mass analysis. *Anal. Chem.* **2000**, *72* (6), 1156–1162. DOI: 10.1021/ac991131p.

(17) Xian, F.; Hendrickson, C. L.; Marshall, A. G. High resolution mass spectrometry. *Anal. Chem.* **2012**, *84* (2), 708–719. DOI: 10.1021/ac203191t.

(18) Awad, H.; Khamis, M. M.; El-Aneed, A. Mass Spectrometry, Review of the Basics: Ionization. *Appl. Spectrosc. Rev.* **2015**, *50* (2), 158–175. DOI: 10.1080/05704928.2014.954046.

(19) Maciel, E. V. S.; Pereira Dos Santos, N. G.; Vargas Medina, D. A.; Lanças, F. M. Electron ionization mass spectrometry: Quo vadis? *Electrophoresis* **2022**, *43* (15), 1587–1600. DOI: 10.1002/elps.202100392.

(20) Klyba, L. V.; Nedolya, N. A.; Sanzheeva, E. R.; Tarasova, O. A. Mass Spectra of New Heterocycles: XXI. Study of Alkyl [(5-Amino-1H-pyrrol-2-yl)sulfanyl]acetates by Electron and Chemical Ionization Mass Spectrometry. *Russ J Org Chem* **2020**, *56* (5), 768–774. DOI: 10.1134/S1070428020050073.

(21) Karas, M.; Bachmann, D.; Bahr, U.; Hillenkamp, F. Matrix-assisted ultraviolet laser desorption of non-volatile compounds. *Int. J. Mass Spectrom. Ion Processes* **1987**, *78*, 53–68. DOI: 10.1016/0168-1176(87)87041-6.

(22) Tanaka, K.; Waki, H.; Ido, Y.; Akita, S.; Yoshida, Y.; Yoshida, T.; Matsuo, T. Protein and polymer analyses up to m/z 100 000 by laser ionization time-of-flight mass spectrometry. *Rapid Commun. Mass Spectrom.* **1988**, *2* (8), 151–153. DOI: 10.1002/rcm.1290020802.
(23) Fenn, J. B.; Mann, M.; Meng, C. K.; Wong, S. F.; Whitehouse, C. M. Electrospray ionization for mass spectrometry of large biomolecules. *Science* **1989**, *246* (4926), 64–71. DOI: 10.1126/science.2675315.
(24) Karas, M.; Bachmann, D.; Hillenkamp, F. Influence of the wavelength in high-irradiance ultraviolet laser desorption mass spectrometry of organic molecules. *Anal. Chem.* **1985**, *57* (14), 2935–2939. DOI: 10.1021/ac00291a042.
(25) Taylor, G. I. Disintegration of water drops in an electric field. *Proc. R. Soc. Lond. A* **1964**, *280* (1382), 383–397. DOI: 10.1098/rspa.1964.0151.
(26) Dole, M.; Mack, L. L.; Hines, R. L.; Mobley, R. C.; Ferguson, L. D.; Alice, M. B. Molecular Beams of Macroions. *J. Chem. Phys.* **1968**, *49* (5), 2240–2249. DOI: 10.1063/1.1670391.
(27) Wilm, M. Principles of electrospray ionization. *Mol. Cell. Proteom.* **2011**, *10* (7), M111.009407. DOI: 10.1074/mcp.M111.009407.
(28) Konermann, L.; Ahadi, E.; Rodriguez, A. D.; Vahidi, S. Unraveling the mechanism of electrospray ionization. *Anal. Chem.* **2013**, *85* (1), 2–9. DOI: 10.1021/ac302789c.
(29) Covey, T. R.; Thomson, B. A.; Schneider, B. B. Atmospheric pressure ion sources. *Mass Spectrom. Rev.* **2009**, *28* (6), 870–897. DOI: 10.1002/mas.20246.
(30) Jemal, M. High-throughput quantitative bioanalysis by LC/MS/MS. *Biomed. Chromatogr.* **2000**, *14* (6), 422–429. DOI: 10.1002/1099-0801(200010)14:6<422:AID-BMC25>3.0.CO;2-I.
(31) Wilm, M. S.; Mann, M. Electrospray and Taylor-Cone theory, Dole's beam of macromolecules at last? *Int. J. Mass Spectrom. and Ion Processes* **1994**, *136* (2-3), 167–180. DOI: 10.1016/0168-1176(94)04024-9.
(32) Wilm, M.; Mann, M. Analytical properties of the nanoelectrospray ion source. *Anal. Chem.* **1996**, *68* (1), 1–8. DOI: 10.1021/ac9509519.
(33) Juraschek, R.; Dülcks, T.; Karas, M. Nanoelectrospray--more than just a minimized-flow electrospray ionization source. *J. Am. Soc. Mass Spectrom.* **1999**, *10* (4), 300–308. DOI: 10.1016/S1044-0305(98)00157-3.
(34) Schmidt, A.; Karas, M.; Dülcks, T. Effect of different solution flow rates on analyte ion signals in nano-ESI MS, or: when does ESI turn into nano-ESI? *J. Am. Soc. Mass Spectrom.* **2003**, *14* (5), 492–500. DOI: 10.1016/S1044-0305(03)00128-4.
(35) Fligge, T. A.; Bruns, K.; Przybylski, M. Analytical development of electrospray and nanoelectrospray mass spectrometry in combination with liquid chromatography for the characterization of proteins. *J. Chromatogr. B Biomed. Appl.* **1998**, *706* (1), 91–100. DOI: 10.1016/S0378-4347(97)00535-5.
(36) Bahr, U.; Pfenninger, A.; Karas, M.; Stahl, B. High-sensitivity analysis of neutral underivatized oligosaccharides by nanoelectrospray mass spectrometry. *Anal. Chem.* **1997**, *69* (22), 4530–4535. DOI: 10.1021/ac970624w.
(37) Karas, M.; Bahr, U.; Dülcks, T. Nano-electrospray ionization mass spectrometry: addressing analytical problems beyond routine. *Fresenius' J. Anal. Chem.* **2000**, *366* (6-7), 669–676. DOI: 10.1007/s002160051561.
(38) Calvano, C. D.; Monopoli, A.; Cataldi, T. R. I.; Palmisano, F. MALDI matrices for low molecular weight compounds: an endless story? *Anal. Bioanal. Chem.* **2018**, *410* (17), 4015–4038. DOI: 10.1007/s00216-018-1014-x.
(39) Karas, M.; Hillenkamp, F. Laser desorption ionization of proteins with molecular masses exceeding 10,000 daltons. *Anal. Chem.* **1988**, *60* (20), 2299–2301. DOI: 10.1021/ac00171a028.
(40) Nishikaze, T.; Okumura, H.; Jinmei, H.; Amano, J. Correlation between Sweet Spots of Glycopeptides and Polymorphism of the Matrix Crystal in MALDI Samples. *Mass spectrometry (Tokyo, Japan)* **2012**, *1* (1), A0006. DOI: 10.5702/massspectrometry.A0006.

(41) Gemperline, E.; Rawson, S.; Li, L. Optimization and comparison of multiple MALDI matrix application methods for small molecule mass spectrometric imaging. *Anal. Chem.* **2014**, *86* (20), 10030–10035. DOI: 10.1021/ac5028534.
(42) Krüger, R.; Pfenninger, A.; Fournier, I.; Gluckmann, M.; Karas, M. Analyte incorporation and ionization in matrix-assisted laser desorption/ionization visualized by pH indicator molecular probes. *Anal. Chem.* **2001**, *73* (24), 5812–5821. DOI: 10.1021/ac010827r.
(43) Strupat, K.; Karas, M.; Hillenkamp, F. 2,5-Dihydroxybenzoic acid: a new matrix for laser desorption—ionization mass spectrometry. *Int. J. Mass Spectrom. and Ion Processes* **1991**, *111*, 89–102. DOI: 10.1016/0168-1176(91)85050-V.
(44) Soltwisch, J.; Jaskolla, T. W.; Hillenkamp, F.; Karas, M.; Dreisewerd, K. Ion yields in UV-MALDI mass spectrometry as a function of excitation laser wavelength and optical and physico-chemical properties of classical and halogen-substituted MALDI matrixes. *Anal. Chem.* **2012**, *84* (15), 6567–6576. DOI: 10.1021/ac3008434.
(45) Knochenmuss, R. Ion formation mechanisms in UV-MALDI. *The Analyst* **2006**, *131* (9), 966–986. DOI: 10.1039/B605646F.
(46) Laiko, V. V.; Baldwin, M. A.; Burlingame, A. L. Atmospheric pressure matrix-assisted laser desorption/ionization mass spectrometry. *Anal. Chem.* **2000**, *72* (4), 652–657. DOI: 10.1021/ac990998k.
(47) Laiko, V. V.; Moyer, S. C.; Cotter, R. J. Atmospheric pressure MALDI/ion trap mass spectrometry. *Anal. Chem.* **2000**, *72* (21), 5239–5243. DOI: 10.1021/ac000530d.
(48) Buchberger, A. R.; DeLaney, K.; Johnson, J.; Li, L. Mass Spectrometry Imaging: A Review of Emerging Advancements and Future Insights. *Anal. Chem.* **2018**, *90* (1), 240–265. DOI: 10.1021/acs.analchem.7b04733.
(49) Spengler, B. Mass spectrometry imaging of biomolecular information. *Anal. Chem.* **2015**, *87* (1), 64–82. DOI: 10.1021/ac504543v.
(50) Spengler, B.; Hubert, M.; Kaufmann, R. MALDI ion imaging and biological ion imaging with a new scanning UV-laser microprobe. *Proceedings of the 42nd ASMS Conference on Mass Spectrometry and Allied Topics*, Chicago, IL, USA, 29 May - 3 June 1994, 1041.
(51) Caprioli, R. M.; Farmer, T. B.; Gile, J. Molecular imaging of biological samples: localization of peptides and proteins using MALDI-TOF MS. *Anal. Chem.* **1997**, *69* (23), 4751–4760. DOI: 10.1021/ac970888i.
(52) Gilmore, I. S.; Heiles, S.; Pieterse, C. L. Metabolic Imaging at the Single-Cell Scale: Recent Advances in Mass Spectrometry Imaging. *Annu. Rev. Anal. Chem.* **2019**, *12* (1), 201–224. DOI: 10.1146/annurev-anchem-061318-115516.
(53) Kompauer, M.; Heiles, S.; Spengler, B. Atmospheric pressure MALDI mass spectrometry imaging of tissues and cells at 1.4-µm lateral resolution. *Nat. methods* **2017**, *14* (1), 90–96. DOI: 10.1038/nmeth.4071.
(54) Niehaus, M.; Soltwisch, J.; Belov, M. E.; Dreisewerd, K. Transmission-mode MALDI-2 mass spectrometry imaging of cells and tissues at subcellular resolution. *Nat. methods* **2019**, *16* (9), 925–931. DOI: 10.1038/s41592-019-0536-2.
(55) Kompauer, M.; Heiles, S.; Spengler, B. Autofocusing MALDI mass spectrometry imaging of tissue sections and 3D chemical topography of nonflat surfaces. *Nat. methods* **2017**, *14* (12), 1156–1158. DOI: 10.1038/nmeth.4433.
(56) Kadesch, P.; Quack, T.; Gerbig, S.; Grevelding, C. G.; Spengler, B. Tissue- and sex-specific lipidomic analysis of Schistosoma mansoni using high-resolution atmospheric pressure scanning microprobe matrix-assisted laser desorption/ionization mass spectrometry imaging. *PLoS Negl. Trop. Dis.* **2020**, *14* (5), e0008145. DOI: 10.1371/journal.pntd.0008145.
(57) Liu, H.; Han, M.; Li, J.; Qin, L.; Chen, L.; Hao, Q.; Jiang, D.; Chen, D.; Ji, Y.; Han, H.; Long, C.; Zhou, Y.; Feng, J.; Wang, X. A Caffeic Acid Matrix Improves In Situ Detection and Imaging of Proteins with High Molecular Weight Close to 200,000 Da in Tissues by Matrix-Assisted Laser Desorption/Ionization Mass Spectrometry Imaging. *Anal. Chem.* **2021**, *93* (35), 11920–11928. DOI: 10.1021/acs.analchem.0c05480.

(58) Römpp, A.; Spengler, B. Mass spectrometry imaging with high resolution in mass and space. *Histochem. Cell Biol.* **2013**, *139* (6), 759–783. DOI: 10.1007/s00418-013-1097-6.
(59) Moore, J. L.; Charkoftaki, G. A Guide to MALDI Imaging Mass Spectrometry for Tissues. *J. Proteome Res.* **2023**, *22* (11), 3401–3417. DOI: 10.1021/acs.jproteome.3c00167.
(60) Kadesch, P.; Quack, T.; Gerbig, S.; Grevelding, C. G.; Spengler, B. Lipid Topography in Schistosoma mansoni Cryosections, Revealed by Microembedding and High-Resolution Atmospheric-Pressure Matrix-Assisted Laser Desorption/Ionization (MALDI) Mass Spectrometry Imaging. *Anal. Chem.* **2019**, *91* (7), 4520–4528. DOI: 10.1021/acs.analchem.8b05440.
(61) Spengler, B.; Luetzenkirchen, F.; Metzger, S.; Chaurand, P.; Kaufmann, R.; Jeffery, W.; Bartlet-Jones, M.; Pappin, D. J. Peptide sequencing of charged derivatives by postsource decay MALDI mass spectrometry. *Int. J. Mass Spectrom. and Ion Processes* **1997**, *169-170*, 127–140. DOI: 10.1016/S0168-1176(97)00218-8.
(62) Cobice, D. F.; Mackay, C. L.; Goodwin, R. J. A.; McBride, A.; Langridge-Smith, P. R.; Webster, S. P.; Walker, B. R.; Andrew, R. Mass spectrometry imaging for dissecting steroid intracrinology within target tissues. *Anal. Chem.* **2013**, *85* (23), 11576–11584. DOI: 10.1021/ac402777k.
(63) Dreisbach, D.; Heiles, S.; Bhandari, D. R.; Petschenka, G.; Spengler, B. Molecular Networking and On-Tissue Chemical Derivatization for Enhanced Identification and Visualization of Steroid Glycosides by MALDI Mass Spectrometry Imaging. *Anal. Chem.* **2022**, *94* (46), 15971–15979. DOI: 10.1021/acs.analchem.2c02694.
(64) Lemaire, R.; Wisztorski, M.; Desmons, A.; Tabet, J. C.; Day, R.; Salzet, M.; Fournier, I. MALDI-MS direct tissue analysis of proteins: Improving signal sensitivity using organic treatments. *Anal. Chem.* **2006**, *78* (20), 7145–7153. DOI: 10.1021/ac060565z.
(65) Huber, K.; Khamehgir-Silz, P.; Schramm, T.; Gorshkov, V.; Spengler, B.; Römpp, A. Approaching cellular resolution and reliable identification in mass spectrometry imaging of tryptic peptides. *Anal. Bioanal. Chem.* **2018**, *410* (23), 5825–5837. DOI: 10.1007/s00216-018-1199-z.
(66) Powers, T. W.; Jones, E. E.; Betesh, L. R.; Romano, P. R.; Gao, P.; Copland, J. A.; Mehta, A. S.; Drake, R. R. Matrix assisted laser desorption ionization imaging mass spectrometry workflow for spatial profiling analysis of N-linked glycan expression in tissues. *Anal. Chem.* **2013**, *85* (20), 9799–9806. DOI: 10.1021/ac402108x.
(67) Wäldchen, F.; Spengler, B.; Heiles, S. Reactive Matrix-Assisted Laser Desorption/Ionization Mass Spectrometry Imaging Using an Intrinsically Photoreactive Paternò-Büchi Matrix for Double-Bond Localization in Isomeric Phospholipids. *J. Am. Chem. Soc.* **2019**, *141* (30), 11816–11820. DOI: 10.1021/jacs.9b05868.
(68) Hankin, J. A.; Barkley, R. M.; Murphy, R. C. Sublimation as a method of matrix application for mass spectrometric imaging. *J. Am. Soc. Mass Spectrom.* **2007**, *18* (9), 1646–1652. DOI: 10.1016/j.jasms.2007.06.010.
(69) Paschke, C.; Leisner, A.; Hester, A.; Maass, K.; Guenther, S.; Bouschen, W.; Spengler, B. Mirion--a software package for automatic processing of mass spectrometric images. *J. Am. Soc. Mass Spectrom.* **2013**, *24* (8), 1296–1306. DOI: 10.1007/s13361-013-0667-0.
(70) Robichaud, G.; Garrard, K. P.; Barry, J. A.; Muddiman, D. C. MSiReader: an open-source interface to view and analyze high resolving power MS imaging files on Matlab platform. *J. Am. Soc. Mass Spectrom.* **2013**, *24* (5), 718–721. DOI: 10.1007/s13361-013-0607-z.
(71) Bokhart, M. T.; Nazari, M.; Garrard, K. P.; Muddiman, D. C. MSiReader v1.0: Evolving Open-Source Mass Spectrometry Imaging Software for Targeted and Untargeted Analyses. *J. Am. Soc. Mass Spectrom.* **2018**, *29* (1), 8–16. DOI: 10.1007/s13361-017-1809-6.
(72) Oetjen, J.; Veselkov, K.; Watrous, J.; McKenzie, J. S.; Becker, M.; Hauberg-Lotte, L.; Kobarg, J. H.; Strittmatter, N.; Mróz, A. K.; Hoffmann, F.; Trede, D.; Palmer, A.; Schiffler, S.; Steinhorst, K.; Aichler, M.; Goldin, R.; Guntinas-Lichius, O.; Eggeling, F. von; Thiele, H.; Maedler, K.; Walch, A.; Maass, P.; Dorrestein, P. C.; Takats, Z.; Alexandrov, T. Benchmark datasets for 3D MALDI- and DESI-imaging mass spectrometry. *GigaScience* **2015**, *4* (1), s13742-015-0059-4. DOI: 10.1186/s13742-015-0059-4.

(73) Palmer, A.; Phapale, P.; Chernyavsky, I.; Lavigne, R.; Fay, D.; Tarasov, A.; Kovalev, V.; Fuchser, J.; Nikolenko, S.; Pineau, C.; Becker, M.; Alexandrov, T. FDR-controlled metabolite annotation for high-resolution imaging mass spectrometry. *Nat. methods* **2017**, *14* (1), 57–60. DOI: 10.1038/nmeth.4072.
(74) Guo, X.; Cao, W.; Fan, X.; Guo, Z.; Zhang, D.; Zhang, H.; Ma, X.; Dong, J.; Wang, Y.; Zhang, W.; Ouyang, Z. Tandem Mass Spectrometry Imaging Enables High Definition for Mapping Lipids in Tissues. *Angew Chem. Int. Ed. Engl.* **2023**, *62* (9), e202214804. DOI: 10.1002/anie.202214804.
(75) Kanu, A. B. Recent developments in sample preparation techniques combined with high-performance liquid chromatography: A critical review. *J. Chromatogr. A* **2021**, *1654*, 462444. DOI: 10.1016/j.chroma.2021.462444.
(76) Tswett, M. S. Über eine neue Kategorie von Adsorptionserscheinungen und ihre Anwendung in der biochemischen Analyse. *Trudy kasansk. Obschtschesstwa Jessterstoi rspytat Otd. Biol.*, **1903** *14*, 20–26.
(77) Martin, A. J.; Synge, R. L. A new form of chromatogram employing two liquid phases: A theory of chromatography. 2. Application to the micro-determination of the higher monoamino-acids in proteins. *Biochem. J.* **1941**, *35* (12), 1358–1368. DOI: 10.1042/bj0351358.
(78) Horvath, C. G.; Preiss, B. A.; Lipsky, S. R. Fast liquid chromatography: an investigation of operating parameters and the separation of nucleotides on pellicular ion exchangers. *Anal. Chem.* **1967**, *39* (12), 1422–1428. DOI: 10.1021/ac60256a003.
(79) Huber, J. F.; Hulsman, J. A. A study of liquid chromatography in columns. The time of separation. *Anal. Chim. Acta* **1967**, *38* (1), 305–313. DOI: 10.1016/S0003-2670(01)80592-4.
(80) Wicke, E. J. C. Giddings: Dynamics of Chromatography. Part. I: Principles and Theory. *Bunsenges. Phys. Chem.* **1967**, *71* (2), 236. DOI: 10.1002/bbpc.19670710222.
(81) Kirkland, J. J. High-Speed Liquid Chromatography With Controlled Surface Porosity Supports. *J. Chromatogr. Sci.* **1969**, *7* (1), 7–12. DOI: 10.1093/chromsci/7.1.7.
(82) Horvath, C. G.; Lipsky, S. R. Use of liquid ion exchange chromatography for the separation of organic compounds. *Nature* **1966**, *211* (5050), 748–749. DOI: 10.1038/211748a0.
(83) Snyder, L. R.; Dolan, J. W. Chapter 1 - Milestones in the development of liquid chromatography. In Fanali, S.; Haddad P. R.; Poole, C. F.; Riekkola M.-L. (Eds.),
Liquid Chromatography, 2. ed. (pp. 1-15), Elsevier, 2017. 1–15. DOI: 10.1016/B978-0-12-805393-5.00001-4.
(84) Snyder, L. R.; Kirkland, J. J.; Dolan, J. W., Eds. *Introduction to modern liquid chromatography*, 3. ed.; Hoboken, John Wiley & Sons, 2010.
(85) Unger, K. K.; Ditz, R.; Machtejevas, E.; Skudas, R. Liquid chromatography--its development and key role in life science applications. *Angew Chem. Int. Ed. Engl.)* **2010**, *49* (13), 2300–2312. DOI: 10.1002/anie.200906976.
(86) Cajka, T.; Fiehn, O. Comprehensive analysis of lipids in biological systems by liquid chromatography-mass spectrometry. *TrAC, Trends Anal. Chem.* **2014**, *61*, 192–206. DOI: 10.1016/j.trac.2014.04.017.
(87) Eriksson, K.-O.; Belew, M. Hydrophobic interaction chromatography. In Jan-Christer Janson (Ed), *Protein Purification: Principles, High Resolution Methods, and Applications* (pp. 165-181), Hoboken, John Wiley & Sons, 2011. DOI: 10.1002/9780470939932.ch6.
(88) Alpert, A. J. Hydrophilic-interaction chromatography for the separation of peptides, nucleic acids and other polar compounds. *J. Chromatogr. A* **1990**, *499*, 177–196. DOI: 10.1016/S0021-9673(00)96972-3.
(89) Buszewski, B.; Noga, S. Hydrophilic interaction liquid chromatography (HILIC)--a powerful separation technique. *Anal. Bioanal. Chem.* **2012**, *402* (1), 231–247. DOI: 10.1007/s00216-011-5308-5.
(90) Karatapanis, A. E.; Fiamegos, Y. C.; Stalikas, C. D. A revisit to the retention mechanism of hydrophilic interaction liquid chromatography using model organic compounds. *J. Chromatogr.. A* **2011**, *1218* (20), 2871–2879. DOI: 10.1016/j.chroma.2011.02.069.
(91) Hanai, T. Definition of HILIC System and Quantitative Analysis of Retention Mechanisms. *Curr. Chromatogr.* **2018**, *5* (1), 43–52. DOI: 10.2174/2213240605666180207093716.

(92) Vissers, J. P.; Claessens, H. A.; Cramers, C. A. Microcolumn liquid chromatography: instrumentation, detection and applications. *J. Chromatogr. A* **1997**, *779* (1-2), 1–28. DOI: 10.1016/S0021-9673(97)00422-6.
(93) Tsuda, T.; Novotny, M. Packed microcapillary columns in high performance liquid chromatography. *Anal. Chem.* **1978**, *50* (2), 271–275. DOI: 10.1021/ac50024a026.
(94) Knox, J. H.; Gilbert, M. T. Kinetic optimization of straight open-tubular liquid chromatography. *J. Chromatogr. A* **1979**, *186*, 405–418. DOI: 10.1016/S0021-9673(00)95263-4.
(95) Asensio-Ramos, M.; Fanali, C.; D'Orazio, G.; Fanali, S. Nano-liquid chromatography. In Fanali, S.; Haddad P. R.; Poole, C. F.; Riekkola M.-L. (Eds.), *Liquid Chromatography*, 2. ed. (pp. 637-695), Elsevier, 2017. DOI: 10.1016/B978-0-12-805393-5.00027-0
(96) Šesták, J.; Moravcová, D.; Kahle, V. Instrument platforms for nano liquid chromatography. *J. Chromatogr. A* **2015**, *1421*, 2–17. DOI: 10.1016/j.chroma.2015.07.090.
(97) Shen, Y.; Zhao, R.; Berger, S. J.; Anderson, G. A.; Rodriguez, N.; Smith, R. D. High-efficiency nanoscale liquid chromatography coupled on-line with mass spectrometry using nanoelectrospray ionization for proteomics. *Anal. Chem.* **2002**, *74* (16), 4235–4249. DOI: 10.1021/ac0202280.
(98) Krisp, C.; Yang, H.; van Soest, R.; Molloy, M. P. Online Peptide fractionation using a multiphasic microfluidic liquid chromatography chip improves reproducibility and detection limits for quantitation in discovery and targeted proteomics. *Mol. Cell. Proteom.* **2015**, *14* (6), 1708–1719. DOI: 10.1074/mcp.M114.046425.
(99) Wilson, S. R.; Vehus, T.; Berg, H. S.; Lundanes, E. Nano-LC in proteomics: recent advances and approaches. *Bioanalysis* **2015**, *7* (14), 1799–1815. DOI: 10.4155/bio.15.92.
(100) Aydoğan, C.; Beltekin, B.; Aslan, H.; Yılmaz, F.; Göktürk, I.; Denizli, A.; El-Rassi, Z. Nanoscale separations: Recent achievements. *J. Chromatogr. Open* **2022**, *2*, 100066. DOI: 10.1016/j.jcoa.2022.100066.
(101) Moss, G. P.; Smith, P. A. S.; Tavernier, D. Glossary of class names of organic compounds and reactivity intermediates based on structure (IUPAC Recommendations 1995). *Pure Appl. Chem.* **1995**, *67* (8-9), 1307–1375. DOI: 10.1351/pac199567081307.
(102) Varki, A.; Kornfeld, S, Historical Background and Overview. In Varki, A.; Cummings, R. D.; Esko, J. D.; Stanley, P.; Hart, G. W.; Aebi, M.; Mohnen, D.; Kinoshita, T.; Packer, N. H.; Prestegard, J. H.; Schnaar, R. L.; Seeberger, P. H. (Eds.), *Essentials of Glycobiology*, 4. ed., Cold Spring Habor (NY), Cold Spring Harbor Laboratory Press, 2022. DOI: 10.1101/glycobiology.4e.1.
(103) Moremen, K. W.; Tiemeyer, M.; Nairn, A. V. Vertebrate protein glycosylation: diversity, synthesis and function. *Nat. Rev. Mol. Cell Biol.* **2012**, *13* (7), 448–462. DOI: 10.1038/nrm3383.
(104) Paulick, M. G.; Bertozzi, C. R. The glycosylphosphatidylinositol anchor: a complex membrane-anchoring structure for proteins. *Biochemistry* **2008**, *47* (27), 6991–7000. DOI: 10.1021/bi8006324.
(105) Merrill, A. H. Sphingolipid and glycosphingolipid metabolic pathways in the era of sphingolipidomics. *Chem. Rev.* **2011**, *111* (10), 6387–6422. DOI: 10.1021/cr2002917.
(106) Varki, A. Biological roles of glycans. *Glycobiology* **2017**, *27* (1), 3–49. DOI: 10.1093/glycob/cww086.
(107) Di Wu; Struwe, W. B.; Harvey, D. J.; Ferguson, M. A. J.; Robinson, C. V. N-glycan microheterogeneity regulates interactions of plasma proteins. *Proc. Natl. Acad. Sci. U. S. A.* **2018**, *115* (35), 8763–8768. DOI: 10.1073/pnas.1807439115.
(108) Sato, Y.; Takahashi, M.; Shibukawa, Y.; Jain, S. K.; Hamaoka, R.; Miyagawa, J.; Yaginuma, Y.; Honke, K.; Ishikawa, M.; Taniguchi, N. Overexpression of N-acetylglucosaminyltransferase III enhances the epidermal growth factor-induced phosphorylation of ERK in HeLaS3 cells by up-regulation of the internalization rate of the receptors. *J. Biol. Chem.* **2001**, *276* (15), 11956–11962. DOI: 10.1074/jbc.M008551200.
(109) Takahashi, M.; Kuroki, Y.; Ohtsubo, K.; Taniguchi, N. Core fucose and bisecting GlcNAc, the direct modifiers of the N-glycan core: their functions and target proteins. *Carbohydr. Res.* **2009**, *344* (12), 1387–1390. DOI: 10.1016/j.carres.2009.04.031.
(110) Gagneux, P.; Hennet, T.; Varki, A. Biological Functions of Glycans. In Varki, A.; Cummings, R. D.; Esko, J. D.; Stanley, P.; Hart, G. W.; Aebi, M.; Mohnen, D.; Kinoshita, T.; Packer, N. H.; Prestegard, J.

H.; Schnaar, R. L.; Seeberger, P. H. (Eds.), *Essentials of Glycobiology*, 4. ed., Cold Spring Habor (NY), Cold Spring Harbor Laboratory Press, 2022**.** DOI: 10.1101/glycobiology.4e.7.
(111) Grabarics, M.; Lettow, M.; Kirschbaum, C.; Greis, K.; Manz, C.; Pagel, K. Mass Spectrometry-Based Techniques to Elucidate the Sugar Code. *Chem. Rev.* **2022**, *122* (8), 7840–7908. DOI: 10.1021/acs.chemrev.1c00380.
(112) Barrientos, R. C.; Zhang, Q. Recent advances in the mass spectrometric analysis of glycosphingolipidome - A review. *Anal. Chim. Acta* **2020**, *1132*, 134–155. DOI: 10.1016/j.aca.2020.05.051.
(113) Schnaar, R. L.; Sandhoff, R.; Tiemeyer, M.; Kinoshita, T. Glycosphingolipids. In Varki, A.; Cummings, R. D.; Esko, J. D.; Stanley, P.; Hart, G. W.; Aebi, M.; Mohnen, D.; Kinoshita, T.; Packer, N. H.; Prestegard, J. H.; Schnaar, R. L.; Seeberger, P. H. (Eds.), *Essentials of Glycobiology*, 4. ed., Cold Spring Habor (NY), Cold Spring Harbor Laboratory Press, 2022 DOI: 10.1101/glycobiology.4e.11.
(114) Chen, Y.; Liu, Y.; Sullards, M. C.; Merrill, A. H. An introduction to sphingolipid metabolism and analysis by new technologies. *NeuroMolecular Med.* **2010**, *12* (4), 306–319. DOI: 10.1007/s12017-010-8132-8.
(115) Fahy, E.; Subramaniam, S.; Brown, H. A.; Glass, C. K.; Merrill, A. H.; Murphy, R. C.; Raetz, C. R. H.; Russell, D. W.; Seyama, Y.; Shaw, W.; Shimizu, T.; Spener, F.; van Meer, G.; VanNieuwenhze, M. S.; White, S. H.; Witztum, J. L.; Dennis, E. A. A comprehensive classification system for lipids. *J. Lipid Res.* **2005**, *46* (5), 839–861. DOI: 10.1194/jlr.E400004-JLR200.
(116) Liebisch, G.; Fahy, E.; Aoki, J.; Dennis, E. A.; Durand, T.; Ejsing, C. S.; Fedorova, M.; Feussner, I.; Griffiths, W. J.; Köfeler, H.; Merrill, A. H.; Murphy, R. C.; O'Donnell, V. B.; Oskolkova, O.; Subramaniam, S.; Wakelam, M. J. O.; Spener, F. Update on LIPID MAPS classification, nomenclature, and shorthand notation for MS-derived lipid structures. *J. Lipid Res.* **2020**, *61* (12), 1539–1555. DOI: 10.1194/jlr.S120001025.
(117) Varki, A.; Cummings, R. D.; Aebi, M.; Packer, N. H.; Seeberger, P. H.; Esko, J. D.; Stanley, P.; Hart, G.; Darvill, A.; Kinoshita, T.; Prestegard, J. J.; Schnaar, R. L.; Freeze, H. H.; Marth, J. D.; Bertozzi, C. R.; Etzler, M. E.; Frank, M.; Vliegenthart, J. F.; Lütteke, T.; Perez, S.; Bolton, E.; Rudd, P.; Paulson, J.; Kanehisa, M.; Toukach, P.; Aoki-Kinoshita, K. F.; Dell, A.; Narimatsu, H.; York, W.; Taniguchi, N.; Kornfeld, S., Eds. *S*ymbol Nomenclature for Graphical Representations of Glycans. *Glycobiology* **2015**, *25* (12), 1323-1324. DOI: 10.1093/glycob/cwv091.
(118) Mallard, F.; Johannes, L. Shiga toxin B-subunit as a tool to study retrograde transport. *Methods Mol. Biol.* **2003**, *73*, 209–220. DOI: 10.1385/1-59259-316-X:209.
(119) Lee, H.; German, J. B.; Kjelden, R.; Lebrilla, C. B.; Barile, D. Quantitative analysis of gangliosides in bovine milk and colostrum-based dairy products by ultrahigh performance liquid chromatography-tandem mass spectrometry. *J. Agric. Food Chem.* **2013**, *61* (40), 9689–9696. DOI: 10.1021/jf402255g.
(120) Park, H.; Zhou, Y.; Costello, C. E. Direct analysis of sialylated or sulfated glycosphingolipids and other polar and neutral lipids using TLC-MS interfaces. *J. Lipid Res.* **2014**, *55* (4), 773–781. DOI: 10.1194/jlr.D046128.
(121) Sauvageau, J.; Ryan, J.; Lagutin, K.; Sims, I. M.; Stocker, B. L.; Timmer, M. S. M. Isolation and structural characterisation of the major glycolipids from Lactobacillus plantarum. *Carbohydr. Res.* **2012**, *357*, 151–156. DOI: 10.1016/j.carres.2012.05.011.
(122) Sarbu, M.; Vukelić, Ž.; Clemmer, D. E.; Zamfir, A. D. Electrospray ionization ion mobility mass spectrometry provides novel insights into the pattern and activity of fetal hippocampus gangliosides. *Biochimie* **2017**, *139*, 81–94. DOI: 10.1016/j.biochi.2017.05.016.
(123) Du, H.; Yu, H.; Yang, F.; Li, Z. Comprehensive analysis of glycosphingolipid glycans by lectin microarrays and MALDI-TOF mass spectrometry. *Nat. Protoc.* **2021**, *16* (7), 3470–3491. DOI: 10.1038/s41596-021-00544-y.
(124) Haan, N. de; Yang, S.; Cipollo, J.; Wuhrer, M. Glycomics studies using sialic acid derivatization and mass spectrometry. *Nat. Rev. Chem.* **2020**, *4* (5), 229–242. DOI: 10.1038/s41570-020-0174-3.
(125) Ernst, B.; Müller, D. R.; Richter, W. J. False sugar sequence ions in electrospray tandem mass spectrometry of underivatized sialyl-Lewis-type oligosaccharides. *Int. J. Mass Spectrom. Ion Processes* **1997**, *160* (1-3), 283–290. DOI: 10.1016/S0168-1176(96)04487-4.

(126) Harvey, D. J.; Mattu, T. S.; Wormald, M. R.; Royle, L.; Dwek, R. A.; Rudd, P. M. "Internal residue loss": rearrangements occurring during the fragmentation of carbohydrates derivatized at the reducing terminus. *Anal. Chem.* **2002**, *74* (4), 734–740. DOI: 10.1021/ac0109321.
(127) Mucha, E.; Lettow, M.; Marianski, M.; Thomas, D. A.; Struwe, W. B.; Harvey, D. J.; Meijer, G.; Seeberger, P. H.; Helden, G. von; Pagel, K. Fucose Migration in Intact Protonated Glycan Ions: A Universal Phenomenon in Mass Spectrometry. *Angew Chem. Int. Ed. Engl.* **2018**, *57* (25), 7440–7443. DOI: 10.1002/anie.201801418.
(128) Domon, B.; Costello, C. E. A systematic nomenclature for carbohydrate fragmentations in FAB-MS/MS spectra of glycoconjugates. *Glycoconj. J.* **1988**, *5* (4), 397–409. DOI: 10.1007/BF01049915.
(129) Merrill, A. H.; Sullards, M. C.; Allegood, J. C.; Kelly, S.; Wang, E. Sphingolipidomics: high-throughput, structure-specific, and quantitative analysis of sphingolipids by liquid chromatography tandem mass spectrometry. *Methods* **2005**, *36* (2), 207–224. DOI: 10.1016/j.ymeth.2005.01.009.
(130) Grabarics, M.; Lettow, M.; Kirschbaum, C.; Greis, K.; Manz, C.; Pagel, K. Mass Spectrometry-Based Techniques to Elucidate the Sugar Code. *Chem. Rev.* **2022**, *122* (8), 7840–7908. DOI: 10.1021/acs.chemrev.1c00380.
(131) McFarland, M. A.; Marshall, A. G.; Hendrickson, C. L.; Nilsson, C. L.; Fredman, P.; Månsson, J.-E. Structural characterization of the GM1 ganglioside by infrared multiphoton dissociation, electron capture dissociation, and electron detachment dissociation electrospray ionization FT-ICR MS/MS. *J. Am. Soc. Mass Spectrom.* **2005**, *16* (5), 752–762. DOI: 10.1016/j.jasms.2005.02.001.
(132) Pham, H. T.; Julian, R. R. Characterization of glycosphingolipid epimers by radical-directed dissociation mass spectrometry. *The Analyst* **2016**, *141* (4), 1273–1278. DOI: 10.1039/C5AN02383A.
(133) Barrientos, R. C.; Vu, N.; Zhang, Q. Structural Analysis of Unsaturated Glycosphingolipids Using Shotgun Ozone-Induced Dissociation Mass Spectrometry. *J. Am. Soc. Mass Spectrom.* **2017**, *28* (11), 2330–2343. DOI: 10.1007/s13361-017-1772-2.
(134) O'Brien, J. P.; Brodbelt, J. S. Structural characterization of gangliosides and glycolipids via ultraviolet photodissociation mass spectrometry. *Anal. Chem.* **2013**, *85* (21), 10399–10407. DOI: 10.1021/ac402379y.
(135) Arigi, E.; Blixt, O.; Buschard, K.; Clausen, H.; Levery, S. B. Design of a covalently bonded glycosphingolipid microarray. *Glycoconj. J.* **2012**, *29* (1), 1–12. DOI: 10.1007/s10719-011-9359-9.
(136) Anugraham, M.; Everest-Dass, A. V.; Jacob, F.; Packer, N. H. A platform for the structural characterization of glycans enzymatically released from glycosphingolipids extracted from tissue and cells. *Rapid Commun. Mass Spectrom.* **2015**, *29* (7), 545–561. DOI: 10.1002/rcm.7130.
(137) Huang, Q.; Liu, D.; Xin, B.; Cechner, K.; Zhou, X.; Wang, H.; Zhou, A. Quantification of monosialogangliosides in human plasma through chemical derivatization for signal enhancement in LC-ESI-MS. *Anal. Chim. Acta* **2016**, *929*, 31–38. DOI: 10.1016/j.aca.2016.04.043.
(138) Hanamatsu, H.; Nishikaze, T.; Miura, N.; Piao, J.; Okada, K.; Sekiya, S.; Iwamoto, S.; Sakamoto, N.; Tanaka, K.; Furukawa, J.-I. Sialic Acid Linkage Specific Derivatization of Glycosphingolipid Glycans by Ring-Opening Aminolysis of Lactones. *Anal. Chem.* **2018**, *90* (22), 13193–13199. DOI: 10.1021/acs.analchem.8b02775.
(139) Ciucanu, I. Per-O-methylation reaction for structural analysis of carbohydrates by mass spectrometry. *Anal. Chim. Acta* **2006**, *576* (2), 147–155. DOI: 10.1016/j.aca.2006.06.009.
(140) Barrientos, R. C.; Zhang, Q. Differential Isotope Labeling by Permethylation and Reversed-Phase Liquid Chromatography-Mass Spectrometry for Relative Quantification of Intact Neutral Glycolipids in Mammalian Cells. *Anal. Chem.* **2019**, *91* (15), 9673–9681. DOI: 10.1021/acs.analchem.9b01206.
(141) *Global report on neglected tropical diseases* 2024. Geneva, World Health Organization; **2024**.
(142) WHO, https://www.who.int/health-topics/neglected-tropical-diseases#tab=tab_2 (accessed 2024-08-26).
(143) Bhutta, Z. A.; Sommerfeld, J.; Lassi, Z. S.; Salam, R. A.; Das, J. K. Global burden, distribution, and interventions for infectious diseases of poverty. *Infect. Dis. Poverty* **2014**, *3*, 21. DOI: 10.1186/2049-9957-3-21.

(144) https://globalhealthprogress.org/collaboration/the-london-declaration-on-ntds/ (accessed 2024-08-26).
(145) *Ending the neglect to attain the Sustainable Development Goals: a rationale for continued investment in tackling neglected tropical diseases 2021–2030.* Geneva, World Health Organization; **2022**.
(146) Pilotte, N.; Manuel, M.; Walson, J. L.; Ajjampur, S. S. R. Community-wide mass drug administration for soil-transmitted helminths – risk of drug resistance and mitigation strategies. *Front. Trop. Dis* **2022**, *3.* DOI: 10.3389/fitd.2022.897155.
(147) Bunte, M. J. M.; Schots, A.; Kammenga, J. E.; Wilbers, R. H. P. Helminth Glycans at the Host-Parasite Interface and Their Potential for Developing Novel Therapeutics. *Front. Mol. Biosci.* **2021**, *8*. DOI: 10.3389/fmolb.2021.807821.
(148) WHO, https://www.who.int/news-room/fact-sheets/detail/schistosomiasis (accessed 2024-08-26).
(149) Colley, D. G.; Bustinduy, A. L.; Secor, W. E.; King, C. H. Human schistosomiasis. *Lancet* **2014**, *383* (9936), 2253–2264. DOI: 10.1016/S0140-6736(13)61949-2.
(150) Doenhoff, M. J.; Cioli, D.; Utzinger, J. Praziquantel: mechanisms of action, resistance and new derivatives for schistosomiasis. *Curr. Opin. Infect. Dis.* **2008**, *21* (6), 659–667. DOI: 10.1097/QCO.0b013e328318978f.
(151) Couto, F. F. B.; Coelho, P. M. Z.; Araújo, N.; Kusel, J. R.; Katz, N.; Jannotti-Passos, L. K.; Mattos, A. C. A. Schistosoma mansoni: a method for inducing resistance to praziquantel using infected Biomphalaria glabrata snails. *Mem. Inst. Oswaldo Cruz* **2011**, *106* (2), 153–157. DOI: 10.1590/S0074-02762011000200006.
(152) Schramm, G.; Hamilton, J. V.; Balog, C. I. A.; Wuhrer, M.; Gronow, A.; Beckmann, S.; Wippersteg, V.; Grevelding, C. G.; Goldmann, T.; Weber, E.; Brattig, N. W.; Deelder, A. M.; Dunne, D. W.; Hokke, C. H.; Haas, H.; Doenhoff, M. J. Molecular characterisation of kappa-5, a major antigenic glycoprotein from Schistosoma mansoni eggs. *Mol. Biochem. Parasitol.* **2009**, *166* (1), 4–14. DOI: 10.1016/j.molbiopara.2009.02.003.
(153) Pearce, E. J.; MacDonald, A. S. The immunobiology of schistosomiasis. *Nature reviews. Immunol.* **2002**, *2* (7), 499–511. DOI: 10.1038/nri843.
(154) Hams, E.; Aviello, G.; Fallon, P. G. The schistosoma granuloma: friend or foe? *Front. Immunol.* **2013**, *4*, 89. DOI: 10.3389/fimmu.2013.00089.
(155) Llanwarne, F.; Helmby, H. Granuloma formation and tissue pathology in Schistosoma japonicum versus Schistosoma mansoni infections. *Parasite Immunol.* **2021**, *43* (2), e12778. DOI: 10.1111/pim.12778.
(156) Hunter, G. W.; Crandall, R. B. Studies on Schistosomiasis. XIX. Results of Preliminary Experiments on the Antigenic Significance of the Schistosome Egg. *Mil. Med.* **1962**, *127* (2), 101–104. DOI: 10.1093/milmed/127.2.101.
(157) Kagan, I. G.; Goodchild, C. G. Polysaccharide content of schistosome skin test antigens and the reactivity of nitgogenous and carbohydrate components. *Am. J. Trop. Med. Hyg.* **1963**, *12*, 179–183. DOI: 10.4269/ajtmh.1963.12.179.
(158) Toro-Goyco, E.; Del Valle, M. R. Schistosoma mansoni. I. Chemical composition of eggs. *Exp. Parasitol.* **1970**, *27* (2), 265–272. DOI: 10.1016/0014-4894(70)90031-7.
(159) Carter, C. E.; Colley, D. G. Partial Purification and Characterization of Schistosoma Mansoni Soluble Egg Antigen with Con A-Sepharose Chromatography. *J. Immunol.* **1979**, *122* (6), 2204–2209. DOI: 10.4049/jimmunol.122.6.2204.
(160) Harrison, D. J.; Carter, C. E.; Colley, D. G. Immunoaffinity Purification of Schistosoma Mansoni Soluble Egg Antigens. *J. Immunol.* **1979**, *122* (6), 2210–2217. DOI: 10.4049/jimmunol.122.6.2210.
(161) Norden, A. P.; Strand, M. Schistosoma mansoni, S. haematobium, and S. japonicum: identification of genus-, species-, and gender-specific antigenic worm glycoproteins. *Exp. Parasitol.* **1984**, *57* (1), 110–123. DOI: 10.1016/0014-4894(84)90070-5.
(162) Levery, S. B.; Weiss, J. B.; Salyan, M. E.; Roberts, C. E.; Hakomori, S.; Magnani, J. L.; Strand, M. Characterization of a series of novel fucose-containing glycosphingolipid immunogens from eggs of

Schistosoma mansoni. *J. Biol. Chem.* **1992**, *267* (8), 5542–5551. DOI: 10.1016/S0021-9258(18)42800-1.
(163) Hokke, C. H.; Yazdanbakhsh, M. Schistosome glycans and innate immunity. *Parasite Immunol.* **2005**, *27* (7-8), 257–264. DOI: 10.1111/j.1365-3024.2005.00781.x.
(164) Hokke, C. H.; Deelder, A. M.; Hoffmann, K. F.; Wuhrer, M. Glycomics-driven discoveries in schistosome research. *Exp. Parasitol.* **2007**, *117* (3), 275–283. DOI: 10.1016/j.exppara.2007.06.003.
(165) van Diepen, A.; van der Velden, N. S. J.; Smit, C. H.; Meevissen, M. H. J.; Hokke, C. H. Parasite glycans and antibody-mediated immune responses in Schistosoma infection. *Parasitology* **2012**, *139* (9), 1219–1230. DOI: 10.1017/S0031182012000273.
(166) Prasanphanich, N. S.; Mickum, M. L.; Heimburg-Molinaro, J.; Cummings, R. D. Glycoconjugates in host-helminth interactions. *Front. Immunol.* **2013**, *4*, 240. DOI: 10.3389/fimmu.2013.00240.
(167) van Remoortere, A.; Hokke, C. H.; van Dam, G. J.; van Die, I.; Deelder, A. M.; van den Eijnden, D. H. Various stages of schistosoma express Lewis(x), LacdiNAc, GalNAcbeta1-4 (Fucalpha1-3)GlcNAc and GalNAcbeta1-4(Fucalpha1-2Fucalpha1-3)GlcNAc carbohydrate epitopes: detection with monoclonal antibodies that are characterized by enzymatically synthesized neoglycoproteins. *Glycobiology* **2000**, *10* (6), 601–609. DOI: 10.1093/glycob/10.6.601.
(168) Nyame, A. K.; Lewis, F. A.; Doughty, B. L.; Correa-Oliveira, R.; Cummings, R. D. Immunity to schistosomiasis: glycans are potential antigenic targets for immune intervention. *Exp. Parasitol.* **2003**, *104* (1-2), 1–13. DOI: 10.1016/S0014-4894(03)00110-3.
(169) van Die, I.; van Vliet, S. J.; Nyame, A. K.; Cummings, R. D.; Bank, C. M. C.; Appelmelk, B.; Geijtenbeek, T. B. H.; van Kooyk, Y. The dendritic cell-specific C-type lectin DC-SIGN is a receptor for Schistosoma mansoni egg antigens and recognizes the glycan antigen Lewis x. *Glycobiology* **2003**, *13* (6), 471–478. DOI: 10.1093/glycob/cwg052.
(170) Robijn, M. L. M.; Wuhrer, M.; Kornelis, D.; Deelder, A. M.; Geyer, R.; Hokke, C. H. Mapping fucosylated epitopes on glycoproteins and glycolipids of Schistosoma mansoni cercariae, adult worms and eggs. *Parasitology* **2005**, *130* (Pt 1), 67–77. DOI: 10.1017/S0031182004006390.
(171) Smit, C. H.; Homann, A.; van Hensbergen, V. P.; Schramm, G.; Haas, H.; van Diepen, A.; Hokke, C. H. Surface expression patterns of defined glycan antigens change during Schistosoma mansoni cercarial transformation and development of schistosomula. *Glycobiology* **2015**, *25* (12), 1465–1479. DOI: 10.1093/glycob/cwv066.
(172) Prasanphanich, N. S.; Leon, K.; Secor, W. E.; Shoemaker, C. B.; Heimburg-Molinaro, J.; Cummings, R. D. Anti-schistosomal immunity to core xylose/fucose in N-glycans. *Front. Mol. Biosci.* **2023**, *10*, 1142620. DOI: 10.3389/fmolb.2023.1142620.
(173) Smit, C. H.; van Diepen, A.; Nguyen, D. L.; Wuhrer, M.; Hoffmann, K. F.; Deelder, A. M.; Hokke, C. H. Glycomic Analysis of Life Stages of the Human Parasite Schistosoma mansoni Reveals Developmental Expression Profiles of Functional and Antigenic Glycan Motifs. *Mol. Cell. Proteom.* **2015**, *14* (7), 1750–1769. DOI: 10.1074/mcp.M115.048280.
(174) van Liempt, E.; Bank, C. M. C.; Mehta, P.; Garciá-Vallejo, J. J.; Kawar, Z. S.; Geyer, R.; Alvarez, R. A.; Cummings, R. D.; van Kooyk, Y.; van Die, I. Specificity of DC-SIGN for mannose- and fucose-containing glycans. *FEBS Lett.* **2006**, *580* (26), 6123–6131. DOI: 10.1016/j.febslet.2006.10.009.
(175) van Vliet, S. J.; van Liempt, E.; Saeland, E.; Aarnoudse, C. A.; Appelmelk, B.; Irimura, T.; Geijtenbeek, T. B. H.; Blixt, O.; Alvarez, R.; van Die, I.; van Kooyk, Y. Carbohydrate profiling reveals a distinctive role for the C-type lectin MGL in the recognition of helminth parasites and tumor antigens by dendritic cells. *Int. Immunol.* **2005**, *17* (5), 661–669. DOI: 10.1093/intimm/dxh246.
(176) Kariuki, T. M.; Farah, I. O.; Yole, D. S.; Mwenda, J. M.; van Dam, G. J.; Deelder, A. M.; Wilson, R. A.; Coulson, P. S. Parameters of the attenuated schistosome vaccine evaluated in the olive baboon. *Infect. Immun.* **2004**, *72* (9), 5526–5529. DOI: 10.1128/iai.72.9.5526-5529.2004.
(177) Prasanphanich, N. S.; Luyai, A. E.; Song, X.; Heimburg-Molinaro, J.; Mandalasi, M.; Mickum, M.; Smith, D. F.; Nyame, A. K.; Cummings, R. D. Immunization with recombinantly expressed glycan antigens from Schistosoma mansoni induces glycan-specific antibodies against the parasite. *Glycobiology* **2014**, *24* (7), 619–637. DOI: 10.1093/glycob/cwu027.

(178) van Dam, G. J.; Wichers, J. H.; Ferreira, T. M. F.; Ghati, D.; van Amerongen, A.; Deelder, A. M. Diagnosis of schistosomiasis by reagent strip test for detection of circulating cathodic antigen. *J. Clin. Microbiol.* **2004**, *42* (12), 5458–5461. DOI: 10.1128/jcm.42.12.5458-5461.2004.
(179) van de Vijver, K. K.; Deelder, A. M.; Jacobs, W.; van Marck, E. A.; Hokke, C. H. LacdiNAc- and LacNAc-containing glycans induce granulomas in an in vivo model for schistosome egg-induced hepatic granuloma formation. *Glycobiology* **2006**, *16* (3), 237–243. DOI: 10.1093/glycob/cwj058.
(180) Mehmood, K.; Zhang, H.; Sabir, A. J.; Abbas, R. Z.; Ijaz, M.; Durrani, A. Z.; Saleem, M. H.; Ur Rehman, M.; Iqbal, M. K.; Wang, Y.; Ahmad, H. I.; Abbas, T.; Hussain, R.; Ghori, M. T.; Ali, S.; Khan, A. U.; Li, J. A review on epidemiology, global prevalence and economical losses of fasciolosis in ruminants. *Microb. Pathog.* **2017**, *109*, 253–262. DOI: 10.1016/j.micpath.2017.06.006.
(181) Lalor, R.; Cwiklinski, K.; Calvani, N. E. D.; Dorey, A.; Hamon, S.; Corrales, J. L.; Dalton, J. P.; Marco Verissimo, C. de. Pathogenicity and virulence of the liver flukes Fasciola hepatica and FasciolaGigantica that cause the zoonosis Fasciolosis. *Virulence* **2021**, *12* (1), 2839–2867. DOI: 10.1080/21505594.2021.1996520.
(182) WHO, https://www.who.int/news-room/questions-and-answers/item/q-a-on-fascioliasis (accessed 2024-08-27).
(183) CDC. https://www.cdc.gov/dpdx/fascioliasis/index.html (accessed 2024-08-27).
(184) Kelley, J. M.; Elliott, T. P.; Beddoe, T.; Anderson, G.; Skuce, P.; Spithill, T. W. Current Threat of Triclabendazole Resistance in Fasciola hepatica. *Trends Parasitol.* **2016**, *32* (6), 458–469. DOI: 10.1016/j.pt.2016.03.002.
(185) Fairweather, I.; Brennan, G. P.; Hanna, R. E. B.; Robinson, M. W.; Skuce, P. J. Drug resistance in liver flukes. *Int. J. Parasitol.: Drugs Drug Resist.* **2020**, *12*, 39–59. DOI: 10.1016/j.ijpddr.2019.11.003.
(186) Mas-Coma, S.; Valero, M. A.; Bargues, M. D. Fascioliasis. *Adv. Exp. Med. Biol.* **2019**, *1154*, 71–103. DOI: 10.1007/978-3-030-18616-6_4.
(187) Sumruayphol, S.; Siribat, P.; Dujardin, J.-P.; Dujardin, S.; Komalamisra, C.; Thaenkham, U. Fasciola gigantica, F. hepatica and Fasciola intermediate forms: geometric morphometrics and an artificial neural network to help morphological identification. *PeerJ* **2020**, *8*, e8597. DOI: 10.7717/peerj.8597.
(188) Wuhrer, M.; Berkefeld, C.; Dennis, R. D.; Idris, M. A.; Geyer, R. The liver flukes Fasciola gigantica and Fasciola hepatica express the leucocyte cluster of differentiation marker CD77 (globotriaosylceramide) in their tegument. *J. Biol. Chem.* **2001**, *382* (2), 195–207. DOI: 10.1515/BC.2001.027.
(189) Wuhrer, M.; Grimm, C.; Zahringer, U.; Dennis, R. D.; Berkefeld, C. M.; Idris, M. A.; Geyer, R. A novel GlcNAcalpha1-HPO3-6Gal(1-1)ceramide antigen and alkylated inositol-phosphoglycerolipids expressed by the liver fluke Fasciola hepatica. *Glycobiology* **2003**, *13* (2), 129–137. DOI: 10.1093/glycob/cwg005.
(190) Wuhrer, M.; Grimm, C.; Dennis, R. D.; Idris, M. A.; Geyer, R. The parasitic trematode Fasciola hepatica exhibits mammalian-type glycolipids as well as Gal(beta1-6)Gal-terminating glycolipids that account for cestode serological cross-reactivity. *Glycobiology* **2004**, *14* (2), 115–126. DOI: 10.1093/glycob/cwh021.
(191) Ravidà, A.; Aldridge, A. M.; Driessen, N. N.; Heus, F. A. H.; Hokke, C. H.; O'Neill, S. M. Fasciola hepatica Surface Coat Glycoproteins Contain Mannosylated and Phosphorylated N-glycans and Exhibit Immune Modulatory Properties Independent of the Mannose Receptor. *PLoS Negl. Trop. Dis.* **2016**, *10* (4), e0004601. DOI: 10.1371/journal.pntd.0004601.
(192) Garcia-Campos, A.; Ravidà, A.; Nguyen, D. L.; Cwiklinski, K.; Dalton, J. P.; Hokke, C. H.; O'Neill, S.; Mulcahy, G. Tegument Glycoproteins and Cathepsins of Newly Excysted Juvenile Fasciola hepatica Carry Mannosidic and Paucimannosidic N-glycans. *PLoS Negl. Trop. Dis.* **2016**, *10* (5), e0004688. DOI: 10.1371/journal.pntd.0004688.
(193) Murphy, A.; Cwiklinski, K.; Lalor, R.; O'Connell, B.; Robinson, M. W.; Gerlach, J.; Joshi, L.; Kilcoyne, M.; Dalton, J. P.; O'Neill, S. M. Fasciola hepatica Extracellular Vesicles isolated from excretory-secretory products using a gravity flow method modulate dendritic cell phenotype and activity. *PLoS Negl. Trop. Dis.* **2020**, *14* (9), e0008626. DOI: 10.1371/journal.pntd.0008626.

(194) Marco Verissimo, C. de; Cwiklinski, K.; Nilsson, J.; Mirgorodskaya, E.; Jin, C.; Karlsson, N. G.; Dalton, J. P. Glycan Complexity and Heterogeneity of Glycoproteins in Somatic Extracts and Secretome of the Infective Stage of the Helminth Fasciola hepatica. *Mol. Cell. Proteom.* **2023**, *22* (12), 100684. DOI: 10.1016/j.mcpro.2023.100684.
(195) Rodríguez, E.; Kalay, H.; Noya, V.; Brossard, N.; Giacomini, C.; van Kooyk, Y.; García-Vallejo, J. J.; Freire, T. Fasciola hepatica glycoconjugates immuneregulate dendritic cells through the Dendritic Cell-Specific Intercellular adhesion molecule-3-Grabbing Non-integrin inducing T cell anergy. *Sci. Rep.* **2017**, *7*, 46748. DOI: 10.1038/srep46748.
(196) Costa, M.; Da Costa, V.; Lores, P.; Landeira, M.; Rodríguez-Zraquia, S. A.; Festari, M. F.; Freire, T. Macrophage Gal/GalNAc lectin 2 (MGL2)+ peritoneal antigen presenting cells during Fasciola hepatica infection are essential for regulatory T cell induction. *Sci. Rep.* **2022**, *12* (1), 17661. DOI: 10.1038/s41598-022-21520-w.
(197) Garcia-Campos, A.; Baird, A. W.; Mulcahy, G. Migration of Fasciola hepatica newly excysted juveniles is inhibited by high-mannose and oligomannose-type N-glycan-binding lectins. *Parasitology* **2017**, *144* (13), 1708–1717. DOI: 10.1017/S003118201700124X.
(198) Boskamp, M. S.; Soltwisch, J. Charge Distribution between Different Classes of Glycerophospolipids in MALDI-MS Imaging. *Anal. Chem.* **2020**, *92* (7), 5222–5230. DOI: 10.1021/acs.analchem.9b05761.
(199) Bien, T.; Perl, M.; Machmüller, A. C.; Nitsche, U.; Conrad, A.; Johannes, L.; Müthing, J.; Soltwisch, J.; Janssen, K.-P.; Dreisewerd, K. MALDI-2 Mass Spectrometry and Immunohistochemistry Imaging of Gb3Cer, Gb4Cer, and Further Glycosphingolipids in Human Colorectal Cancer Tissue. *Anal. Chem.* **2020**, *92* (10), 7096–7105. DOI: 10.1021/acs.analchem.0c00480.
(200) Chan, K.; Lanthier, P.; Liu, X.; Sandhu, J. K.; Stanimirovic, D.; Li, J. MALDI mass spectrometry imaging of gangliosides in mouse brain using ionic liquid matrix. *Anal. Chim. Acta* **2009**, *639* (1-2), 57–61. DOI: 10.1016/j.aca.2009.02.051.
(201) Colsch, B.; Woods, A. S. Localization and imaging of sialylated glycosphingolipids in brain tissue sections by MALDI mass spectrometry. *Glycobiology* **2010**, *20* (6), 661–667. DOI: 10.1093/glycob/cwq031.
(202) Zhang, Y.; Wang, J.; Liu, J.; Han, J.; Xiong, S.; Yong, W.; Zhao, Z. Combination of ESI and MALDI mass spectrometry for qualitative, semi-quantitative and in situ analysis of gangliosides in brain. *Sci. Rep.* **2016**, *6*, 25289. DOI: 10.1038/srep25289.
(203) Vens-Cappell, S.; Kouzel, I. U.; Kettling, H.; Soltwisch, J.; Bauwens, A.; Porubsky, S.; Müthing, J.; Dreisewerd, K. On-Tissue Phospholipase C Digestion for Enhanced MALDI-MS Imaging of Neutral Glycosphingolipids. *Anal. Chem.* **2016**, *88* (11), 5595–5599. DOI: 10.1021/acs.analchem.6b01084.
(204) Tobias, F.; Olson, M. T.; Cologna, S. M. Mass spectrometry imaging of lipids: untargeted consensus spectra reveal spatial distributions in Niemann-Pick disease type C1. *J. Lipid Res.* **2018**, *59* (12), 2446–2455. DOI: 10.1194/jlr.D086090.
(205) Harris, A.; Roseborough, A.; Mor, R.; Yeung, K. K.-C.; Whitehead, S. N. Ganglioside Detection from Formalin-Fixed Human Brain Tissue Utilizing MALDI Imaging Mass Spectrometry. *J. Am. Soc. Mass Spectrom.* **2020**, *31* (3), 479–487. DOI: 10.1021/jasms.9b00110.
(206) Andres, D. A.; Young, L. E. A.; Gentry, M. S.; Sun, R. C. Spatial profiling of gangliosides in mouse brain by mass spectrometry imaging. *J. Lipid Res.* **2020**, *61* (12), 1537. DOI: 10.1194/jlr.ILR120000870.
(207) Zhang, Q.; Li, Y.; Sui, P.; Sun, X.-H.; Gao, Y.; Wang, C.-Y. MALDI mass spectrometry imaging discloses the decline of sulfoglycosphingolipid and glycerophosphoinositol species in the brain regions related to cognition in a mouse model of Alzheimer's disease. *Talanta* **2024**, *266* (Pt 2), 125022. DOI: 10.1016/j.talanta.2023.125022.
(208) Ollen-Bittle, N.; Pejhan, S.; Pasternak, S. H.; Keene, C. D.; Zhang, Q.; Whitehead, S. N. Co-registration of MALDI-MSI and histology demonstrates gangliosides co-localize with amyloid beta plaques in Alzheimer's disease. *Acta Neuropathol.* **2024**, *147* (1), 105. DOI: 10.1007/s00401-024-02759-1.

(209) Luk, F. C. Y.; Johnson, T. M.; Beckers, C. J. N-linked glycosylation of proteins in the protozoan parasite Toxoplasma gondii. *Mol. Biochem. Parasitol.* **2008**, *157* (2), 169–178. DOI: 10.1016/j.molbiopara.2007.10.012.
(210) Fauquenoy, S.; Morelle, W.; Hovasse, A.; Bednarczyk, A.; Slomianny, C.; Schaeffer, C.; van Dorsselaer, A.; Tomavo, S. Proteomics and glycomics analyses of N-glycosylated structures involved in Toxoplasma gondii--host cell interactions. *Mol. Cell. Proteom.* **2008**, *7* (5), 891–910. DOI: 10.1074/mcp.M700391-MCP200.
(211) Dagenais, M.; Gerlach, J. Q.; Wendt, G. R.; Collins, J. J.; Atkinson, L. E.; Mousley, A.; Geary, T. G.; Long, T. Analysis of Schistosoma mansoni Extracellular Vesicles Surface Glycans Reveals Potential Immune Evasion Mechanism and New Insights on Their Origins of Biogenesis. *Pathogens* **2021**, *10* (11). DOI: 10.3390/pathogens10111401.
(212) Maizels, R. M.; Yazdanbakhsh, M. Immune regulation by helminth parasites: cellular and molecular mechanisms. *Nat. Rev. Immunol.* **2003**, *3* (9), 733–744. DOI: 10.1038/nri1183.
(213) Zhang, T.; Waard, A. A. de; Wuhrer, M.; Spaapen, R. M. The Role of Glycosphingolipids in Immune Cell FunctionsFront. Immunol. **2019**, *10*, 90. DOI: 10.3389/fimmu.2019.00090.
(214) Hokke, C. H.; van Diepen, A. Helminth glycomics - glycan repertoires and host-parasite interactions. *Mol. Biochem. Parasitol.* **2017**, *215*, 47–57. DOI: 10.1016/j.molbiopara.2016.12.001.
(215) Bunte, M. J. M.; Schots, A.; Kammenga, J. E.; Wilbers, R. H. P. Helminth Glycans at the Host-Parasite Interface and Their Potential for Developing Novel Therapeutics. *Front. Mol. Biosci.* **2021**, *8*, 807821. DOI: 10.3389/fmolb.2021.807821.
(216) Kirsch, S.; Müthing, J.; Peter-Katalinić, J.; Bindila, L. On-line nano-HPLC/ESI QTOF MS monitoring of alpha2-3 and alpha2-6 sialylation in granulocyte glycosphingolipidome. *J. Biol. Chem.* **2009**, *390* (7), 657–672. DOI: 10.1515/BC.2009.066.
(217) Skelly, P. J.; Da'dara, A. A.; Li, X.-H.; Castro-Borges, W.; Wilson, R. A. Schistosome feeding and regurgitation. *PLoS Pathog.* **2014**, *10* (8), e1004246. DOI: 10.1371/journal.ppat.1004246.
(218) Moné, H.; Boissier, J. Sexual biology of schistosomes. *Adv. Parasitol.* **2004**, *57*, 89–189. DOI: 10.1016/S0065-308X(04)57002-1.
(219) Shaw, M. K. Schistosoma mansoni: vitelline gland development in females from single sex infections. *J. Helminthol.* **1987**, *61* (3), 253–259. DOI: 10.1017/s0022149x00010117.
(220) Amaral, K. B.; Silva, T. P.; Dias, F. F.; Malta, K. K.; Rosa, F. M.; Costa-Neto, S. F.; Gentile, R.; Melo, R. C. N. Histological assessment of granulomas in natural and experimental Schistosoma mansoni infections using whole slide imaging. *PloS one* **2017**, *12* (9), e0184696. DOI: 10.1371/journal.pone.0184696.
(221) Malta, K. K.; Silva, T. P.; Palazzi, C.; Neves, V. H.; Carmo, L. A. S.; Cardoso, S. J.; Melo, R. C. N. Changing our view of the Schistosoma granuloma to an ecological standpoint. *Biol. Rev. Cambridge Philos. Soc.* **2021**, *96* (4), 1404–1420. DOI: 10.1111/brv.12708.
(222) Kawanishi, K.; Dhar, C.; Do, R.; Varki, N.; Gordts, P. L. S. M.; Varki, A. Human species-specific loss of CMP-N-acetylneuraminic acid hydroxylase enhances atherosclerosis via intrinsic and extrinsic mechanisms. *Proc. Natl. Acad. Sci. U. S. A.* **2019**, *116* (32), 16036–16045. DOI: 10.1073/pnas.1902902116.
(223) Oldenborg, V.; van Vugt, F.; van Golde, L. M. Composition and metabolism of phospholipids of Fasciola hepatics, the common liver fluke. *Biochim. Biophys. Acta, Lipids Lipid Metab.***1975**, *398* (1), 101–110. DOI: 10.1016/0005-2760(75)90173-3.
(224) Bennett, C. E.; Threadgold, L. T. Fasciola hepatica: development of tegument during migration in mouse. *Exp. Parasitol.* **1975**, *38* (1), 38–55. DOI: 10.1016/0014-4894(75)90036-3.
(225) Jennemann, R.; Rabionet, M.; Gorgas, K.; Epstein, S.; Dalpke, A.; Rothermel, U.; Bayerle, A.; van der Hoeven, F.; Imgrund, S.; Kirsch, J.; Nickel, W.; Willecke, K.; Riezman, H.; Gröne, H.-J.; Sandhoff, R. Loss of ceramide synthase 3 causes lethal skin barrier disruption. *Hum. Mol. Genet.* **2012**, *21* (3), 586–608. DOI: 10.1093/hmg/ddr494.
(226) Sassa, T.; Kihara, A. Metabolism of very long-chain Fatty acids: genes and pathophysiology. *Biomol. Ther.* **2014**, *22* (2), 83–92. DOI: 10.4062/biomolther.2014.017.

(227) Robinson, M. W.; Harmon, C.; O'Farrelly, C. Liver immunology and its role in inflammation and homeostasis. *Cell. Mol. Immunol.* **2016**, *13* (3), 267–276. DOI: 10.1038/cmi.2016.3.
(228) Gonzalez-Carmona, M. A.; Sandhoff, R.; Tacke, F.; Vogt, A.; Weber, S.; Canbay, A. E.; Rogler, G.; Sauerbruch, T.; Lammert, F.; Yildiz, Y. Beta-glucosidase 2 knockout mice with increased glucosylceramide show impaired liver regeneration. *Liver Int.* **2012**, *32* (9), 1354–1362. DOI: 10.1111/j.1478-3231.2012.02841.x.
(229) Frigerio, S.; Da Costa, V.; Costa, M.; Festari, M. F.; Landeira, M.; Rodríguez-Zraquia, S. A.; Härtel, S.; Toledo, J.; Freire, T. Eosinophils Control Liver Damage by Modulating Immune Responses Against Fasciola hepatica. *Front. Immunol.* **2020**, *11*, 579801. DOI: 10.3389/fimmu.2020.579801.
(230) Goh, Y. P. S.; Henderson, N. C.; Heredia, J. E.; Red Eagle, A.; Odegaard, J. I.; Lehwald, N.; Nguyen, K. D.; Sheppard, D.; Mukundan, L.; Locksley, R. M.; Chawla, A. Eosinophils secrete IL-4 to facilitate liver regeneration. *Proc. Natl. Acad. Sci. U. S. A.* **2013**, *110* (24), 9914–9919. DOI: 10.1073/pnas.1304046110.
(231) Riboni, L.; Ghidoni, R.; Benevento, A.; Tettamanti, G. Content, pattern and metabolic processing of rat-liver gangliosides during liver regeneration. *Eur. J. Biochem.* **1990**, *194* (2), 377–382. DOI: 10.1111/j.1432-1033.1990.tb15630.x.
(232) Burren, C. H.; Ehrlich, I.; Johnson, P. Excretion of lipids by the liver fluke (Fasciola Hepatica L). *Lipids* **1967**, *2* (5), 353–356. DOI: 10.1007/BF02531847.
(233) Wilkie, J.; Cameron, T. C.; Beddoe, T. Characterization of a profilin-like protein from Fasciola hepatica. *PeerJ* **2020**, *8*, e10503. DOI: 10.7717/peerj.10503
(234) Stein, T. A.; Burns, G. P.; Tropp, B. E.; Wise, L. Hepatic fat accumulation during liver regeneration. *J. Surg. Res.* **1985**, *39* (4), 338–343. DOI: 10.1016/0022-4804(85)90112-X.
(235) Bottari, N. B.; Mendes, R. E.; Lucca, N. J.; Schwertz, C. I.; Henker, L. C.; Olsson, D. C.; Piva, M. M.; Sangoi, M.; Campos, L. P.; Moresco, R. N.; Jaques, J. A.; Da silva, A. S. Oxidative stress associated with pathological lesions in the liver of rats experimentally infected by Fasciola hepatica. *Exp.Parasitol.* **2015**, *159*, 24–28. DOI: 10.1016/j.exppara.2015.08.008.
(236) Albano, E.; Mottaran, E.; Occhino, G.; Reale, E.; Vidali, M. Review article: role of oxidative stress in the progression of non-alcoholic steatosis. *Aliment. Pharmacol. Ther.* **2005**, *22 Suppl 2*, 71–73. DOI: 10.1111/j.1365-2036.2005.02601.x.
(237) Gramberg, S.; Puckelwaldt, O.; Schmitt, T.; Lu, Z.; Haeberlein, S. Spatial transcriptomics of a parasitic flatworm provides a molecular map of drug targets and drug resistance genes. *Nat. Commun.* **2024**, *15* (1), 8918. DOI: 10.1038/s41467-024-53215-3.
(238) Praveena, T.; Le Nours, J. State of play in the molecular presentation and recognition of anti-tumor lipid-based analogues. *Front. Immunol.* **2024**, *15*, 1479382. DOI: 10.3389/fimmu.2024.1479382.
(239) Hohenwallner, K.; Troppmair, N.; Panzenboeck, L.; Kasper, C.; El Abiead, Y.; Koellensperger, G.; Lamp, L. M.; Hartler, J.; Egger, D.; Rampler, E. Decoding Distinct Ganglioside Patterns of Native and Differentiated Mesenchymal Stem Cells by a Novel Glycolipidomics Profiling Strategy. *JACS Au* **2022**, *2* (11), 2466–2480. DOI: 10.1021/jacsau.2c00230.
(240) Biswas, S.; Biswas, K.; Richmond, A.; Ko, J.; Ghosh, S.; Simmons, M.; Rayman, P.; Rini, B.; Gill, I.; Tannenbaum, C. S.; Finke, J. H. Elevated levels of select gangliosides in T cells from renal cell carcinoma patients is associated with T cell dysfunction. *J. Immunol.* **2009**, *183* (8), 5050–5058. DOI: 10.4049/jimmunol.0900259.
(241) Brennan, P. J.; Cheng, T.-Y.; Pellicci, D. G.; Watts, G. F. M.; Veerapen, N.; Young, D. C.; Rossjohn, J.; Besra, G. S.; Godfrey, D. I.; Brenner, M. B.; Moody, D. B. Structural determination of lipid antigens captured at the CD1d-T-cell receptor interface. *Proc. Natl. Acad. Sci. U. S. A.* **2017**, *114* (31), 8348–8353. DOI: 10.1073/pnas.1705882114.
(242) Dufresne, M.; Patterson, N. H.; Norris, J. L.; Caprioli, R. M. Combining Salt Doping and Matrix Sublimation for High Spatial Resolution MALDI Imaging Mass Spectrometry of Neutral Lipids. *Anal. Chem.* **2019**, *91* (20), 12928–12934. DOI: 10.1021/acs.analchem.9b02974.
(243) Paveley, R. A.; Aynsley, S. A.; Turner, J. D.; Bourke, C. D.; Jenkins, S. J.; Cook, P. C.; Martinez-Pomares, L.; Mountford, A. P. The Mannose Receptor (CD206) is an important pattern recognition

receptor (PRR) in the detection of the infective stage of the helminth Schistosoma mansoni and modulates IFNγ production. *Int. J. Parasitol* **2011**, *41* (13-14), 1335–1345. DOI: 10.1016/j.ijpara.2011.08.005.

Chapter II

Hepatic Topology of Glycosphingolipids in Schistosoma mansoni Infected Hamsters

David Luh[1], Sven Heiles[1,2,3], Martin Roderfeld[4], Christoph G. Grevelding[5], Elke Roeb[4] and Bernhard Spengler[1,*]

[1]Institute of Inorganic and Analytical Chemistry, Justus Liebig University Giessen, 35392 Giessen, Germany

[2]Leibniz-Institut für Analytische Wissenschaften - ISAS - e.V., 44139 Dortmund, Germany

[3]Lipidomics, Faculty of Chemistry, University of Duisburg-Essen, 45141 Essen, Germany

[4]Gastroenterology, Justus Liebig University Giessen, 35392 Giessen, Germany

[5]Institute for Parasitology, Justus Liebig University Giessen, 35392 Giessen, Germany

Anal. Chem. **2024**, 96, 16, 6311-6320

doi:10.1021/acs.analchem.3c05846

Supporting information: https://pubs.acs.org/doi/10.1021/acs.analchem.3c05846#_i19

analytical chemistry

pubs.acs.org/ac
Article

Hepatic Topology of Glycosphingolipids in *Schistosoma mansoni*-Infected Hamsters

David Luh, Sven Heiles, Martin Roderfeld, Christoph G. Grevelding, Elke Roeb, and Bernhard Spengler*

Cite This: https://doi.org/10.1021/acs.analchem.3c05846
Read Online

ABSTRACT: Schistosomiasis is a neglected tropical disease caused by worm parasites of the genus *Schistosoma*. Upon infection, parasite eggs can lodge inside of host organs like the liver. This leads to granuloma formation, which is the main cause of the pathology of schistosomiasis. To better understand the different levels of host−pathogen interaction and pathology, our study focused on the characterization of glycosphingolipids (GSLs). For this purpose, GSLs in livers of infected and noninfected hamsters were studied by combining high-spatial-resolution atmospheric-pressure scanning microprobe matrix-assisted laser desorption/ionization mass spectrometry imaging (AP-SMALDI MSI) with nanoscale hydrophilic interaction liquid chromatography tandem mass spectrometry (nano-HILIC MS/MS). Nano-HILIC MS/MS revealed 60 GSL species with a distinct saccharide and ceramide composition. AP-SMALDI MSI measurements were conducted in positive- and negative-ion mode for the visualization of neutral and acidic GSLs. Based on nano-HILIC MS/MS results, we discovered no downregulated but 50 significantly upregulated GSLs in liver samples of infected hamsters. AP-SMALDI MSI showed that 44 of these GSL species were associated with the granulomas in the liver tissue. Our findings suggest an important role of GSLs during granuloma formation.

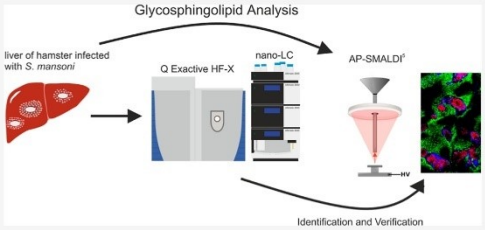

INTRODUCTION

Glycomics is an emerging field within omics-technologies, dealing with the structural and functional elucidation of N- and O-glycans, glycoproteins, or glycosphingolipids (GSLs). These molecular classes are involved in cellular communication as epitopes of pathogen recognition or play roles during immune response.[1] Understanding the fundamental roles of these molecules is helpful to monitor metabolic processes or to facilitate drug and vaccine development.[2] For these purposes, it is beneficial to analyze the spatial distribution of the analytes. A powerful molecular imaging technique is matrix-assisted laser desorption/ionization (MALDI) mass spectrometry imaging (MSI).[3,4] In an MSI experiment, the distribution of several hundred molecular species can be resolved. This is a major advantage over other imaging methods such as immunohistochemistry (IHC). Here, individual staining is required for each antibody, and the total number of stainings within one experiment is limited to a few antibodies. However, the results of IHC can validate the MSI results and link them to specific cells or proteins, as shown in the work of Bien et al.[5]

A challenge for MSI in some cases is the low ionization efficiency for some compounds, which can result in low signal intensities, especially in high-spatial-resolution MALDI MSI.[6] For high-resolution MALDI MSI, atmospheric-pressure scanning microprobe matrix-assisted laser desorption/ionization mass spectrometry imaging (AP-SMALDI MSI) with a spatial resolution of 1.4 μm has recently been developed.[7]

Successful AP-SMALDI MSI application was used for phospholipid analysis of livers of hamsters infected by *Schistosoma mansoni*.[8] Besides other Schistosoma species, *S. mansoni* is responsible for schistosomiasis, an infectious disease classified as one of the neglected tropical diseases by the World Health Organization. Schistosomiasis affects over 200 million people worldwide and is mostly distributed in tropical and subtropical areas. The pathology of schistosomiasis can be divided into an acute and a chronic phase.[9] Here, the chronic phase is more severe and can potentially lead to death.[10] The morbidity during this stage is caused by eggs trapped inside organs, like the liver and spleen. Granuloma formation around eggs is the typical host response and can lead to chronic inflammation with excessive wound healing, leading to hepatic fibrosis.[11] *S. mansoni* eggs are even able to mobilize, incorporate, and store host lipids, thereby provoking hepatic exhaustion of neutral lipids and glycogen.[12] To understand the host−parasite interaction, it is necessary to identify and characterize the molecules involved in signal transduction

Received: December 21, 2023
Revised: March 1, 2024
Accepted: March 11, 2024

https://doi.org/10.1021/acs.analchem.3c05846
Anal. Chem. XXXX, XXX, XXX−XXX

followed by the immune response. To the best of our knowledge, no studies have yet focused on the interaction between host and parasite eggs, leading to granuloma formation and resulting GSL responses. This, however, can be important because GSLs are involved in the immune responses of the host. GSLs, known to be crucial for signal transduction and membrane organization,[13] are involved in forming microdomains essential for signal transduction in activated immune cells.[14] Furthermore, they can directly regulate immune receptors, with GM3 as a regulator for the inhibition of insulin-induced signaling as one of the best understood examples.[15,16] While some examples for GSL-specific roles are known, there is a general lack of analytical methods to study GSL profiles globally and locally.[17]

A promising approach to overcome these shortcomings is the combination of nanoscale hydrophilic interaction liquid chromatography tandem mass spectrometry (nano-HILIC MS/MS) with AP-SMALDI MSI to structurally characterize GSLs and to visualize their distributions in tissue sections.[3,4] With this setup, we profiled hepatic GSLs in *S. mansoni*-infected hamsters. We analyzed, as controls, the livers of hamsters infected by only female worms (no egg production) or noninfected. We used nano-HILIC MS/MS for the detection of neutral and acidic GSLs to curate a GSL database.[18] Statistic evaluation of nano-HILIC MS/MS data revealed significant differences between infected and non-infected samples. Subsequently, optimized AP-SMALDI MSI provided information about the topography of the GSL species in infected tissue. Semiquantitative evaluation of AP-SMALDI MSI data was found to be in line with nano-HILIC MS/MS results, providing evidence that AP-SMALDI MSI allows one to locally quantify GSLs. The abundance changes of GSL species during granuloma formation indicate a potential connection between GSLs and immune cell differentiation. Furthermore, AP-SMALDI MSI measurements of granulomas with 3 μm step size enabled us to resolve ultrafine structures.

EXPERIMENTAL SECTION

Chemicals. Acetonitrile, methanol, and water (HiPerSolv) were purchased from VWR International GmbH (Darmstadt, Germany). Chloroform (Rotipuran) was purchased from Carl Roth GmbH + Co. KG (Karlsruhe, Germany). 2,5-Dihydroxybenzoic acid (DHB), ethanol, glacial acetic acid, and trifluoroacetic acid were purchased from Merck (Darmstadt, Germany). Hematoxylin, eosin Y, Eukitt, and α-cyano-4-hydroxycinnamic acid (CHCA) were purchased from Sigma-Aldrich (Darmstadt, Germany). 1,5-Diaminonapthalene (DAN) was purchased from Acros Organics (Geel, Belgium). 2,5-Dihydroxyacetophenone (DHAP) and ammonium acetate were purchased from Alfa Aesar (Kandel, Germany). 9-Aminoacridine (9-AA) was purchased from TCI (Eschborn, Germany).

Tissue and Sample Preparation. All animal experiments were approved by the Regierungspraesidium Giessen (V54-19 c 20/15 c GI 18/10 140 Nr. A26/2018) and performed in accordance with the European Convention for the Protection of Vertebrate Animals used for experimental and other scientific purposes (ETS no. 123; revised Appendix A). Tissue samples were obtained as described elsewhere.[8] Briefly, three different groups of hamster livers were used. Hamsters infected with both sexes of *S. mansoni* cercariae (bs-infected), hamsters infected with only one sex of *S. mansoni* cercariae (ss-infected), and noninfected hamsters.[19−21] For each group, three randomly chosen biological replicates were used throughout the study.

AP-SMALDI MSI Sample Preparation. For AP-SMALDI MSI measurements, fresh frozen hamster livers were sectioned with a cryotome (Thermo Scientific Microm HM 525 Cryostat) and thaw mounted onto a microscopic slide. 20 μm thick sections were used for AP-SMALDI MSI measurements. Sections were stored at −80 °C until further use. During thawing, tissue slides were placed in a desiccator for 20 min followed by matrix application. The matrices 9-AA, DAN, DHB, and CHCA were applied by pneumatic spraying (SMALDIPrep, TransMIT GmbH, Giessen, Germany) with parameters listed in Table S1. For DHAP matrix application, sublimation experiments were performed with a home-built sublimation setup (Figure S1). Sublimation parameters are given in Table S1.

Nano-HILIC Sample Preparation. Hamster liver homogenates were extracted without an exogenous standard, followed by saponification and SPE purification, to obtain GSL extracts for subsequent nano-HILIC MS/MS experiments. More detailed experimental procedures are included in Supplementary Protocol 1.

AP-SMALDI MSI Experiments and Data Analysis. Measurements with 10 and 15 μm step size were performed on an AP-SMALDI^5 AF ion source (TransMIT GmbH, Giessen, Germany)[22] coupled to an orbital trapping mass spectrometer [Thermo Scientific Q Exactive HF, Thermo Fisher Scientific (Bremen) GmbH, Germany] with a mass resolution of 240,000 at m/z 200. The measurements with a 3 μm step size were performed using an ultrahigh-resolution prototype AP-SMALDI ion source (TransMIT GmbH)[7] coupled to an orbital trapping mass spectrometer [Thermo Scientific Q Exactive, Thermo Fisher Scientific (Bremen) GmbH] with a mass resolution of 140,000 at m/z 200. More details are included in Supplementary Note 1.

The matrix DHAP was compared to DHB and CHCA in positive-ion mode for neutral GSLs. In negative-ion mode, DHAP was compared to 9-AA and DAN for acidic GSLs. Matrix evaluation was carried out by performing AP-SMALDI MSI measurements of consecutive mouse brain tissue sections on the same day. For each measurement, a region of interest (ROI) was generated with Mirion.[23] The ROI represents the distribution patterns of GSL compounds used for comparison. Expected distribution patterns are known from previous studies.[24,25] Signal intensities per pixel were calculated as the sum of the intensities of a GSL compound divided by the number of pixels in the ROI.

Raw-files were recalibrated with ReCal Offline. Ion-images were generated with Mirion. The brightness of the images was adjusted to provide better visualization. Statistical comparison of livers of *S. mansoni* bs-infected, ss-infected, and noninfected hamsters was carried out based on AP-SMALDI MSI results. For the bs-infected samples, two ROIs were defined, one including granulomas and eggs and one as a control without granulomatous tissue and without eggs. Figure S2f−h shows the ROIs for one biological replicate. In total, 2500 spectra for each biological replicate were statistically evaluated. Signal intensities of the evaluated compounds were summed up and divided by the sum of the total ion counts per pixel of all 2500 spectra in the ROI to obtain the mean intensities per pixel. Histograms were generated with Excel. Error bars represent the standard error. Statistical evaluation was performed with Perseus, with more details in Supplementary Note 2. Data

https://doi.org/10.1021/acs.analchem.3c05846
Anal. Chem. XXXX, XXX, XXX−XXX

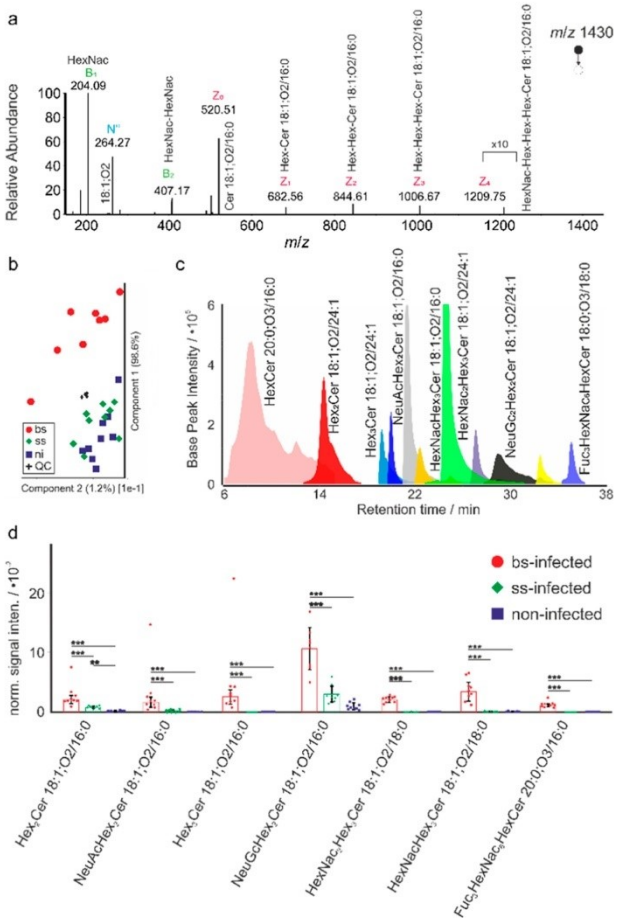

Figure 1. Nano-HILIC MS/MS analysis for GSL profiling. (a) Tandem mass spectrum for a singly charged precursor ion at m/z 1430, assigned as $HexNac_2Hex_3Cer$ 18:1;O2/16:0, based on headgroup and backbone fragment ions. (b) Principal component analysis of nano-HILIC MS/MS data in positive-ion mode with "●" for bs-infected, "◊" for ss-infected, "□" for noninfected hamster, and "+" for quality control samples. (c) Extracted ion chromatogram (EIC) for GSLs from the liver of bs-infected hamsters. (d) Histograms for GSL species based on nano-HILIC MS/MS data. Black lines above two bars indicate the difference between the two corresponding samples, with "***" representing a significant difference with $p < 0.001$ and "**" with $p < 0.01$, respectively. Error bars show the standard error.

underlying this study are openly available in the Metaspace database at https://metaspace2020.eu/project/Luh-GSL_in_liver upon publication.

Nano-HILIC Experiments and Data Analysis. Nano-HILIC MS/MS measurements were performed with an UltiMate 3000 RSLCnano System (Thermo Fisher Scientific, Dreieich, Germany) equipped with an Accucore 150 amide-HILIC column (0.075 mm × 150 mm) coupled to an orbital trapping mass spectrometer [Thermo Scientific Q Exactive HF-X, Thermo Fisher Scientific (Bremen) GmbH]. The method was adapted from Bindila et al.[26] with some modifications. More experimental details are included in Supplementary Note 3 and Tables S2 and S3.

Xcalibur was used to generate mass spectra and extract ion chromatograms. A GSL database was generated manually, and subsequently, nano-HILIC MS/MS data were processed with MZMine 2.33.[27,28] For statistical analysis, Perseus[29] was used, with details in Supplementary Note 4. Histograms were generated in Excel.

Data Processing. All of the graphics and mass spectra shown were processed with CorelDraw.

Nomenclature. To describe lipids and especially GSLs, the shorthand nomenclature of LIPIDMAPS[30,31] and the nomenclature for glycans[32] are used in this article. Simple hexoses, like glucose, galactose, or mannose, are abbreviated as Hex. Hexosamines are abbreviated HexNac and fucose as Fuc. The acidic saccharides *N*-acetylneuraminic acid and *N*-glycolylneur-

https://doi.org/10.1021/acs.analchem.3c05846
Anal. Chem. XXXX, XXX, XXX−XXX

aminic acid are abbreviated as NeuAc and NeuGc, respectively. For example, a GSL with one *N*-acetylneuraminic acid and two hexoses and a ceramide with a D-erythro-sphingosine and a hexadecanoic acid is abbreviated as $NeuAcHex_2Cer$ 18:1;O2/16:0. The structure of monosaccharide units used in this article and the fragment ion nomenclature of GSLs after Domon and Costello and Merrill et al. are shown in Figure S5.[33,34]

RESULTS AND DISCUSSION

S. mansoni Infection Raised the Hepatic Amount of Distinct GSLs. In order to characterize and quantify as many GSLs as possible, nano-HILIC MS/MS measurements with GSL extracts from the livers of hamsters infected with *S. mansoni* were performed. For these experiments, the main parameter for the separation of GSLs is their saccharide headgroup, with a representative chromatogram in Figure 1c. In total, we identified 60 molecularly different GSLs by ESI-MS/MS. For all 60 compounds, the ceramide backbone was determined, and for 47 compounds, the composition and sequence of the saccharide headgroup were assigned. A detailed list of the assigned GSL species is included in the Supporting Information. For acidic GSLs with more than three monosaccharide units (above 1400 Da), doubly charged ions were of higher signal intensities than singly charged GSLs, whereas for neutral GSLs, doubly charged ions above 1600 Da were more abundant than singly charged ions.

GSL ions were fragmented in positive- and negative-ion mode to resolve the saccharide headgroup composition and chemical makeup of the ceramide backbone. An example is shown in Figure 1a for a precursor ion at m/z 1430.8468. The Z-fragments (see Figure S5) at m/z 1209.75 and m/z 1006.67 correspond to neutral losses of hexosamine units. The next three Z-fragments at m/z 884.61, m/z 682.56, and m/z 520.51 correspond to consecutive neutral losses of hexose moieties. The complete series of Z-fragments allowed the saccharide sequence. Together with the sphingoid-base-specific N''-fragment, the structure of the GSL has been identified. The same feature is shown in Figure S6 for the negative-ion mode. Annotations for all other GSLs derived from MS^2 results are summarized in the Supporting Information.

By conducting the experiments, we created a database. This was necessary because databases such as LIPIDMAPS are incomplete with respect to GSL compounds. This especially applies to parasite-specific GSLs.

The power of high resolution and high mass accuracy is apparent when the precursor intensity for MS^2 experiments is low, resulting in an incomplete series of fragments for GSL annotation. Based on the accurate mass and the retention time, a reasonable annotation of an unknown GSL is still possible. Also, for compounds like $Fuc_3HexNac_7HexCer$ 18:0;O3/18:0 with limited sequence coverage, a literature comparison can verify the annotation.[35] Nanoscale liquid chromatography in comparison to normal liquid chromatography has the advantage of a higher sensitivity and improved dynamic range,[36] beneficial for GSLs of low abundance. Currently, a bottleneck is the manual analysis of the nano-HILIC MS/MS data of GSLs. In order to investigate a potential link of GSL in granuloma formation upon *S. mansoni* infection, we compared the relative signal intensities of GSLs in the livers of noninfected, ss-infected, and bs-infected hamsters. For each group, nano-HILIC MS/MS measurements were conducted for three biological replicates, each measured as three technical replicates. The resulting data were first analyzed by principal component analysis (PCA) (Figure 1b). Separation of the groups was achieved based on GSL identities and signal intensities, indicating alterations of GSLs upon *S. mansoni* infection. Analysis of PCA loadings revealed that GSL species significantly contributed to the separation of the different groups. These GSL species and their abundance were statistically analyzed (Figure 1d). All identified GSLs that showed a change in abundance upon infection were upregulated. Downregulation was not observed. For example, $Fuc_3HexNac_6HexCer$ 20:0;O3/16:0, which is an *S. mansoni*-egg-specific GSL, consequently represents a significant difference between bs-infected hamsters and ss-infected hamsters as well as controls ($p < 0.001$).

Other GSLs like $HexNac_2Hex_3Cer$ 18:1;O2/18:0 or $NeuAcHex_2Cer$ 18:1;O2/16:0 were also detected in the liver of ss-infected hamsters but were found to be significantly increased ($p < 0.001$) in intensity upon bs-infection. Some compounds such as Hex_3Cer 18:1;O2/16:0 showed significant upregulation not only in bs-infected animals ($p < 0.001$) but also in ss-infected animals ($p < 0.01$) compared to that observed in noninfected controls. Several compounds, including $NeuGcHex_2Cer$ 18:1;O2/16:0, were detected in all samples but with a significant increase in abundance ($p < 0.001$) in bs-infected individuals.

GSLs are known to be involved in immune response, during which several types of immune cells are recruited, including B- and T cells, eosinophils, and macrophages,[11,37,38] which form granulomas around *Schistosoma manonsi* eggs. Therefore, the upregulation of GSLs in bs-infected hamsters compared to that in ss- and noninfected controls was expected. Unexpected were the different results for GSL species in ss-infected and noninfected animals. The nano-HILIC MS/MS data revealed six significantly upregulated GSLs in the ss group compared to noninfected controls. Although ss-infected hamsters are not expected to show egg deposition, earlier reports had shown that unpaired worms can induce immune responses.[39−41] One possible mechanism is that up to 85% of unpaired female worms and 65% of unpaired male worms are found in the mouse liver after infection, which results in an accumulation of inflammatory cells in blood vessels and hepatic tissue.[39] Additionally, worms fed on the host's blood and regurgitated the digesta into the host's blood circle. This especially leads to bacteria and hemosiderin deposition in the liver, which results in inflammatory infiltrates.[41] Also, the accidental secretion of nonfertilized egg-like structures by unpaired female worms was reported to cause a host immune response.[40]

Overall, the nano-HILIC MS/MS data revealed that GSL identities and abundances were significantly altered upon *S. mansoni* infection. Next, we studied the local changes in GSLs via AP-SMALDI MSI to identify the histological features that may be associated with altered GSL profiles. Therefore, we developed a dedicated AP-SMALDI MSI workflow.

DHAP Is a Suitable Matrix for GSL Analysis by AP-SMALDI MSI. Matrices such as DHB, CHCA, 9-AA, and DAN have been used for AP-SMALDI MSI of lipids. For GSLs, DHAP and its derivatives are known to serve as potent AP-SMALDI matrices.[42,43] The performance of these matrices for efficiently ionizing GSLs was compared in experiments using mouse brain tissue sections. The results are summarized in Table S4. Comparison of AP-SMALDI MSI data of four HexCer-compounds acquired in positive-ion mode showed a 1.2- to 1.5-fold enhancement of signal intensities for DHAP compared to that for DHB and a fold change of 2.2 to 3.5

https://doi.org/10.1021/acs.analchem.3c05846
Anal. Chem. XXXX, XXX, XXX−XXX

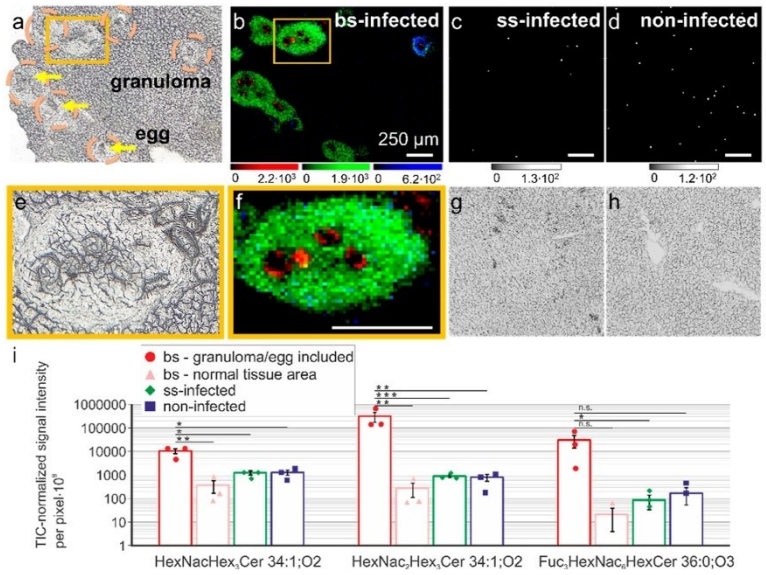

Figure 2. AP-SMALDI analysis of neutral GSLs. (a) Microscopic image of an *S. mansoni*-liver tissue section of bs-infected hamster, with yellow arrows exemplarily pointing at *S. mansoni* eggs and orange-dotted circles highlighting granulomas. (b) RGB image corresponding to the microscopic image in (a), showing $Fuc_3HexNac_6HexCer$ 20:0;O3/16:0 ($[M + K]^+$, at m/z 2442.2211) in red, $HexNac_2Hex_3Cer$ 18:1;O2/16:0 ($[M + K]^+$, at m/z 1468.7919) in green, and $HexNacHex_3Cer$ 18:1;O2/16:0 ($[M + K]^+$, at m/z 1265.7134) in blue. Magnifications of parts (a,b) are shown in parts (e,f). (c) Ion image of a ss-infected hamster liver tissue section showing m/z 1468.7939 with the corresponding microscopic image (g). (d) Ion image of a noninfected hamster showing m/z 1468.7946 with the corresponding microscopic image (h). All scale bars are 250 μm. (i) Semiquantitative evaluation of ion images of $Fuc_3HexNac_6HexCer$ 20:0;O3/16:0, $HexNac_2Hex_3Cer$ 18:1;O2/16:0, and $HexNacHex_3Cer$ 18:1;O2/16:0, with a 50 × 50 pixel ROI showing the intensity per pixel for $n = 3$ with standard error as error bars. Red—bs-infected sample ROI with granuloma included, pink—bs-infected samples without granuloma included, green—ss-infected sample, and blue—noninfected sample. Black lines centered above two bars indicate the difference between the two corresponding ROIs, with "***" representing a significant difference with $p < 0.001$, "**" with $p < 0.01$, and "*" with $p < 0.05$. "n.s." indicates a nonsignificant difference. Error bars show the standard error.

when compared to that for CHCA. In negative-ion mode, GSL signal intensities ($NeuAcHexNacHex_3Cer$ 36:1;O2 and $NeuAcHexNacHex_2Cer$ 36:1;O2) were increased 2.1- to 2.3-fold for DHAP compared to that for 9-AA and 3.9- to 6.6-fold compared to that for DAN. Additionally, a comparison on other lipid classes was performed showing similar annotation numbers for the different matrices, with more details in Supplementary Note 5. Overall, the results indicate that DHAP is best suited among the tested matrices for GSL analysis by AP-SMALDI MSI. Consequently, DHAP was used in all following AP-SMALDI MSI experiments.

Distinct Neutral GSLs Were Enriched in Hepatic Granuloma of *S. mansoni*-Infected Hamsters. We employed our optimized AP-SMALDI MSI protocol to match the histological features with *S. mansoni* infection-specific GSLs, identified by nano-HILIC MS/MS. Liver tissue sections of bs-infected ($n = 3$), ss-infected ($n = 3$), and noninfected hamsters ($n = 3$) were measured. Representative images and results are shown in Figure 2. Data obtained in positive-ion mode were used to visualize neutral GSLs. A total of 25 ion images assigned to neutral GSL species, representing nine different saccharide compositions, were obtained from livers of bs-infected hamsters. Annotations were based on our nano-HILIC MS/MS database. Compounds were detected either in the granulomas (HexCer, Hex_2Cer, Hex_3Cer, $HexNacHex_3Cer$, and $HexNac_2Hex_3Cer$) or in the *S. mansoni* eggs (HexCer, $Fuc_3HexNac_6HexCer$, $Fuc_2HexNac_6HexCer$, $Fuc_3HexNac_5HexCer$, and $Fuc_3HexNac_7HexCer$). For the ceramide composition, we observed mainly sphingosine 18:1;O2 for GSLs distributed in the hepatic tissue, with C16:0, C24:0, and C24:1 as the most prominent fatty acids. For egg-specific GSL, we found phytosphingosines as the dominant sphingoid base.

Egg-specific saccharide- and ceramide moieties of GSLs were investigated separately in a previous bulk analysis.[35] We compared these results with our data for egg-specific GSLs obtained by AP-SMALDI MSI. As an example, the GSL $Fuc_3HexNac_6HexCer$ 20:0;O3/16:0 at m/z 2442.2230 is shown in Figure 2b in red. The GSLs associated with the outer surface of the egg are in line with the previously reported data on saccharide and ceramide moieties of *S. mansoni* egg-specific GSLs.[35] We were able to detect 5 out of the 17 previously reported saccharide compositions, with each composition appearing in one or several different complex GSL species. Interestingly, we only detected GSL compounds with a maximum number of three fucose moieties, different from up to eight fucose moieties of GSLs reported in the literature.[35] Further studies are necessary to elucidate the reason for this discrepancy. Because our AP-SMALDI MSI and nano-HILIC MS data consistently indicated these five

https://doi.org/10.1021/acs.analchem.3c05846
Anal. Chem. XXXX, XXX, XXX−XXX

saccharide compounds, we assume biological variability between our sample material and that investigated in the previous study.

Besides the egg-specific GSLs, the observed distributions of hepatic GSLs are also in line with histological features visible in the corresponding optical image (Figure 2a). Examples for granuloma-specific GSL distributions are shown in Figure 2b, with $HexNac_2Hex_3Cer$ 18:1;O2/16:0 as well as $HexNAcHex_3Cer$ 18:1;O2/16:0 associated with granulomas. This indicates that specific GSLs are expressed within *S. mansoni* eggs and granulomas. To test this assumption, livers of ss- and noninfected hamsters were measured. The mass spectrometric images of $HexNac_2Hex_3Cer$ 18:1;O2/16:0 in the liver sections of ss- and noninfected hamsters are shown in Figure 2c,d. Corresponding optical images are shown in Figure 2g,h. The ion-images indicated no accumulation of this GSL species in the tissues for either sample type. The same was found for the other granuloma-specific GSLs. Even though most granulomas could be associated with elevated signal intensities of $HexNac_2Hex_3Cer$ 18:1;O2/16:0, some granulomas, relatively small in size, showed increased signal intensities of $HexNAcHex_3Cer$ compared to those of $HexNac_2Hex_3Cer$ (Figure 2b). Here, H&E staining also indicated differences between granulomas (Figure S7). The granuloma highlighted by a red-dotted circle shows a homogeneous distribution of $HexNac_2Hex_3Cer$. The granuloma highlighted by an orange-dotted circle shows a homogeneous distribution of $HexNAcHex_3Cer$ and appears more purple, indicating a different cellular composition. This might indicate that different granuloma growth states are characterized by specific GSL species. For example, $HexNAcHex_3Cer$ 18:1;O2/16:0 at m/z 1265.7135 in blue in Figure 2b was found to be highly abundant in only one granuloma in this tissue section and was found to accumulate only slightly at the borders of larger granulomas (magnified ion-image in Figure S2i). The same distribution as that for $HexNAcHex_3Cer$ 18:1;O2/16:0 was observed for HexCer 18:1;O2/16:0, Hex_2Cer 18:1;O2/16:0 and Hex_3Cer 18:1;O2/16:0 (Figure S2j–l).

Granuloma formation is induced by the immune response and results in subsequent recruitment of immune cells in *S. mansoni* infections, allowing the observation of different stages of granuloma formation within the same tissue sample. This is also influenced by the time when an egg is trapped in the liver tissue because schistosomes constantly produce eggs in a host over many years.[11,44] Against this background, we suggest that the signals specifically found in smaller granulomas, namely, Hex_2Cer 18:1;O2/16:0, Hex_3Cer 18:1;O2/16:0, and $HexNAcHex_3Cer$ 18:1;O2/16:0, might be markers for an early stage of granuloma development. This stage is termed pregranulomatous exudative (PE) stage in the literature and an initial recruitment of leucocytes (T- and B-cells) is typical.[45] A schematic cell model of this stage is shown in Figure S8a. After further granuloma development, the granulomatous exudative-productive (EP) stage is formed. The EP stage is characterized by a highly ordered structure with macrophages and eosinophils as the inner layer, surrounded by fibroblasts/hepatic stellate cells, and a collagen layer, which is surrounded by an outer layer of T- and B-cells (Figure S8b).[38] Based on the infection time of the hamsters and the size of the granulomas, most were probably in the EP-stage. In these regions, we detected $HexNac_2Hex_3Cers$ as the main granuloma markers, all with the same lateral distribution, similar to $HexNac_2Hex_3Cer$ 18:1;O2/16:0 (Figure 2b, green). Because these GSL compounds were not observed during the assumed PE-stage, they were potentially formed during macrophage or eosinophil infiltration. In addition, we find for the suggested EP-stage granulomas a slight accumulation of $HexNacHex_3Cer$ 18:1;O2/16:0 in the outer layer of the granulomas, as shown in Figure S2i, which is in line with the model of the EP-stage. To further substantiate our assumption, AP-SMALDI MSI combined with IHC could help to link GSL distributions to specific cell types. A first example of IHC compared to ion images obtained by AP-SMALDI MSI is shown in Figure S9, where tissue sections neighboring those used for AP-SMALDI MSI were analyzed. While the highlighted granuloma in Figure S9 (top row) indicates the presence of $HexNacHex_3Cer$ 18:0;O2/16:0 throughout the granuloma and also T-cell-specific CD3-staining across the granuloma, the bottom row only shows signals at the outer layer of the granuloma for $HexNacHex_3Cer$ 18:0;O2/16:0 as well as CD3-positive cells. Due to the limited reactivity of available antibodies with hamster antigens, immunofluorescence experiments are challenging. Nonetheless, our experiments provide the first hints for a possible link between GSLs and infiltrating immune cells.

To semiquantitatively evaluate the increased signal intensities of specific GSLs in granuloma/egg compared to the surrounding tissue, signal intensities of each selected GSL were summed up in a defined ROI and normalized to the TIC of the ROI. For three GSL compounds, $Fuc_3HexNac_6HexCer$ 20:0;O3/16:0, $HexNac_2Hex_3Cer$ 18:1;O2/16:0, and $HexNAcHex_3Cer$ 18:1;O2/16:0, the results are shown in Figure 2i. The normalized signal intensity per pixel of $Fuc_3HexNac_6HexCer$ 20:0;O3/16:0 for granuloma and eggs of bs-infected samples was found to be 180- to 1400-fold increased compared to the other three ROI (normal tissue of bs-infected, ss-infected, and noninfected samples). For the compounds $HexNac_2Hex_3Cer$ 18:1;O2/16:0 and $HexNAcHex_3Cer$ 18:1;O2/16:0, the signal intensities per pixel were found to be 350- to 1100-fold and 8- to 28-fold increased, respectively. The semiquantitative data were also in line with our nano-HILIC MS/MS data, where we observed a significant increase ($p < 0.001$) for the compounds $Fuc_3HexNac_6HexCer$ 20:0;O3/16:0, $HexNac_2Hex_3Cer$ 18:1;O2/16:0, and $HexNAcHex_3Cer$ 18:1;O2/16:0. These results for neutral GSLs indicated that specific GSL regulation in granuloma occurred upon *S. mansoni* infection, providing potential GSL markers for granuloma formation.

In total, we were able to visualize 21 neutral GSLs out of the 31 compounds identified via nano-HILIC MS/MS and to locally pinpoint most of these GSL species, significantly upregulated in bs-infected tissue, to granuloma/eggs. An earlier study of cancer tissue already demonstrated the analysis of neutral complex GSLs by high-resolution MSI with a 15 μm step size.[5] With our AP-SMALDI MSI setup, we were able to routinely use a spatial resolution of 10 μm step size to resolve the different morphological structures in our samples. The high mass resolution and accuracy provided by our orbitrap mass spectrometer was essential for signals in the lower mass range (700−1000) to obtain true assignments and authentic distributions of compounds.

To characterize GSL regulation in granulomas, GSL species preferentially ionized in negative-ion mode are described in the next section.

Acidic Glycosphingolipids Were Enriched in Distinct Areas of Hepatic Granuloma. AP-SMALDI MSI measure-

https://doi.org/10.1021/acs.analchem.3c05846
Anal. Chem. XXXX, XXX, XXX−XXX

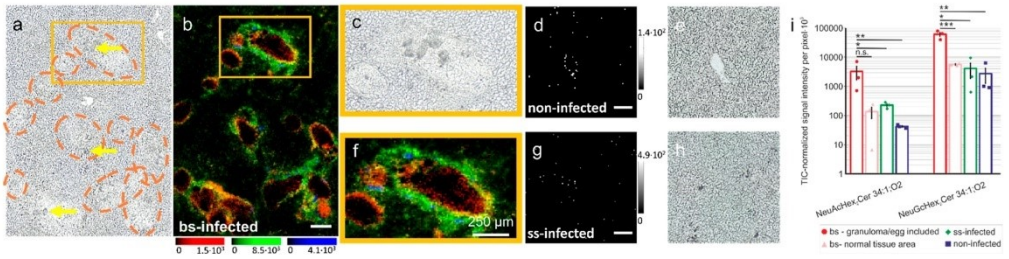

Figure 3. AP-SMALDI analysis of acidic GSLs. (a) Microscopic image of a liver tissue section of a bs-infected hamster, with yellow arrows exemplarily pointing at *S. mansoni* eggs and orange-dotted circles highlighting granuloma. (b) RGB image corresponding to the microscopic image in (a), showing $NeuAcHex_2Cer$ 18:1;O2/16:0 ($[M-H]^-$ at m/z 1151.7058) in red, $NeuGcHex_2Cer$ 18:1;O2/16:0 ($[M-H]^-$ at m/z 1167.7008) in green, and SHexCer 18:1;O2/16:0 ($[M-H]^-$ at m/z 778.5148) in blue. Magnifications of (a,b) are shown in (c,f). (d) Ion image of a liver tissue section of a noninfected hamster of $NeuGcHex_2Cer$ 18:1;O2/16:0 ($[M-H]^-$ at m/z 1167.6977) with the corresponding microscopic image (e). (g) Ion image of a liver tissue section of an ss-infected hamster of $NeuGcHex_2Cer$ 18:1;O2/16:0 ($[M-H]^-$ at m/z 1167.6987) with corresponding the microscopic image (h). Scale bars indicate a length of 250 μm. (i) Histograms for the GSL species shown in the RGB-overlay based on the semiquantitative analysis of AP-SMALDI data. Black lines centered above two bars indicate the difference between the two corresponding ROIs, with "***" representing a significant difference with $p < 0.001$, "**" with $p < 0.01$, and "*" with $p < 0.05$. Error bars show the standard error.

ments were conducted in negative-ion mode for the detection of acidic GSLs. In total, ion images of 32 GSLs with five different saccharide compositions were generated for bs-infected samples. The acidic GSL species were found to contain $NeuGcHex_2$, $NeuAcHex_2$, $NeuGc_2Hex_2$, and $NeuGcHexNacHex_2$. In addition, neutral GSLs were also visualized in negative-ion mode. As an example, $HexNac_2Hex_3Cer$ 18:1;O2/16:0 is shown as the deprotonated species (Figure S10l). The negative-ion mode can thus be employed for cross validation of results obtained in the positive-ion mode. Representative AP-SMALDI images for acidic GSLs and corresponding microscopic images are shown in Figure 3. The spatial distributions for acidic GSLs showed specific accumulations within the granulomas. Here, acidic GSLs containing NeuGc and NeuAc were found to differ.

As an example, the compound $NeuAcHex_2Cer$ 18:1;O2/16:0 at m/z 1151.7058 is shown in red in Figure 3b. It exhibited high signal intensities in the middle layer of the granulomas, referring to the proposed granuloma model of the EP-stage (Figure S8b). In contrast, the compound $NeuGcHex_2Cer$ 18:1;O2/16:0 at m/z 1167.7009, shown in green (Figure 3b), exhibited high signal intensities in the outer layer of granulomas. The compound was also detected in the surrounding tissue of the granulomas. Therefore, this compound might correspond to T- and B-cells, which are the main cells of the outer granuloma layer. Small populations of these cells are also expected in healthy hepatic tissue. Additionally, in the RGB image (Figure S11b), the compound $HexNac_2Hex_3Cer$ 18:0/16:0 is shown in red. This compound may represent a marker for the inner layer of the EP-stage. Together with the compounds $NeuAcHex_2Cer$ 18:1;O2/16:0 and $NeuGcHex_2Cer$ 18:1;O2/16:0, we were able to describe all three different layers of the granuloma in the EP-stage with different GSL compositions.

Moreover, we detected only five compounds containing a NeuAc moiety, all showing a similar spatial distribution. Species containing a NeuGc moiety were detected in various molecular compositions. For $NeuGcHex_2$, 13 different ceramide compositions were detected, with examples in Figure S10a–d. In the noninfected sample shown in Figure 3d, $NeuGcHex_2Cer$ 18:1;O2/16:0 at m/z 1167.6977 was detected with low signal intensities around the blood vessels, whereas no accumulation was observed for the ss-infected sample (Figure 3g).

Another aspect becomes apparent when analyzing the data sets, which is the possibility of monitoring GSL metabolic processes. An example highlighting the benefits of combining nano-HILIC MS/MS and AP-SMALDI MSI data for metabolic GSL transformations during immune responses is the known conversion of NeuAc into NeuGc GSLs.[46] In hamsters and other mammals, the enzyme cytidine monophosphate-*N*-acetylneuraminic acid hydroxylase (CMAH) catalyzes the required transformation. GSLs containing these head groups are shown in Figure 3b, namely, $NeuGcHex_2Cer$ 18:1;O2/16:0 in green and $NeuAcHex_2Cer$ 18:1;O2/16:0 in red. These compounds were found to locally overlap and to be significantly upregulated upon infection. Thus, it is tempting to speculate that CMAH activation during immune response results in increased production of $NeuGcHex_2Cer$ 18:1;O2/16:0. If this hypothesis is correct, the tools developed here could allow one to track specifically the end product of enzymatic cascades as a function of time and link the GSL expression profiles to specific regions with altered immune activity during *S. mansoni* infection. This could help to systematically investigate GSL transformations in tissues during disease progression. The advantage of AP-SMALDI MSI with the simultaneous visualization of various compounds outperforms classical, targeted imaging techniques.

In addition to the detectability of acidic GSL compounds, the negative-ion mode is also suitable for the detection of sulfated GSLs. As an example, SHexCer 18:1;O2/16:0 at m/z 778.5148 is shown in blue in Figure 3b, partially surrounding the granulomas. The same distribution pattern was observed for seven other SHex compounds with different ceramide compositions (Figure S10e–k). For sulfated compounds, our annotations were based on the accurate mass only because we did not detect these compounds with nano-HILIC MS/MS. Here, the advantage of the orthogonality of MALDI MSI and nano-HILIC MS/MS becomes apparent. While nano-HILIC MS/MS allows for a more detailed structural elucidation of

https://doi.org/10.1021/acs.analchem.3c05846
Anal. Chem. XXXX, XXX, XXX−XXX

GSL compounds, it does have some limitations. If, for example, species like SHexCers are only partially accumulated throughout the whole tissue, then they will be possibly too low in concentration in a bulk analysis. In contrast, by using MALDI MSI and therefore maintaining spatial information, high local concentrations make the detection and visualization of such species possible.

The semiquantitative evaluation of $NeuAcHex_2Cer$ 18:1;O2/16:0 and $NeuGcHex_2Cer$ 18:1;O2/16:0 signals is presented in Figure 3i. For the two compounds, the TIC-normalized signal intensities per pixel were found to be increased 14- to 78-fold and 11- to 22-fold, respectively, for granuloma/egg ROIs compared to those for the other three ROI (normal tissue of bs-infected samples and ss- and noninfected samples). These results are in line with our nano-HILIC MS/MS data, where significant differences in these GSLs were observed between bs-infected samples and controls. Out of the 30 GSLs identified by nano-HILIC, negative-ion mode AP-SMALDI MSI allowed local tracking of the distribution of 17 of these compounds. These acidic GSLs were predominantly accumulated around or on the outer borders of granulomas. In addition, these results are consistent with the evaluation of positively charged GSLs. Together with the positive-ion mode analysis, a comprehensive and locally resolved overview of GSLs involved in immune response during *S. mansoni* infection and granuloma formation was obtained. As reported in the literature and confirmed by our initial experiments, DHAP is the matrix of choice for AP-SMALDI measurements of acidic GSL.[42,43] Whereas most studies focused on brain tissue,[47−49] we show the first application to hamster liver tissue. We also demonstrate that high-resolution AP-SMALDI MSI of GSLs can be routinely performed with a 10 μm step size. Importantly, we included no additional washing steps for the tissue sections prior to analysis. This is relevant when comparing our study to the literature, where at a lower spatial resolution, an increased detection sensitivity of acidic GSL was achieved by additionally washing the tissue slide.[48] While additional washing steps can be useful to increase sensitivity, they generally limit the spatial resolution due to wash-out effects.

Mass Spectrometry Imaging Was Optimized Down to 3 μm Lateral Resolution. In order to distinguish additional histological features within granulomas at the molecular level, the effective lateral resolution of the method was further improved by employing an experimental ion source setup with a smaller laser focus. Mass spectrometric images with 15, 10, and 3 μm pixel size are shown for comparison in Figure 4. The RGB overlay images show HexCer 20:0;O3/16:0 in red, $HexNac_2Hex_3Cer$ 18:1;O2/16:0 as a granuloma marker in green, and PC 38:1 as a marker for *Schistosoma* eggs in blue. HexCer 20:0;O3/16:0 can be assigned to the surface of the *S. mansoni* eggs from the 10 μm step size image but not from the 15 μm step size image. The assignment and interpretation are obviously much clearer and more trustworthy when using the 3 μm experimental setup and method (Figure 4c). These first experiments, using DHAP as a matrix, demonstrate the capability of our workflow to track GSLs with cellular resolution.

CONCLUSIONS

In this study, we optimized a high-resolution AP-SMALDI MSI approach in combination with nano-HILIC MS/MS to reveal the global and local hepatic GSL profiles of liver samples

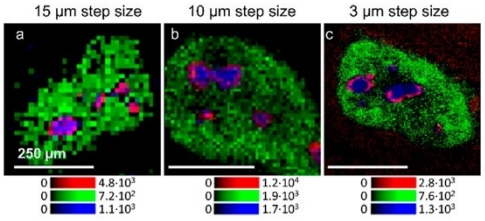

Figure 4. Increasing the lateral resolution enables the localization of substructures in *S. mansoni* eggs. (a) RGB overlay images of three granulomas measured with a 15 μm step size, (b) 10 μm step size, and (c) 3 μm step size using an experimental AP-SMALDI imaging setup, showing HexCer 20:0;O3/16:0 ($[M + K]^+$ at m/z 784.5715) in red, $HexNac_2Hex_3Cer$ 18:1;O2/16:0 ($[M + K]^+$, at m/z 1468.7913) in green, and PC 38:1 ($[M + K]^+$ at m/z 854.6042) in blue.

of *S. mansoni*-infected hamsters compared to that of non-infected controls. Overall, we found statistically significant differences between the hepatic GSL profiles of infected and noninfected animals. Based on high-resolution AP-SMALDI MSI data, upregulated GSLs primarily localized within granulomas surrounding *S. mansoni* eggs in the liver. This suggests that GSL topology is associated with granuloma formation, potentially related to infiltrating and differentiating immune cells. Whether the determined GSL species are merely markers for granuloma formation and whether they are associated with particular cell states and used for intercellular communication or cell differentiation will be a matter of future longitudinal studies. Linking GSL topography with specific granuloma stages is crucial to reveal the time courses of GSL development and to connect GSL species with defined immune cell differentiation stages.

ASSOCIATED CONTENT

Supporting Information

The Supporting Information is available free of charge at https://pubs.acs.org/doi/10.1021/acs.analchem.3c05846.

Additional experimental protocols, experimental parameters, data-processing steps, additional results for the matrix evaluation of DHAP compared to other matrices, sublimation setup, more ion images for neutral GSL of bs-infected hamsters, structures of a GSL and monosaccharide units, MS^2 spectra of $HexNac_2Hex_3Cer$ 18:1;O2/16:0 in negative-ion mode, H&E-stained section and the corresponding RGB-overlay of the liver of a bs-infected hamster, granuloma model for the PE- and EP-stages, IHC results compared to MALDI MSI results, and additional ion images for acidic GSL and an H&E-stained section and the corresponding RGB-overlay of the liver of bs-infected hamsters with three different distributions of GSLs within a granuloma (PDF)

Glycosphingolipid database (XLSX)

AUTHOR INFORMATION

Corresponding Author

Bernhard Spengler − *Institute of Inorganic and Analytical Chemistry, Justus Liebig University Giessen, 35392 Giessen, Germany;* orcid.org/0000-0003-0179-5653;
Email: bernhard.spengler@anorg.chemie.uni-giessen.de

Authors

David Luh − *Institute of Inorganic and Analytical Chemistry, Justus Liebig University Giessen, 35392 Giessen, Germany*

Sven Heiles − *Institute of Inorganic and Analytical Chemistry, Justus Liebig University Giessen, 35392 Giessen, Germany; Leibniz-Institut für Analytische Wissenschaften—ISAS—e.V., 44139 Dortmund, Germany; Lipidomics, Faculty of Chemistry, University of Duisburg-Essen, 45141 Essen, Germany;* orcid.org/0000-0003-3779-8071

Martin Roderfeld − *Gastroenterology, Justus Liebig University Giessen, 35392 Giessen, Germany*

Christoph G. Grevelding − *Institute for Parasitology, Justus Liebig University Giessen, 35392 Giessen, Germany*

Elke Roeb − *Gastroenterology, Justus Liebig University Giessen, 35392 Giessen, Germany*

Complete contact information is available at: https://pubs.acs.org/10.1021/acs.analchem.3c05846

Author Contributions

B.S. supervised the project. D.L., S.H., M.R., and B.S. designed the study. D.L. performed all the experiments, except immunohistochemistry. This was done by M.R. D.L. performed the data analysis and wrote the original draft. All authors reviewed and edited the manuscript. All authors have given approval to the final version of the manuscript.

Notes

The authors declare the following competing financial interest(s): B.S. and C.G.G are consultants of TransMIT GmbH, Giessen, Germany. All others declare no conflicts of interest.

■ ACKNOWLEDGMENTS

We gratefully acknowledge financial support by the German Science Foundation (DFG) under the grants RO3714/4-2 for M.R. and SP314/23-1 and INST 162/500-1 FUGG for B.S. and by the Hessian Ministry of Science, Higher Education and Art (HMWK), LOEWE Center DRUID. S.H. thanks the Fonds der Chemischen Industrie for granting a Liebig fellowship, and financial support by the Deutsche Forschungsgemeinschaft (HE 8521/1-1) is gratefully acknowledged. S.H. acknowledges the support by the "Ministerium für Kultur und Wissenschaft des Landes Nordrhein-Westfalen" and the German Ministry of Research and Education (BMBF) and is grateful for financial support by the Justus Liebig University via the JLU award 2022.

■ REFERENCES

(1) Varki, A. *Glycobiology* **2017**, *27*, 3−49.

(2) Aerts, J. M. F. G.; Artola, M.; van Eijk, M.; Ferraz, M. J.; Boot, R. G. *Front. Cell Dev. Biol.* **2019**, *7*, 324.

(3) Spengler, B.; Hubert, M.; Kaufmann, R. MALDI ion imaging and biological ion imaging with a new scanning UV-laser microprobe. *Proceedings of the 42nd Annual Conference on Mass Spectrometry and Allied Topics*, 1994; Vol. *1040*.

(4) Koestler, M.; Kirsch, D.; Hester, A.; Leisner, A.; Guenther, S.; Spengler, B. *Rapid Commun. Mass Spectrom.* **2008**, *22*, 3275−3285.

(5) Bien, T.; Perl, M.; Machmüller, A. C.; Nitsche, U.; Conrad, A.; Johannes, L.; Müthing, J.; Soltwisch, J.; Janssen, K.-P.; Dreisewerd, K. *Anal. Chem.* **2020**, *92*, 7096−7105.

(6) Dreisewerd, K. *Chem. Rev.* **2003**, *34*, 395−426.

(7) Kompauer, M.; Heiles, S.; Spengler, B. *Nat. Methods* **2017**, *14*, 90−96.

(8) Wiedemann, K. R.; Peter Ventura, A.; Gerbig, S.; Roderfeld, M.; Quack, T.; Grevelding, C. G.; Roeb, E.; Spengler, B. *Anal. Bioanal. Chem.* **2022**, *414*, 3653−3665.

(9) Burke, M. L.; Jones, M. K.; Gobert, G. N.; Li, Y. S.; Ellis, M. K.; McManus, D. P. *Parasite Immunol.* **2009**, *31*, 163−176.

(10) Richter, J.; Correia Dacal, A. R.; Vergetti Siqueira, J. G.; Poggensee, G.; Mannsmann, U.; Deelder, A.; Feldmeier, H. *Trop. Med. Int. Health* **1998**, *3*, 728−735.

(11) Schwartz, C.; Fallon, P. G. *Front. Immunol.* **2018**, *9*, 2492.

(12) von Bülow, V.; Gindner, S.; Baier, A.; Hehr, L.; Buss, N.; Russ, L.; Wrobel, S.; Wirth, V.; Tabatabai, K.; Quack, T.; Haeberlein, S.; Kadesch, P.; Gerbig, S.; Wiedemann, K. R.; Spengler, B.; Mehl, A.; Morlock, G.; Schramm, G.; Pons-Kühnemann, J.; Falcone, F. H.; Wilson, R. A.; Bankov, K.; Wild, P.; Grevelding, C. G.; Roeb, E.; Roderfeld, M. *JHEP Rep.* **2023**, *5* (2), 100625.

(13) Zhang, T.; de Waard, A. A.; Wuhrer, M.; Spaapen, R. M. *Front. Immunol.* **2019**, *10*, 90.

(14) Tuosto, L.; Parolini, I.; Schröder, S.; Sargiacomo, M.; Lanzavecchia, A.; Viola, A. *Eur. J. Immunol.* **2001**, *31*, 345−349.

(15) Tagami, S.; Inokuchi, J. i.; Kabayama, K.; Yoshimura, H.; Kitamura, F.; Uemura, S.; Ogawa, C.; Ishii, A.; Saito, M.; Ohtsuka, Y.; Sakaue, S.; Igarashi, Y. *Biol. Chem.* **2002**, *277*, 3085−3092.

(16) Kabayama, K.; Sato, T.; Saito, K.; Loberto, N.; Prinetti, A.; Sonnino, S.; Kinjo, M.; Igarashi, Y.; Inokuchi, J. *Proc. Natl. Acad. Sci. U.S.A.* **2007**, *104*, 13678−13683.

(17) Barrientos, R. C.; Zhang, Q. *Anal. Chim. Acta* **2020**, *1132*, 134−155.

(18) Hořejší, K.; Jirásko, R.; Chocholoušková, M.; Wolrab, D.; Kahoun, D.; Holčapek, M. *Metabolites* **2021**, *11*, 140.

(19) Grevelding, C. G. *Mol. Biochem. Parasitol.* **1999**, *101*, 207−216.

(20) Roderfeld, M.; Padem, S.; Lichtenberger, J.; Quack, T.; Weiskirchen, R.; Longerich, T.; Schramm, G.; Churin, Y.; Irungbam, K.; Tschuschner, A.; Windhorst, A.; Grevelding, C. G.; Roeb, E. *Hepatology* **2020**, *72*, 626−641.

(21) Weglage, J.; Wolters, F.; Hehr, L.; Lichtenberger, J.; Wulz, C.; Hempel, F.; Baier, A.; Quack, T.; Köhler, K.; Longerich, T.; Schramm, G.; Irungbam, K.; Mueller, H.; von Buelow, V.; Tschuschner, A.; Odenthal, M.; Drebber, U.; Arousy, M. E.; Ramalho, L. N. Z.; Bankov, K.; Wild, P.; Pons-Kühnemann, J.; Tschammer, J.; Grevelding, C. G.; Roeb, E.; Roderfeld, M. *Sci. Rep.* **2020**, *10*, 22373.

(22) Kompauer, M.; Heiles, S.; Spengler, B. *Nat. Methods* **2017**, *14*, 1156−1158.

(23) Paschke, C.; Leisner, A.; Hester, A.; Maass, K.; Guenther, S.; Bouschen, W.; Spengler, B. *J. Am. Soc. Mass Spectrom.* **2013**, *24*, 1296−1306.

(24) Vajn, K.; Viljetić, B.; Degmečić, I. V.; Schnaar, R. L.; Heffer, M. *PLoS One* **2013**, *8*, No. e75720.

(25) Vens-Cappell, S.; Kouzel, I. U.; Kettling, H.; Soltwisch, J.; Bauwens, A.; Porubsky, S.; Müthing, J.; Dreisewerd, K. *Anal. Chem.* **2016**, *88*, 5595−5599.

(26) Kirsch, S.; Müthing, J.; Peter-Katalinić, J.; Bindila, L. *Biol. Chem.* **2009**, *390*, 657−672.

(27) Katajamaa, M.; Miettinen, J.; Oresic, M. *Bioinformatics* **2006**, *22*, 634−636.

(28) Pluskal, T.; Castillo, S.; Villar-Briones, A.; Oresic, M. *BMC Bioinf.* **2010**, *11*, 395.

(29) Tyanova, S.; Temu, T.; Sinitcyn, P.; Carlson, A.; Hein, M. Y.; Geiger, T.; Mann, M.; Cox, J. *Nat. Methods* **2016**, *13*, 731−740.

(30) Fahy, E.; Subramaniam, S.; Brown, H. A.; Glass, C. K.; Merrill, A. H.; Murphy, R. C.; Raetz, C. R. H.; Russell, D. W.; Seyama, Y.; Shaw, W.; Shimizu, T.; Spener, F.; van Meer, G.; VanNieuwenhze, M. S.; White, S. H.; Witztum, J. L.; Dennis, E. A. *J. Lipid Res.* **2005**, *46*, 839−861.

(31) Liebisch, G.; Fahy, E.; Aoki, J.; Dennis, E. A.; Durand, T.; Ejsing, C. S.; Fedorova, M.; Feussner, I.; Griffiths, W. J.; Köfeler, H.; Merrill, A. H.; Murphy, R. C.; O'Donnell, V. B.; Oskolkova, O.; Subramaniam, S.; Wakelam, M. J. O.; Spener, F. *J. Lipid Res.* **2020**, *61*, 1539−1555.

(32) Varki, A.; Cummings, R. D.; Aebi, M.; Packer, N. H.; Seeberger, P. H.; Esko, J. D.; Stanley, P.; Hart, G.; Darvill, A.; Kinoshita, T.; Prestegard, J. J.; Schnaar, R. L.; Freeze, H. H.; Marth, J. D.; Bertozzi, C. R.; Etzler, M. E.; Frank, M.; Vliegenthart, J. F.; Lütteke, T.; Perez, S.; Bolton, E.; Rudd, P.; Paulson, J.; Kanehisa, M.; Toukach, P.; Aoki-Kinoshita, K. F.; Dell, A.; Narimatsu, H.; York, W.; Taniguchi, N.; Kornfeld, S. *Glycobiology* **2015**, *25*, 1323−1324.
(33) Domon, B.; Costello, C. E. *Glycoconjugate J.* **1988**, *5*, 397−409.
(34) Merrill, A. H.; Sullards, M. C.; Allegood, J. C.; Kelly, S.; Wang, E. *Methods* **2005**, *36*, 207−224.
(35) Smit, C. H.; van Diepen, A.; Nguyen, D. L.; Wuhrer, M.; Hoffmann, K. F.; Deelder, A. M.; Hokke, C. H. *Mol. Cell. Proteomics* **2015**, *14*, 1750−1769.
(36) Danne-Rasche, N.; Coman, C.; Ahrends, R. *Anal. Chem.* **2018**, *90*, 8093−8101.
(37) Hams, E.; Aviello, G.; Fallon, P. G. *Front. Immunol.* **2013**, *4*, 89.
(38) Llanwarne, F.; Helmby, H. *Parasite Immunol.* **2021**, *43*, No. e12778.
(39) Moné, H.; Boissier, J. *J. Adv. Parasitol.* **2004**, *57*, 89−189.
(40) Shaw, M. K. *J. Helminthol.* **1987**, *61*, 253−259.
(41) Skelly, P. J.; Da'dara, A. A.; Li, X.-H.; Castro-Borges, W.; Wilson, R. A. *PLoS Pathog.* **2014**, *10* (8), No. e1004246.
(42) Hayasaka, T.; Goto-Inoue, N.; Masaki, N.; Ikegami, K.; Setou, M. *Surf. Interface Anal.* **2014**, *46*, 1219−1222.
(43) Jackson, S. N.; Muller, L.; Roux, A.; Oktem, B.; Moskovets, E.; Doroshenko, V. M.; Woods, A. S. *J. Am. Soc. Mass Spectrom.* **2018**, *29*, 1463−1472.
(44) Amaral, K. B.; Silva, T. P.; Dias, F. F.; Malta, K. K.; Rosa, F. M.; Costa-Neto, S. F.; Gentile, R.; Melo, R. C. N. *PLoS One* **2017**, *12*, No. e0184696.
(45) Malta, K. K.; Silva, T. P.; Palazzi, C.; Neves, V. H.; Carmo, L. A. S.; Cardoso, S. J.; Melo, R. C. N. *Biol. Rev. Cambridge Philos. Soc.* **2021**, *96*, 1404−1420.
(46) Kawanishi, K.; Dhar, C.; Do, R.; Varki, N.; Gordts, P. L. S. M.; Varki, A. *Proc. Natl. Acad. Sci. U.S.A.* **2019**, *116*, 16036−16045.
(47) *Structure and Function of Gangliosides. Advances in Experimental Medicine and Biology*; Svennerholm, L., Mandel, P., Dreyfus, H., Urban, P.-F., Eds; Springer: Boston, MA, 1980.
(48) Zhang, Y.; Wang, J.; Liu, J.; Han, J.; Xiong, S.; Yong, W.; Zhao, Z. *Sci. Rep.* **2016**, *6*, 25289.
(49) Colsch, B.; Jackson, S. N.; Dutta, S.; Woods, A. S. *ACS Chem. Neurosci.* **2011**, *2*, 213−222.

https://doi.org/10.1021/acs.analchem.3c05846
Anal. Chem. XXXX, XXX, XXX−XXX

Supporting information

Hepatic topology of glycosphingolipids in *Schistosoma mansoni*-infected hamsters

David Luh[1], Sven Heiles[1,2,3], Martin Roderfeld[4], Christoph G. Grevelding[5], Elke Roeb[4] and Bernhard Spengler[1,*]

[1]Institute of Inorganic and Analytical Chemistry, Justus Liebig University Giessen, 35392 Giessen, Germany

[2]Leibniz-Institut für Analytische Wissenschaften - ISAS - e.V., 44139 Dortmund, Germany

[3]Lipidomics, Faculty of Chemistry, University of Duisburg-Essen, 45141 Essen, Germany

[4]Gastroenterology, Justus Liebig University Giessen, 35392 Giessen, Germany

[5]Institute for Parasitology, Justus Liebig University Giessen, 35392 Giessen, Germany

Table of contents

Supplementary Protocol 1: Sample preparation for nano-HILIC MS/MS measurements

For nano-HILIC MS/MS, GSLs were extracted as follows. Starting with hamster liver homogenate, 240 µL water, 640 µL methanol and 320 µL chloroform were added, followed by a two-hour incubation at 38 °C with intermediate mixing every 15 minutes. The suspension was centrifuged with 1400 g for 5 minutes. The supernatant was removed and kept on ice. With the remaining pellet, the previous steps were repeated and the supernatants were combined. Solvents were evaporated under a stream of nitrogen. Subsequently, the samples were dissolved in 1.5 mL of 0.1 mol/L sodium hydroxide in methanol and incubated at 38 °C for saponification of phospholipids. This was followed by neutralization of the sample solutions with glacial acetic acid and evaporation of the solvents under a nitrogen flow.

For purification and desalting, dried GSLs extracts were dissolved in chloroform/methanol/water (3:98:74, v/v/v) and applied to a C18-SPE cartridge (Chromabond C18ec, Macherey and Nagel, Düren, Germany), according to Wuhrer et al.[1] Before applying the sample, the cartridges were washed with 10 column volumes of methanol, 10 column volumes of chloroform/methanol (2:1, v/v) and again 10 column volumes of methanol. Equilibration was done with five column volumes of chloroform/methanol/water (3:98:74, v/v/v). After applying the sample, the SPE cartridges were washed with 10 column volumes of water and the sample was then eluted with five column volumes of methanol. The samples were dried under a stream of nitrogen, dissolved in 1.5 mL methanol/water (1:1, v/v) and further diluted by a factor of 15 with the same solvents for analysis. The pooled quality control sample was a mix of 1 µL from the stock solution of each second biological replicate with in total 91 µL methanol/water (1:1, v/v).

Supplementary Protocol 2: H&E staining protocol

Hematoxylin and eosin (H&E) staining was performed after AP-SMALDI MSI measurements. First, matrix was rinsed off with ethanol and then dehydrated for 2 min in ethanol followed by a 2 min incubation in 70% ethanol. Then the sample was incubated for 2 min in 40% ethanol followed by a 2 min incubation step in HPLC-grade water. Staining with hematoxylin for 12 min, washing with tap water for 15 min and staining with 1% Eosin Y solution for 1 min and differentiation with HPLC-grade water for 2 min, 40% ethanol for 2 min, 70% ethanol for 2 min and 100% ethanol for 2 min were subsequently carried out. Clearing with xylol for 2 min and covering with Eukitt and a cover slide completed the staining protocol.

Supplementary Note 1: Experimental parameters for AP-SMALDI analysis

For AP-SMALDI MSI measurements, the mass range was set to *m*/*z* 700-2,800 for 10 µm and 15 µm step size measurements and *m*/*z* 600-1,800 for 3 µm step size measurements, respectively. Measurements were performed in 2-D pixel mode[2] with 50 laser pulses per pixel at a wavelength of 343 nm. Capillary temperature was set to 250 °C and the S-lens was set to 100. For Q Exactive HF, the acceleration voltage was set to ±3 kV and for Q Exactive, the acceleration voltage was set to 2.5 kV.

Supplementary Note 2: Processing for statistical evaluation of AP-SMALDI MSI data

For statistical comparison the mean intensities per pixel were loaded into Perseus for each biological replicate (n=3). After a $\log_2$ transformation, a two-sided student's T-test was performed, were the ROIs of tissue sections including granulomas/eggs of bs-infected hamsters was compared to each of the remaining three groups (ROIs of liver tissue sections without granulomas/eggs of bs-infected hamsters, ROIs of liver tissue sections of ss- and non-infected hamsters).

Supplementary Note 3: Experimental parameters for HILIC MS/MS analysis

In short, solvent A consisted of acetonitrile/methanol (99/1, v/v) and solvent B of methanol/water (8/2, v/v), both with 5 mmol/L ammonium acetate. For injection, the pre-concentration setup was used with microliter-pickup injection. The sample injection volume was 1 µL. Further parameters are described in detail in the Table S2/S3.

Supplementary Note 4: Data Processing – nano-HILIC

For relative quantification of GSL species we chose SM 40:1;O2 as a endogenous reference, as no significant difference was observed between the three sample types in the nano-HILIC MS/MS data, where experiments with three technical replicates for each biological replicate (n=3) were conducted. As can be seen from the ion-image of SM 40:1;O2 shown in Figure S3 b, the signal was homogeneously distributed over the tissue but no signal was observed for the eggs. The .raw files were converted with msconvert to mzXML-files, which were uploaded in MZMine 2.33 and GSLs were identified based on our manually curated database. The coefficient of variation (CV) for each identified GSL was calculated for the pooled QC sample, which was measured five times as a technical replicate. The peak areas were used for the calculation of the CV. The resulting box plot for positive- and negative-ion mode data is shown in Figure S4. While a median close to 20% for the CV values for the positive-ion data indicates a sufficient reproducibility, a median close to 50% for the CV in the negative ion-mode should be optimized in further studies. Therefore, we decided to perform our relative quantification based on our positive-ion mode data. Here, the initial PCA plot including all biological and

technical replicates is shown in Figure S3 c. Based on optical evaluation, bs77_1, highlighted in the PCA plot, was excluded from further statistical analysis. The peak areas were used for relative quantification to the endogenous standard and mean and standard error were calculated in Excel. Data was uploaded in Perseus and the samples were categorially annotated into bs-, ss- and non-infected samples types. ANOVA tests with p-values of 0.05, 0.01 and 0.001 were used and significant different groups identified by a post hoc tests with an FDR of 0.05. Although no exogenous standards were utilized in this study, we believe that normalization to the endogenous species SM 40:1, which showed comparable peak areas throughout all sample types, provides a semi-quantitative statement. However, the use of exogenous internal standards would increase the precision of the semi-quantitative statements and would allow to move towards absolute quantification. Unfortunately, availability of deuterated GSL standards is very limited.

Supplementary Note 5: DHAP compared to DHB, CHCA, 9-AA and DAN

When comparing matrices regarding the number of annotations in positive-ion mode using LIPIDMAPS, we found 111 annotations for phospholipids and 1 triglyceride with DHAP matrix. For DHB and CHCA matrix, the number of annotations were 82 and 55 for phospholipids, and 0 and 1 for triglycerides, respectively. For the negative-ion mode, again more lipids were annotated with DHAP matrix (30 phospholipids, 11 SHex compounds) than with 9-AA (26 phospholipids, 11 SHex compounds) and DAN matrix (28 phospholipids, 10 SHex compounds).

Supplementary Table 1. Protocols for matrix application, sublimation parameters for DHAP and pneumatic spraying parameters for used matrices

Matrix	Parameters
DHAP	- oil bath 130 °C - cool finger -15 °C to -20 °C - duration 5 minutes
9-AA	-7 mg/mL -acetone/water 6/4 -5 µL/min -160 µL
DAN	- 3 mg/mL - methanol/water; 9/1; v/v -15 µL/min - 225 µL
DHB	- 30 mg/mL - acetone/water; 1/1; v/v + 0.1% TFA - 10 µL/min - 100 µL
CHCA	- 7 mg/mL - acetone/water; 1/1; v/v + 0.1% TFA - 10 µL/min - 110 µL

Supplementary Table 2: nano-HILIC Parameter used for separation of glycosphingolipids.

Property	Setting
Mobile Phase A	acetonitrile/methanol (99/1, v/v), 5 mM AmAc
Mobile Phase B	methanol/water (8/2, v/v), 5 mM AmAc
Loading Solvents	same as starting conditions
Injection volume	1 µL
Loading Time	0.5 minutes
Gradient	5% B for 5 minutes, to 100% B in 45 minutes, hold 100% B for 10 minutes, to 5% B in 5 minutes, hold 5% B for 55 minutes
Oven temperature	40 °C
Autosampler temperature	4 °C
Loading flow rate	30 µL/min
NC flow rate	300 nL/min

Supplementary Table 3: MS and MS/MS parameters (in brackets) used for identification of GSL after nano-HILIC separation

Parameter	Setting
Spray voltage	±1.9 kV
Capillary temperature	350 °C
S-lens setting	100
Mass resolution at m/z 200	120000 (45000)
MS AGC target	1000000 (100000)
MS max. injection time	100 ms (50 ms)
Scan range	*m*/*z* 600 - 2400
Top N	15
Isolation window Δ (*m*/*z*)	0.8
Stepped NCE	20;25;30
Dynamic exclusion	3.6 seconds

Supplementary Table 4: Glycosphingolipid species with mean intensities per pixel for each matrix. DHAP was evaluated in positive- and negative-ion mode. The other matrices were either evaluated in positive- (DHB, CHCA), or negative-ion mode (9-AA, DAN).

Species	DHAP (+)	DHB	CHCA	DHAP (-)	9-AA	DAN
HexCer 18:1;O2/18:0	$4.56 \cdot 10^2$	$3.44 \cdot 10^2$	$1.86 \cdot 10^2$			
HexCer 18:1;O2/20:0	$1.11 \cdot 10^2$	$7.69 \cdot 10^1$	$3.29 \cdot 10^1$			
HexCer 18:1;O2/22:0	$7.73 \cdot 10^2$	$6.46 \cdot 10^2$	$3.34 \cdot 10^2$			
HexCer 18:1;O2/24:1	$4.81 \cdot 10^3$	$4.01 \cdot 10^3$	$2.27 \cdot 10^3$			
GM1 18:1;O2/18:0				$7.44 \cdot 10^2$	$3.61 \cdot 10^2$	$1.90 \cdot 10^2$
GM2 18:1;O2/18:0				$8.19 \cdot 10^1$	$3.58 \cdot 10^1$	$1.24 \cdot 10^1$

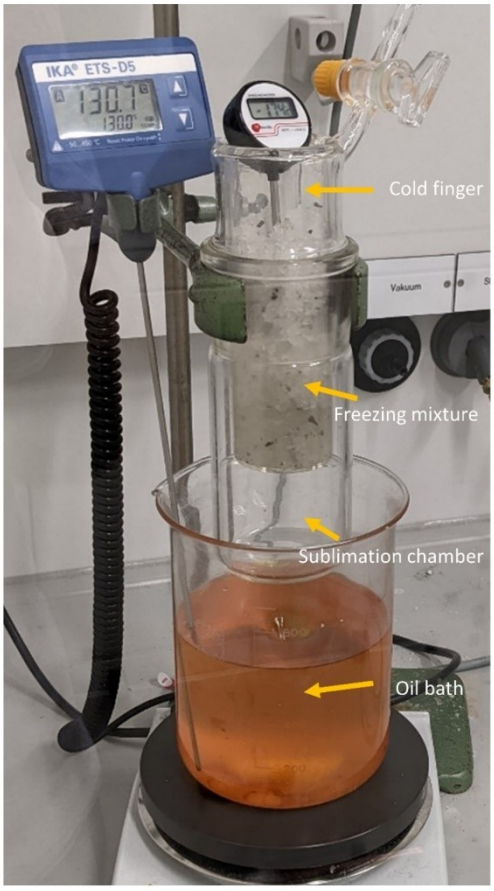

Figure S1: Sublimation apparatus. Arrows indicate the different components, namely the cold finger, the freezing mixture consisting of ice and salt, the sublimation chamber and the heated oil bath.

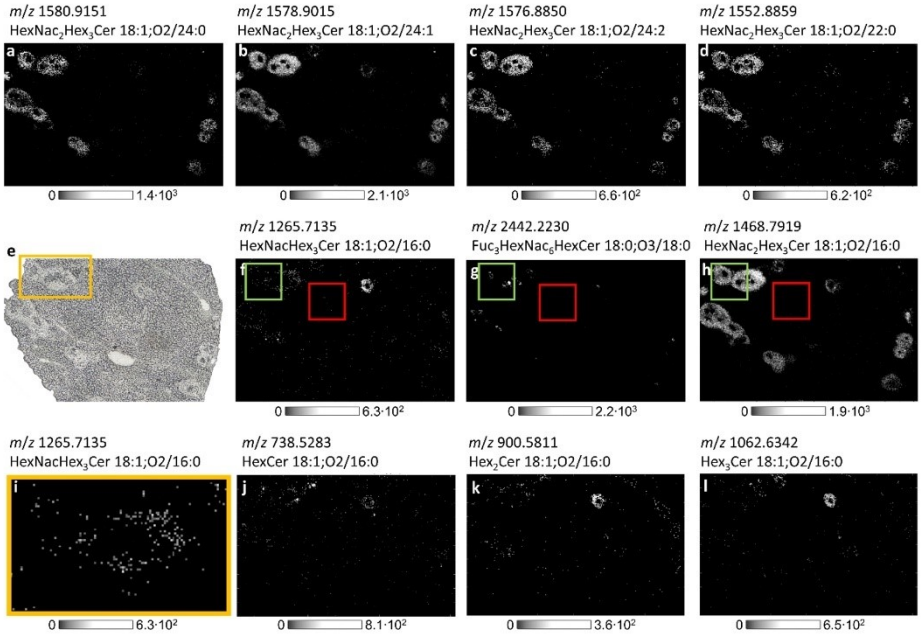

Figure S2: Various $HexNac_2Hex_3$ species with different ceramide compositions (top row + h), all representing the same spatial distribution as markers for most granulomas when compared to the corresponding microscopic image (e). Single-ion images (f-h) used for the RGB-overlay in Figure 2, showing $HexNacHex_3$Cer 18:1;O2/16:0 at *m/z* 1265.7135 (f), $Fuc_3HexNac_6$HexCer 20:0;O3/16:0 at *m/z* 2442.2230 (g), and $HexNac_2Hex_3$Cer 18:1;O2/16:0 at *m/z* 1468.7919 (h). The green area represents the ROI used for statistical evaluation of the liver of a bisex-infected hamster including morphologically changed tissue upon infection compared to healthy hepatic tissue. The red area represents the ROI of the bisex-infected sample without granulomas or eggs used as a control for semi-quantitative analysis. Magnification of the single-ion image representing the distribution of $HexNacHex_3$Cer 18:1;O2/16:0 at *m/z* 1265.7135 showing the granuloma area (i) highlighted by the orange square in the corresponding microscopic image. Ion images of HexCer 18:1;O2/16:0 at *m/z* 738.5283 (j), Hex_2Cer 18:1;O2/16:0 at *m/z* 900.5811 (k) and Hex_3Cer 18:1;O2/16:0 at *m/z* 1062.6342 (l), all showing a similar distribution as $HexNacHex_3$Cer 18:1;O2/16:0 at *m/z* 1265.7135 (f). All ion images are created from the potassium-adduct signal.

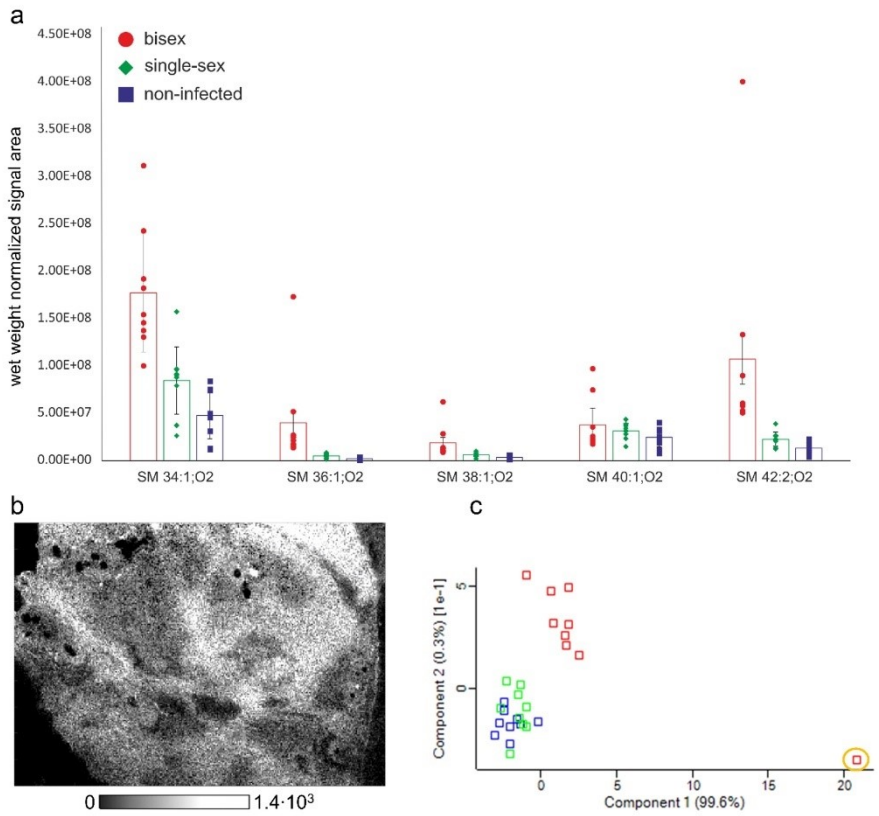

Figure S3: (a) Histograms for endogenous SM compounds showing the peak areas. Error bars indicate the standard deviation. (b) Representative ion-image of SM 40:1;O2 of a liver tissue section of a bs-infected hamster, indicating an almost homogenous distribution across the section with no signal for the eggs. (c) PCA plot including all three biological replicates with three technical replicates each for non-infected (blue), ss-infected (green) and bs-infected (red) GSL extracts based on nano-HILIC MS/MS data. The data point for bs77_1, highlighted by an orange circle, was not included in further statistical evaluation.

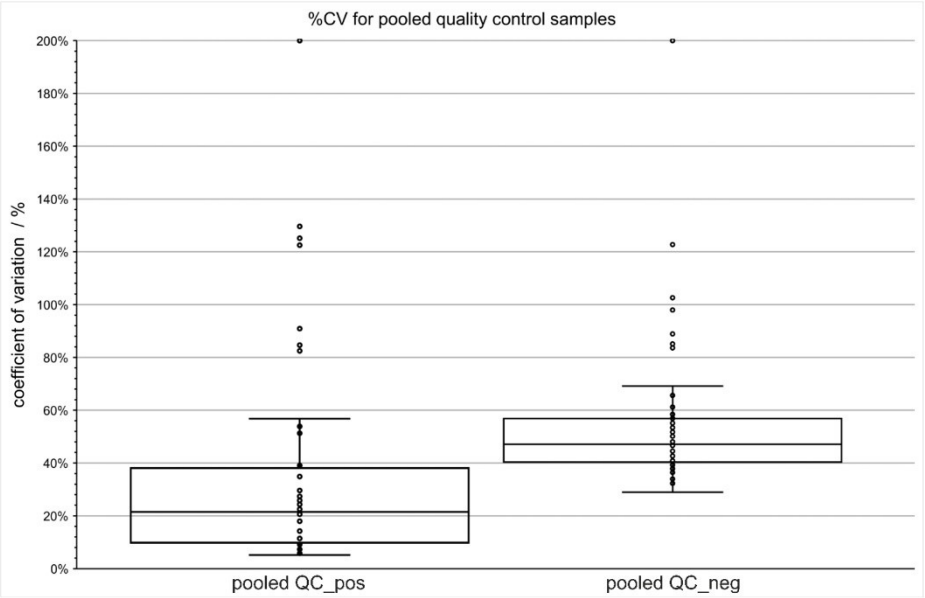

Figure S4: Box plot showing the coefficient of variation (CV). The %CV was calculated for each identified GSL species in positive- as well as negative-ion mode for the pooled QC sample, which was measured as a replicate five-times for each polarity.

I

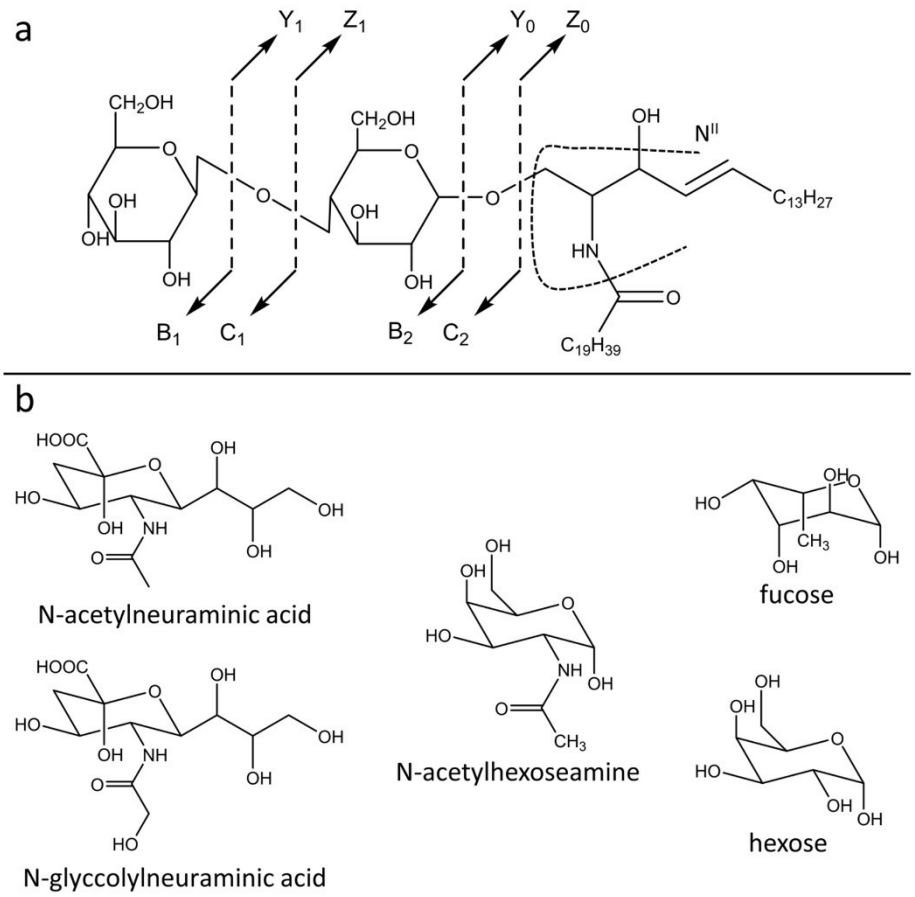

Figure S5: A GSL consisting of two monosaccharide units and a ceramide head group (a). Cleavage sites upon HCD fragmentation are indicated by dotted lines resulting in Y-, Z-, B, and C-fragment ions for the glyosidic cleavage of the saccharide units and the N^{II}-fragment ion for the sphingoid base. Nomenclature according to Domon and Costello[3] and Merrill et al.[4]. Different monosaccharide units, which can be discriminated by tandem mass spectrometry (b) showing NeuAc, NeuGc, HexNac, Fuc and Hex as the saccharides reported in this article.

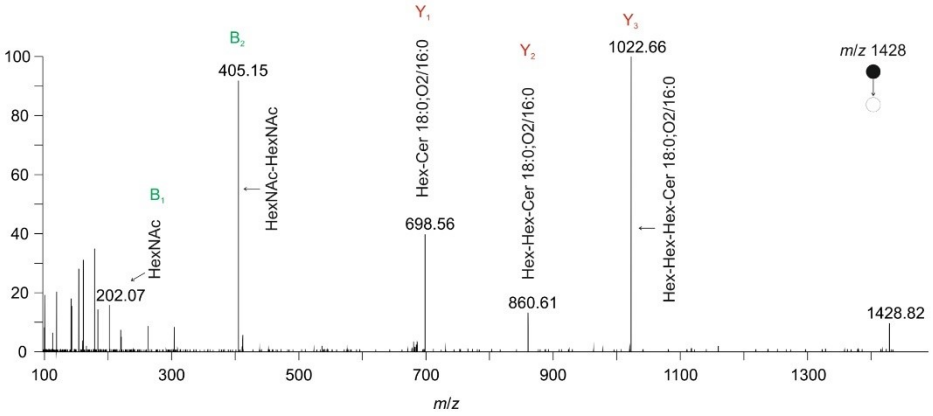

Figure S6: Tandem MS of [$HexNac_2Hex_3Cer$ 18:1;O2/16:0 – H]$^-$ with specific fragment ions. B_1- and B_2-fragments for glyosidic cleavage by HCD beginning at the saccharide head-group, and Y_1-, Y_2- and Y_3-fragments for glyosidic cleavage by HCD counting from the ceramide-backbone are indicated. Fragment ion nomenclature according to Domon and Costello.[3]

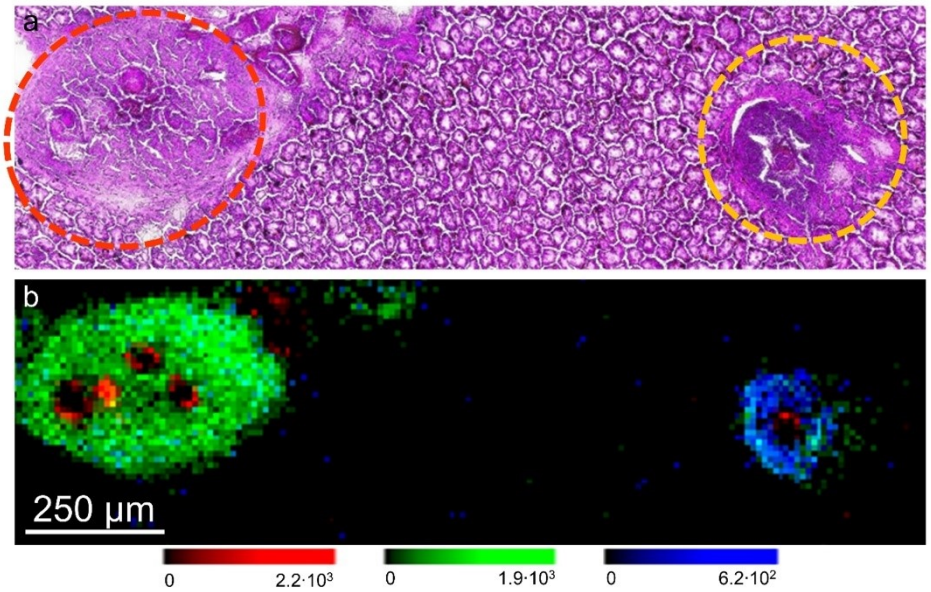

Figure S7: H&E-staining (a) of the tissue after AP-SMALDI MSI measurement showing two granulomas, one highlighted with a red-dotted circle and the other with an orange-dotted circle, respectively. Corresponding RGB image (b), showing $Fuc_3HexNac_6HexCer$ 20:0;O3/16:0, $[M+K]^+$, at *m/z* 2442.2230 in red, $HexNac_2Hex_3Cer$ 18:1;O2/16:0, $[M+K]^+$, at *m/z* 1468.7919 in green and $HexNacHex_3Cer$ 18:1;O2/16:0, $[M+K]^+$, at *m/z* 1265.7135 in blue.

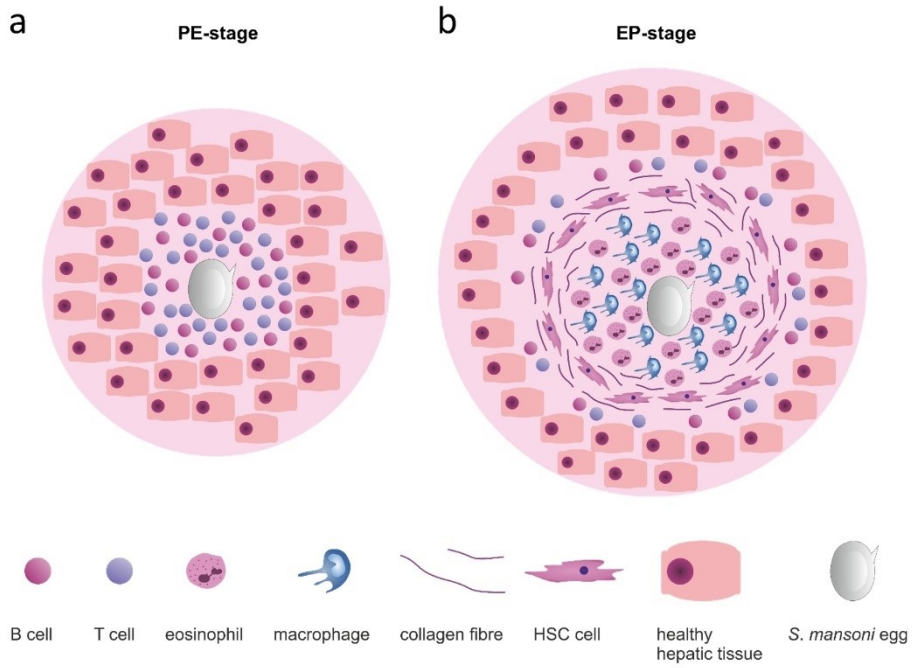

Figure S8: (a) Granuloma model of the pre-granulomatous exudative (PE) stage (a) with B and T cells surrounding the *S. mansoni* eggs. (b) Granuloma model of the exudative-productive (EP) stage, representing a highly ordered structure with eosinophils and macrophages as the inner layer around the egg, surrounded by collagen fiber and hepatic stellate cells as a middle layer and with B and T cells as the outer layer. In both granuloma stages, cell types with low abundance are not included in the model.

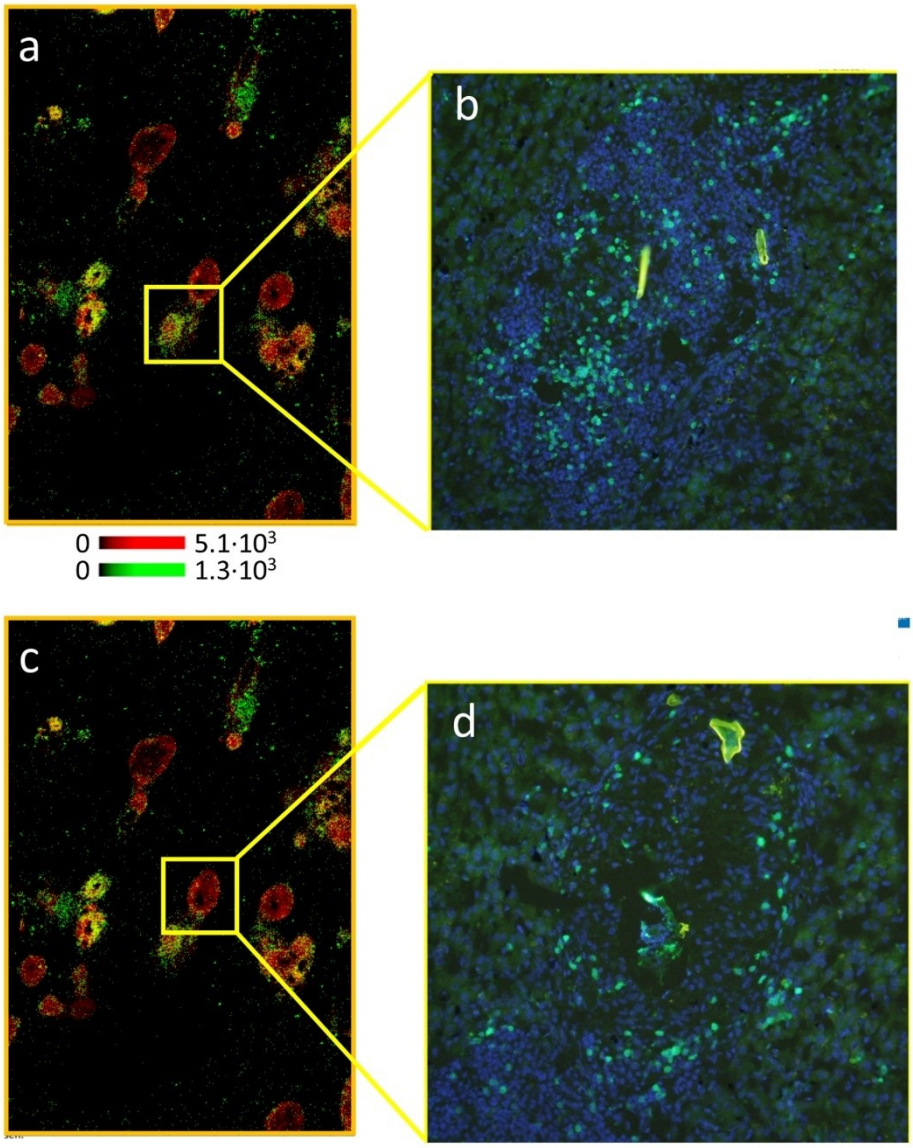

Figure S9: Red-green overlay images showing $HexNac_2Hex_3Cer$ 18:0,O2/16:0 at *m/z* 1468.7925 as $[M+K]^+$ in red and $HexNacHex_3Cer$ 18:0,O2/16:0 at *m/z* 1265.7131 as $[M+K]^+$ in green (a,c same section). Corresponding immunohistochemistry experiments with CD3 staining (green) and DAPI (blue) of the neighboring section of the AP-SMALDI measurement (b,d).

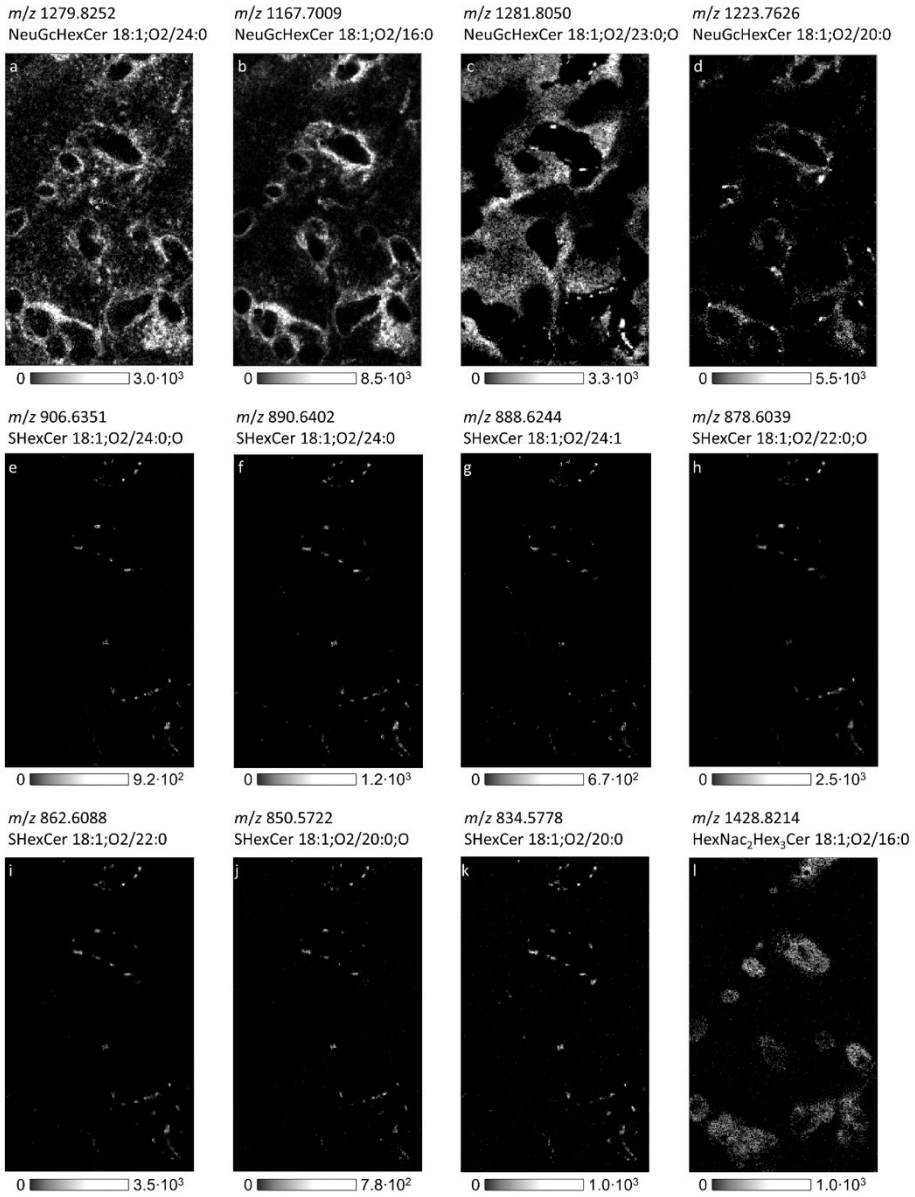

Figure S10: AP-SMALDI MS images of GSLs obtained in negative-ion mode as $[M-H]^-$. (a-d) NeuGcHexCer compounds with different ceramide compositions, showing distinguishable distributions. (e-k) SulfoHex compounds with different ceramides backbones, all showing similar distributions with accumulations at the outer surface of granulomas. (l) Neutral GSL $HexNac_2Hex_3Cer$ 18:1;O2/16:0. The corresponding microscopic image is shown in Figure 3a.

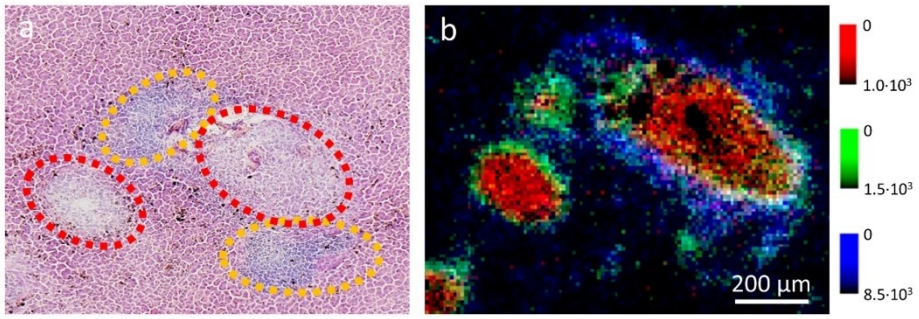

Figure S11. (a) H&E-stained liver tissue section of a bs-infected hamster after AP-SMALDI measurement. Granulomas are highlighted with red-dotted circles. Assumed accumulation of immune cells is highlighted with orange-dotted circles. (b) Corresponding RGB overlay image with $NeuGcHex_2Cer$ 18:0;O2/20:0 in blue, $NeuAcHex_2Cer$ 18:0;O2/16:0 in green and $HexNac_2Hex_3Cer$ 18:0;O2/16:0 in red.

References

(1) Meyer, S.; van Liempt, E.; Imberty, A.; van Kooyk, Y.; Geyer, H.; Geyer, R.; van Die, I. DC-SIGN Mediates Binding of Dendritic Cells to Authentic Pseudo-LewisY Glycolipids of Schistosoma mansoni Cercariae, the First Parasite-specific Ligand of DC-SIGN, *J. Biol. Chem.* 2005, 280, 37349-37359.

(2) Müller, M. A.; Kompauer, M.; Strupat, K.; Heiles, S.; Spengler, B. Implementation of a High-Repetition-Rate Laser in an AP-SMALDI MSI System for Enhanced Measurement Performance, *J. Am. Soc. Mass Spectrom.* 2021, 32, 465-472.

(3) Domon, B.; Costello, C. E. A systematic nomenclature for carbohydrate fragmentations in FAB-MS/MS spectra of glycoconjugates, *Glycoconjugate J.* 1988, 5, 397-409.

(4) Merrill, A. H.; Sullards, M. C.; Allegood, J. C.; Kelly, S.; Wang, E. Sphingolipidomics: high-throughput, structure-specific, and quanti-tative analysis of sphingolipids by liquid chromatography tandem mass spectrometry, *Methods* 2005, 36, 207-224.

Chapter III

Glycolipidomics of Liver Flukes and Host Tissues during Fascioliasis: Insights from Mass Spectrometry Imaging

David Luh[1], Parviz Ghezellou[1], Sven Heiles[2,3], Svenja Gramberg[4], Simone Haeberlein[4] and Bernhard Spengler[1,*]

[1]Institute of Inorganic and Analytical Chemistry, Justus Liebig University Giessen, 35392 Giessen, Germany

[2]Leibniz-Institut für Analytische Wissenschaften - ISAS - e.V., 44139 Dortmund, Germany

[3]Lipidomics, Faculty of Chemistry, University of Duisburg-Essen, 45141 Essen, Germany

[4]Institute of Parasitology, Biomedical Research Center Seltersberg (BFS), Justus Liebig University Giessen, 35392 Giessen, Germany

ACS Infect. Dis. **2024**, 10 (12), 4233-4245

doi:10.1021/acsinfecdis.4c00551

Supporting information: https://pubs.acs.org/doi/10.1021/acsinfecdis.4c00551#_i24

ACS Infectious Diseases

pubs.acs.org/journal/aidcbc

Article

Glycolipidomics of Liver Flukes and Host Tissues during Fascioliasis: Insights from Mass Spectrometry Imaging

David Luh, Parviz Ghezellou, Sven Heiles, Svenja Gramberg, Simone Haeberlein, and Bernhard Spengler*

Cite This: *ACS Infect. Dis.* 2024, 10, 4233−4245

Read Online

ACCESS | Metrics & More | Article Recommendations | Supporting Information

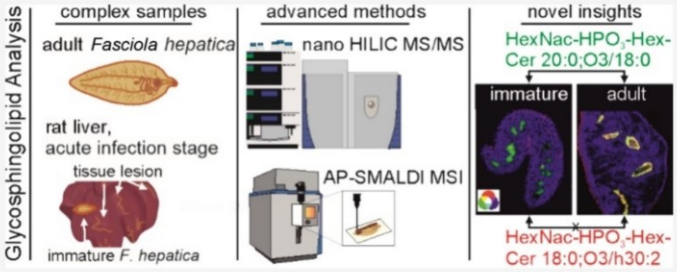

ABSTRACT: Fascioliasis, a zoonotic disease caused by liver flukes of the genus *Fasciola*, poses significant health threats to both humans and livestock. While some infections remain asymptomatic, others can lead to fatal outcomes, particularly during the acute phase characterized by the migration of immature parasites causing severe liver damage. Through the combination of data acquired via high-spatial-resolution atmospheric-pressure scanning microprobe matrix-assisted laser desorption/ionization mass spectrometry imaging (AP-SMALDI MSI) and nanohydrophilic interaction chromatography tandem mass spectrometry, we investigated glycosphingolipids (GSLs) in both adult and immature parasite stages as well as the host liver and bile duct to unravel the intricacies of the host−pathogen interplay and associated pathology. Several GSLs showed characteristic distribution patterns within the parasite depending on the fatty acid composition of their ceramides, notably including GSLs carrying very long-chain fatty acids. Additionally, GSL compositions within the tegument of immature versus adult parasites varied, suggestive of tissue remodeling upon maturation. AP-SMALDI MSI further enabled the identification of GSLs potentially involved in *in vivo* interactions between the host and immature parasites. Moreover, our experiments unveiled alterations in other lipid classes during *Fasciola* infection, providing a broader understanding of lipidomic changes associated with the disease. Collectively, our findings contribute to a deeper comprehension of the molecular intricacies underlying fascioliasis, with a specific focus on GSLs.

KEYWORDS: *host−pathogen interactions, trematodes, Fasciola hepatica, glycosphingolipids, high-resolution MALDI mass spectrometry imaging, nanoscale liquid chromatography*

Fascioliasis is a foodborne trematode infection affecting livestock, resulting in huge economic losses.[1] This zoonotic infection also poses a threat to human health, with an estimated 2.4 million people affected worldwide.[2] Although classified as a neglected tropical disease (NTD) by the world health organization (WHO), fascioliasis is prevalent on all inhabited continents.

Fasciola (*F.*) spp. have a complex life cycle, which includes an intermediate snail host and a mammalian final host (sheep, cattle, and humans among others). The final host is infected by ingestion of encysted larvae (metacercariae), attached to vegetation or floating in water. Within the intestine, newly excysted juveniles hatch from the cysts and penetrate the intestinal wall to reach the liver. There, the immature worms migrate through and feed on the liver tissue until they have grown into adult (mature) flukes. Adults reside within the bile duct.[3]

The migration of immature parasites through the liver parenchyma during the acute stage of infection is causing most of the pathogenesis.[3] Tissue damage can be caused mechanically or by digestive enzymes of the parasite and also by inflammatory reactions of the host.[3] The severity of

Received: July 13, 2024
Revised: September 18, 2024
Accepted: September 20, 2024
Published: November 7, 2024

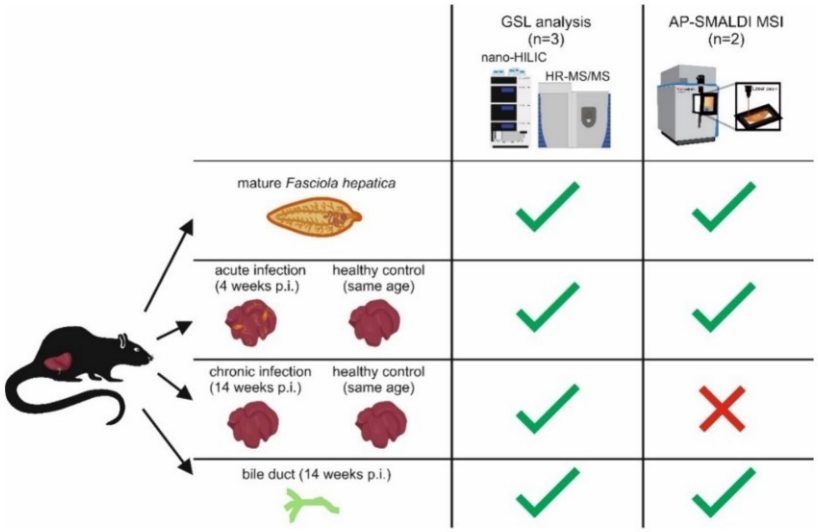

Figure 1. Overview of the study workflow. Adult *F. hepatica*were subjected to glycosphingolipid analysis, using nano-HLIIC MS/MS and AP-SMALDI MSI techniques. Rats were used as a model system for *F. hepatica* infection. Livers were collected 4 weeks post infection and 14 weeks post infection, representing the acute and chronic infection stage. For both stages, livers of uninfected rats of the same age served as control samples. In addition to noninfected controls, the bile duct of the chronic infection stage was also isolated and used for comparative glycosphingolipidome analysis using nano-HILIC MS/MS experiments. Furthermore, AP-SMALDI measurements were performed for rat livers at the acute infection stage and their corresponding control as well as bile duct samples. For chronic infection, tissue sections of rat livers were not subjected to AP-SMALDI analysis. "Tick" and "cross" indicate whether measurements were performed or not performed, respectively.

symptoms (fever, anemia, weight loss, abdominal pain, and death) as well as the extent of liver damage varies depending on the number of parasites, the host's immune response, and other factors.[4] In parallel, mechanisms of liver regeneration and repair are initiated, which may either restore liver function or lead to liver fibrosis and cirrhosis in severe cases.[5] The chronic stage of infection, marked by adult worms present in the bile ducts, is often asymptomatic but can also be associated with signs of biliary obstruction and abdominal pain. Fascioliasis is mainly treated with triclabendazole, which is effective against adult and juvenile worms. However, emerging resistance against the drug necessitates the search for novel treatments.[6,7] Understanding the fundamental biology of the parasite and the host immune response is therefore required.

The generation of comprehensive omics data sets for *Fasciola* spp. has accelerated the study of key molecules involved in the biology, pathogenicity, and virulence of liver flukes and has opened new avenues for the development of novel control strategies.[8] For *Fasciola hepatica* (*F. hepatica*), it has been shown that there are clear differences in the excreted proteins during the developmental stages of the parasites.[9,10] Furthermore, glycans from adult *F. hepatica* and recently from newly excysted juveniles were studied for their influence on the host immune response.[11,12] For example, Rodríguez et al. demonstrated by comparison of lectin assays from *F. hepatica* glycans and their corresponding oxidized glycans (without function) that specific glycan components of *F. hepatica* are relevant for the release of interleukin 4 and 10.[11] The huge variability of N- and O-glycans from newly excysted juveniles, recently analyzed by de Marco Verissimo et al. using liquid chromatography electrospray tandem mass spectrometry (LC ESI MS/MS), provides the fundamental to elucidate the role of glycans during the migratory phase of the parasite.[12] However, limited data are available for glycosphingolipids (GSLs), a molecular class known to be generally involved in the host immune response.[13−15] Studies from Wuhrer et al. utilizing several analytical methods, such as high-performance thin-layer chromatography, matrix-assisted laser desorption/ionization (MALDI) time-of-flight mass spectrometry (MS), ESI MS, immunostaining, and NMR analysis, suggest high antigenicity of GSLs from adult *F. hepatica* as well as a mimicry of mammalian glycosphingolipids.[16−18] However, there is a lack of information about the localization of these glycosphingolipids, and no information about GSLs from the immature stage or from the host is available. In addition, *in situ* studies on parasites in the host tissue that examined the lipidome are rare.

Mass spectrometry is often utilized to study the molecular composition of biological samples. Coupled with separation methods like LC, even complex biological mixtures can be comprehensively analyzed. However, tissue regional information or cell-specific biomolecular alterations are not available from MS-based bulk analyses. For this purpose instead, mass spectrometry imaging (MSI) and most prominently MALDI MSI enable visualization of localized biomolecular events.[19,20] Here, the local information on hundreds to thousands of intact biomolecules can be obtained simultaneously during a nontargeted analysis. Improvements over the past years now routinely facilitate MALDI MSI analyses with a <10 μm spatial resolution.[21] A more advanced setup even enables a spatial resolution down to 1.4 μm, moving forward to routine single-cell analysis.[22]

https://doi.org/10.1021/acsinfecdis.4c00551
ACS Infect. Dis. 2024, 10, 4233−4245

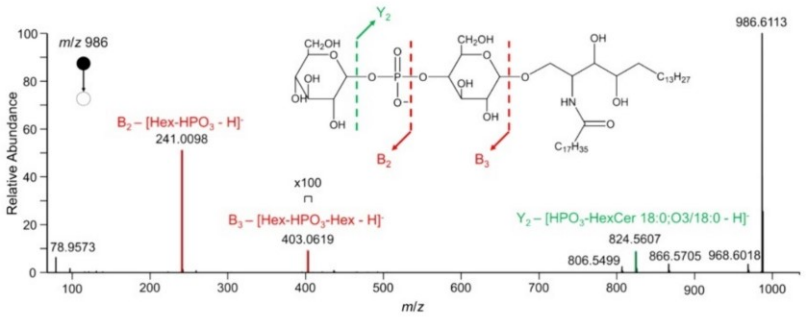

Figure 2. Tandem mass spectrum for Hex-HPO_3-Hex-Cer 18:0;O3/18:0 ($[M-H]^-$ at m/z 986.6113). The fragment ion at m/z 241.0098 represents the B_2-fragment ion. The fragment ion at m/z 403.0619 corresponds to the B_3-fragment ion. The fragment ion at m/z 824.5607 corresponds to the Y_2-fragment ion.

By a combination of MALDI MSI and reversed-phase LC tandem MS/MS (RP-LC MS/MS), the lipidome can be elucidated in detail. In addition, the combination with state-of-the-art nanohydrophilic interaction chromatography (nano-HILIC) MS/MS recently allowed us to globally and locally profile the GSLs of livers from *Schistosoma mansoni*-infected hamsters. Thereby, we revealed several GSLs potentially involved in immune response.[23]

In this study, we combined MALDI MSI and chromatography data to analyze various aspects of fascioliasis at the lipidomic level in depth. In this way, we hope to contribute to the fundamental understanding of the infection. For this purpose, different sample types from our rat model of both the chronic and acute infection stage were analyzed. A particular focus was set on the analysis of GSLs. The diversity of GSL species identified highlights a possible role during infection. We show that it is necessary to elucidate the structure of the GSLs at the molecular level as well as their distributions in the organism in order to propose new hypotheses. Additionally, state-of-the-art atmospheric-pressure scanning microprobe matrix-assisted laser desorption/ionization (AP-SMALDI) MSI experiments enabled an investigation of *in vivo* host–parasite interactions on a lipidomic level during the acute infection stage. We provide novel data, which can help to elucidate a small part of the complex interplay between the parasite and the host.

■ RESULTS AND DISCUSSION

Study Design. To comprehensively investigate the GSLs in isolated adult *F. hepatica* and parasites within the host organ, we employed nano-HILIC MS/MS and AP-SMALDI MSI. For the experiments, rat was used as an animal model. For global GSL characterization, nano-HILIC MS/MS was used, and the resulting curated databases guided AP-SMALDI MSI investigations. In order to study different stages of *F. hepatica* infection, livers after 4 weeks and after 14 weeks of infection were compared to control tissues (Figure 1). To minimize confounding variables of the control tissue, appropriate control samples with the same age of the rats, which were kept under the same conditions, were selected for the acute and chronic infection, respectively. These conditions were meant to probe the lipid composition during the acute (4 weeks) and chronic (14 weeks) infection phase in which *F. hepatica* are immature and adult, respectively. In addition, AP-SMALDI MSI measurements were performed with tissue sections of the rat liver during acute infection, which included migrating immature *F. hepatica* to examine *in vivo* host–parasite interactions. In the Supplementary Note 7 and Figure S1, we offer a detailed description of several different tissue areas in the liver of rats during the acute infection stage. As *F. hepatica* reside in bile ducts after maturation, no AP-SMALDI MSI of the liver from the chronic infection phase was performed, but MS imaging of isolated bile ducts was conducted. Three and two biological replicates were analyzed by nano-HILIC MS/MS and AP-SMALDI MSI measurements, respectively.

Glycosphingolipids in Isolated Adult *F. hepatica* Parasites. To benchmark our nano-HILIC MS/MS method for parasites, we compared its performance on isolated adult *F. hepatica* with the GSL annotations reported for adult *F. hepatica* in previous studies, which were isolated without further *in vitro* incubation.[16−18] We found that our GSL profile for neutral GSLs closely aligns with the species reported previously, with almost the same saccharide compositions and the same ceramide moieties identified (Table S11). This is an important indication that the short *in vitro* incubation of our isolated *F. hepatica* does not seem to profoundly affect the GSL profile. Apart from Hex_1Cer, Hex_2Cer, Hex_3Cer, and Hex_5Cer species, we also identified the presence of Hex_6Cer species. Furthermore, our analysis was extended to intact GSLs, including the more intricate GSL-like $Hex_{3-4}HexNac_{2-7}Cer$, as listed in Table S11. For GSLs, variations in the ceramide backbone compositions were observed. We detected several phytosphingosines, but also, octadecasphinganine was consistently detected as part of the ceramide moiety in the GSLs throughout this study (Table S11). Notably, an *F. hepatica*-specific phosphate-containing GSL, a GlcNacα1-HPO_3-6Gal-(1−1) ceramide, with 14 different ceramide compositions, was identified as described by Wuhrer et al.[17] In total, our analysis unveiled 35 GSL species containing a phosphate group, including various HPO_3-Hex-Cer species with diverse ceramide backbones (a representative tandem mass spectrum is shown in Figure S2). In addition, we described for the first time the GSL Hex-HPO_3-Hex-Cer for *F. hepatica*, with a representative tandem mass spectrum for this identified species being showcased in Figure 2. Fragment ions for this species are highlighted, such as the B_2 and B_3 ion with m/z 241.0098 and m/z 403.0619, respectively. Together with the Y_2 ion (m/z 824.56070), we were able to determine the sequence. In

https://doi.org/10.1021/acsinfecdis.4c00551
ACS Infect. Dis. 2024, 10, 4233−4245

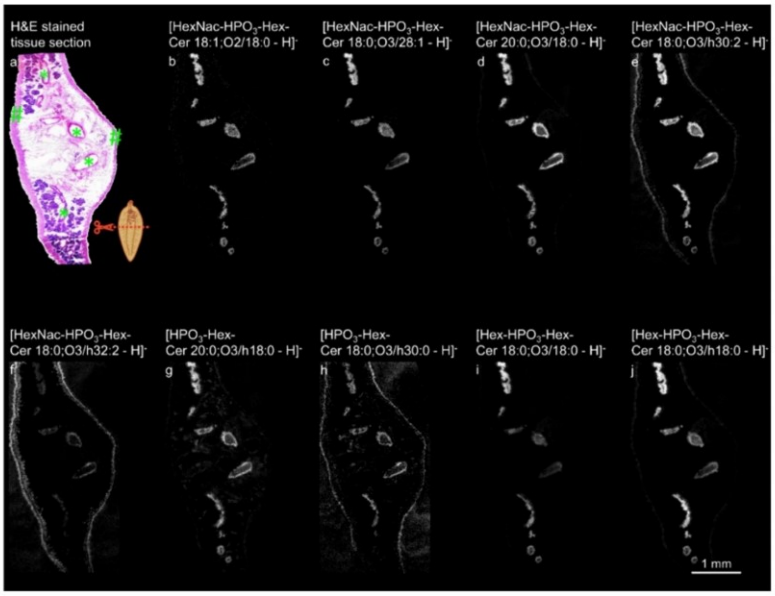

Figure 3. Spatial distributions of phosphate-containing glycosphingolipids in a cross section of adult *F. hepatica*. (a) Hematoxylin and eosin (H&E) staining of an *F. hepatica*transversal section after AP-SMALDI MSI measurement. The *F. hepatica* pictogram illustrates the transverse sectional plane. Intestines are signed with asterisks and the tegument with hashes. (b) Single-ion image of HexNac-HPO_3-Hex-Cer 18:1;O2/18:0 ($[M\text{-}H]^-$ at m/z 1009.6349). (c) Single-ion image of HexNac-HPO_3-Hex-Cer 18:0;O3/28:1 ($[M\text{-}H]^-$ at m/z 1165.7861). (d) Single-ion image of HexNac-HPO_3-Hex-Cer 20:0;O3/18:0 ($[M\text{-}H]^-$ at m/z 1055.6769). (e) Single-ion image of HexNac-HPO_3-Hex-Cer 18:0;O3/h30:2 ($[M\text{-}H]^-$ at m/z 1207.8279). (f) Single-ion image of HexNac-HPO_3-Hex-Cer 18:0;O3/h32:2 ($[M\text{-}H]^-$ at m/z 1235.8279). (g) Single-ion image of HPO_3-Hex-Cer-20:0;O3/h18:0 ($[M\text{-}H]^-$ at m/z 868.5921). (h) Single-ion image of HPO_3-Hex-Cer-18:0;O3/h30:0 ($[M\text{-}H]^-$ at m/z 1008.7822). (i) Single-ion image of Hex-HPO_3-Hex-Cer 18:0;O3/18:0 ($[M\text{-}H]^-$ at m/z 986.6187). (j) Single-ion image of Hex-HPO_3-Hex-Cer 18:0;O3/h18:0 ($[M\text{-}H]^-$ at m/z 1002.6136). The AP-SMALDI MSI measurement was performed with a 10 μm step size.

comparison to the previously described GlcNacα1-HPO_3-6Gal(1−1) ceramides, the newly discovered GSLs differ in the terminal saccharide unit.

Distribution Patterns of Different Glycosphingolipids in Adult *F. hepatica*Parasites. To spatially map these GSLs within the tissue, we employed AP-SMALDI MSI experiments in negative-ion mode, making use of the GSLs identified by nano-HILIC MS/MS. This approach was sensitive enough to facilitate the visualization of 30 out of the 35 phosphate-containing GSLs. For the remaining five GSL species, the abundance was too low to image the ion signal of these species. Figure 3 illustrates representative examples, emphasizing diverse compositions of GSLs showing different distribution patterns.

Three GSLs (saccharide composition HexNac-HPO_3-Hex) associated with the ceramide composition Cer 18:1;O2/18:0 ($[M\text{-}H]^-$ at m/z 1009.6349), Cer 18:1;O3/28:1 ($[M\text{-}H]^-$ at m/z 1165.7861), and Cer 20:0;O3/18:0 ($[M\text{-}H]^-$ at m/z 1055.6769) were predominately found concentrated across the intestine (Figure 3b−d). In contrast, the species HexNac-HPO_3-Hex-Cer 18:0;O3/h30:2 ($[M\text{-}H]^-$ at m/z 1207.8279 and HexNac-HPO_3-Hex-Cer 18:0;O3/h32:2 ($[M\text{-}H]^-$ at m/z 1235.8279) exhibited a distribution encompassing both the intestine and tegument of *F. hepatica* (Figure 3e,f). GSLs HPO_3-Hex-Cer-20:0;O3/h18:0 ($[M\text{-}H]^-$ at m/z 868.5921) and HPO_3-Hex-Cer-18:0;O3/h30:0 ($[M\text{-}H]^-$ at m/z 1008.7822) had distribution patterns similar to the previously mentioned two species (Figure 3g,h). Regarding the new head group composition Hex-HPO_3-Hex, two GSLs, Hex-HPO_3-Hex-Cer 18:0;O3/18:0 ($[M\text{-}H]^-$ at m/z 986.6187) and Hex-HPO_3-Hex-Cer 18:0;O3/h18:0 ($[M\text{-}H]^-$ at m/z 1002.6136), were identified. Their spatial distributions are depicted in Figure 3i,j. Both species showed a prominent accumulation in the intestine, and the latter was also detected in the tegument.

These findings underscore the importance of assessing GSL distributions at a molecularly intact level without ceramide moiety cleavage, different from common practice in a previous study.[24] Our results suggest that the phosphate-containing GSLs can be categorized into two groups, based on the contained fatty acids (FAs)—hydroxylated and nonhydroxylated FAs. While the former group exhibited a distribution spanning both the intestine and tegument, the latter was predominantly found in the intestine. This indicates a potential relevance of the hydroxylated fatty acid for the host−parasite interaction. The location of nonhydroxylated fatty acids of phosphate-containing GSLs may reflect the specific lipid metabolism of the parasite, including the modification and utilization of FAs in its intestine. A study by Wuhrer and coworkers reported that trihexosylceramides of *Fasciola gigantica* (*F. gigantica*), containing dihydroxylated ceramides, exhibited the strongest recognition to the Shiga toxin B1 subunit, which is known to bind to Gb_3 species. In contrast, the Shiga toxin B1

https://doi.org/10.1021/acsinfecdis.4c00551
ACS Infect. Dis. 2024, 10, 4233−4245

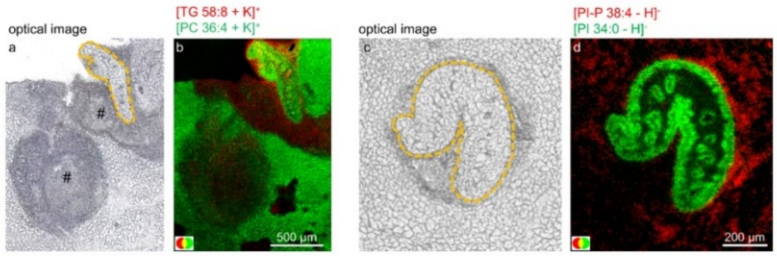

Figure 4. Lipidomics analysis of the rat liver infected with *F. hepatica*at the acute infection stage. (a) Optical image before AP-SMALDI MSI analysis of a rat liver tissue section during the acute infection stage. The outline of the migrating *F. hepatica*is emphasized with an orange dotted line, and tissue lesions are highlighted by a hash. (b) Positive-ion RG-overlay image corresponding to the optical image (a), showing TG 58:8 ($[M+K]^+$ at m/z 969.7308) in red and PC 36:4 ($[M+K]^+$ at m/z 820.5253) in green. (c) Optical image before AP-SMALDI MSI analysis of a rat liver tissue section during the acute infection stage. The outline of the migrating *F. hepatica*is emphasized with an orange dotted line. (d) Negative-ion RG-overlay image corresponding to (h), showing PI−P 38:4 ($[M-H]^-$ at m/z 869.5549) in red and PI 34:0 ($[M-H]^-$ at m/z 837.5499) in green. AP-SMALDI MSI measurements in this figure were performed with a 7 μm step size.

subunit only exhibited a weak binding to trihexosylceramides with tri- and tetrahydroxylated ceramides of *F. gigantica*, which were dominant in their LC fractions.[16] This supports our hypothesis that the ceramide moiety potentially plays a role in GSL function.

Moreover, we identified very long-chain fatty acids (VLCFA), with up to 32 carbon atoms incorporated into phosphate-containing GSLs. Next, we conducted AP-SMALDI MSI experiments in positive-ion mode with adult *F. hepatica*, to determine whether the spatial distributions of neutral GSLs exhibit a similar ceramide dependence. In general, we noted a predominant distribution of mono- or trihexoses across the tegument and intestine. Among the visualized compounds, GSL species with a VLCFA as part of the ceramide were found accumulated in the tegument, as exemplarily shown in Figure S3. While the function of these atypical FAs in *F. hepatica* is unknown, we may learn from their role in mammals. For example, ceramides with VLCFA are known to be important for the permeability integrity of the epidermis in mammals, with disorders leading to skin barrier defects.[25,26] Therefore, incorporating GSL with different ceramides into the glycocalyx might represent a protective mechanism for the parasite.

As *F. hepatica* is not capable of *de novo* FA synthesis, these VLCFA must either be taken up from the host, or produced by the parasite via FA elongation.[27] We were able to identify four elongase genes in the *F. hepatica* genome (D915_006030, D915_002071, D915_002072, and D915_004203), which supports the mechanism of chain elongation by the parasite. The tissue types showing expression of three of these genes were identified with the help of our spatial transcriptome of adult *F. hepatica* (Figure S4a).[28] The elongases D915_006030 and D915_002072 were detected across several different tissue types with the strongest expression in the tegument, as shown in Figure S4b. Future knockdown or inhibitor experiments might reveal if there is a direct connection between the expression of these genes and the presence of the VLCFA in GSLs.

The curated GSL database for adult *F. hepatica* was subsequently utilized to investigate the local distributions of GSLs of migrating *F. hepatica* in the liver parenchyma, which cause most of the pathogenesis.

AP-SMALDI MSI Reveals the Presence of Plasmalogen Phospholipids at the Host−Parasite Interface. To study acute infection and effects of parasite migration, tissue sections of the rat liver harboring migrating *F. hepatica* (Figure 4a,c) were evaluated on the lipid level first before investigating GSL distributions. Lipids are well-known indicators for parasite and tissue anatomy and molecular interactions and are easily accessible in AP-SMALDI MSI experiments.[29−31] As illustrated in the MS image in Figure 4b in red, the triacylglyceride (TG) 58:8 ($[M+K]^+$ at m/z 969.7308) exemplifies an upregulated lipid, appearing more abundant in areas of tissue lesions compared to healthy rat liver controls (Figure S5c). This observed trend extended across various species annotated as TGs, as illustrated in Figure S6. This aligns with our supporting semiquantitative RP-LC MS/MS data, which are described in Supplementary Note 8, indicating an upregulation of TGs in acutely infected rat livers (Figure S7). This observation is congruent with the literature, associating TGs with energy supply during tissue repair.[32] Additionally, TGs seem to be higher in abundance in the tissue lesion surrounding the migrating *F. hepatica* compared to the other tissue lesion. This accumulation of TGs can potentially be explained with *F. hepatica* inducing oxidative stress,[33] which in general can lead to the accumulation of triglycerides.[34]

In contrast, phosphatidylcholine (PC) 36:4 ($[M+K]^+$ at m/z 820.5253) shown in Figure 4b in green exhibits decreased abundance in the regions impacted by tissue lesions compared to the surrounding healthy tissue but was found to be homogeneously distributed in the liver tissue of healthy control rats (Figure S5b). Here, our supporting RP-LC MS/MS data again align with this observation, with several phospholipids being significantly decreased in the rat liver in the acute infection stage compared to the control (Figure S7). The observed decrease in phospholipids concurs with the established enzymatic activity of *F. hepatica:* phospholipases in the tegument, vomitus, or secretions produce free FAs.[6,7] As the parasite cannot synthesize fatty acids *de novo*,[35] degrading phospholipids in the liver tissue can prove beneficial. By this, the amount of small building blocks, which are taken up through the tegument, like free FAs as well as phospholipid headgroups such as choline, can be increased.

Beyond the unique distribution of lipids in healthy hepatic tissues or lesions, a subset of lipids exhibited elevated abundances at the host−parasite interface. For example, PI−P 38:4 ($[M-H]^-$ at m/z 869.5549) in Figure 4d in red showed

https://doi.org/10.1021/acsinfecdis.4c00551
ACS Infect. Dis. 2024, 10, 4233−4245

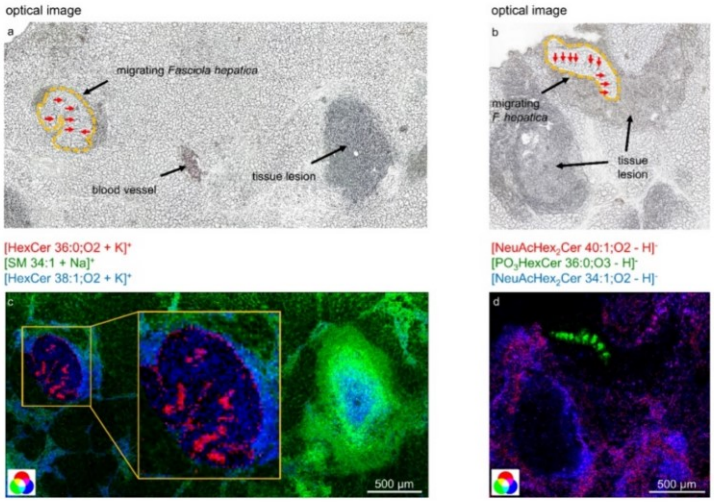

Figure 5. Glycosphingolipids characteristic of the rat liver infected with *F. hepatica*at the acute infection stage. (a,b) Optical images of liver tissue sections of rats during the acute infection stage. The outlines of the migrating parasites are emphasized with an orange dotted line, and the intestine is indicated by red arrows. (c) Positive-ion AP-SMALDI RGB-overlay image corresponding to (a) Hex-Cer 36:0;O2 ($[M+K]^+$ at m/z 768.5750) in red, SM 34:1 ($[M + Na]^+$ m/z 725.5568) in green, and Hex-Cer 38:1;O2 ($[M+K]^+$ m/z 794.5907) in blue. The measurement was performed with a 10 μm step size. (d) Negative-ion AP-SMALDI RGB-overlay image corresponding to (b), showing $NeuAcHex_2Cer$ 40:1;O2 ($[M-H]^-$ at m/z 1235.8002) in red, HPO_3-Hex-Cer 36:0;O3 ($[M-H]^-$ at m/z 824.5661) in green, and $NeuAcHex_2Cer$ 34:1;O2 ($[M-H]^-$ at m/z 1151.7063) in blue. The measurement was performed with a 7 μm step size.

an accumulation in tissues directly adjacent to the parasite but had low pixel coverage in the control sample as shown in Figure S8. The accumulation of several other plasmalogen phospholipids, highlighted in Figure S9, at the host−parasite interface raises the question of their potential association with immune cells of the host as levels of plasmalogen species are usually low in the liver.[36] Potentially, plasmalogen species could serve as markers for macrophages. These types of immune cells are highly relevant in regulating the immune response during fascioliasis, and they are known to contain several plasmalogen species.[37,38] A similar distribution to that for PI−P 38:4 was also found for the annotation bis-(monoacylglycero)phosphate (BMP) 34:0, shown in Figure S10b. This supports our hypothesis of plasmalogens as immune cell markers in fascioliasis infection, as it has already been shown in the mouse brain tissue that BMP species can serve as macrophage markers.[39] However, to establish a firm link between the two studies, it is crucial for our data set to confirm BMP 34:0 by MS/MS experiments as BMPs are structural isomers to phosphatidylglycerols. In addition, immunohistochemical experiments will also prove beneficial in future studies.

Furthermore, we found distributions of lipid species specific for migrating *F. hepatica*. For example, PI 34:0 ($[M-H]^-$ at m/z 837.5499) is shown in Figure 4d in green, which was neither detected during our AP-SMALDI MSI analysis in hepatic tissues nor was it identified during RP-LC MS/MS data analysis. Although not capable of *de novo* fatty acid synthesis, it is known that *Fasciola* spp. can modify fatty acids.[27]

AP-SMALDI MSI of GSLs in Immature Migrating F. hepatica Indicates Tegument Remodeling. To study the effects of parasite migration in host tissues on a higher systemic level, rat liver tissue sections containing immature *F. hepatica* (Figure 5a,b) were investigated by imaging the GSL species expected from the nano-HILIC MS/MS results for isolated adult *F. hepatica*. By performing AP-SMALDI MSI experiments in positive- and negative-ion modes, we were able to detect GSL species that were only present in immature *F. hepatica* and not in the liver tissue. As an example for the positive-ion mode, Figure 5c showcases Hex-Cer 36:0;O2 ($[M+K]^+$ at m/z 768.5750) as a representative GSL, highlighted in red. For the negative-ion mode, HPO_3-Hex-Cer 36:0;O3 ($[M-H]^-$ at m/z 824.5661) is shown in Figure 5d in green. Both examples are well-suited to showcase the benefits of a spatial resolution below 20 μm pixel size in order to resolve small histological features in the tissue sections such as the tegument (10−15 μm) and the intestine (10−60 μm) of the migrating parasite. Here, Hex-Cer 36:0;O2 was found to be distributed in the tegument and intestine of the migrating parasite and HPO_3-Hex-Cer 36:0;O3 in the intestine.

Previous investigations have explored various glycoconjugates, such as like N-glycans, during the migratory stages, and a reduction of high mannose and fucose-containing glycans upon an earlier migration phase of the worms across the jejunum.[40,41] However, to the best of our knowledge, the role of GSLs within the migratory stage has not been the subject of studies so far. Therefore, with our AP-SMALDI MSI data, we provide for the first time insights into the distribution of GSLs of migrating immature parasites through liver parenchyma and contribute to a better understanding of this class of molecules.

Simple hexosylceramides specific for immature *F. hepatica* (Figure 5c) and also trihexosylceramide species, distributed across the tegument (Figure S11), were detected. The

https://doi.org/10.1021/acsinfecdis.4c00551
ACS Infect. Dis. 2024, 10, 4233−4245

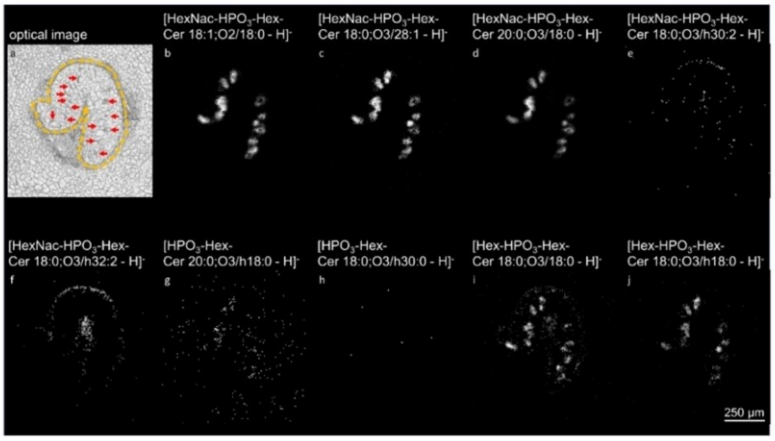

Figure 6. Spatial distribution of phosphate-containing glycosphingolipids in immature *F. hepatica*. (a) Optical image of a section of an immature *F. hepatica*, emphasized by an orange dotted line, surrounded by a hepatic tissue. The intestine of the parasite is highlighted by red arrows. (b) Single-ion image of HexNac-HPO_3-Hex-Cer 18:1;O2/18:0 ($[M-H]^-$ at m/z 1009.6349). (c) Single-ion image of HexNac-HPO_3-Hex-Cer 18:0;O3/28:1 ($[M-H]^-$ at m/z 1165.7861). (d) Single-ion image of HexNac-HPO_3-Hex-Cer 20:0;O3/18:0 ($[M-H]^-$ at m/z 1055.6769). (e) Single-ion image of HexNac-HPO_3-Hex-Cer 18:0;O3/h30:2 ($[M-H]^-$ at m/z 1207.8279). (f) Single-ion image of HexNac-HPO_3-Hex-Cer 18:0;O3/h32:2 ($[M-H]^-$ at m/z 1235.8279). (g) Single-ion image of HPO_3-Hex-Cer-20:0;O3/h18:0 ($[M-H]^-$ at m/z 868.5921). (h) Single-ion image of HPO_3-Hex-Cer-18:0;O3/h30:0 ($[M-H]^-$ at m/z 1008.7822. (i) Single-ion image of Hex-HPO_3-Hex-Cer 18:0;O3/18:0 ($[M-H]^-$ at m/z 986.6187). (j) Single-ion image of Hex-HPO_3-Hex-Cer 18:0;O3/h18:0 ($[M-H]^-$ at m/z 1002.6136). The AP-SMALDI MSI measurement was performed with a 7 μm step size.

detection of mainly mono- or trihexosylceramide species is in line with our previous observation on GSLs in adult *F. hepatica*. Unlike specific monohexosylceramides, trihexosylceramides were not detected in the intestine. This disparity suggests a potential mechanism wherein monohexosyl GSLs are assimilated from the host through feeding via the oral sucker (scavenge nutrients from their hosts), subsequently undergoing metabolism to yield more parasite-specific GSLs. This hypothesis is supported by the fact that larger molecules are acquired by the parasite from the host by the oral sucker and not via the tegument. The tegument, on the other hand, is responsible for the uptake of low-molecular-weight molecules like FAs, amino acids, and monosaccharides.[42] Further experiments are required to validate the significance of these GSLs, distributed across the tegument, for liver migration.

The distribution patterns of specific phosphate-containing GSL species without hydroxylated FAs as part of their ceramides were similar in migrating liver flukes compared to adult parasites. We successfully detected these GSLs in migrating *F. hepatica* across the intestine. They appeared comparable in abundance to the levels found in the adult *F. hepatica*. Figure 6 shows the same GSL species for immature *F. hepatica* as discussed above for adult *F. hepatica*, which are HexNac-HOP_3-Hex-Cer 18:1;O2/18:0, HexNac-HOP_3-Hex-Cer 18:1;O2/18:0, HexNac-HOP_3-Hex-Cer 18:1;O2/18:0, HexNac-HOP_3-Hex-Cer 18:1;O2/18:0, and HexNac-HOP_3-Hex-Cer 18:1;O2/18:0 (Figure 6b–d,i,j). However, there are also clear differences between adult and immature *F. hepatica*, when looking at GSL species with a hydroxylated FA as part of the ceramide moiety. These species were hardly detectable in the migrating *F. hepatica*. As examples, the GSL species HexNac-HOP_3-Hex-Cer 18:1;O2/18:0, HexNac-HOP_3-Hex-Cer 18:1;O2/18:0, HexNac-HOP_3-Hex-Cer 18:1;O2/18:0, and HexNac-HOP_3-Hex-Cer 18:1;O2/18:0 are shown in Figure 6e–h. Each of these species in immature *F. hepatica* was found less accumulated in the intestine or tegument compared to the results for adult *F. hepatica*. An exception was the GSL Hex-HPO_3-Hex-Cer 18:0;O3/h18:0, which was found to be distributed across the intestine. These results raise the question of whether this is an example for tegumental remodeling, a well-known phenomenon in *F. hepatica*.[43] There is a chance that phosphate-containing GSLs are more relevant for tegumental function in the adult life stage of *F. hepatica*, with several species found to be distributed in the tegument in direct contact with the host. However, it should be considered that there are possible *in vivo* and *in vitro* differences between the two parasite stages that could have an influence on the GSL distribution. However, we believe that this effect does not have a major impact because the GSL profile of adult *F. hepatica* is close to previous studies as described earlier. In addition, the existing overlap in both parasite stages of some of the identified GSL species suggests that they are robust against different methods of treatment. Therefore, we favor the conclusion that the differences are not due to differences in handling but to age dependence and may be relevant to natural infection.

Another phenomenon is illustrated by the ion image of HexNac-HPO_3-Hex-Cer 18:1;O2/18:0, maximally brightened in Figure S12. It shows HexNac-HPO_3-Hex-Cer 18:1;O2/18:0 mainly detected across the entire immature *F. hepatica* but with low signal intensities also in hepatic tissue lesions. This led us to the hypothesis that these specific GSLs might be excreted during the migration process and might be part of the host–parasite interaction during the migratory phase.

Besides parasite-typical GSL species, profiling of host GSLs can also be valuable to better understand the interaction of the

https://doi.org/10.1021/acsinfecdis.4c00551
ACS Infect. Dis. 2024, 10, 4233–4245

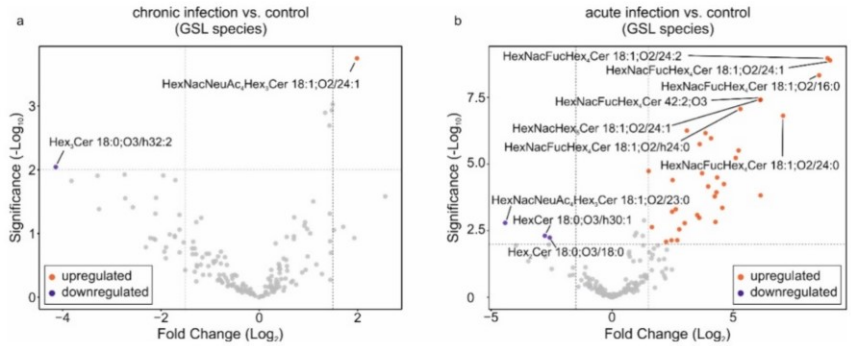

Figure 7. (a) Volcano plot comparing the results from MS-DIAL data analysis for GSLs after normalization. Livers from rats at the chronic infection stage were compared to healthy control livers. Red circles correspond to an increased species and a blue circle to decreased species. (b) Volcano plot comparing the results from MS-DIAL data analysis for GSLs after normalization. Livers from rats at the acute infection stage were compared to healthy control livers. Red circles correspond to increased species and blue circles to decreased species. The fold-change threshold was set to −1.5 to 1.5, and the significance threshold was set to $p < 0.01$ for both plots.

host and the parasite and in particular the host's immune response. GSL species are generally known to be involved in immune responses.[44] Therefore, we additionally profiled GSL species of the liver and bile duct samples at the acute and chronic infection stage.

Comprehensive GSL Profiling Unveils Elevated Levels in Rat Livers during Acute Infection. After nano-HILIC MS/MS analysis, we classified the identified GSL species into five different groups, including mono/di/trihexossylceramides, complex neutral GSLs with at least four saccharide units, neutral GSLs containing at least one fucose moiety, and acidic GSLs and GSLs with a phosphate group (see Figure S13). Regarding the mono/di/trihexoses, we identified a higher number of species for the acute infection stage (11) and the bile duct (18) compared to the chronic infection (6) and the controls for the acute infection (4) and chronic infection (7). For the more complex GSLs with at least four saccharide units, the bile duct showed an increased number of identifications (12) compared to all liver samples. Neutral GSLs containing a fucose saccharide were higher in number for the bile duct (9) but also for the liver samples from the acute infection stage (8), compared to the other three groups. The number of identified acidic GSLs was the highest across all samples. However, we could not observe a specific trend. For the rat liver of the acute infection stage, we identified 41 and for the corresponding control 38 acidic GSL species, respectively. A similar number of identifications was observed for the rat liver of the chronic infection stage (40) compared to their control (37). Only the bile duct sample showed a larger difference with 50 identified acidic GSLs. The identification numbers for GSLs containing a phosphate group were small across all groups, with 4 identifications for the acute infection, 1 for the corresponding control, 2 for the chronic infection, 6 for the corresponding control, and 4 for the bile duct.

Through the integration of an internal standard into our nano-HILIC MS methodology, we enabled the adjustment of signal intensities but also contributed to the enhancement of data accuracy and reliability. Principal component analysis (PCA) based on GSLs delineated all examined rat liver and bile duct tissue samples (Figure S14). Notably, the acute infection stage demonstrates a separation from the chronic infection stage and both control groups. As the liver tissue of chronically infected animals in this study did not show gross pathological lesions (Figure S15), it can be assumed that liver regeneration had already taken place, so that the tissue resembled a healthy tissue again. Indeed, the volcano plot shown in Figure 7a indicates a normalization in GSL levels, although this molecule class is potentially relevant during infection. In the plot, only minor differences are apparent for the comparison of the GSLs from the liver of the chronic infection stage to the control. In contrast, we detected increased levels of GSLs in the livers of rats undergoing acute infection compared to healthy controls (Figure 7b). In particular, fucose-containing GSLs showed significant upregulation for the acute infection compared to the control. These results support the conjecture of GSL participation in infection-related immune responses. In comparison to the adult *F. hepatica*, the heat map shown in Figure S16 clearly highlights the differences between parasite- and tissue-specific GSLs, with many GSL species being specific for the parasite or the host.

AP-SMALDI MSI of the Rat Liver at the Acute Infection Stage to Study Host−Parasite Interactions. Understanding the spatial distribution of GSLs within tissues is helpful for identifying those species potentially involved in direct host−parasite interactions. Here, the tissue sections containing the immature *F. hepatica* but also areas of tissue lesions were re-evaluated (Figure 5a,b). For annotations of GSLs, we integrated our curated GSL database into METASPACE. For that, we combined the GSL identifications of host tissue samples as well as isolated adult *F. hepatica*. For the AP-SMALDI MSI measurements, distinct distribution patterns were discernible for neutral GSL species. Some monohexosylceramides were characteristic of both *F. hepatica* and the surrounding liver tissue. The GSL Hex-Cer 38:1;O2 ($[M+K]^+$ m/z 794.5907) in Figure 5c in blue is given as an example. The species appeared to be accumulated at the host−parasite interface and the center of the tissue lesion. Here, the question arises if the parasite eventually sheds these GSLs to slow down liver regeneration. A previous study already showed that glucosylceramides impaired liver regeneration, which led to our hypothesis.[45] Alternatively, different GSLs may be associated

https://doi.org/10.1021/acsinfecdis.4c00551
ACS Infect. Dis. 2024, 10, 4233−4245

with the presence of certain immune cells, as we suggested in our previous study for the hamster liver.[23] Because Hex-Cer 38:1;O2 is not exclusively distributed at the host−parasite interface, this species could also serve as a marker for specific immune cells. Eosinophils, for example, are known to limit tissue damage induced by *F. hepatica*.[46] Moreover, eosinophils are known to promote liver regeneration.[47]

Additionally, the distribution of SM 34:1 ($[M + Na]^+$ m/z 725.5568) is shown in Figure 5c in green. This species showed an accumulation within the tissue lesion, with less accumulation in the center of the lesion. Other distributions of SM species are shown in Figure S17. As SMs and GSLs both belong to the class of sphingolipids, investigating SMs in addition to GSLs can help to reveal metabolic processes. Therefore, it is beneficial that we also detect SM species during our nano-HILIC MS/MS analyses. Regarding more complex GSLs, we were not able to visualize fucose-containing GSLs in the liver of the acutely infected rats, although identified as a significant upregulated group of GSL species through our nano-HILIC MS/MS data analysis. Nevertheless, we were able to visualize fucose-containing GSL species in bile duct tissue sections, as exemplarily shown in Figure S18. However, the lack of local information in rat liver tissue sections from acute infection makes it difficult to interpret the possible role of fucose-containing GSL species. Improving the detection of glycosphingolipids during MALDI MSI analysis and thus revealing their distributions in the tissue may help to narrow down a possible role in biological processes in the future.

In the case of acidic GSLs, we mainly observed the distributions of $NeuAcHex_2Cer$ species. Among these, we found similar distribution patterns. As depicted in the RGB-overlay image in Figure 5d, $NeuAcHex_2Cer$ 34:1;O2 ($[M-H]^-$ at m/z 1151.7063) shown in blue has a similar distribution compared to $NeuAcHex_2Cer$ 40:1;O2 ($[M-H]^-$ at m/z 1235.8002) shown in red. The results align with a study demonstrating an increase in ganglioside production during liver regeneration several days after partial hepatectomy.[48] The AP-SMALDI MSI data for $NeuAcHex_2Cer$ signals are furthermore backed by the semiquantitative nano-HILIC MS/MS data. Here, 13 out of 19 compounds included in our database showed a significant ($p < 0.05$) upregulation in the rat liver of the acute infection stage compared to the control.

■ CONCLUSIONS

Our previously reported method for studying GSLs has proven applicable for parasite samples. We identified the spatial distribution of GSLs in isolated adult *F. hepatica*. We were able to identify GSLs with VLCFA as part of the tegument and revealed a local overlap with the host's own elongase enzymes. As the parasite may actively synthesize these GSLs with VLCFA, this could indicate a protective function for the parasite and thus represent a feasible drug target. The spatially resolved AP-SMALDI analysis of GSLs also provides indications about the metabolism. Here, we may ascertain that *F. hepatica* converts hexosylceramides to trihexosylceramides. Because these species are mainly distributed in the tegument, they may also be an important component in the host−parasite interaction, with the function still to be determined. Additionally, we presented the first identification of GSL species in the migratory stage, including the visualization of the distributions of phosphate-containing glycosphingolipids specific for the liver fluke *F. hepatica*. Here, the differences from adult *F. hepatica* indicate that we can elucidate tegument remodeling. In particular, a hydroxyl group in the FAs of the GSL of adult *F. hepatica* appears to be a major difference between the two growth stages. Because for adult *F. hepatica*, the hydroxylated GSLs are located within the tegument, they could be crucial for the host−parasite interaction at this stage. Thus, this structural feature at the molecular level could be targeted in future drug development studies. GSL profiling of different infection stages additionally revealed elevated levels of GSLs, especially for tissues in direct contact with the parasite: the rat liver during the acute infection stage and the bile duct during the chronic infection stage. Furthermore, we employed high-resolution AP-SMALDI MSI for the first time to scrutinize the interaction of migrating *F. hepatica* with the surrounding liver tissue. This enabled us to identify potential immune cell markers. The distribution of some hexosylceramides might be characteristic of eosinophils. In addition to GSLs, there were also distinctive characteristics among other lipid classes. In particular, plasmalogenic phospholipids showed an accumulation at the host−parasite interface and could serve as immune cell markers for macrophages. Therefore, future more detailed studies on other lipid classes seem equally useful to better understand the complex interplay between the host and the parasite. In this context, it will also be important in the future to determine whether the findings obtained for our rat model can be transferred to human infections. Overall, besides the phospholipids, our data identified further different GSL species such as fucose-containing GSLs, phosphate-containing GSLs, or simple hexosylceramides in the tissue, which are possibly involved in the host−parasite interaction and form the basis for further investigations.

■ MATERIALS AND METHODS

Chemicals. Acetonitrile, isopropanol, methanol, water (HiPerSolv), and gelatin powder were purchased from VWR International GmbH (Darmstadt, Germany). Ammonium acetate (AmAc) and 2,5-dihydroxyacetophenone (DHAP) were purchased from Alfa Aesar (Kandel, Germany). Formic acid (FA), methyl-*tert*-butylether (MTBE), hematoxylin, eosin Y, and Eukitt were purchased from Sigma-Aldrich (Darmstadt, Germany). Chloroform and sodium hydroxide were purchased from Carl Roth GmbH + Co. KG (Kalsruhe, Germany), and ammonium formate (AmF) was purchased from Acros Organics (Geel, Belgium). Ethanol, isopentane, xylene, and glacial acetic acid were purchased from Merck (Darmstadt, Germany).

Tissue and Sample Preparation. *Ethical Statement.* Animal experiments using rats (*Rattus norvegicus*) as model hosts were performed in accordance with Directive 2010/63/EU on the protection of animals used for scientific purposes and the German Animal Welfare Act. The experiments were approved by the Regional Council (Regierungspraesidium) Giessen (V54-19c20 15 h 02 GI 18/10 Nr. A16/2018).

Animal Experiments. Male Wistar rats RjHan:WI (*Rattus norvegicus*, Janvier, France) were used as model hosts for *F. hepatica* infection. Animals (5−7-weeks-old) were orally infected with 25 metacercariae of an Italian parasite strain (Ridgeway Research, UK) or kept as uninfected controls. Infected and control animals were kept in the same facility and were housed under controlled conditions (light cycle, temperature, humidity, water, and food).

https://doi.org/10.1021/acsinfecdis.4c00551
ACS Infect. Dis. 2024, 10, 4233−4245

Harvesting of F. hepatica. Adult flukes were collected from the common bile duct at 14 and 20 weeks p.i. Worms were kept in RPMI 1640 (Gibco, Thermo Fisher Scientific, Germany) supplemented with a 5% chicken serum (Gibco, Thermo Fisher Scientific) and 1% ABAM solution (c.c.pro, Germany) at 37 °C and 5% CO_2 overnight to allow clearance of gut contents. Parasites were then flash frozen in liquid nitrogen for lipid extraction or embedded in 8 wt % aqueous gelatin solution and frozen on dry ice for AP-SMALDI MSI analyses. Worm samples were stored at −80 °C until further use.

Tissue Sampling. Liver samples were collected from *F. hepatica*-infected animals as well as noninfected controls at 4 and 14 weeks p.i. (9−11 and 20−21 weeks animal age). Samples were all taken from the right median lobe, where yellowish tortuous tracts were visible in the parenchyma of animals infected with immature worms (4 weeks p.i.). From animals infected with adult worms (14 weeks p.i.), we additionally sampled the dilated and thickened proximal part of the common bile duct, after removal of the worms. Tissue samples were frozen in isopentane prechilled on dry ice and stored at −80 °C until further use.

AP-SMALDI MSI. To conduct AP-SMALDI MSI measurements, we subjected the samples to a cryochamber at −20 °C for 30 min. *F. hepatica* worms, embedded in gelatin, were sliced into 20 μm-thick transversal sections using a cryotome (HM525 cryostat, Thermo Fisher Scientific, Bremen, Germany). Care was taken to ensure that the tissue sections included intestines as well as the tegument as histological features, while other organs of *F. hepatica* were optional. Rat liver and bile duct tissues underwent the same cutting process but without prior embedding. The sections were thaw-mounted onto microscopic glass slides, and microscopic images of them were recorded (VHX-5000; Keyence, Osaka, Japan) before matrix application. Tissue sections were stored at −80 °C until further use. Prior to AP-SMALDI measurements, tissue sections were thawed for 20 min in a desiccator at room temperature. The matrix 2,5-dihydroxyacetophenone (DHAP) was applied by sublimation as described previously.[23]

All MSI experiments were performed using a high-resolution atmospheric-pressure autofocusing scanning microprobe MALDI imaging ion source (AP-SMALDI[5] AF, TransMIT GmbH, Giessen, Germany)[21] coupled to an orbital trapping mass spectrometer (Thermo Scientific Q Exactive HF, Thermo Fisher Scientific, Bremen, Germany). More details are described in the Supplementary Note 1.

AP-SMALDI MSI data underlying this study are openly available in the METASPACE database at https://metaspace2020.eu/project/GSL_and_LIPIDS_Fhepatica_and_Inf. For GSL annotation, we uploaded a GSL database to METASPACE, which was based on the nano-HILIC MS/MS experiments described in the upcoming section.

LC MS/MS. For LC MS/MS, tissue samples were homogenized by using a bead mill (Mini-Mill PULVERISETTE 23, Fritsch, Idar-Oberstein, Germany). Prior to homogenization, 50 μL of AmAc solution (50 mmol/L) and 25 μL of the SPLASH LIPIDOMIX Mass Spec Standard were added. Lipids were then extracted according to Matyash et al. with some modifications.[49] Details are described in the Supplementary Note 2.

LC-MS/MS measurements were performed on an UltiMate 3000 UHPLC system (Thermo Fisher Scientific, Bremen, Germany) equipped with a reversed-phase ACQUITY UPLC HSS T3 column (1.8 μm, 2.1 × 100 mm, Waters GmbH, Eschborn, Germany) coupled to an orbital trapping mass spectrometer (Q Exactive HF-X, Thermo Fisher Scientific, Bremen, Germany). The UHPLC separation method was adapted from our previous publication,[50] using water/acetonitrile (4/6; v/v) as mobile phase A and isopropanol/acetonitrile (9/1, v/v) as mobile phase B, both containing 0.1% formic acid and 10 mM ammonium formate. The solvent flow rate was set to 0.26 mL/min, the injection volume was 10 μL, and the column oven temperature was kept constant at 40 °C. Measurements were conducted in the positive- and negative-ion mode. Detailed information about the gradient, ion-source parameters, and mass spectrometric parameters are listed in Tables S1−S3. The raw data are freely available under ftp://massive.ucsd.edu/v08/MSV000095777/.

For data analysis, MS-DIAL software[51] (version 5.1.230517) was used with the project parameters shown in Table S4. For statistical analysis, Perseus software (version 2.0.10.0) was used,[52] and for the generation of volcano plots, the online tool VolcaNoseR (https://huygens.science.uva.nl/VolcaNoseR/) was used.[53] Other graphics were generated with Microsoft Excel. More details can be found in the Supplementary Note 3.

Nano-HILIC MS/MS. For nano-HILIC MS/MS, tissue samples were homogenized by bead milling (Mini-Mill PULVERISETTE 23, Fritsch, Idar-Oberstein, Germany). Then, the extraction and purification of GSLs were carried out according to our previous publication.[23] The SM(d9) 18:1;O2/18:1 species of the SPLASH LIPIDOMIX Mass Spec Standard (Avanti Polar Lipids, Inc.) was used as a reference for relative quantification and was added prior to injection, to account for technical variations.

The samples were analyzed using an UltiMate 3000 RSLCnano system (Thermo Fisher Scientific, Dreieich, Germany) equipped with an Accucore 150 amide-HILIC column (0.075 mm × 150 mm) coupled to an orbital trapping mass spectrometer (Thermo Scientific Q Exactive HF-X). The same method as for our previous publication was used with parameters given in the Supplementary Note 4 and Tables S5 and S6.[23] The raw data are freely available under ftp://massive.ucsd.edu/v08/MSV000095777/.

To analyze the data, MS-DIAL was employed semi-quantitatively for the creation of a GSL database. In the initial step, features were detected by MS-DIAL, applying various parameters for optimal feature detection, using insights gained from a prior data set. The final settings are shown in the Supporting Information in Table S7. Next, we used the MS-DIAL MS/MS search module with neutral losses and ions typical for glycosphingolipids. A list of m/z values used for this processing step is given in Tables S8 and S9. The features were then inspected manually to create a GSL database. Subsequently, this database was used in MS-DIAL for post identification in positive-ion mode, with parameters outlined in Table S10. More details are described in the Supplementary Note 5.

Identification of F. hepatica Elongase. *F. hepatica* orthologues of *Homo sapiens* very long-chain fatty acid elongase 1 (NP_001243328.1) were identified by WormBase ParaSite BLAST with standard parameters.[54] We found four *F. hepatica* elongase genes within the *F. hepatica* proteome in Wormbase ParaSite (PRJNA179522). SMART confirmed the presence of an ELO domain in all of the four proteins.[55] ELO domains had 33.6−49.0% amino acid identity with the human sequence (aligned in Clustal Omega (v1.2.4).[56] The spatial

https://doi.org/10.1021/acsinfecdis.4c00551
ACS Infect. Dis. 2024, 10, 4233−4245

distribution of elongase expression (transcripts) in liver fluke tissues was then assessed with help of a liver fluke spatial transcriptomics data set. This data set was generated in a separate study, which is currently under review.[28] The spatial transcriptomics data set will be available as an online platform upon publication and will allow researchers to search the data set for their needs, as it was done for the elongases in this manuscript.

Data Processing. All graphical representations and mass spectra presented were processed using CorelDRAW 2021 software (version 23.1.0.389).

Nomenclature. To describe lipids and GSLs, the shorthand nomenclature of LIPIDMAPS and the nomenclature for glycans are used in this manuscript.[57,58] Hexoses, like glucose, galactose, or mannose, are abbreviated as Hex. Hexosamines are abbreviated as HexNac and fucose as Fuc. The acidic saccharides *N*-acetylneuraminic acid and *N*-glycolylneuraminic acid are abbreviated as NeuAc and NeuGc, respectively. For example, a GSL with one hexosamine and two hexoses and a ceramide with a D-erythro-hydroxysphinganine and a hydroxypalmitoyl acid is abbreviated as $HexNacHex_2Cer$ 18:0;O3/h16:0. The fragment ion nomenclature of GSLs after Domon and Costello and Merrill et al. is shown in Figure 8, indicating GSL-specific cleavage sites.[59,60]

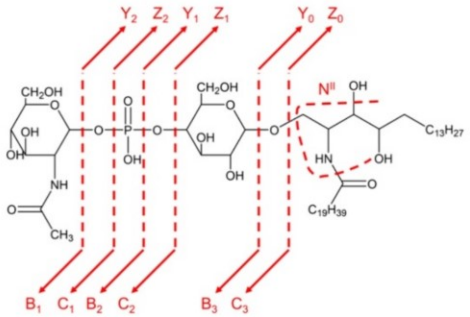

Figure 8. Fragment ion nomenclature after Domon and Costello and Merrill et al. for a glycosphingolipid, consisting of two monosaccharides linked by a phosphate group and a ceramide head group. Cleavage sites are indicated upon HCD fragmentation by dashed lines, resulting in Y-, Z-, B, and C-fragment ions for the glyosidic cleavage of the saccharide units and the N^{II}-fragment ion for the sphingoid base. As a sphingoid base, a phytosphingosine is shown exemplarily because glycosphingolipids of parasites often consist of these sphingoid bases.

■ ASSOCIATED CONTENT

Supporting Information

The Supporting Information is available free of charge at https://pubs.acs.org/doi/10.1021/acsinfecdis.4c00551.

Additional experimental protocols and experimental parameters, data processing steps (Supplementary Notes S1−S6, Tables S1−S10, and Figures S1−S18), identification of GSLs for each sample group (Table S11), and additional results of RP-LC MS/MS experiments (Supplementary Note S8, Figures S19 and S20, and Table S12) (PDF)

In-house created GSL database and RP-LC MS/MS identifications (XLSX)

■ AUTHOR INFORMATION

Corresponding Author

Bernhard Spengler − *Institute of Inorganic and Analytical Chemistry, Justus Liebig University Giessen, Giessen 35392, Germany*; orcid.org/0000-0003-0179-5653; Email: Bernhard.Spengler@anorg.chemie.uni-giessen.de

Authors

David Luh − *Institute of Inorganic and Analytical Chemistry, Justus Liebig University Giessen, Giessen 35392, Germany*

Parviz Ghezellou − *Institute of Inorganic and Analytical Chemistry, Justus Liebig University Giessen, Giessen 35392, Germany*

Sven Heiles − *Leibniz-Institut für Analytische Wissenschaften-ISAS-e.V., Dortmund 44139, Germany; Lipidomics, Faculty of Chemistry, University of Duisburg-Essen, Essen 45141, Germany*; orcid.org/0000-0003-3779-8071

Svenja Gramberg − *Institute of Parasitology, Biomedical Research Center Seltersberg (BFS), Justus Liebig University Giessen, Giessen 35392, Germany*

Simone Haeberlein − *Institute of Parasitology, Biomedical Research Center Seltersberg (BFS), Justus Liebig University Giessen, Giessen 35392, Germany*

Complete contact information is available at: https://pubs.acs.org/10.1021/acsinfecdis.4c00551

Author Contributions

B.S. supervised the project; D.L., S.H., Si.H., and B.S. designed the study. D.L. performed all experiments except harvesting of *F. hepatica*and tissue sampling, which was done by S.G. D.L. performed data analysis. S.G. and Si.H. provided spatial transcriptomics data of Figure S4, and S.G. annotated the different regions in Figure S1. D.L. wrote the original draft. All authors reviewed and edited the manuscript. All authors have given approval to the final version of the manuscript.

Notes

The authors declare the following competing financial interest(s): B.S. is a consultant of TransMIT GmbH, Giessen, Germany. All others declare no conflicts of interest.

■ ACKNOWLEDGMENTS

We gratefully acknowledge financial support by the Hessian Ministry of Science, Higher Education and Art (HMWK), LOEWE Center DRUID (LOEWE/1/10/519/03/03.001(0016)/53). S.H. acknowledges funding by the Bundesministerium für Bildung und Forschung (BMBF) and by the Ministerium für Kultur und Wissenschaft des Landes Nordrhein-Westfalen (MKW). The authors thank Carolin M. Morawietz for preparing some of the *F. hepatica*tissue sections.

■ REFERENCES

(1) Mehmood, K.; Zhang, H.; Sabir, A. J.; Abbas, R. Z.; Ijaz, M.; Durrani, A. Z.; Saleem, M. H.; Ur Rehman, M.; Iqbal, M. K.; Wang, Y.; Ahmad, H. I.; Abbas, T.; Hussain, R.; Ghori, M. T.; Ali, S.; Khan, A. U.; Li, J. A review on epidemiology, global prevalence and economical losses of fasciolosis in ruminants. *Microbial pathogenesis.* **2017**, *109*, 253−262.

(2) World Health Organization https://www.who.int/news-room/questions-and-answers/item/q-a-on-fascioliasis, 2020.

(3) Lalor, R.; Cwiklinski, K.; Calvani, N. E. D.; Dorey, A.; Hamon, S.; Corrales, J. L.; Dalton, J. P.; De Marco Verissimo, C. Pathogenicity and virulence of the liver flukes Fasciola hepatica and Fasciola Gigantica that cause the zoonosis Fasciolosis. *Virulence* **2021**, *12*, 2839−2867.
(4) Harrington, D.; Lamberton, P. H. L.; McGregor, A. Human liver flukes. *Lancet Gastroenterol. Hepatol.* **2017**, *2*, 680−689.
(5) Robinson, M. W.; Harmon, C.; O'Farrelly, C. Liver immunology and its role in inflammation and homeostasis. *Cellular & molecular immunology.* **2016**, *13*, 267−276.
(6) Kelley, J. M.; Elliott, T. P.; Beddoe, T.; Anderson, G.; Skuce, P.; Spithill, T. W. Current Threat of Triclabendazole Resistance in Fasciola hepatica. *Trends in parasitology.* **2016**, *32*, 458−469.
(7) Fairweather, I.; Brennan, G. P.; Hanna, R. E. B.; Robinson, M. W.; Skuce, P. J. Drug resistance in liver flukes. *International journal for parasitology Drugs and drug resistance.* **2020**, *12*, 39−59.
(8) Cwiklinski, K.; Dalton, J. P. Omics tools enabling vaccine discovery against fasciolosis. *Trends in parasitology.* **2022**, *38*, 1068−1079.
(9) Cwiklinski, K.; Dalton, J. P. Advances in Fasciola hepatica research using 'omics' technologies. *International journal for parasitology.* **2018**, *48*, 321−331.
(10) Cwiklinski, K.; Robinson, M. W.; Donnelly, S.; Dalton, J. P. Complementary transcriptomic and proteomic analyses reveal the cellular and molecular processes that drive growth and development of Fasciola hepatica in the host liver. *BMC Genomics* **2021**, *22*, 46.
(11) Rodríguez, E.; Noya, V.; Cervi, L.; Chiribao, M. L.; Brossard, N.; Chiale, C.; Carmona, C.; Giacomini, C.; Freire, T. Glycans from Fasciola hepatica Modulate the Host Immune Response and TLR-Induced Maturation of Dendritic Cells. *PLoS neglected tropical diseases.* **2015**, *9*, No. e0004234.
(12) de Marco Verissimo, C.; Cwiklinski, K.; Nilsson, J.; Mirgorodskaya, E.; Jin, C.; Karlsson, N. G.; Dalton, J. P. Glycan Complexity and Heterogeneity of Glycoproteins in Somatic Extracts and Secretome of the Infective Stage of the Helminth Fasciola hepatica. *Molecular & cellular proteomics: MCP.* **2023**, *22*, No. 100684.
(13) Kabayama, K.; Sato, T.; Saito, K.; Loberto, N.; Prinetti, A.; Sonnino, S.; Kinjo, M.; Igarashi, Y.; Inokuchi, J. Dissociation of the insulin receptor and caveolin-1 complex by ganglioside GM3 in the state of insulin resistance. *Proceedings of the National Academy of Sciences of the United States of America.* **2007**, *104*, 13678−13683.
(14) Tuosto, L.; Parolini, I.; Schröder, S.; Sargiacomo, M.; Lanzavecchia, A.; Viola, A. Organization of plasma membrane functional rafts upon T cell activation. *Eur. J. Immunol.* **2001**, *31*, 345−349.
(15) Zhang, T.; de Waard, A. A.; Wuhrer, M.; Spaapen, R. M. The Role of Glycosphingolipids in Immune Cell Functions. *Front. Immunol.* **2019**, *10*, 90.
(16) Wuhrer, M.; Berkefeld, C.; Dennis, R. D.; Idris, M. A.; Geyer, R. The liver flukes Fasciola gigantica and Fasciola hepatica express the leucocyte cluster of differentiation marker CD77 (globotriaosylceramide) in their tegument. *Biol. Chem.* **2001**, *382*, 195−207.
(17) Wuhrer, M.; Grimm, C.; Zahringer, U.; Dennis, R. D.; Berkefeld, C. M.; Idris, M. A.; Geyer, R. A novel GlcNAcalpha1-HPO3−6Gal(1−1)ceramide antigen and alkylated inositol-phosphoglycerolipids expressed by the liver fluke Fasciola hepatica. *Glycobiology.* **2003**, *13*, 129−137.
(18) Wuhrer, M.; Grimm, C.; Dennis, R. D.; Idris, M. A.; Geyer, R. The parasitic trematode Fasciola hepatica exhibits mammalian-type glycolipids as well as Gal(beta1−6)Gal-terminating glycolipids that account for cestode serological cross-reactivity. *Glycobiology* **2003**, *14*, 115−126.
(19) Spengler, B.; Hubert, M.; Kaufmann, R. MALDI ion imaging and biological ion imaging with a new scanning UV-laser microprobe, *Proceedings 42nd ASMS Conference on Mass Spectrometry and Allied Topics*, Chicago, IL, 1994; p 1041.
(20) Koestler, M.; Kirsch, D.; Hester, A.; Leisner, A.; Guenther, S.; Spengler, B. A high-resolution scanning microprobe matrix-assisted laser desorption/ionization ion source for imaging analysis on an ion trap/Fourier transform ion cyclotron resonance mass spectrometer. *Rapid communications in mass spectrometry: RCM.* **2008**, *22*, 3275−3285.
(21) Kompauer, M.; Heiles, S.; Spengler, B. Autofocusing MALDI mass spectrometry imaging of tissue sections and 3D chemical topography of nonflat surfaces. *Nature methods.* **2017**, *14*, 1156−1158.
(22) Kompauer, M.; Heiles, S.; Spengler, B. Atmospheric pressure MALDI mass spectrometry imaging of tissues and cells at 1.4-μm lateral resolution. *Nature methods.* **2017**, *14*, 90−96.
(23) Luh, D.; Heiles, S.; Roderfeld, M.; Grevelding, C. G.; Roeb, E.; Spengler, B. Hepatic Topology of Glycosphingolipids in Schistosoma mansoni-Infected Hamsters. *Analytical chemistry.* **2024**, *96*, 6311−6320.
(24) Barrientos, R. C.; Zhang, Q. Recent advances in the mass spectrometric analysis of glycosphingolipidome - A review. *Analytica chimica acta.* **2020**, *1132*, 134−155.
(25) Jennemann, R.; Rabionet, M.; Gorgas, K.; Epstein, S.; Dalpke, A.; Rothermel, U.; Bayerle, A.; van der Hoeven, F.; Imgrund, S.; Kirsch, J.; Nickel, W.; Willecke, K.; Riezman, H.; Gröne, H.-J.; Sandhoff, R. Loss of ceramide synthase 3 causes lethal skin barrier disruption. *Human molecular genetics.* **2012**, *21*, 586−608.
(26) Sassa, T.; Kihara, A. Metabolism of very long-chain Fatty acids: genes and pathophysiology. *Biomolecules & therapeutics.* **2014**, *22*, 83−92.
(27) Oldenborg, V.; van Vugt, F.; van Golde, L. M. Composition and metabolism of phospholipids of Fasciola hepatics, the common liver fluke. *Biochimica et biophysica acta.* **1975**, *398*, 101−110.
(28) Gramberg, S.; Puckelwaldt, O.; Schmitt, T.; Lu, Z.; Haeberlein, S. Spatial transcriptomics of a parasitic flatworm provides a molecular map of vaccine candidates, drug targets and drug resistance genes, *BioRxiv*. **2023**.
(29) Kadesch, P.; Quack, T.; Gerbig, S.; Grevelding, C. G.; Spengler, B. Lipid Topography in Schistosoma mansoni Cryosections, Revealed by Microembedding and High-Resolution Atmospheric-Pressure Matrix-Assisted Laser Desorption/Ionization (MALDI) Mass Spectrometry Imaging. *Analytical chemistry.* **2019**, *91*, 4520−4528.
(30) Kadesch, P.; Quack, T.; Gerbig, S.; Grevelding, C. G.; Spengler, B. Tissue- and sex-specific lipidomic analysis of Schistosoma mansoni using high-resolution atmospheric pressure scanning microprobe matrix-assisted laser desorption/ionization mass spectrometry imaging. *PLoS neglected tropical diseases.* **2020**, *14*, No. e0008145.
(31) Wiedemann, K. R.; Peter Ventura, A.; Gerbig, S.; Roderfeld, M.; Quack, T.; Grevelding, C. G.; Roeb, E.; Spengler, B. Changes in the lipid profile of hamster liver after Schistosoma mansoni infection, characterized by mass spectrometry imaging and LC-MS/MS analysis. *Analytical and bioanalytical chemistry.* **2022**, *414*, 3653−3665.
(32) Stein, T. A.; Burns, G. P.; Tropp, B. E.; Wise, L. Hepatic fat accumulation during liver regeneration. *Journal of surgical research.* **1985**, *39*, 338−343.
(33) Bottari, N. B.; Mendes, R. E.; Lucca, N. J.; Schwertz, C. I.; Henker, L. C.; Olsson, D. C.; Piva, M. M.; Sangoi, M.; Campos, L. P.; Moresco, R. N.; Jaques, J. A.; Da silva, A. S. Oxidative stress associated with pathological lesions in the liver of rats experimentally infected by Fasciola hepatica. *Experimental parasitology.* **2015**, *159*, 24−28.
(34) Albano, E.; Mottaran, E.; Occhino, G.; Reale, E.; Vidali, M. Review article: role of oxidative stress in the progression of non-alcoholic steatosis. *Aliment. Pharmacol. Ther.* **2005**, *22* (Suppl 2), 71−73.
(35) Dalton, J. P., Ed. *Fasciolosis;* CABI: UK, 2021.
(36) Koch, J.; Lackner, K.; Wohlfarter, Y.; Sailer, S.; Zschocke, J.; Werner, E. R.; Watschinger, K.; Keller, M. A. Unequivocal Mapping of Molecular Ether Lipid Species by LC-MS/MS in Plasmalogen-Deficient Mice. *Analytical chemistry.* **2020**, *92*, 11268−11276.
(37) Ruiz-Campillo, M. T.; Molina-Hernández, V.; Pérez, J.; Pacheco, I. L.; Pérez, R.; Escamilla, A.; Martínez-Moreno, F. J.; Martínez-Moreno, A.; Zafra, R. Study of peritoneal macrophage immunophenotype in sheep experimentally infected with Fasciola hepatica. *Veterinary parasitology.* **2018**, *257*, 34−39.

https://doi.org/10.1021/acsinfecdis.4c00551
ACS Infect. Dis. 2024, 10, 4233−4245

(38) Wallner, S.; Grandl, M.; Konovalova, T.; Sigrüner, A.; Kopf, T.; Peer, M.; Orsó, E.; Liebisch, G.; Schmitz, G. Monocyte to macrophage differentiation goes along with modulation of the plasmalogen pattern through transcriptional regulation. *PloS one.* **2014**, *9*, No. e94102.
(39) Nielsen, M. M. B.; Lambertsen, K. L.; Clausen, B. H.; Meyer, M.; Bhandari, D. R.; Larsen, S. T.; Poulsen, S. S.; Spengler, B.; Janfelt, C.; Hansen, H. S. Mass spectrometry imaging of biomarker lipids for phagocytosis and signalling during focal cerebral ischaemia. *Sci. Rep.* **2016**, *6*, 39571.
(40) Garcia-Campos, A.; Baird, A. W.; Mulcahy, G. Migration of Fasciola hepatica newly excysted juveniles is inhibited by high-mannose and oligomannose-type N-glycan-binding lectins. *Parasitology.* **2017**, *144*, 1708−1717.
(41) Garcia-Campos, A.; Ravidà, A.; Nguyen, D. L.; Cwiklinski, K.; Dalton, J. P.; Hokke, C. H.; O'Neill, S.; Mulcahy, G. Tegument Glycoproteins and Cathepsins of Newly Excysted Juvenile Fasciola hepatica Carry Mannosidic and Paucimannosidic N-glycans. *PLoS neglected tropical diseases.* **2016**, *10*, No. e0004688.
(42) Dalton, J. P.; Skelly, P.; Halton, D. W. Role of the tegument and gut in nutrient uptake by parasitic platyhelminths. *Can. J. Zool.* **2004**, *82*, 211−232.
(43) Bennett, C. E.; Threadgold, L. T. Fasciola hepatica: development of tegument during migration in mouse. *Experimental parasitology.* **1975**, *38*, 38−55.
(44) Cummings, R. D. Glycosphingolipids in human parasites. *FEBS open bio.* **2023**, *13*, 1625−1635.
(45) Gonzalez-Carmona, M. A.; Sandhoff, R.; Tacke, F.; Vogt, A.; Weber, S.; Canbay, A. E.; Rogler, G.; Sauerbruch, T.; Lammert, F.; Yildiz, Y. Beta-glucosidase 2 knockout mice with increased glucosylceramide show impaired liver regeneration. *Liver international.* **2012**, *32*, 1354−1362.
(46) Frigerio, S.; Da Costa, V.; Costa, M.; Festari, M. F.; Landeira, M.; Rodríguez-Zraquia, S. A.; Härtel, S.; Toledo, J.; Freire, T. Eosinophils Control Liver Damage by Modulating Immune Responses Against Fasciola hepatica. *Frontiers in immunology.* **2020**, *11*, No. 579801.
(47) Goh, Y. P. S.; Henderson, N. C.; Heredia, J. E.; Red Eagle, A.; Odegaard, J. I.; Lehwald, N.; Nguyen, K. D.; Sheppard, D.; Mukundan, L.; Locksley, R. M.; Chawla, A. Eosinophils secrete IL-4 to facilitate liver regeneration. *Proceedings of the National Academy of Sciences of the United States of America.* **2013**, *110*, 9914−9919.
(48) Riboni, L.; Ghidoni, R.; Benevento, A.; Tettamanti, G. Content, pattern and metabolic processing of rat-liver gangliosides during liver regeneration. *European journal of biochemistry.* **1990**, *194*, 377−382.
(49) Matyash, V.; Liebisch, G.; Kurzchalia, T. V.; Shevchenko, A.; Schwudke, D. Lipid extraction by methyl-tert-butyl ether for high-throughput lipidomics. *Journal of lipid research.* **2008**, *49*, 1137−1146.
(50) Garikapati, V.; Colasante, C.; Baumgart-Vogt, E.; Spengler, B. Sequential lipidomic, metabolomic, and proteomic analyses of serum, liver, and heart tissue specimens from peroxisomal biogenesis factor 11α knockout mice. *Analytical and bioanalytical chemistry.* **2022**, *414*, 2235−2250.
(51) Tsugawa, H.; Cajka, T.; Kind, T.; Ma, Y.; Higgins, B.; Ikeda, K.; Kanazawa, M.; VanderGheynst, J.; Fiehn, O.; Arita, M. MS-DIAL: data-independent MS/MS deconvolution for comprehensive metabolome analysis. *Nature methods.* **2015**, *12*, 523−526.
(52) Tyanova, S.; Temu, T.; Sinitcyn, P.; Carlson, A.; Hein, M. Y.; Geiger, T.; Mann, M.; Cox, J. The Perseus computational platform for comprehensive analysis of (prote)omics data. *Nature methods.* **2016**, *13*, 731−740.
(53) Goedhart, J.; Luijsterburg, M. S. VolcaNoseR is a web app for creating, exploring, labeling and sharing volcano plots. *Sci. Rep.* **2020**, *10*, 20560.
(54) Howe, K. L.; Bolt, B. J.; Shafie, M.; Kersey, P.; Berriman, M. WormBase ParaSite - a comprehensive resource for helminth genomics. *Molecular and biochemical parasitology.* **2017**, *215*, 2−10.
(55) Letunic, I.; Khedkar, S.; Bork, P. SMART: recent updates, new developments and status in 2020. *Nucleic acids research.* **2021**, *49*, D458−D460.
(56) Madeira, F.; Madhusoodanan, N.; Lee, J.; Eusebi, A.; Niewielska, A.; Tivey, A. R. N.; Lopez, R.; Butcher, S. The EMBL-EBI Job Dispatcher sequence analysis tools framework in 2024. *Nucleic acids research.* **2024**, *52*, W521−W525.
(57) Fahy, E.; Subramaniam, S.; Brown, H. A.; Glass, C. K.; Merrill, A. H.; Murphy, R. C.; Raetz, C. R. H.; Russell, D. W.; Seyama, Y.; Shaw, W.; Shimizu, T.; Spener, F.; van Meer, G.; VanNieuwenhze, M. S.; White, S. H.; Witztum, J. L.; Dennis, E. A. A comprehensive classification system for lipids. *Journal of lipid research.* **2005**, *46*, 839−861.
(58) Liebisch, G.; Fahy, E.; Aoki, J.; Dennis, E. A.; Durand, T.; Ejsing, C. S.; Fedorova, M.; Feussner, I.; Griffiths, W. J.; Köfeler, H.; Merrill, A. H.; Murphy, R. C.; O'Donnell, V. B.; Oskolkova, O.; Subramaniam, S.; Wakelam, M. J. O.; Spener, F. Update on LIPID MAPS classification, nomenclature, and shorthand notation for MS-derived lipid structures. *Journal of lipid research.* **2020**, *61*, 1539−1555.
(59) Domon, B.; Costello, C. E. A systematic nomenclature for carbohydrate fragmentations in FAB-MS/MS spectra of glycoconjugates. *Glycoconjugate J.* **1988**, *5*, 397−409.
(60) Merrill, A. H.; Sullards, M. C.; Allegood, J. C.; Kelly, S.; Wang, E. Sphingolipidomics: high-throughput, structure-specific, and quantitative analysis of sphingolipids by liquid chromatography tandem mass spectrometry. *Methods.* **2005**, *36*, 207−224.

https://doi.org/10.1021/acsinfecdis.4c00551
ACS Infect. Dis. 2024, 10, 4233−4245

Supporting Information

Supporting Information

Glycolipidomics of liver flukes and host tissues during fascioliasis – insights from mass spectrometry imaging

David Luh,[1] Parviz Ghezellou,[1] Sven Heiles,[2,3] Svenja Gramberg,[4] Simone Haeberlein,[4] Bernhard Spengler[1,*]

[1]Institute of Inorganic and Analytical Chemistry, Justus Liebig University Giessen, 35392 Giessen, Germany

[2]Leibniz-Institut für Analytische Wissenschaften - ISAS - e.V., 44139 Dortmund, Germany

[3]Lipidomics, Faculty of Chemistry, University of Duisburg-Essen, 45141 Essen, Germany

[4]Institute of Parasitology, Biomedical Research Center Seltersberg (BFS), Justus Liebig University Giessen, 35392 Giessen, Germany

* - Corresponding Author, email address: Bernhard.Spengler@anorg.chemie.uni-giessen.de

Supplementary Note 1 – AP-SMALDI MSI

AP-SMALDI measurements were performed with different step sizes down to 5 µm as mentioned for each figure separately. The measurements were performed with a mass range of *m/z* 550 – 2200 for rat tissue samples and *m/z* 700 -2800 for isolated adult *F. hepatica*. The mass resolution was set to 240 000 at *m/z* 200. Measurements were performed with 50 laser pulses per pixel at a wavelength of 343 nm. Capillary temperature was set to 250 °C, the S-lens was set to 100 and the acceleration voltage was set to ± 3 kV.

Raw files were recalibrated with ReCal Offline. Ion images were generated with Mirion, the brightness was adjusted for better visualization.[1]

Supplementary Note 2 – Lipid Extraction for HPLC-MS/MS

For lipid extraction, 100 µL ice-cold methanol and 400 µL MTBE were added to each tissue homogenate. The sample was shortly vortexed, followed by shaking for one hour in a Thermomixer C (Eppendorf SE, Hamburg, Germany) at 4 °C and 1000 rpm. Then, 200 µL ice-cold water was added and the sample was centrifuged for 10 min at 1000 g. The upper organic layer was removed and stored in an Eppendorf tube at -20 °C. The extraction procedure was repeated with the remaining aqueous layer by adding a mixture of MTBE/MeOH/water (4/1.2/1, v/v/v). Subsequently, the sample was shaken for one hour at 4 °C and 1000 rpm, followed by centrifugation for 10 min at 1000 g. The organic layers were combined and evaporated under a stream of nitrogen and stored at -80 °C. Samples were resuspended in 500 µL acetonitrile/isopropanol/water (65/30/5, v/v/v). For LC-MS/MS measurements, samples were diluted by using 2 µL of the sample and adding 198 µL of acetonitrile/isopropanol/water (65/30/5, v/v/v).

Supplementary Note 3 – LC-MS/MS data analysis with Perseus software

Identification results obtained by MS-DIAL were normalized to the internal standard and wet-tissue weight, positive- and negative-ion mode data were combined, double annotations were removed while the most intense entry was kept, and then uploaded into Perseus. In Perseus, a $\log_2$-transformation was performed, and missing values were replaced by "0". For revealing significant up- and down-regulation between two biological groups, a two-sided Student's T-tests with a threshold p-value of 0.05 was performed. Volcano plots were generated and the corresponding data matrix was used for the upload to https://huygens.science.uva.nl/VolcaNoseR/. Here, the fold change threshold was set to -1.5 to 1.5 and the significance threshold was set to 1.3.

Supplementary Note 4 – Experimental parameters for nano-HILIC MS/MS analysis

For nano-HILIC MS/MS experiments, solvent A consisted of acetonitrile/methanol (99/1, v/v) and solvent B of methanol/water (8/2, v/v), both with 5 mmol/L ammonium acetate. For injection, the pre-concentration setup was used with microliter-pickup injection. The sample injection volume was 1 µL. Further parameters are described in detail in Table S5/S6.

Supplementary Note 5 – GSL database generation for data dependent acquisition of nano-HILIC MS/MS experiments

For data analysis we conducted MS DIAL feature detection on all samples within this study, identifying 170,583 alignment spots for positive-ion mode and 37,149 for negative-ion mode. Employing MS DIAL feature MS/MS search, tailored explicitly for glycolipid fragments, we identified 9,423 features in positive-ion mode and 1,252 features in negative-ion mode. Through a preliminary manual inspection of the corresponding MS/MS spectra within the MS-DIAL interface, we streamlined the data matrix to 1,154 features in positive- and 1,104 in negative-ion mode. Ultimately, our analysis revealed 212 GSLs

across all samples validated by MS^2 fragmentation patterns in combination with the retention time. 104 GSLs were detected in both polarities, 61 exclusively in positive- and 47 exclusively in negative-ion mode. The comprehensive database, detailed in the Supplementary File 1, encompasses a total of 37 distinct saccharide compositions. Additionally, 57 different compositions are delineated for the ceramide backbone, with a preference for selecting the most intense N^{II}-fragment for ceramide identification. By using MS-DIAL and its available features, it was possible to reduce the time-consuming manual evaluation of data dependent nano-HILIC MS/MS analysis, while simultaneously mitigating researcher dependencies in recognizing GSL fragmentation patterns. Nevertheless, while a fully automated software solution holds the potential to expedite processes further and diminish human errors, our curated database, coupled with additional GSL species, positions MS-DIAL as a robust platform for the comprehensive analysis of nano-HILIC MS/MS data.

Because we aimed for as many identifications as possible for curating the database, multiple annotations for the same feature were obtained. However, precise computations of the signal intensities or areas are a vital requirement for normalization with subsequent relative quantification. Therefore, we reprocessed the nano-HILIC MS/MS data in MS-DIAL with more robust parameters, leading, for example, to less multiple-annotated features. Therefore, our curated database was deployed for post-identification in MS-DIAL. With the more robust parameters, we successfully identified 163 out of 209 GSLs across all samples in the positive-ion mode.

For statistical analysis, areas based on MS-DIAL post-identification in positive-ion mode were normalized to the weight and the reference signal intensity of (SM(d9) 18:1;O2/18:1). For double-identified GSLs, the compound with the lowest mass deviation was kept. Double identification mostly occurred when the singly- and doubly-charged adducts of GSL compounds were both identified or when isobaric species were present. The resulting data matrix was then imported in Perseus. In Perseus, a $\log_2$-transformation was performed, and missing values were replaced by “0”. For revealing significant up- and downregulation between two biological groups, a two-sided Student’s T-test with a threshold p-value of 0.05 was performed. The volcano plot was generated and the corresponding

data matrix was used for the upload to https://huygens.science.uva.nl/VolcaNoseR/.[2] For the hierarchical clustering, the normalized data was uploaded to https://biit.cs.ut.ee/clustvis/.[3]

The normalized data are presented in a heatmap in Figure S16. It is obvious that the isolated adult *F. hepatica* shows up with various characteristic GSL species, but also for the bile duct of rats in the chronic infection stage, many characteristic GSL species were observed. In Table S11, the different GSLs are listed, with an "x" indicating that this species was identified in the post-identification analysis. The total identification number slightly differs from the previously mentioned 166, because the post-identification was carried out in positive- and additionally in negative-ion mode, whereas for the normalized data only the positive-ion mode was used. For pure post-identification we also applied the peak count filter to 33% and the mass deviation for identification to 0.01 Da and analyzed each biological group separately.

Supplementary Note 6 – Hematoxylin and eosin staining protocol

Hematoxylin and eosin (H&E) staining was performed after AP-SMALDI MSI measurements. First, matrix was rinsed off with ethanol and then the sample was dehydrated for 2 min in ethanol, followed by a 2 min incubation in 70% ethanol. Then, the sample was incubated for 2 min in 40% ethanol followed by a 2 min incubation step in HPLC-grade water. Staining with hematoxylin, washing with tap water for 15 min and staining with 1% Eosin Y solution for 1 min and differentiation with HPLC-grade water for 2 min, 40% ethanol for 2 min, 70% ethanol for 2 min and 100% ethanol for 2 min were subsequently carried out. Clearing with xylol for 2 min and covering with Eukitt and a cover slide completed the staining protocol.

Supplementary Note 7 – Description of H&E-stained tissue sections of rat liver during the acute infection stage

During acute infection with fascioliasis, immature *F. hepatica* (Figure S2 in black) are migrating through the liver parenchyma. These parasites cause mechanical damage as well as damage caused by shedding digestive enzymes, resulting in visible migratory tracts. The centers of these tracts are marked in orange in Figure S2 and are rich in leukocyte infiltrates. The centers are surrounded by necrotic liver tissue, which is highlighted in Figure S2 in blue. This necrotic tissue is often still rich in leukocyte infiltrates. Additionally, several blood vessels are highlighted in red, with perivascular leukocyte infiltrates, marked in purple as shown in Figure S2. Furthermore, several areas are highlighted in white. These areas may represent swollen liver tissue.

Supplementary Note 8 – Supporting RP-LC MS/MS data

We investigated alterations in the hepatic lipidome during acute *F. hepatica* infection compared to healthy controls. As depicted in Figure S19, the total number of identified lipid species exhibits a remarkable similarity with subtle distinctions. As an example, in the acutely infected sample, eleven LPE-O species were identified, whereas in the control sample only six were identified. However, statistical analysis revealed more profound differences. A significant downregulation ($p < 0.05$) was observed in glycerophospholipids such as phosphatidylcholines (PCs), phosphatidylserines (PSs), and phosphatidylinositols (PIs), along with their corresponding ether-lipid classes (Figure S7). Interestingly, exceptions to this trend were noted, highlighting an upregulation of phosphatidylethanolamines (PEs), ether-linked phosphatidylethanolamines (PE-Os), and lysophosphatidylethanolamines (LPE-Os). Furthermore, we identified a significant upregulation in glycerolipids, encompassing triacylglycerols (TGs), diacylglycerols (DGs), as well as free fatty acids (FAs), oxidized free fatty acids (FA-Os), and ceramides (Cer) in the samples from acutely infected subjects. In contrast, cardiolipins (CLs) and sphingomyelins (SMs) exhibited a distinct downregulation. The summarized results are visually

represented in Figure S7, while the corresponding volcano plot in Figure S20 illustrates the down- and upregulated lipid species in acutely infected samples compared to the control. Highlighted in green are the two lipids PC 36:4 and TG 58:8, which are shown in the main manuscript in the RG-overlay image (Figure 4b). Furthermore, the volcano plot also includes 363 unknown lipid species. These species are annotated from the RIKEN database, lacking specificity regarding molecular species.

With respect to the rat liver of the chronic infection stage, only 11 lipid species appeared significantly up- or downregulated ($p < 0.05$) compared to the same-aged healthy control, with the species listed in Table S12. Therefore, we assume that a normalization in the lipid metabolism is almost reached at the chronic time point of infection, and that we rather observe biological variations and measurement inaccuracies. Interestingly, a statistical comparison between the bile duct at the chronic infection stage and the rat liver of the healthy control (20-21 weeks of age) revealed, among others, eleven significantly ($p < 0.05$) upregulated LPE-O species. Together with the outcome of non-significant changes in LPE-O species between the bile duct sample and the rat liver at the acute infection stage, this molecular class can potentially be linked to the host-parasite interaction. Our supplementary file 1 encompasses a comprehensive lipid database, derived from our RP-LC MS/MS measurements, providing reference data.

Figure S1: H&E-stained tissue section of a rat liver during the acute infection stage. Different histological regions are highlighted. The migrating immature *F. hepatica* in black, connective tissue in green, foci of migratory tracts in orange, rim of migratory tracts in blue, blood vessels in red, perivascular tissue in purple and swollen hepatocytes in white.

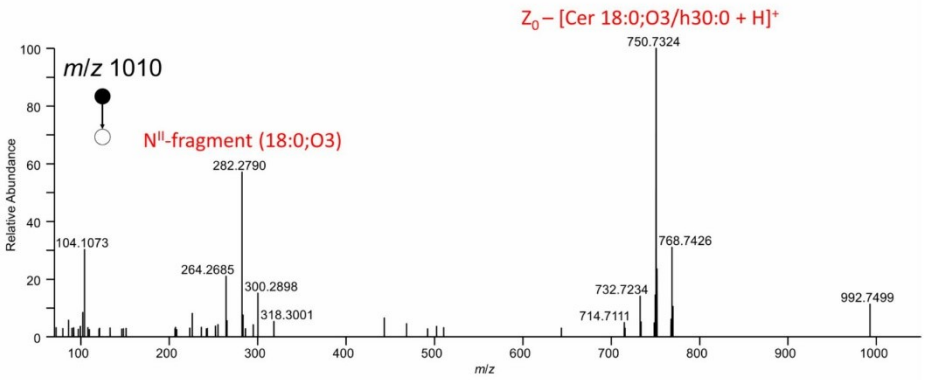

Figure S2: Tandem mass spectrum for HPO_3-Hex-Cer 18:0;O3/h30:0 ($[M+H]^+$ at *m/z* 1010.76). The fragment ion at *m/z* 282.28 corresponds to the N^{II}-fragment. The fragment ion at *m/z* 750.73 represents the Z_0-fragment ion with a neutral loss of 260.03 Da (Hex+HPO_3) from the parent ion.

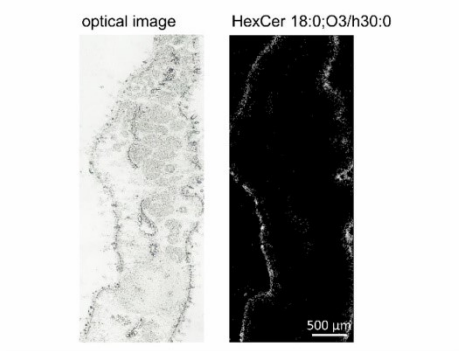

Figure S3: (left) Optical image of a transversal *F. hepatica* tissue section. (right) Single-ion image showing the distribution of HexCer 18:0;O3/h30:0 ([M+K]+ at *m/z* 968.7527) across the tegument.

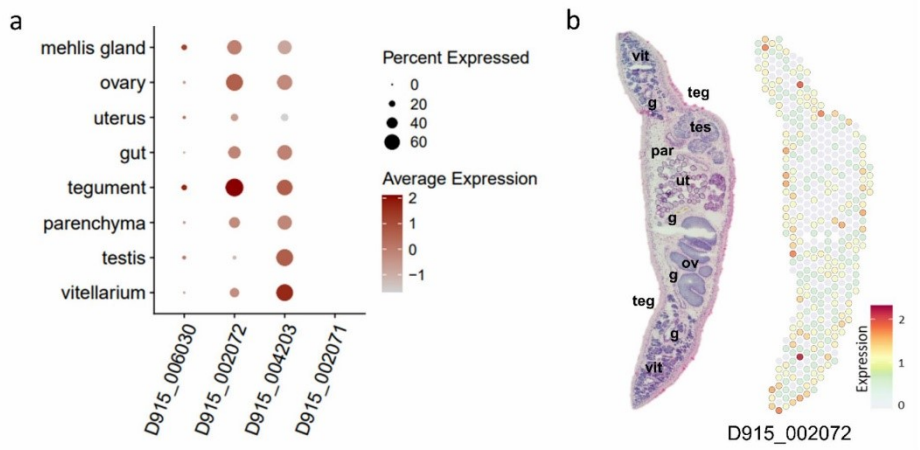

Figure S4: Spatial transcriptomics data for the elongase genes D915_006030, D915_002072, D915_004203 and D915_002071 in adult *F. hepatica*. (a) DotPlot showing elongase expression profiles across eight liver fluke tissues. Dot color encodes the average expression level in a given tissue. Dot size encodes the percentage of spots assigned to a tissue that have captured elongase transcripts. (b) H&E-stained tissue section and corresponding spatial projection showing the expression pattern of D915_002072. Expression level encoded by color (grey = low, red = high). g: gut, ov: ovary, par: parenchyma, teg: tegument, tes: testis, ut: uterus, vit: vitellarium.

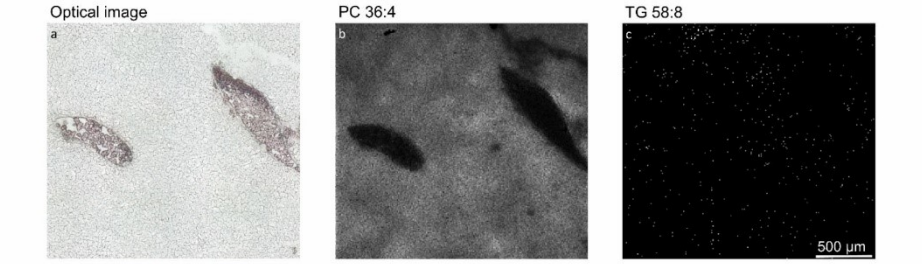

Figure S5: (a) Optical image of a control liver tissue section from a healthy rat, which was the same age as the rat of the acute infection stage. (b) Single-ion image showing PC 36:4 ($[M+K]^+$ at *m/z* 820.5253). (c) Single-ion image of TG 58:8 ($[M+K]^+$ at *m/z* 969.7308). The AP-SMALDI MSI measurement was performed with 10 µm step size.

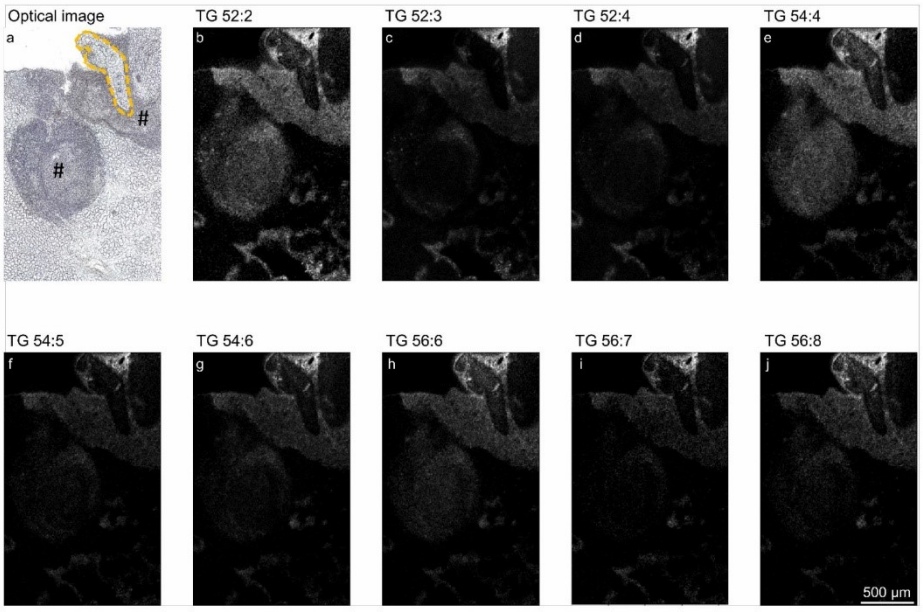

Figure S6: (a) Optical image of liver tissue section from a rat at the acute infection stage. The migrating *F. hepatica* is outlined by an orange-dotted line, and tissue lesions are marked by a hash. (b) Single-ion image showing TG 52:2 ($[M+K]^+$ at *m/z* 897.7308). (c) Single-ion image showing TG 52:3 ($[M+K]^+$ at *m/z* 895.7151). (d) Single-ion image showing TG 52:4 ($[M+K]^+$ at *m/z* 893.6995). (e) Single-ion image showing TG 54:4 ($[M+K]^+$ at *m/z* 921.7308). (f) Single-ion image showing TG 54:5 ($[M+K]^+$ at *m/z* 919.7308). (g) Single-ion image showing TG 54:6 ($[M+K]^+$ at *m/z* 919.7151). (h) Single-ion image showing TG 56:6 ($[M+K]^+$ at *m/z* 945.7308). (i) Single-ion image showing TG 56:7 ($[M+K]^+$ at *m/z* 943.7151). (j) Single-ion image showing TG 56:8 ($[M+K]^+$ at *m/z* 941.6995). The AP-SMALDI MSI measurement was performed with 7 µm step size.

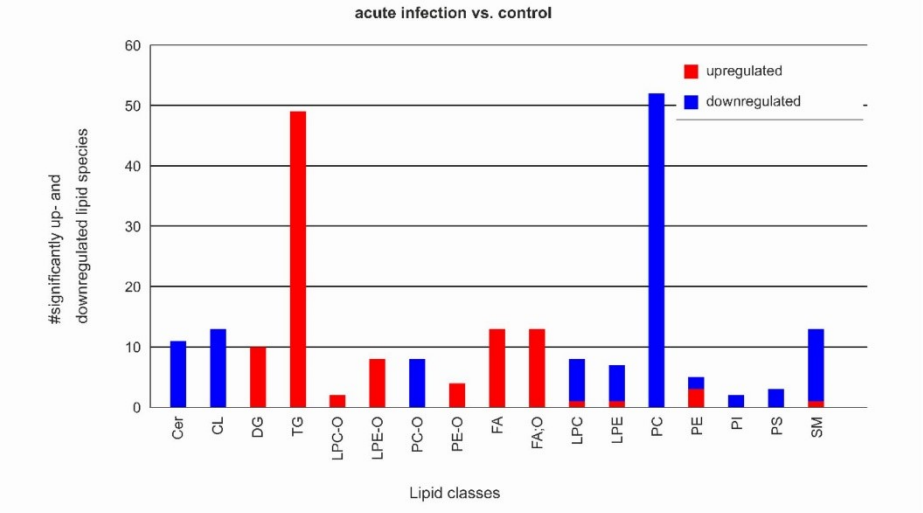

Figure S7: Overview of the number of significantly ($p < 0.05$) up- or downregulated lipid classes in rat liver during the acute infection stage compared to healthy controls. Data is based on semi-quantitative RP-LC MS/MS data analysis. A two-sided Student's T-tests with a threshold p-value of 0.05 was performed. More details are described in the supplementary note 3.

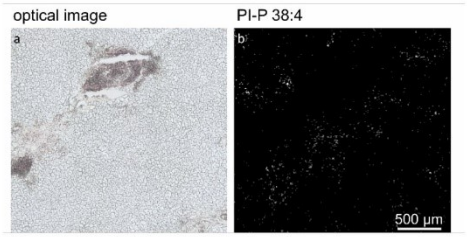

Figure S8: (a) Optical image of a control liver tissue section from a healthy rat, which was the same age as the rat of the acute infection stage. (b) Single-ion image showing PI-P 38:4 ($[M-H]^-$ at *m/z* 869.5544. The AP-SMALDI MSI measurement was performed with 10 µm step size.

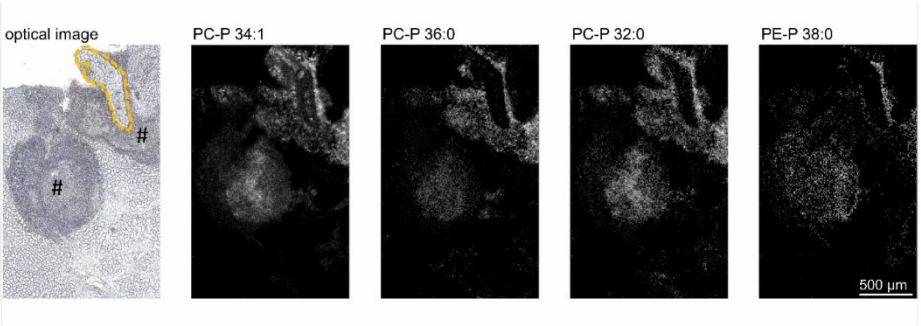

Figure S9: (a) Single-ion images showing PC-P 34:1 ($[M+K]^+$ at *m/z* 782.5460). The migrating *F. hepatica* is outlined by an orange-dotted line, and tissue lesions are marked by a hash. (b) Single-ion image showing PC-P 34:1 ($[M+K]^+$ at *m/z* 782.5460). (c) Single-ion image showing PC-P 36:0 ($[M+K]^+$ at *m/z* 812.5930). (d) Single-ion image showing PC-P 32:0 ($[M+K]^+$ at *m/z* 756.5304). (e) Single-ion image showing PE-P 38:0 ($[M+Na]^+$ at *m/z* 782.6034). The AP-SMALDI MSI measurement was performed with 7 µm step size.

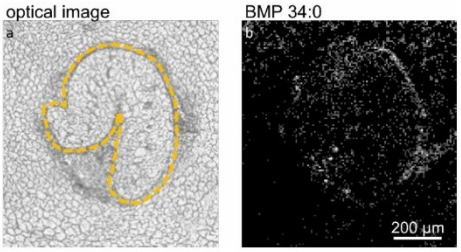

Figure S10*:* (a) Optical image of liver tissue section from a rat at the acute infection stage. The migrating *F. hepatica* is outlined by an orange dotted line. (b) Single-ion image showing BMP 34:0 ($[M-H]^-$ at *m/z* 749.5325). The AP-SMALDI MSI measurement was performed with 7 µm step size.

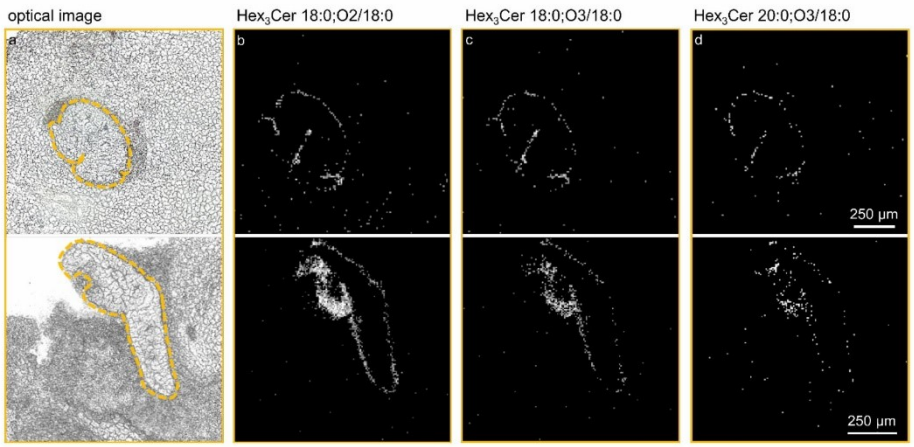

Figure S11: (a) Optical image of 1. replicate in the top row and 2. replicate in the bottom row. The migrating *F. hepatica* is outlined by an orange-dotted line. (b) Single-ion images for Hex_3Cer 18:0;O2/18:0 ($[M+K]^+$ at *m/z* 1092.6787). (c) Single-ion images for Hex_3Cer 18:0;O3/18:0 ($[M+K]^+$ at *m/z* 1108.6738). (d) Single-ion images for Hex_3Cer 20:0;O3/18:0 ($[M+K]^+$ at *m/z* 1136.7057) for each migrating *F. hepatica*. The AP-SMALDI MSI measurement in the upper row was performed with 10 µm step size. The AP-SMALDI MSI measurement in the bottom row was performed with 7 µm step size.

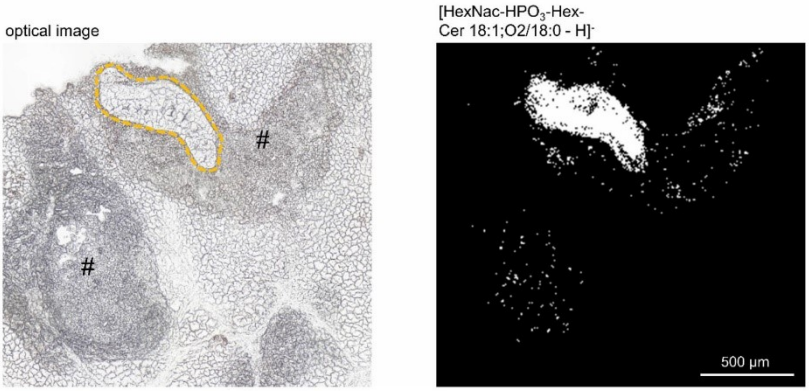

Figure S12: (a) Optical image of liver tissue section from a rat at the acute infection stage. The migrating *F. hepatica* is outlined by an orange dotted line. (b) Single-ion image showing HexNac-HPO_3-Hex-Cer 18:1;O2/18:0 ($[M-H]^-$ at *m/z* 1027.6452). The ion image is maximally overexposed to enhance the visibility of the low-intensity signals distributed across the tissue lesions. The AP-SMALDI MSI measurement was performed with 7 µm step size.

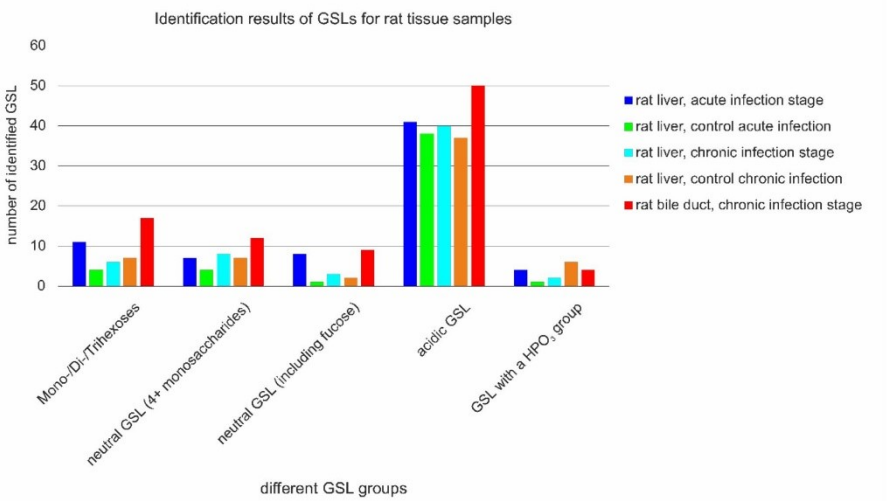

Figure S13: Total number of GLS species in host tissue samples identified through nano-HILIC MS/MS analysis with the data analysis described in Supplementary note 5. The identification results were grouped, namely as mono-/di-/trihexoses, neutral GSLs with more than four saccharide units, neutral GSLs containing at least one fucose moiety, acidic GSLs and GSLs bearing with a phosphate group.

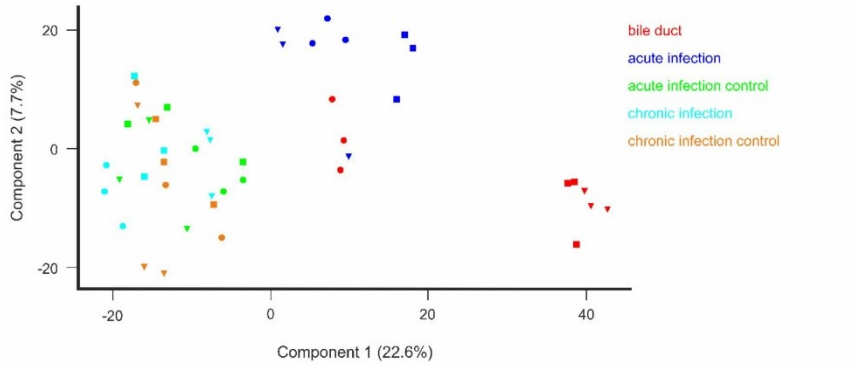

Figure S14: PCA Plot created with normalized nano-HILIC post-identification results for GSL species in positive-ion mode. Color-coded for biological groups with the bile duct samples in red, the rat liver of acute infection stage in blue, the corresponding control in green, the rat liver of chronic infection stage in turquoise and the corresponding control in yellow. Different symbols within one biological group represent biological replicates. Consequently, the same symbol within one biological group represents a technical replicate.

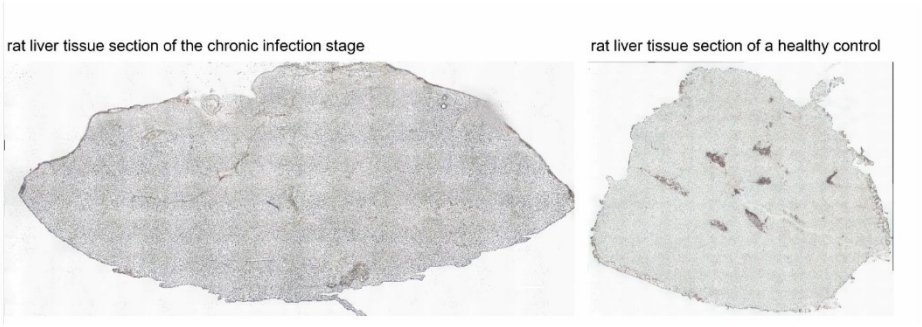

Figure S15: Optical images of rat liver tissue sections. (Left) Rat liver tissue section of the chronic *F. hepatica* infection stage (left). (Right) rat liver tissue section of a healthy control. Several blood vessels can be seen as dark areas in this tissue section.

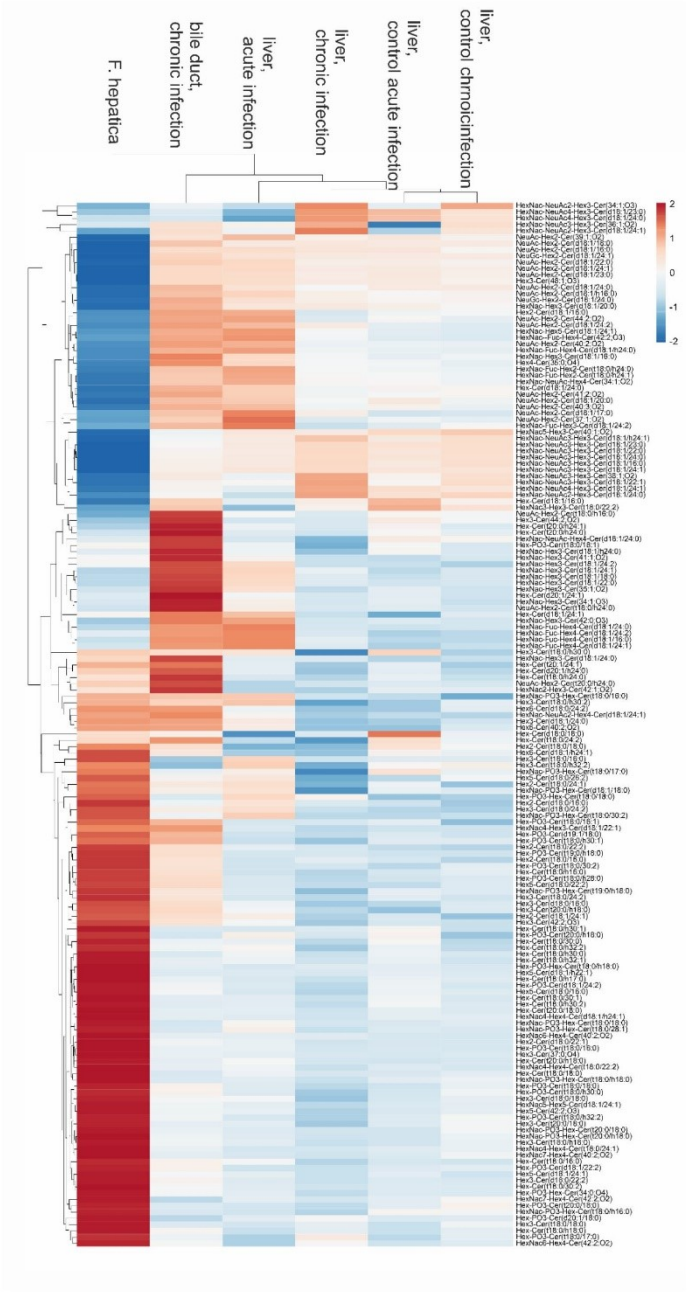

Figure S16: Hierarchical Clustering of normalized GSL profiling data. Red color represents enhanced signals, and blue color reduced signals within the different groups, respectively. The pre-processing

options “row centering” and “unit variance row scaling” were chosen. The heatmap was then generated with following parameters: Clustering distance for rows and columns: Elucidan. Clustering method for rows and columns: average. Tree ordering for rows: tightest cluster first.

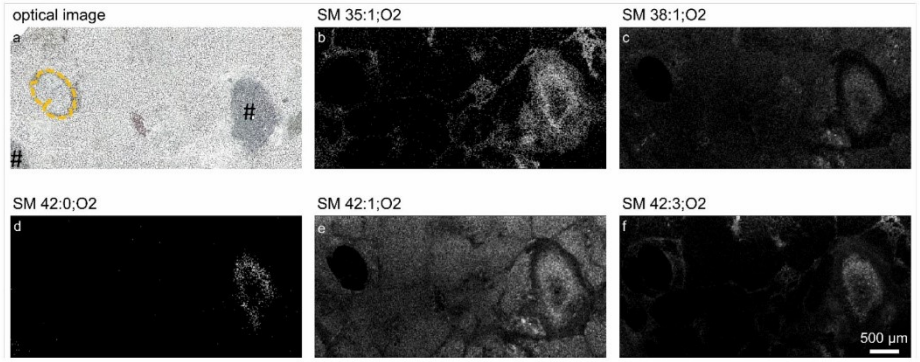

Figure S17: (a) Optical image of a liver tissue section from rat at the acute infection stage. The migrating *F. hepatica* is outlined by orange-dotted line, and tissue lesions are marked by a hash. (b) Single-ion image showing SM 35:1;O2 ($[M+Na]^+$ at *m/z* 739.5725). (c) Single-ion image showing SM 38:1;O2 ($[M+Na]^+$ at *m/z* 809.6507). (d) Single-ion image showing SM 42:0;O2 ($[M+Na]^+$ at *m/z* 839.6976). (e) Single-ion image showing SM 42:1;O2 ($[M+Na]^+$ at *m/z* 837.6820). (f) Single-ion image to (a) showing SM 42:3;O2 ($[M+Na]^+$ at *m/z* 8333.6507). The AP-SMALDI MSI measurement was performed with 10 µm step size.

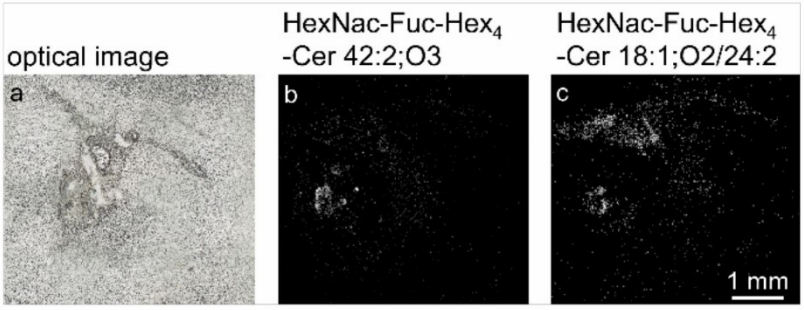

Figure S18: (a) bile duct tissue section from rat at the chronic infection stage. (b) Single-ion image showing HexNacFucHex$_4$Cer 42:2;O3 ([M+K]$^+$ at *m/z* 1699.9388). (c) Single-ion image showing HexNacFucHex$_4$Cer 18:1;O2/24:2 ([M+K]$^+$ at *m/z* 1681.9191. The AP-SMALDI MSI measurement was performed with 20 µm step size in continuous mode.

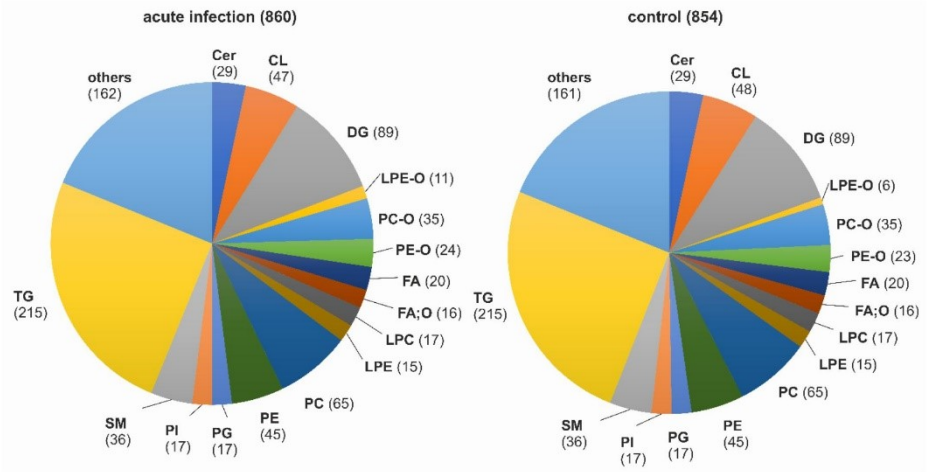

Figure S19: Pie charts showing the identified lipid species using RP-LC MS/MS analysis of liver of rat at the acute infection stage (left)) and liver of healthy controls at the same age (right). "Others" include acylsphingomyelin, bile acids, bismonoacylglycerophosphate, acylcarnitine, sterols, prenol lipids, (di)lysocardiolipin, oxidized triglyceride, GM3, N-acyl-lysophosphatidylethanolamine, lysophosphatidic acid, lysophosphatidylglycerol, lysophosphatidylinositol, lysophosphatidylserine, monoacylglycerol, fatty amides, oxidized phosphatidylethanolamine, oxidized phosphatidylinositol, oxidized triglyceride, phosphatidic acid, phosphatidylethanol, phosphatidylmethanol, phosphatidylserine, sulfatide, sulfonolipid sterol sulfate.

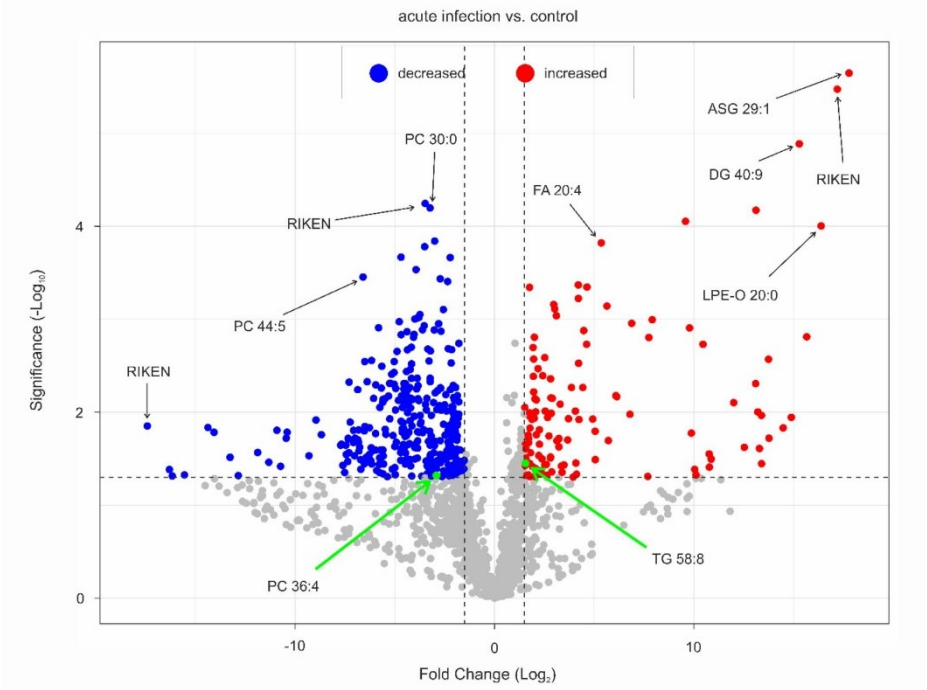

Figure S20: Volcano plot including all data points from RP-LC MS/MS analysis after MS-DIAL analysis and normalization, revealing pronounced differences between the acute infection stage and the corresponding control. The fold-change threshold was set to -1.5 to 1.5 and the significance threshold was set to $p<0.05$.

Table S1: Gradient for RP-LC MS/MS analysis.

Time / min	Mobile Phase A / %	Mobile Phase B / %
0	68	32
1.5	68	32
4	55	45
5	48	52
8	42	58
11	34	66
14	30	70
18	25	75
21	3	97
25	3	97
26	68	32
32	68	32

Table S2: Heated electrospray ionization (HESI-II) source parameters for RP-LC MS/MS analysis.

Parameter	Setting
Spray voltage / kV	±3.5
Capillary temperature / °C	300 (+), 320 (-)
Sheath gas / a.u	40 (+), 45 (-)
Aux gas / a.u.	12
Sweep gas / a.u.	2
S-Lens	55
Auxiliary heater temperature / °C	300

Table S3: Full scan (data-dependent MS/MS) acquisition method parameters for RP-LC MS/MS analysis.

Parameter	Setting
Resolution	120000 (45000)
Automatic Gain Control	$1 \cdot 10^6$ ($2 \cdot 10^5$)
Max. injection time / ms	250 (75)
Top N	15
Scan range	300 – 1800 (automatic)
Isolation window / m/z	1.0
NCE	25; 30
Intensity threshold	$1.3 \cdot 10^4$
Dynamic exclusion / s	8.0

Table S4: MS-DIAL settings for the data analysis of reversed phase RP-LC MS/MS experiments.

Task	Setting	Value
Data collection	MS 1 tolerance	0.01 Da
	MS2 tolerance	0.025 Da
	Retention time begin	0 min
	Retention time range end	25 min
	MS1 mass range begin	200 Da
	MS1 mass rage end	1800 Da
	MS/MS mass range begin	0 Da
	MS/MS mass range end	2000 Da
Peak detection	Minimum peak height	1000 amplitude
	Mass slice width	0.4
	Smoothing method	Linear weighted moving average
	Smoothing level	8 scans
	Minimum peak width	5 scans
Spectrum deconvolution	Sigma window value	0.5
	MS/MS abundance cut off	0 amplitude
	Exclude after precursor ion	check
	Keep the isotopic ions until	1
Identification (SplashLipidomix)	Accurate mass tolerance (MS1)	0.01 Da
	Retention time tolerance	4 min
	Use retention time for scoring	Check
	Use retention time for filtering	Check
Identification (Lipid Database)	Accurate Mass tolerance (MS1)	0.01 Da
	Accurate mass tolerance (MS2)	0.025 Da
	Retention time tolerance	100 min
Alignment parameters	Reference file	QC_pos_5 / QC_neg_5
	Retention time tolerance	2 min
	MS1 tolerance	0.01 Da
	Retention time factor	0.5
	MS1 factor	0.5
	Peak count filter	0%
	N% detected in at least one group	80%
	Remove features based on blank information	Check
	Sample max / blank average	5 fold change

Table S5: nano-HILIC Parameter used for separation of glycosphingolipids.

Property	Setting
Mobile Phase A	acetonitrile/methanol (99/1, v/v), 5 mM AmAc
Mobile Phase B	methanol/water (8/2, v/v), 5 mM AmAc
Loading Solvents	same as starting conditions
Injection volume	1 µL
Loading Time	0.5 minutes
Gradient	5% B for 5 minutes, to 95% B in 45 minutes, hold 95% B for 10 minutes, to 5% B in 5 minutes, hold 5% B for 35 minutes
Oven temperature	40 °C
Autosampler temperature	4 °C
Loading flow rate	30 µL/min
NC flow rate	300 nL/min

Table S6: MS and MS/MS parameters (in brackets) used for identification of GSL after nano-HILIC separation.

Parameter	Setting
Spray voltage / kV	±2.0
Capillary temperature/ °C	200
S-lens setting	100
Mass resolution at *m/z* 200	120000 (45000)
MS AGC target	$3 \cdot 10^6$ ($1 \cdot 10^5$)
MS max. injection time/ ms	100 (100)
Scan range	*m/z* 500 - 2000
Top N	15
Isolation window / Δ *m/z*	2.0
Stepped NCE	20; 25; 30
Dynamic exclusion / s	6.0

Table S7: MS-DIAL settings for the initial data analysis of the nano-HILIC MS/MS experiments. Parameters were chosen such that many features were detected. Several features were detected multiple times.

Task	Setting	Value
Data collection	MS 1 tolerance	0.05 Da
	MS2 tolerance	0.1 Da
	Retention time begin	0 min
	Retention time range end	60 min
	MS1 mass range begin	500 Da
	MS1 mass rage end	2000 Da
	MS/MS mass range begin	0
	MS/MS mass range end	2000 Da
Peak detection	Minimum peak height	5000 amplitude
	Mass slice width	0.005
	Smoothing method	Linear weighted moving average
	Smoothing level	2 scans
	Minimum peak width	3 scans
Spectrum deconvolution	Sigma window value	0.1
	MS/MS abundance cut off	0 amplitude
	Exclude after precursor ion	Check
	Keep the isotopic ions until	3
Identification (SplashLipidomix)	Accurate mass tolerance (MS1)	0.01
	Retention time tolerance	100
Alignment parameters	Reference file	QC_pos_5 / QC_neg_5
	Retention time tolerance	2 min
	MS1 tolerance	0.01 Da
	Retention time factor	0.5
	MS1 factor	0.5
	Peak count filter	0%
	N% detected in at least one group	0%

Table S8: MS/MS search parameters in MS-DIAL for the positive-ion mode. Neutral losses or product ions are listed, including the common saccharides for GSL and the mass values for the typical N^{II}-fragments.

Species	mass / u	Tolerance / Da	abundance	type
Fuc	146.057908	0.005	0.01	NeutralLoss
Fuc	147.065184	0.005	0.01	ProductIon
Hex	162.052823	0.005	0.01	NeutralLoss
Hex	163.060099	0.005	0.01	ProductIon
Fuc	164.068473	0.005	0.01	NeutralLoss
Fuc	165.075749	0.005	0.01	ProductIon
Hex	180.063388	0.005	0.01	NeutralLoss
Hex	181.070664	0.005	0.01	ProductIon
HexNac	203.079372	0.005	0.01	NeutralLoss
HexNac	204.086648	0.005	0.01	ProductIon
HexNac	221.089937	0.005	0.01	NeutralLoss
HexNac	222.097213	0.005	0.01	ProductIon
16:2;O2	234.221619	0.005	0.01	ProductIon
16:1;O2	236.237269	0.005	0.01	ProductIon
16:0;O2	238.252919	0.005	0.01	ProductIon
Hex + SO_3	242.009636	0.005	0.01	NeutralLoss
17:2;O2	248.237269	0.005	0.01	ProductIon
17:1;O2	250.252919	0.005	0.01	ProductIon
16:1;O3	252.232184	0.005	0.01	ProductIon
17:0;O2	252.268569	0.005	0.01	ProductIon
16:0;O3	254.247834	0.005	0.01	ProductIon
16:0;O2+H_2O	256.263484	0.005	0.01	ProductIon
Hex + SO3	260.020201	0.005	0.01	NeutralLoss
18:2;O2	262.252919	0.005	0.01	ProductIon
18:1;O2	264.268569	0.005	0.01	ProductIon
17:1;O3	266.247834	0.005	0.01	ProductIon
18:0;O2	266.284219	0.005	0.01	ProductIon
17:0;O3	268.263484	0.005	0.01	ProductIon
16:1;O3+H_2O	270.242749	0.005	0.01	ProductIon
17:0;O2+H_2O	270.279134	0.005	0.01	ProductIon
16:0;O3+H_2O	272.258399	0.005	0.01	ProductIon
16:0;O2+2 H_2O	274.274049	0.005	0.01	ProductIon
19:2;O2	276.268569	0.005	0.01	ProductIon
19:1;O2	278.284219	0.005	0.01	ProductIon
18:1;O3	280.263484	0.005	0.01	ProductIon
19:0;O2	280.299869	0.005	0.01	ProductIon
18:0;O3	282.279134	0.005	0.01	ProductIon
HexNac + SO_3	283.036185	0.005	0.01	NeutralLoss

17:1;O3+H_2O	284.258399	0.005	0.01	ProductIon
18:0;O2+H_2O	284.294784	0.005	0.01	ProductIon
17:0;O3+H_2O	286.274049	0.005	0.01	ProductIon
16:1;O3+2 H_2O	288.253314	0.005	0.01	ProductIon
17:0;O2+2 H_2O	288.289699	0.005	0.01	ProductIon
16:0;O3+2 H_2O	290.268964	0.005	0.01	ProductIon
20:2;O2	290.284219	0.005	0.01	ProductIon
NeuAc	291.095415	0.005	0.01	NeutralLoss
NeuAc	292.102692	0.005	0.01	ProductIon
20:1;O2	292.299869	0.005	0.01	ProductIon
t19:1	294.279134	0.005	0.01	ProductIon
20:0;O2	294.315519	0.005	0.01	ProductIon
t19:0	296.294784	0.005	0.01	ProductIon
18:1;O3+H_2O	298.274049	0.005	0.01	ProductIon
19:0;O2+H_2O	298.310434	0.005	0.01	ProductIon
18:0;O3+H_2O	300.289699	0.005	0.01	ProductIon
HexNac + SO_3	301.04675	0.005	0.01	NeutralLoss
17:1;O3+2 H_2O	302.268964	0.005	0.01	ProductIon
18:0;O2+2 H_2O	302.305349	0.005	0.01	ProductIon
17:0;O3+2 H_2O	304.284614	0.005	0.01	ProductIon
NeuGc	307.09033	0.005	0.01	NeutralLoss
NeuGc	308.097606	0.005	0.01	ProductIon
20:1;O3	308.294784	0.005	0.01	ProductIon
NeuAc	309.10598	0.005	0.01	NeutralLoss
NeuAc	310.113257	0.005	0.01	ProductIon
20:0;O3	310.310434	0.005	0.01	ProductIon
19:2;O2+2 H_2O	312.289699	0.005	0.01	ProductIon
20:0;O2+H_2O	312.326084	0.005	0.01	ProductIon
19:0;O3+H_2O	314.305349	0.005	0.01	ProductIon
18:1;O3+2 H_2O	316.284614	0.005	0.01	ProductIon
19:0;O2+2 H_2O	316.320999	0.005	0.01	ProductIon
18:0;O3+2 H2O	318.300264	0.005	0.01	ProductIon
22:2;O2	318.315519	0.005	0.01	ProductIon
22:1;O2	320.331169	0.005	0.01	ProductIon
22:0;O2	322.346819	0.005	0.01	ProductIon
NeuGc	325.100895	0.005	0.01	NeutralLoss
2 x Hex	325.112922	0.005	0.01	ProductIon
NeuGc	326.108171	0.005	0.01	ProductIon
20:1;O3+H_2O	326.305349	0.005	0.01	ProductIon
20:1;O2+2 H_2O	328.320999	0.005	0.01	ProductIon
19:1;O3+2 H_2O	330.300264	0.005	0.01	ProductIon
20:0;O2+2 H_2O	330.336649	0.005	0.01	ProductIon
19:0;O3+2 H_2O	332.315914	0.005	0.01	ProductIon
22:1;O3	336.326084	0.005	0.01	ProductIon
22:1;O2+H_2O	338.341734	0.005	0.01	ProductIon

22:0;O2+H_2O	340.357384	0.005	0.01	ProductIon
2 x Hex	342.11621	0.005	0.01	NeutralLoss
20:1;O3+2 H_2O	344.315914	0.005	0.01	ProductIon
20:0;O3+2 H_2O	346.331564	0.005	0.01	ProductIon
22:1;O3+H_2O	354.336649	0.005	0.01	ProductIon
22:1;O2+2 H_2O	356.352299	0.005	0.01	ProductIon
22:0;O2+2 H_2O	358.367949	0.005	0.01	ProductIon
2 x Hex	360.126775	0.005	0.01	NeutralLoss
2 x Hex	361.134052	0.005	0.01	ProductIon
Hex + HexNac	366.139471	0.005	0.01	ProductIon
22:1;O3+2 H_2O	372.347214	0.005	0.01	ProductIon
22:0;O3+2 H_2O	374.362864	0.005	0.01	ProductIon
Hex + HexNac	383.142759	0.005	0.01	NeutralLoss
Hex + HexNac	401.153324	0.005	0.01	NeutralLoss
Hex + HexNac	402.160601	0.005	0.01	ProductIon
2 x HexNac	407.16602	0.005	0.01	ProductIon
2 x HexNac	424.169308	0.005	0.01	NeutralLoss
2 x HexNac	442.179873	0.005	0.01	NeutralLoss
2 x HexNac	443.18715	0.005	0.01	ProductIon

Table S9: MS/MS search parameters in MS-DIAL for the negative-ion mode.

Species	Mass / u	Tolerance / Da	abundance	Type
HexNac	220.08266	0.005	0.001	ProductIon
Hex	179.056111	0.005	0.001	ProductIon
Fucose	163.061197	0.005	0.001	ProductIon
NeuAc	308.098704	0.005	0.001	ProductIon
NeuGc	324.093619	0.005	0.001	ProductIon
2 x HexNac	441.172597	0.005	0.001	ProductIon
2 x Hex	359.119499	0.005	0.001	ProductIon
Hex + HexNac	400.146048	0.005	0.001	ProductIon
HexNac + SO_3 - H	300.039474	0.005	0.001	ProductIon
Hex + SO_3 - H	259.012925	0.005	0.001	ProductIon
HexNac	221.089937	0.005	0.001	NeutralLoss
Hex	180.063388	0.005	0.001	NeutralLoss
Fucose	164.068473	0.005	0.001	NeutralLoss
NeuAc	309.10598	0.005	0.001	NeutralLoss
NeuGc	325.100895	0.005	0.001	NeutralLoss
2 x HexNac	442.179873	0.005	0.001	NeutralLoss
2 x Hex	360.126775	0.005	0.001	NeutralLoss
Hex + HexNac	401.153324	0.005	0.001	NeutralLoss
HexNac	203.079372	0.005	0.001	NeutralLoss
Hex	162.052823	0.005	0.001	NeutralLoss

Fucose	146.057908	0.005	0.001	NeutralLoss
NeuAc	291.095415	0.005	0.001	NeutralLoss
NeuGc	307.09033	0.005	0.001	NeutralLoss
2 x HexNac	424.169308	0.005	0.001	NeutralLoss
2 x Hex	342.11621	0.005	0.001	NeutralLoss
Hex + HexNac	383.142759	0.005	0.001	NeutralLoss
HexNac + SO_3 - H_2O	283.036185	0.005	0.001	ProductIon
Hex + SO_3 – H_2O	242.009636	0.005	0.001	ProductIon
HexNac	202.072095	0.005	0.001	ProductIon
Hex	161.045546	0.005	0.001	ProductIon
Fuc	145.050632	0.005	0.001	ProductIon
NeuAc	290.088139	0.005	0.001	ProductIon
NeuGc	306.083054	0.005	0.001	ProductIon
2 x HexNac	423.162032	0.005	0.001	ProductIon
2 x Hex	341.108934	0.005	0.001	ProductIon
HexNac + Hex	382.135483	0.005	0.001	ProductIon

Table S10: MS-DIAL settings for the post-identification data analysis. Parameters were optimized to avoid multiple annotations for the same feature while still annotating most of the glycosphingolipids from the database. As both criteria are contrary for the data analysis, the resulting parameters were chosen as a reasonable compromise.

Task	Setting	Value
Data collection	MS 1 tolerance	0.05 Da
	MS2 tolerance	0.025 Da
	Retention time begin	0 min
	Retention time range end	50 min
	MS1 mass range begin	500 Da
	MS1 mass rage end	2000 Da
	MS/MS mass range begin	0 Da
	MS/MS mass range end	3000 Da
Peak detection	Minimum peak height	10000 amplitude
	Mass slice width	0.25
	Smoothing method	Linear weighted moving average
	Smoothing level	15 scans
	Minimum peak width	5 scans
Spectrum deconvolution	Sigma window value	0.5
	MS/MS abundance cut off	0 amplitude
	Exclude after precursor ion	Check
	Keep the isotopic ions until	1
Identification (GSL database_Post Identification)	Accurate mass tolerance (MS1)	0.05
	Retention time tolerance	2

	Use retention time for scoring	Check
	Use retention time for filtering	Check
Alignment parameters	Reference file	QC_Pos_5
	Retention time tolerance	5 min
	MS1 tolerance	0.05 Da
	Retention time factor	0.5
	MS1 factor	0.5
	Peak count filter	0%
	N% detected in at least one group	80%
	Remove features based on blank information	Check
	Sample max / blank average	5

Table S11: GSL species identified during this study by nano-HILIC MS/MS experiments. An "x" indicates the identification in the corresponding biological group, according to the supplementary note S5.

F. hepatica	**rat liver, acute infection**	**rat liver, control acute infection**	**rat liver, chronic infection**	**rat liver, control chronic infection**	**rat bile duct, chronic infection**	**Glycosphingolipid**
x	x					Hex-Cer 18:0;O2/16:0
x	x					Hex-Cer 18:0;O2/18:0
x	x	x	x			Hex-Cer 18:1;O2/16:0
	x		x	x		Hex-Cer 18:1;O2/24:0
	x				x	Hex-Cer 18:1;O2/24:1
					x	Hex-Cer 20:1;O2/24:1
					x	Hex-Cer 20:1;O2/h24:0
x						Hex-Cer 18:0;O3/16:0
x						Hex-Cer 18:0;O3/18:0
x	x		x	x	x	Hex-Cer 18:0;O3/24:2
x						Hex-Cer 18:0;O3/30:0
x						Hex-Cer18:0;O3/30:1
x						Hex-Cer 18:0;O3/30:2
x				x	x	Hex-Cer 18:0;O3/h16:0
x						Hex-Cer 18:0;O3/h17:0
x			x		x	Hex-Cer 18:0;O3/h18:0
x					x	Hex-Cer 18:0;O3/h24:0
x						Hex-Cer 18:0;O3/h30:0
x						Hex-Cer 18:0;O3/h30:1
x						Hex-Cer 18:0;O3/h30:2
x						Hex-Cer 18:0;O3/h32:1
x						Hex-Cer 18:0;O3/h32:2
x						Hex-Cer 20:0;O3/18:0
x						Hex-Cer 20:0;O3/h18:0

x					x	Hex-Cer 20:0;O3/h24:0
x					x	Hex-Cer 20:0;O3/h24:1
					x	Hex-Cer 20:1;O3/24:1
x	x	x				Hex_2-Cer 18:0;O2/16:0
x	x					Hex_2-Cer 18:0;O2/22:1
x	x	x		x	x	Hex_2-Cer 18:1;O2/16:0
x	x	x	x	x	x	Hex_2-Cer 18:1;O2/24:1
x						Hex_2-Cer 18:0;O3/16:0
			x			Hex_2-Cer 18:0;O3/18:0
x						Hex_2-Cer 18:0;O3/22:2
						Hex_2-Cer 18:0;O3/24:1
x						Hex_3-Cer 37:0;O4
x					x	Hex_3-Cer 42:2;O3
						Hex_3-Cer 44:2;O2
x						Hex_3-Cer 48:1;O3
x						Hex_3-Cer 18:0;O2/16:0
x						Hex_3-Cer 18:0;O2/18:0
x						Hex_3-Cer 18:0;O2/22:2
x					x	Hex_3-Cer 18:0;O2/24:2
x					x	Hex_3-Cer 18:1;O2/24:0
					x	Hex_3-Cer 18:1;O2/24:1
x	x				x	Hex3-Cer 18:1;O2/24:2
x						Hex_3-Cer 18:0;O3/16:0
x				x		Hex_3-Cer 18:0;O3/18:0
x						Hex_3-Cer 18:0;O3/24:2
x						Hex_3-Cer 18:0;O3/h18:0
x						Hex_3-Cer 18:0;O3/h30:0
x						Hex_3-Cer 18:0;O3/h30:2
x						Hex_3-Cer 18:0;O3/h32:2
x				x		Hex_3-Cer 20:0;O3/18:0
x						Hex_3-Cer 20:0;O3/h18:0
						Hex_4-Cer 35:0;O4
x						Hex_5-Cer 42:2;O3
x						Hex_5-Cer 18:0;O2/16:0
x						Hex_5-Cer 18:0;O2/22:2
x						Hex_5-Cer 18:0;O2/26:2
x						Hex_5-Cer 18:1;O2/24:1
x						Hex_5-Cer 18:1;O2/h22:1
x						Hex_6-Cer 40:2;O2
x						Hex_6-Cer 18:0;O2/24:2
x						Hex_6-Cer 18:1;O2/h24:1
x						Hex_6-Cer 18:0;O3/h24:2
						Hex_8-Cer 42:2;O2
					x	$HexNacHex_3$-Cer 34:1;O3
					x	$HexNacHex_3$-Cer 35:1;O2

	x			x	x	$HexNacHex_3$-Cer 41:1;O2
			x		x	$HexNacHex_3$-Cer 42:0;O3
	x	x	x	x	x	$HexNacHex_3$-Cer 18:1;O2/16:0
			x	x	x	$HexNacHex_3$-Cer 18:1;O2/18:0
					x	$HexNacHex_3$-Cer 18:1;O2/20:0
x	x					$HexNacHex_3$-Cer 18:1;O2/22:0
	x	x	x		x	$HexNacHex_3$-Cer 18:1;O2/24:0
	x	x	x	x	x	$HexNacHex_3$-Cer 18:1;O2/24:1
	x			x	x	$HexNacHex_3$-Cer 18:1;O2/24:2
			x			$HexNacHex_3$-Cer 18:1;O2/h24:0
	x	x	x	x	x	$HexNacHex_5$-Cer 18:1;O2/24:1
x					x	$HexNac_2Hex_3$-Cer 42:1;O2
						$HexNac_2Hex_4$-Cer 18:1;O2/h24:0
x						$HexNac_3Hex_3$-Cer 18:0;O2/24:2
x						$HexNac_3Hex_3$-Cer 18:1;O2/22:1
x				x		$HexNac_3Hex_3$-Cer 18:0;O3/22:2
x			x			$HexNac_3Hex_3$-Cer 18:0;O3/24:2
						$HexNac_3Hex_5$-Cer 42:3;O2
x						$HexNac_4Hex_3$-Cer 18:1;O2/22:1
x						$HexNac_4Hex_3$-Cer 18:1;O2/24:1
x						$HexNac_4Hex_4$-Cer 18:1;O2/h24:1
x						$HexNac_4Hex_4$-Cer 18:0;O3/22:2
x						$HexNac_4Hex_4$-Cer 18:0;O3/24:1
x						$HexNac_5Hex_3$-Cer 40:1;O2
x						$HexNac_5Hex_5$-Cer 18:1;O2/24:1
						$HexNac_5Hex$-Cer 32:0;O2
x						$HexNac_6Hex_4$-Cer 40:2;O2
x						$HexNac_6Hex_4$-Cer 42:2;O2
x						$HexNac_7Hex_4$-Cer 40:2;O2
x						$HexNac_7Hex_4$-Cer 42:2;O2
	x				x	$HexNacFucHex_2$-Cer 18:0;O3/h24:0
	x				x	$HexNacFucHex_2$-Cer 18:0;O3/h24:1

	x				x	$HexNacFucHex_3$-Cer 18:1;O2/24:2
					x	$HexNacFucHex_4$-Cer 42:2;O3
	x		x		x	$HexNacFucHex_4$-Cer 18:1;O2/16:0
	x				x	$HexNacFucHex_4$-Cer 18:1;O2/24:0
	x				x	$HexNacFucHex_4$-Cer 18:1;O2/24:1
	x	x	x	x	x	$HexNacFucHex_4$-Cer 18:1;O2/24:2
	x		x	x	x	$HexNacFucHex_4$-Cer 18:1;O2/h24:0
						$HexNac_2Fuc_2Hex_3$-Cer 18:1;O2/16:0
						$HexNac_2FucHex_4$-Cer 18:1;O2/24:2
	x	x	x	x	x	$NeuAcHex_2$-Cer 37:1;O2
	x	x	x	x	x	$NeuAcHex_2$-Cer 39:1;O2
	x	x	x	x	x	$NeuAcHex_2$-Cer 40:2;O2
						$NeuAcHex_2$-Cer 40:3;O2
						$NeuAcHex_2$-Cer 41:2;O2
	x					$NeuAcHex_2$-Cer 42:1;O3
						$NeuAcHex_2$-Cer 42:2;O3
	x	x	x	x	x	$NeuAcHex_2$-Cer 44:2;O2
	x	x	x	x	x	$NeuAcHex_2$-Cer 18:1;O2/16:0
	x	x				$NeuAcHex_2$-Cer 18:1;O2/17:0
	x	x	x	x	x	$NeuAcHex_2$-Cer 18:1;O2/18:0
	x	x	x	x	x	$NeuAcHex_2$-Cer 18:1;O2/20:0
	x	x	x	x	x	$NeuAcHex_2$-Cer 18:1;O2/22:0
	x	x	x	x	x	$NeuAcHex_2$-Cer 18:1;O2/23:0
x	x	x	x	x	x	$NeuAcHex_2$-Cer 18:1;O2/24:0
	x	x	x	x	x	$NeuAcHex_2$-Cer 18:1;O2/24:1
	x	x	x	x	x	$NeuAcHex_2$-Cer 18:1;O2/24:2
	x		x		x	$NeuAcHex_2$-Cer 18:1;O2/h16:0
		x	x	x	x	$NeuAcHex_2$-Cer 18:0;O3/h16:0
					x	$NeuAcHex_2$-Cer 18:0;O3/h24:0
					x	$NeuAcHex_2$-Cer 20:0;O3/h24:0
		x	x	x		$NeuGcHex_2$-Cer 18:1;O2/16:0

		x	x	x	x	$NeuGcHex_2$-Cer 18:1;O2/24:0
					x	$NeuGcHex_2$-Cer 18:1;O2/24:1
	x		x		x	$HexNacNeuAcHex_4$-Cer 34:1;O2
						$HexNacNeuAcHex_4$-Cer 36:1;O2
					x	$HexNacNeuAcHex_4$-Cer 38:1;O2
					x	$HexNacNeuAcHex_4$-Cer 41:1;O2
					x	$HexNacNeuAcHex_4$-Cer 18:1;O2/24:0
					x	$HexNacNeuAcHex_4$-Cer 18:0;O3/h22:0
		x	x	x		$HexNacNeuGc_2Hex_3$-Cer 36:1;O2
	x	x	x	x	x	$HexNacNeuGc_2Hex_3$-Cer 42:2;O2
	x				x	$HexNacNeuGcHex_3$-Cer 42:3;O2
					x	$HexNacNeuGcHex_4$-Cer 34:1;O2
					x	$HexNacNeuGcHex_4$-Cer 42:1;O2
					x	$HexNacNeuGcHex_4$-Cer 42:1;O3
					x	$HexNacNeuGcHex_4$-Cer 42:2;O2
					x	$HexNacNeuGcHex_4$-Cer 44:1;O4
	x	x				$HexNacNeuAc_2Hex_3$-Cer 34:1;O3
	x	x		x	x	$HexNacNeuAc_2Hex_3$-Cer 36:1;O2
	x	x	x	x		$HexNacNeuAc_2Hex_3$-Cer 38:1;O2
						$HexNacNeuAc_2Hex_3$-Cer 38:1;O2
	x	x	x			$HexNacNeuAc_2Hex_3$-Cer 40:3;O2
						$HexNacNeuAc_2Hex_3$-Cer 42:1;O4
	x	x	x		x	$HexNacNeuAc_2Hex_3$-Cer 18:1;O2/16:0)
	x	x	x	x		$HexNacNeuAc_2Hex_3$-Cer 18:1;O2/22:0
	x	x	x	x	x	$HexNacNeuAc_2Hex_3$-Cer 18:1;O2/22:1
			x			$HexNacNeuAc_2Hex_3$-Cer 18:1;O2/23:0
	x		x	x	x	$HexNacNeuAc_2Hex_3$-Cer 18:1;O2/24:0
x	x	x	x	x		$HexNacNeuAc_2Hex_3$-Cer 18:1;O2/24:1

	x	x	x	x	x	$HexNacNeuAc_2Hex_3$-Cer 18:1;O2/24:2
						$HexNacNeuAc_2Hex_3$-Cer 18:1;O2/h22:1
x					x	$HexNacNeuAc_2Hex_3$-Cer 18:1;O2/h24:1
	x			x	x	$HexNacNeuAc_2Hex_4$-Cer 18:1;O2/16:0
	x	x	x	x	x	$HexNacNeuAc_2Hex_4$-Cer 18:1;O2/24:1
	x		x	x	x	$HexNacNeuAc_3Hex_3$-Cer 36:1;O2
	x	x	x	x	x	$HexNacNeuAc_3Hex_3$-Cer 38:1;O2
	x	x	x	x	x	$HexNacNeuAc_3Hex_3$-Cer 18:1;O2/16:0
	x	x	x	x	x	$HexNacNeuAc_3Hex_3$-Cer 18:1;O2/22:0
	x	x	x	x	x	$HexNacNeuAc_3Hex_3$-Cer 18:1;O2/22:1
	x	x	x	x	x	$HexNacNeuAc_3Hex_3$-Cer 18:1;O2/23:0
	x	x	x	x	x	$HexNacNeuAc_3Hex_3$-Cer 18:1;O2/24:0
	x	x	x	x	x	$HexNacNeuAc_3Hex_3$-Cer 18:1;O2/24:1
					x	$HexNacNeuAc_3Hex_3$-Cer 18:1;O2/h24:1
	x	x	x	x	x	$HexNacNeuAc_4Hex_3$-Cer 18:1;O2/23:0
	x	x	x	x	x	$HexNacNeuAc_4Hex_3$-Cer 18:1;O2/24:0
	x	x	x	x	x	$HexNacNeuAc_4Hex_3$-Cer 18:1;O2/24:1
x						$Hex\text{-}HPO_3$-Cer 18:1;O2/22:2
x						$Hex\text{-}HPO_3$-Cer 18:1;O2/24:2
x						$Hex\text{-}HPO_3$-Cer 19:1;O2/18:0
x						$Hex\text{-}HPO_3$-Cer 20:1;O2/18:0
x						$Hex\text{-}HPO_3$-Cer 18:0;O3/16:0
x						$Hex\text{-}HPO_3$-Cer 18:0;O3/16:1
x						$Hex\text{-}HPO_3$-Cer 18:0;O3/17:0
x	x	x	x		x	$Hex\text{-}HPO_3$-Cer 18:0;O3/18:0
						$Hex\text{-}HPO_3$-Cer 18:0;O3/18:1
x						$Hex\text{-}HPO_3$-Cer 18:0;O3/28:1
x				x		$Hex\text{-}HPO_3$-Cer 18:0;O3/30:2
x						$Hex\text{-}HPO_3$-Cer 18:0;O3/h28:0
x					x	$Hex\text{-}HPO_3$-Cer 18:0;O3/h30:0
x						$Hex\text{-}HPO_3$-Cer 18:0;O3/h30:1
x						$Hex\text{-}HPO_3$-Cer 18:0;O3/h32:2

x						Hex-HPO_3-Cer 19:0;O3/h18:0
x				x		Hex-HPO_3-Cer 20:0;O3/18:0
x						Hex-HPO_3-Cer 20:0;O3/h18:0
x						Hex-HPO_3-Hex-Cer 34:0;O4
x				x		Hex-HPO_3-Hex-Cer 18:0;O3/18:0
x	x		x	x	x	Hex-HPO_3-Hex-Cer 18:0;O3/h18:0
					x	HexNac-HPO_3-Hex-Cer 42:0;O4
x						HexNac-HPO_3-Hex-Cer 18:1;O2/18:0
						HexNac-HPO_3-Hex-Cer 18:0;O3/16:0
x						HexNac-HPO_3-Hex-Cer 18:0;O3/17:0
x	x					HexNac-HPO_3-Hex-Cer 18:0;O3/18:0
x						HexNac-HPO_3-Hex-Cer 18:0;O3/28:1
x	x					HexNac-HPO_3-Hex-Cer 18:0;O3/30:2
x						HexNac-HPO_3-Hex-Cer 18:0;O3/h16:0
x				x		HexNac-HPO_3-Hex-Cer 18:0;O3/h18:0
x						HexNac-HPO_3-Hex-Cer 18:0;O3/h30:2
x						HexNac-HPO_3-Hex-Cer 18:0;O3/h32:2
x						HexNac-HPO_3-Hex-Cer 19:0;O3/h18:0
x						HexNac-HPO_3-Hex-Cer 20:0;O3/18:0
x				x		HexNac-HPO_3-Hex-Cer 20:0;O3/h18:0

Table S12: Significant up- or downregulated species in the chronic infection stage compared to the same-aged healthy control. The RP-LC MS/MS data was analyzed according to the Supplementary Note 3. For revealing significant up- and downregulation between two biological groups, a two-sided Student's T-tests with a threshold p-value of 0.05 was performed. "↑" indicates upregulated species in the chronic infection, and "↓" downregulated species, respectively.

Metabolite Name	**Up- or downregulated at the chronic infection stage**	**p-value**
CAR 16:1	↓	0.01554072
DG 32:4	↑	0.00125331
DG 52:4|DG 16:0_36:4	↓	0.02533482
LPC O-16:0	↑	0.03285521
LPC O-16:1	↑	0.01026609
LPE O-18:1	↑	0.03906403
PEtOH 34:2|PEtOH 16:0_18:2	↑	0.03262315
RIKEN P-VS1 ID-9947 from Mouse_Eye_fads2KO_N_Ctr	↓	0.01181219
ST 24:1;O5	↑	0.00626699
TG 62:14|TG 18:2_22:6_22:6	↓	0.03770863
TG 62:14|TG 20:4_20:4_22:6	↓	0.04641163

References

(1) Paschke, C.; Leisner, A.; Hester, A.; Maass, K.; Guenther, S.; Bouschen, W.; Spengler, B. Mirion--a software package for automatic processing of mass spectrometric images, *Journal of the American Society for Mass Spectrometry.* **2013**, *24,* pp. 1296–1306.

(2) Goedhart, J.; Luijsterburg, M. S. VolcaNoseR is a web app for creating, exploring, labeling and sharing volcano plots, *Scientific reports.* **2020**, *10,* p. 20560.

(3) Metsalu, T.; Vilo, J. ClustVis: a web tool for visualizing clustering of multivariate data using Principal Component Analysis and heatmap, *Nucleic acids research.* **2015**, *43,* W566-70.

Acknowledgements

First, I want to express my deepest gratitude to Professor Dr. Bernhard Spengler for giving me the opportunity to prepare my doctoral thesis under his supervision. This includes the time and outstanding expertise he invested in giving feedback whenever required and also the state-of-the-art instrumental equipment and laboratory. Besides the professional level, he was extremely supportive and made it possible for me to balance my work with starting my own small family.

Further, I especially want to thank Prof. Dr. Sven Heiles. Starting already from the bachelor thesis until volunteering of being the second referee of this doctoral thesis, he accompanied my scientific career. During this period, he invested a lot of effort in discussing ideas and concepts, as well as giving his exceptional advice in every relevant field in academia. Even when he moved away from Giessen, it was always possible to reach out and get advice.

I would also like to honour my collaboration partners. Without their contribution, the realisation of my dissertation would not have been possible. I was always able to rely on their help and support with all my questions and requests. In particular, I have to mention Svenja Gramberg, Simone Haeberlein and Martin Roderfeld.

In addition, I want to thank all former and current members from the working group of Professor Dr. Spengler. The atmosphere and spirit are exceptional, and the readiness to help is outstanding. Special thanks to Dr. Parviz Ghezellou, Dr. Christian Schäfer, Dr. Stefanie Gerbig, Dr. Max Müller and Dr. Domenic Dreisbach for their guidance and constant support.

Last, but of utmost importance, I want to thank my family and my wife for the fundamental and unconditional support during the entire period. I want to thank especially my wife, Bonnie Luh, who always supported and encouraged me, giving me enough energy to persevere during difficult phases. Without you and your love, I would have never been able to complete my doctorate.

Declaration

I declare that I have completed this dissertation without the unauthorized help of a second party and only with the assistance acknowledged therein. I have appropriately acknowledged and referenced all text passages that are derived literally from or are based on the content of published or unpublished work of others, and all information that relates to verbal communications. I have abided by the principles of good scientific conduct laid down in the charter of the Justus Liebig University of Giessen in carrying out the investigations described in the dissertation.

_____

Place, date and signature

Versicherung:

„Ich erkläre: Ich habe die vorgelegte Dissertation selbständig und ohne unerlaubte fremde Hilfe und nur mit den Hilfen angefertigt, die ich in der Dissertation angegeben habe. Alle Textstellen, die wörtlich oder sinngemäß aus veröffentlichten Schriften entnommen sind, und alle Angaben, die auf mündlichen Auskünften beruhen, sind als solche kenntlich gemacht. Bei den von mir durchgeführten und in der Dissertation erwähnten Untersuchungen habe ich die Grundsätze guter wissenschaftlicher Praxis, wie sie in der „Satzung der Justus-Liebig-Universität Gießen zur Sicherung guter wissenschaftlicher Praxis“ niedergelegt sind, eingehalten.“

_____

Ort, Datum und Unterschrift